An Experimental Investigation of the Influence of Inlet Distortion on the Fluid Borne Noise of a Centrifugal Pump

by

Scott Andrew Barton
B.S. Aerospace Engineering, University of Notre Dame (1989)

Submitted to the Department of
Aeronautics and Astronautics
in partial fulfillment of the
requirements for the degree of

Master of Science

at the

Massachusetts Institute of Technology

September, 1991

Signature of Author _____
Department of Aeronautics and Astronautics
August 16, 1991

Certified by _____
Professor Alan H. Epstein
Thesis Supervisor

Accepted by _____
Professor Harold Y. Wachman
Chairman, Department Graduate Committee

An Experimental Investigation of the Influence of Inlet Distortion on the Fluid Borne Noise of a Centrifugal Pump

by

Scott Andrew Barton

Submitted to the Department of Aeronautics and Astronautics
in September 1991 in partial fulfillment of the
requirements for the degree of
Master of Science in Aeronautics and Astronautics

Abstract

Experiments were conducted to investigate the influence of inlet distortion on the noise produced by a centrifugal water pump at the blade passage frequency. A qualitative model is presented whereby such an influence could exist.

A facility consisting of a four inch inlet centrifugal seawater pump with quiet motor, operating in a closed-circuit water loop was designed and constructed for the experiments. A two-dimensional Pitot-static probe traverser was installed at the inlet of the pump in order to measure the steady-state axial velocity profile, and flush mounted hydrophones were placed at inlet and outlet stations to obtain acoustic measurements.

The pump installation configuration was varied in order to obtain four inlet flow profiles with increasing characteristic distortion– a uniform velocity flow, a nearly fully developed turbulent flow, an asymmetric, distorted profile due to secondary flow through a 90° elbow, and a highly distorted flow through an eccentric orifice. Simultaneous inlet flow field and acoustic measurements were made for these four cases, and show that even for large magnitudes of circumferential flow distortion at the inlet, the maximum change in measured blade passage peak levels was 2.7 deciBels.

Thesis Supervisor: Dr. Alan H. Epstein
Title: Professor of Aeronautics and Astronautics

Acknowledgments

The participation of the following individuals is gratefully acknowledged:

Professor Alan H. Epstein, for his guidance and practical insight.

Professors K. U. Ingard, J. E. Ffowcs Williams and A. Von Flotow, all of whom contributed greatly to interpretation of the experimental results.

The staff of the Gas Turbine Laboratory, who helped with the logistics of experimental work.

This research has been supported by the Office of Naval Research, Mr. James Fine, technical monitor. The author is grateful to the Air Force Research in Aerospace Propulsion Technology program (AFRAPT) for personal funding.

Table of Contents

List of Figures

List of Tables

Nomenclature

A	complex amplitude
a	duct radius
c	acoustic wave speed
c_o	free acoustic wave speed
d, D	duct diameter
E	elastic modulus
Δf	frequency spectral bandwidth
f	frequency [Hz]
f_{bp}	blade passage frequency
f_{sh}	shaft frequency
H_{yx}	transfer function of signals x and y
Jn	Bessel function of n^{th} order
$J'n$	first derivative of the Bessel function
K	resistance coefficient of a porous screen
k	wave number
k^r	radial wave number of a shell-fluid combination
M	Mach number
N	shaft speed
p	spectral pressure amplitude distribution
p_o	standard reference pressure for water applications
$\overline{p}_{xx}$	ensemble average autospectrum of signal x
$\overline{p}_{yx}$	ensemble average cross spectrum of signals x and y
p_1, p_2	microphone pressure amplitudes for the reflection coefficient development
Δp	pressure change
$\delta(\Delta p)$	pressure drop perturbation
Δp_c	pump pressure rise correction term for Orifice Distorted case

Δp_d	desired pump pressure rise for Orifice Distorted case
Δp_e	experimentally determined pump pressure rise for Orifice Distorted case
Q	flow rate
q	dynamic pressure
q_{cl}	center line dynamic pressure
R	reflection coefficient
r	radial coordinate of inlet flow field cross section
S_p	non-dimensional pressure spectral density
s	separation distance for the two microphone method
SPL	acoustic sound pressure level
$std()$	standard deviation
T	period
TL	transmission loss
U	center line flow velocity
u	grid point local steady state velocity
$\bar{u}$	Pitot-static probe area averaged steady state velocity
V	volume mean velocity
w	duct wall thickness
x	rectilinear coordinate of inlet flow field cross section, positive parallel to $\theta = 0°$
y	rectilinear coordinate of inlet flow field cross section, positive parallel to $\theta = 270°$
Y	acoustic admittance
Z	acoustic impedance
α	asymmetry parameter
β	orifice diameter ratio
χ	compliance ratio for duct attenuation analysis
ε	elastic modulus loss factor
ϕ_{xx}	autospectral density of signal x

γ^2	coherence function
η	normalized acoustic admittance
κ	fluid compressibility
λ	acoustic wavelength
θ	angular coordinate of inlet flow field cross section, $\theta = 0°$ oriented as shown in Figure 2.15
ρ_f	fluid density
ρ_w	mass density of duct wall
ω	angular frequency
ω_o	resonance frequency
ζ	normalized acoustic impedance
*	conjugate operator

1. Introduction and Background

This thesis presents the results of an investigation of the fluid borne acoustic pressure field, or noise, produced by a centrifugal pump with a vaneless volute. In many applications, pump noise must be minimized to create a tolerable environment for people, or to maintain stealth for military or strategic purposes. Pump noise also tends to vary inversely with efficiency, so that reducing noise levels will generally have the added effect of increasing performance.

Centrifugal pump noise can be classified into two groups: noise caused by mechanical components- motor noise, vibration, etc. and noise caused by fluid interaction with the impeller, casing and vanes. Of the latter, the primary frequencies of interest are the shaft and blade passage frequencies, and their harmonics. The shaft tone occurs at the frequency associated with the rotating speed of the pump, and is generally caused by dynamic imbalance in the impeller or drive system, or by inhomogeneities in impeller blade geometry. The blade passage tone appears at that frequency equal to the shaft speed multiplied by the number of blades. The primary causes are the unsteady interaction between flow leaving the impeller vanes and the cutwater and volute walls, as well as the unsteady pressure field effects due to blades rotating through a circumferentially non-symmetric inlet flow field.

Other sources of flow generated noise include broad band noise generated by turbulence, Strouhal tones due to periodic vortex formation in flows past obstructions and side branches, and relatively high frequency noise caused by cavitation.

The research presented here focused on the blade passage tone, and attempted to determine the influence of inlet distortion on the noise level at that frequency. The approach was entirely experimental, and involved the design and construction of a facility to operate a centrifugal pump in water, under varying inlet conditions.

Simultaneous measurements of inlet flow field and acoustic pressure field were made for four inlet profile cases of varying levels of distortion. The flow field and acoustic data were compared to discern the existence of any correlation.

1.1. Previous Efforts Toward Pump Noise Control

Very little work has thus far been documented in the open literature on the characterization of pump flow noise, much less than that available on the acoustics of fans, blowers, and compressors. What little work that has been done has focused on minimizing the blade passage tone, which generally dominates the noise spectrum.

Simpson[1-3] et. al., in a series of papers between 1966 and 1971, experimentally investigated the effects of varying pump loading, speed, inlet total pressure (NPSH), and volute cutwater geometry on shaft, blade, and total noise levels. An accompanying potential flow theory attempted to correlate these parametric effects, and met with some success, although some assumptions made in the analysis are not confirmed experimentally. Yuasa[4] and Hinata more closely measured the fluctuating flow behind an impeller and showed that blade circulation is a more significant source of exit velocity unsteadiness than viscous wakes, but that wakes are primarily responsible for static pressure fluctuations. Sudo et. al.[5] studied the effect of cutwater clearance and skew angle, with results inconsistent with Simpson.

A recent thesis by Mongeau[6] presents measurements made on a centrifugal pump impeller operating in air with no casing. One conclusion of that work was that the prominent peaks in the acoustic spectrum were caused by the interaction of rotating stall and the impeller blades, a phenomenon which was found to exist even at the design point. This work is also significant in that empirical techniques are applied to separate the overall noise spectrum into a source component due to the impeller and a response

component resulting from propagation effects such as duct resonance and reflection. A better estimate was thereby made of the source noise spectrum.

As previously stated, many studies have been made of acoustic noise sources in air-breathing centrifugal turbomachinery, including fans, blowers, and compressors. These works can be of some qualitative value if differences in fluid properties are considered, but are of little use from a design standpoint. A comprehensive review of research on fan noise is given by Niese[7].

Only one mention was found in the literature concerning the influence of inlet distortion on pump noise. This was made by Deeproose[8], who presents data showing an increase in broad-band noise due to the movement of inlet guide vanes closer to the pump inlet. No effect on blade tone was observed. Beyond this brief test, no work has been presented on the relationship between inlet distortion and noise output, to the knowledge of the author.

1.2. Inlet Distortion as a Noise Source

The conceptual mechanism relating a distorted, or asymmetric inlet flow field to noise at the blade passage tone can be described with reference to Figure 1.1. To a centrifugal impeller blade rotating in a symmetric inlet axial velocity field, as shown in Figure 1.1a, the dynamic pressure loading due to the flow velocity relative to the blade is invariant with time, as represented by the straight, dashed line in Figure 1.1c. But, if the axial velocity field is asymmetric, meaning that it has circumferential variations at the inlet cross section, as shown in Figure 1.1b, then the dynamic pressure loading on a blade will be a harmonic function of time, with period $T=1/f_{sh}$, where f_{sh} is the shaft frequency and is equal to the shaft speed, N in RPM divided by 60.

This relationship of blade loading frequency to shaft speed is true if the fundamental circumferential mode of the inlet velocity profile has angular period 2π, meaning that the velocity pattern as a function of circumferential angle does not repeat itself at angular intervals of less than 180°. It is possible to encounter an inlet profile which has angular period π or $2\pi/3$, in which case the blade loading frequency is some multiple of f_{sh}. These cases are somewhat pathological, however, and are not encountered in common practice. The 2π, or fundamental mode occurs most frequently, resulting

from upstream duct fittings such as bends and branches, as well as circumferential variations in surface roughness.

Applying Newton's third law to the blade–flow field interaction, it can be seen that the dynamic load applied to the blade will be countered by a pressure force applied to the fluid. If the impeller has n blades, the cumulative pressure field generated by all n blades can be shown by a cumulative time history plot, as shown in Figure 1.1d, where a pressure signal is generated with a frequency $1/T = nN/60 = f_{bp}$, the blade passage frequency.

The above analysis hypothesizes the existence of a mechanism by which inlet distortion may have an influence on the blade passage acoustic tone, and provides a basis for the undertaking of the present study. The arguments presented are qualitative– no estimate of amplitude is made relative to other sources of blade passage noise, such as wake interaction at the volute cutoff. Even if the phenomenon described above does exist, the noise thereby generated may not be measurable due to saturation by these other sources. It would be necessary to eliminate extraneous sources by, for example, using a non-cutoff volute, in order to isolate the phenomenon of interest. With these contentions in mind, and as a matter of first course, it was attempted to determine whether the influence of inlet distortion of blade passage noise was significant enough to be measurable in a typical pump configuration.

1.3. Acoustic Conduction in Water-filled Ducts

It is instructive to state in these introductory remarks some standard assumptions made in considering acoustic propagation in water-filled ducts. These simple assumptions are crucial to the analysis of the experimental results.

The key distinguishing feature of water as an acoustic fluid, as opposed to air or some other gas, is its very low compressibility, which makes the speed of sound in water very high. This property manifests itself in many ways, and can be either a liability or a benefit, depending upon the phenomenon of interest.

High sound speed makes acoustic wavelengths in water very large, on the order of meters for frequencies below 1000 Hz. Because variations in

geometry of the conducting medium, ducting in the present case, must have scale on the order of wavelength to effect the acoustic field, minor variations such as small steps, expansions, and bends have little effect on the fluids ability to conduct acoustic waves. Additionally, large wavelengths force the cutoff frequency, above which higher order radial modes can propagate in the duct, to be many kilohertz for typical duct diameters. This condition makes any higher order modes produced by an acoustic source attenuate rapidly, so that a few duct diameters from the source, the acoustic field can be considered to consist solely of zeroth order, planar waves.

Lastly, it is generally understood that the influence of bulk velocity, or volume flow rate of the conducting fluid, on the acoustic field scales with the flow Mach number, so that for velocities very much less than the speed of sound, c_0 = 1500 m/s, the presence of mean flow can be ignored.

The liability of high sound speed is that the resulting impedance of water is more closely matched to that of the ducting and other structural members, so that the likelihood of vibro-acoustic interaction between fluid and structure is increased dramatically compared to that for air. It is therefore necessary to address the possibility of acoustic radiation of structural vibration when assessing the validity of acoustic measurements.

There are some benefits, therefore, to using water as a working fluid for acoustic measurements, if steps are taken to minimize and quantify fluid-structure interaction. Such interaction can be a significant drawback, however, and along with other logistic difficulties, has driven some researchers to use air to study experimental models of hydroacoustic applications. An example is Mongeau[6].

For the purposes of this experiment, water was used as the working fluid, primarily because the pump considered was designed for that fluid.

1.4. Project Goals

The approach taken to the present investigation, to study the relationship between inlet axial velocity distortion and pump noise at the blade passage frequency, can be broken down into four objectives:

(1) Design and build a test facility in which a centrifugal pump could be conventionally installed and operated, and in which

acoustic measurements near the pump inlet and outlet could be made.

(2) Design an assembly for the purpose of generating and measuring the axial velocity of the following pump inlet flow profile cases, under the conditions of typical pump operation, specifically high static pressure and fluid flow rate:
   a. Fully Developed profile, a nominally symmetric profile generated by many diameters of straight ducting upstream of the pump;
   b. Uniform profile, with a constant axial velocity over the cross section at the inlet plane;
   c. Elbow Distorted profile, with mild distortion due to secondary flow, generated by a 90° pipe elbow close-coupled to the pump inlet;
   d. Orifice Distorted profile, a highly asymmetric flow field formed by flow passing through an ASME standard eccentric orifice of diameter ratio 1/2.

(3) Perform evaluation studies to determine the quality of the acoustic measurements with regards to propagation effects such as vibration, reflection, transmission loss and resonance, and flow field effects such as turbulence. Also show that pump performance is comparable under all inlet flow conditions, to validate acoustic comparisons made under these different conditions.

(4) Simultaneously make acoustic and inlet flow field measurements, for a set of inlet profiles with varying degrees of distortion. Compare the results of these measurements to determine the existence of the phenomenon of interest.

Techniques used to achieve these objectives, results obtained and conclusions drawn are described in the remainder of this report. Chapter 2 discusses objectives (1) through (3), the Experimental Approach, first describing the Acoustic Pump Loop facility, including instrumentation and methods used to measure acoustic and vibrational phenomena, as well as to generate and measure the various inlet flow profiles. The remainder of the

chapter then describes validation studies conducted to assess the quality of acoustic measurements made with the facility. Chapter 3 presents the Results of objective (4) with regards to acoustic and flow field measurements for all inlet profile cases, and Chapter 4 gives some Conclusions and Recommendations for improvements and further study.

2. Experimental Approach

2.1. The Acoustic Pump Loop

In order to investigate the influence of inlet distortion on the unsteady pressure field produced by a centrifugal pump, a closed-circuit water loop was designed and constructed, as shown in Figure 2.1. It consists of a 600 gallon stainless steel tank which feeds the pump through two consecutive 100 ft. length sections of 4 in. diameter rubber hose. At the pump outlet is another 100 ft. length of hose, followed by a constriction to a throttle line of 1.5 in. diameter hose, which then discharges to the tank. The pump, tank, and hose were all mounted on a large platform approximately 8 feet from the floor.

The entire system was filled using filtered city water and could be pressurized up to approximately 150 psig using an 11 gallon expansion tank. High static pressure was applied to the system when running to avoid cavitation noise at the pump due to low inlet static pressure, as well as cavitation and flashing at other points in the system where separation may occur. All components of the pump loop were designed to withstand 150 psig static pressure.

The system could be deaerated using a Cenco Hypervac vacuum pump connected to the 600 gallon tank via vacuum hose, another steel tank used as a gravity trap, and an MV Products VisiTrap water trap. The vacuum pump is designed to reach an ultimate vacuum of .005 mmHg, but because of leaks, such low pressure was not attainable, nor was it required. With valves at the inlet and outlet of the 600 gallon tank closed to eliminate the compliance of

the rubber hose, the water pressure in the tank could be reduced to approximately one inHg, and the water allowed to boil, purging trapped air in the process.

2.1.1. The Centrifugal Pump

The pump used in this study was a Navy auxiliary seawater pump, used in nuclear submarines to pump sea water through auxiliary heat exchangers. It was built by the Worthington corporation in 1961. The single-speed motor was rated at 15 hp at 1780 RPM, and was powered by 120V, 60Hz A.C. electricity. In designing this pump, much effort was focused on quieting the motor by reducing mechanical noise from bearings and shaft, and the motor and impeller are carefully balanced to minimize vibration. It is therefore a mechanically quiet pump, and the major portion of the noise produced in the pumped fluid is most likely due to fluid dynamic sources.

Little is known about the impeller geometry, other than that it has a radial intake and seven blades. Although the pump is designed to give 40 psi head rise at 400 gpm, its performance measured in this experiment is much lower, possibly because the original impeller may have been replaced and the performance curve supplied with the pump not updated. In the process of designing the pump loop, head losses in the system were matched to the factory specified pump characteristic to achieve pump design performance. However, because the pump did not perform according to specifications, and because the system head loss was larger than predicted, the design point was not attained. The maximum volume flow rate reported herein is 39.75 psid head rise at 368 gpm, as shown in Figure 2.17, recorded with the pump in the close-coupled elbow configuration of Figure 2.5, which is described in Section 2.1.3.

The pump was mounted vertically on a frame of 4 in. x 2 in. x 3/16 in. thickness mechanical tubing, via four Navy model 7E450 resilient mounts and a 1 in thick steel mounting plate, as shown in Figure 2.2. The frame rested on an elevated platform which provided 10 ft. 2 in. clearance between the lab floor and the pump inlet. The inlet flange was also 18 in. above the platform itself, which allowed clearance for system piping to be run from either the lab floor or the platform and into the pump. These clearances allowed for flexibility in pump inlet configuration.

2.1.2. Acoustic Isolation Techniques

A design goal for the pump loop was to acoustically and vibrationally isolate the pump from other sources, and to minimize acoustic reverberation and resonances. Several features of the loop were designed to ensure this. The pump is mounted on rubber vibration isolators to reduce vibration transmission from the platform. Rubber hose was used as the main fluid-bearing component of the system, and the pump was throttled by a constriction to a 1.5 in. i.d. hose of variable length.

Goodyear Flexwing 4 inch i.d. rubber hose was used as system ducting instead of stainless steel pipe to avoid acoustic interference caused by sound waves travelling around the loop and interacting with the source noise, forming a standing wave, a phenomenon which will for the remainder of this report be referred to as the "ring-around" effect. The rubber hose was employed as an attenuating device which would reduce the levels of ring-around noise by several orders of magnitude, and diminish the amplitude of the resultant standing wave.

Although it will be shown in Section 2.4.6 that the rubber hose effectively attenuated pump noise enough to avoid interference due to the ring-around effect, the impedance boundaries at the steel pipe to rubber hose flange connections, both upstream and downstream of the pump, nevertheless caused interference and the formation of a standing wave. The analysis of this problem and steps taken to correct it are described in Section 2.4.5.

The constriction throttle was used because it is much quieter than the more typical valve throttle, which usually causes severe separation of the flow and generates high levels of cavitation noise. Although the throttle itself was separated from all measurement stations by at least 100 ft. of attenuating hose, and therefore may not have produced detectable noise at those stations, it was nevertheless important as a matter of course to minimize the noise sources.

The throttle, shown in Figure 2.3, consisted of a piece of 1.5 in. i.d. rubber hose, of variable length, connected to the 4 in. system piping via two 28 in. long adaptors. These adaptors, which transitioned the flow from the 4 in. pipe to the 1.5 in. hose, had an included angle of 3°, a geometry chosen to obtain minimum adaptor length while avoiding flow separation in the case where the adaptor was used as a diffuser. The upstream adaptor, used as a

nozzle, was connected to a 1.5 ft. length of pipe immediately downstream of the flow meter. The diffusing adaptor at the other end was connected to the inlet flange of the 600 gallon tank. A valve between the hose and the diffuser, along with another at the tank outlet, allowed the tank to be isolated from the rest of the system. These valves were closed, for example, when the system water was deaerated. The valve at the constriction hose outlet was also used as a throttle for the pumping performance measurements described in Section 2.4.1.

2.1.3. Pump Installation Configurations

Four pump inlet installation configurations were used for the bulk of the work reported herein. The first two configurations, shown in Figures 2.4-2.5, were used to obtain the primary data for this report, the results of which are presented in Chapter 4. They will be referred to as the "Straight Inlet" and "Close-Coupled Elbow" configurations. The last two configurations, shown in Figures 2.6-2.7, were used during the validation studies presented in Section 2.4. They also consist of a straight inlet and a close-coupled inlet, but use an inlet measurement section of different length. For clarity, these will be referred to as "Straight Validation" and "Elbow Validation" configurations.

Most four inch flanges in the pump loop were of ASA standard geometry, with eight bolt holes on a 7.5 in. bolt circle. The pump flange connections, however, were U.S. Navy standard with ten bolt holes on a 7.188 in. bolt circle. In order to connect the pump into the system, an adapter was required to transition from the Navy flanges to the ASA flanges. At the outlet of the pump, for all configurations, a 6 in. long pipe with a Navy flange welded to one end and an ASA flange at the other was used to accomplish this transition. At the inlet, the probe traverser assembly, used to measure inlet axial velocity profiles, was designed with a Navy flange at the downstream end, to connect to the pump inlet, and was connected to upstream ducting via an ASA flange.

The Straight Inlet configuration of Figure 2.4 was used to investigate the Fully Developed, Uniform, and Orifice Distorted inlet profiles. It consisted of five stainless steel pipe sections connected vertically from the pump inlet down to the test cell floor, where the upstream length of rubber hose was connected. The topmost section was the traverser, which is described in detail in Section 2.2.3. The flow conditioner, which was

connected just upstream of the traverser, was used to generate the desired profiles and is described in the following section. A 28 in. long test section, on which could be mounted hydrophones and accelerometers, was placed upstream of the conditioner. The dimensions of this and other measurement sections are given in Figure 2.11 and discussed in Section 2.2.2. The measurement duct was preceded by a 42 in. long extension pipe which dropped nearly to the cell floor, where a 90° elbow turned the piping and was connected to the rubber hose. The total length of the steel piping upstream of the pump for the Straight Inlet configuration was 28.2 diameters, or 114 inches.

At the outlet were two more stainless steel sections, the first one being the adaptor section previously mentioned. The second was a 12 in. test section, the dimensions of which are also given in Figure 2.11. The total length of the downstream piping was 4.64 diameters or 18.7 inches.

The Close-Coupled Elbow configuration of Figure 2.5 consisted of the same piping components as the Straight Inlet, only rearranged so that the elbow was just upstream of the traverser, as close as possible to the pump inlet. To accomplish this, it was necessary to run all the piping above the platform. This configuration was used to investigate the elbow distorted inlet profile, and the inlet and outlet piping lengths were the same as for the Straight Inlet.

The Straight and Elbow Validation configurations of Figures 2.6-2.7 are identical to the previously described sections, except that the flow conditioner, 28 in. test section, and extension section were replaced by a 100 in. long test section. This section, the dimensions of which are given in Figure 2.11, provided two hydrophone/accelerometer mounting positions separated axially by 23 diameters, suitable for measurement of signal coherence and reflection at the steel-rubber flange connection. The substitution of the 100 in. section increased the length of the inlet piping for both Validation configurations to 29.2 diameters or 117.5 inches. The outlet piping was unchanged.

2.1.4. Inlet Velocity Profile Generators

The velocity profile at the inlet of the pump was controlled by placing one of two pipe sections directly upstream of the pump inlet, separated only

by the traverser. One section was a flow conditioner designed specifically for this project, and the other was an ASA standard, 150 psi 90° elbow.

Uniform and Orifice Distorted inlet profiles were produced using the flow conditioner, which is shown in its various configurations in Figure 2.8. For these profile cases, the Straight Inlet configuration was used, and the flow conditioner was configured as desired. The conditioner consists of a 23 in. long stainless steel flanged pipe of approximately 4.25 inch inner diameter, into which a number of 4.02 in. i.d. by 4.25 in. o.d. conditioner element rings could be inserted. The element rings are locked in place by a cover ring which is fixed to the end of the conditioner pipe by four stainless steel screws.

To develop the Uniform Velocity inlet profile, 10 mesh x .023 in wire diameter stainless steel screen with an open area ratio of 0.593 was welded to an open end of six three inch long element rings. A single unit of this type of screen, with an estimated pressure drop of 0.96 dynamic head for typical flow conditions, was theoretically predicted by an analysis due to Taylor and Batchelor[9] to reduce the local variation from volume mean velocity by 67%. The multiplicitive effect of several screens, neglecting interaction effects, should have increased the reduction to over 99%. These elements were inserted into the conditioner duct with the screen in the downstream position, as shown in Figure 2.8a. A three inch long piece of 1/8 in. opening honeycomb was added upstream of the screen elements, to straighten the flow before it entered the screens, and the section was locked with the cover ring.

The Orifice Distorted inlet profile was created by machining an ASME standard eccentric orifice with a diameter ratio of 0.5 into a 1 inch long aluminum element ring. The orifice ring is shown in Figure 2.9. The ring was inserted in the downstream end of the conditioner pipe, and the remaining length of pipe was taken up by open conditioner rings. The orifice flow generator is shown in Figure 2.8b.

Fully Developed profiles were produced by simply filling the conditioner pipe with open element rings. It was assumed that, with 23 diameters of pipe between the upstream elbow and the pump inlet, as shown for the straight inlet configuration of Figure 2.4, the flow would be nearly fully developed by the time it reached the inlet. Development length for turbulent flow in a smooth pipe is typically 20 to 30 diameters. The open

conditioner configuration was also used for the elbow inlet arrangement, to provide a nearly fully developed profile to the elbow inlet.

The Elbow Distorted inlet flow was produced, as mentioned, by connecting the 90° elbow directly to the probe traverser at the inlet of the pump, as shown in Figure 2.5. The elbow was an ASA standard short radius cast stainless steel design, with a bend radius to the pipe center line of 6.5 in.

Approximately 1.4 diameters separated the outlet of the profile generating device and the tip of the Pitot-static probe, and the distance to the pump inlet was approximately 2.6 diameters. These distances were the shortest achievable, and it was assumed that any changes in velocity profile over such a length were unavoidable and most likely small.

It will be shown in the results of Section 4.2.1 that the inlet profiles generated by the flow conditioner did not meet design. The Fully Developed flow was slightly asymmetric, and the Uniform profile was not as uniform as predicted. It should be recognized therefore that, although these profiles will continue to be referenced by the names "Fully Developed" and "Uniform", they are only nominally so.

2.2. Instrumentation

The following sections discuss the instrumentation and mounting techniques used to measure pump performance, acoustic and vibration phenomena, and inlet axial velocity fields.

2.2.1. Pump Performance Measurement

It was desired to monitor pump performance and system conditions during testing, and instrumentation was installed to accomplish this, consisting of a flow meter, thermocouple, two gage pressure gages and two differential pressure gages. A schematic of the system is given in Figure 2.10.

The flow meter was a Sparling FM625 Tigermag magnetic flow meter with remote readout, calibrated to 400 gallons per minute full scale and with a standard accuracy of ±1% full scale. It was mounted 100 ft. downstream of the pump, just upstream of the throttle contraction, and was monitored by remote readout.

Static pressure in the 600 gallon tank and at the flow field measurement plane at the inlet of the pump were measured using single wall

taps and two Ashcroft 0-150 psig dial gages connected by 1/4 in. nylon tubing. Pressure rise across the pump was measured by connecting a Dresser 0-60 psid differential gage between the inlet tap and a static tap on the 12 in. measurement section at the pump outlet. The pressure drop across the throttle was measured by connecting an additional Dresser gage between the outlet tap and the tank tap mentioned above.

Water temperature was measured using an Omega ICIN-14U-18 thermocouple mounted on a .5 in. NPT tap on the stainless steel tank. The thermocouple output was monitored using an Omega model PR-J-24 remote meter.

2.2.2. Acoustic and Vibration Measurement

Three stainless steel test sections of length 12 in. , 28 in. , and 100 in. were designed and built on which to mount hydrophones and accelerometers, and are shown with dimensions in Figure 2.11. The 28 in. test section has a total of seven ports on which to mount instrumentation, with a maximum axial separation distance of 5.22 diameters, or 21 inches. Two sets of three ports are located at the same axial location, and are spaced circumferentially by 90°. This section was usually mounted upstream of the pump in the Straight and Close-Coupled Elbow configurations, and was used to measure inlet noise levels. It was also used in measuring noise level far upstream of the pump, at the far-upstream measurement station of Figure 2.1.

The 100 in. section has only three mounting ports, but has a large maximum axial separation of 93 in., which was employed in making reflection coefficient measurements at the stainless steel-rubber interface. The 12 in. section has three mounting ports, all at the same axial position and circumferentially spaced by 90°. It was mounted directly downstream of the pump in order to measure outlet noise levels.

The mounting ports themselves are depicted in Figure 2.12 and consisted of a 3/4 in. diameter hole drilled through the pipe wall, terminating at a flat boss on the pipe outer surface to which could be fastened both a hydrophone adaptor and an accelerometer bracket. The brass hydrophone adaptor fit inside the 3/4 in. hole and its radiused end was flush with the inner surface of the pipe. An O-ring groove in the shoulder of the adaptor provided a pressure seal, and the adaptor was fixed to the boss using

four 8-32 screws. The accelerometer bracket was machined from a 3 in. x0.5 in. x 3/16 in. thickness aluminum channel, had a clearance hole for the hydrophone, four 8-32 clearance holes for bolts, and stud taps parallel and perpendicular to the axis of the hydrophone on which to mount the accelerometer. In general practice, only the parallel-axis mounting position was used.

Pressure field measurements were made using three PCB 105B piezoelectric hydrophones which have a dynamic range of 215 dB (re 1μPa), and a nominal sensitivity of 300 mV/psi. The hydrophone electrical signal was amplified using a PCB model 483B08 voltage amplifier with a gain range of up to 100 and ±1% gain accuracy. Vibration of the test sections were measured using four Endevco model 7701-50 accelerometers with a nominal sensitivity of 50 pC/g and a dynamic range of more than 2000g. The accelerometers were amplified by a set of four Endevco model 2721B charge amplifiers with an output range between 10 and 1000 mV/g. The signals of both the hydrophones and the accelerometers were filtered using a Frequency Devices 744PL-4 low pass filter and digitized via a Data Translation DT2821 A/D board on a NEC 386SX personal computer. A schematic of the vibro-acoustic measurement system is shown in Figure 2.13.

For all pump installation configurations discussed herein, hydrophones and accelerometers were mounted at one of four consistent measurement positions- inlet, outlet, upstream and far-upstream. The first three positions are labeled in Figures 2.4-2.7, where relevant, and the far-upstream position is shown in Figure 2.1. The inlet position is the axial position of the upstream test section, be it the 28 in. or the 100 in., nearest the pump inlet. The upstream position is that position at the upstream end of the inlet test section. The outlet position is the 12 in. test section at the outlet of the pump.

The measurement positions used to gather the final data presented in Chapter 4 were the inlet and outlet stations. It should be noted here that the distance from the pump inlet to the inlet measurement station was 8.51 diameters for the Straight Inlet, and 11.05 Diameters for the Close-Coupled Elbow, the difference being the change in position of the elbow. For a pure tone at 200 Hz, approximately the blade passage frequency of the pump, this discrepancy in distance is equivalent to .038 wavelengths, small enough to assume that the change in inlet measurement position is not acoustically

important at blade passage frequency. For higher frequencies, it would become significant.

2.2.3. Flow Profile Measurement

Two-dimensional axial velocity profiles at the inlet of the pump were measured using a traversing assembly designed and built specifically for this project. The overall assembly is shown in Figure 2.14. It is built around a rotating inner cylinder on which is mounted a Pitot-static probe. The inner cylinder is held in place by glands welded to upstream and downstream pipe sections. A modified, hand-cranked rotary table mounted on the upstream flange allows for rotation of a bearing-mounted outer cylinder, which drives the inner cylinder through four shoulder screws. The entire assembly is fastened together with six bolts which bind a flange on the downstream side of the outer cylinder to the top of the rotary table, using the T-slots in the table to affix the bolts. The downstream pipe section includes a Navy flange with which it can be connected to the pump inlet. The upstream section includes an ASA standard flange for connection to other system components.

The probe was a United Sensor Model PDA-6-F-5.25-KL Prandtl type Pitot-static probe with a 1/16 in. diameter tip and 1/8 in. diameter reinforcement. It was mounted on the inner cylinder wall by a Cajon gland and clamped to a Velmex Model A1504CE Unislide manual screw-driven linear positioner, used to set the radial position of the probe. The Unislide was manually positioned using a finger knob, and had a screw pitch of 40 turns per inch, and a Vernier scale which allowed for positional precision to 0.001 inch. The rotary table, which controlled the circumferential position of the probe, turned three degrees per turn of the crank, and was positioned according to a scale in degrees etched in the table top and a scale in minutes etched in the crank. The circumferential position was precise to at most ±10 minutes.

The Pitot-Static probe was connected via nylon tubing to a Validyne DP-15 wet-wet differential pressure transducer and a CD223 Digital Indicator. The +10 volt full scale analog output of the indicator was digitized and stored by the DT2821 A/D board.

The transducer diaphragm used depended on the profile to be measured. For the Fully Developed cases and the Uniform case, a #28 diaphragm was used calibrated to 0.8 psid full scale. For the Elbow Distorted

case, a #30 diaphragm was used calibrated to 1.0 psid full scale. For the Orifice Distorted case, a #42 diaphragm was used calibrated to 20.0 psid full scale. The #28 diaphragm was calibrated using a Meriam oil manometer. The #30 and #42 diaphragms were calibrated using a Setra model 325 Digital Pressure Gage. The manometer and digital gage calibrated to each other to within 1% at 0.8 psid.

A Pitot-static probe is designed to measure dynamic pressure in one direction only- the axial direction for the purposes of this study. Significant measurement errors can be incurred if non-axial components of velocity are present in the flow, as was the case for the orifice and elbow flows. These errors can be of order 2% actual velocity for 30° flow angles, and higher as flow angle increases.

2.3. Data Acquisition and Processing

The following sections present the methods used to acquire, reduce and analyze the data presented here. The following discussion covers the approach to acoustical, vibration, and flow field data acquisition.

2.3.1. Acoustic and Vibration Data

Both acoustic and vibration data were acquired digitally using the DT2821 A/D board and ILS Station spectral processing software. The data were typically acquired at a sampling rate of 5000 Hz and the cutoff frequency of the analog filters was set at 1000 Hz, much lower than the Nyquist frequency of 2500 Hz, thereby avoiding aliasing. Up to six channels of data were sampled simultaneously, and were later demultiplexed using ILS software. Five 131,072 sample records, corresponding to a total sample time of 131 seconds, were taken of each channel in order to obtain an accurate statistical estimate of the stationary signals. The data were then transferred to MATLAB file format for spectral processing using MathWorks 386-MATLAB.

Auto-spectral densities and transfer functions were estimated using 32768 point fast Fourier transforms, yielding a bandwidth of 5000/32768 = .1526 Hz. Each of the five 131K data sets were subdivided into seven subsets of 32K each, which overlapped by 50%. Thirty-five (35) spectra could then be calculated and averaged for each channel. Results are presented in terms of sound pressure level, *SPL*, which is defined as

$$SPL\ [\mathrm{dB}] = 10 \log_{10} \frac{\phi_{xx}}{p_o^2}, \quad \phi_{xx} = \overline{p_{xx}} \frac{1}{\Delta f} \qquad [2.1]$$

where ϕ_{xx} is the autospectral density of signal x, $\overline{p_{xx}}$ is the ensemble average autospectrum of signal x, Δf is the bandwidth, and p_o = 1μPa, the standard reference pressure for water applications.

The transfer function H_{yx} was calculated according to the formula

$$H_{yx} = \frac{\overline{p_{yx}}\,\overline{p_{yx}}^*}{\overline{p_{xx}}} \qquad [2.2]$$

where $\overline{p_{yx}}$ is the ensemble average cross spectrum of signals y and x, and the asterisk, (*), denotes the conjugate operator.

The coherence function, γ^2, was also found using the cross-spectral density by

$$\gamma^2 = \frac{\overline{p_{yx}}\,\overline{p_{yx}}^*}{\overline{p_{yy}}\,\overline{p_{xx}}} \qquad [2.3]$$

so that $\gamma^2 = 1$ indicates complete coherence, and $\gamma^2 = 0$ indicates complete incoherence.

The transmission loss, TL, of a signal between station x and station y was calculated by the formula

$$TL\ [\mathrm{dB}] = 10 \log_{10} \frac{\overline{p_{yy}}}{\overline{p_{xx}}} \qquad [2.4]$$

where as before, $\overline{p_{xx}}$ is the ensemble averaged autocorrelation of signal x.

The reader is referred to Bendat and Piersol[10] for a discussion of these formulae.

2.3.2. Flow Field Data

Dynamic pressure was sampled at 258 coordinate positions over the 2.013 inch radius duct cross section near the pump inlet. The grid used is shown in Figure 2.15 and the coordinate pairs are listed in the table of Appendix D. The grid consists of 10 annuli with a radial separation of 0.218 in. For each radial position, the number of angular positions was chosen so as to maintain uniform area coverage. Because of physical limitations, the

maximum radial position able to be measured was 1.965 inches, so that the measured cross sectional area was 12.13 square inches, 95.3% of the total cross sectional area of 12.73 square inches.

Dynamic pressure, as measured by the Pitot-Static probe, was sampled using ILS at 5 Hz for a period of one minute at each grid point, providing a total of 300 samples. Using MATLAB, the dynamic pressure data were then converted to velocity by the transformation

$$u = \sqrt{\frac{2q}{\rho}} \qquad [2.5]$$

The mean value and the standard deviation of the velocity data were calculated for each coordinate position. Standard deviation is defined here as

$$\text{std}(u) = \left[\sum_{i=1}^{N} \frac{(u_i - \bar{u})^2}{(n-1)} \right]^{\frac{1}{2}} \qquad [2.6]$$

For presentational purposes, a second definition of the measurement grid was made, in terms of 461 triangular elements defined by measurement nodes at their corners. Using GRAFIC, a graphics software package, contour plots could then be produced.

The area and mean velocity of each element could then be calculated, multiplied and summed, yielding a measure of volume flow rate, which was compared to the flow rate measured by the magnetic flow meter. The contour plots included in this report present average and standard deviation of velocity normalized to area-weighted mean velocity calculated in this manner.

A quantitative measure of the asymmetry of the flow profile was obtained by calculating the volume flow rate through the two semicircular areas A_1 and A_2 defined by rotating a diametral line through a 180° circumferential range, as shown in Figure 2.16. The Asymmetry Ratio, α, was defined as the maximum ratio of flow rate between these two areas, as shown in the figure below, and gives a quantitative measure of the "amplitude" of dynamic loading that a blade rotating in the flow field would experience.

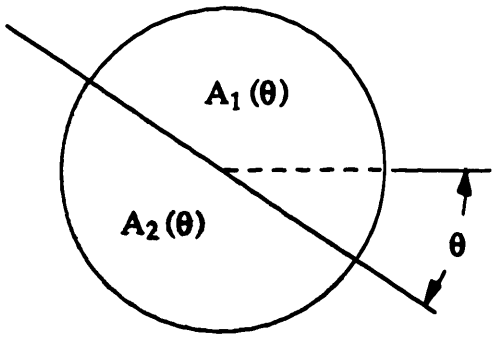

$$\alpha = \max\left|\frac{Q_2}{Q_1}(\theta)\right| \qquad [2.7]$$

Figure 2.16 Definition of the Asymmetry Parameter

This approach only considers the fundamental circumferential mode of the flow field, which is, as mentioned in Section 1.2, the dominant mode found in common practice. A detailed analysis of inlet flow field effects on noise at the blade passage frequency, however, would have to consider higher order modes, up to the number of blades, to be sufficiently rigorous. Furthermore, the estimation is inherently discretized by necessity of defining the angular position of relatively large-area grid elements by the mean angle of their grid points. It would be possible to bisect the area of elements which straddle the dividing line by interpolation, but that extra order of precision was not attempted here.

This method of asymmetry quantification is presented with the above caveats but, as will be seen in the case of very strong asymmetry, such as the orifice distorted case, where the fundamental circumferential mode is dominant, it is sufficient for present purposes.

2.4. Validation Studies

Before final results were obtained, it was necessary to evaluate the performance of the pump loop in terms of acoustic and fluid mechanical parameters. The following sections present the procedures and results of these investigations.

2.4.1. Pump Performance

Before a comparison of acoustic data could be made between the inlet conditions considered, it was necessary to confirm that the pump provided the same head rise and flow rate for each inlet condition. Pump characteristic data for each inlet condition were taken by incrementally closing a 1.5 inch valve at the throttle outlet, as shown in Figure 2.3, and making simultaneous, manual readings of head rise from the differential gage and flow rate from the magnetic flow meter display. The resulting characteristic curves are presented in Figure 2.17.

Head rise curves for the Elbow Distorted and Uniform inlet profiles match that of the Fully Developed profile well, within experimental error of ±0.5 psi. The curve for Orifice Distorted Case shows a strong increase in head rise for constant flow rate, however, due to measurement error caused by placement of the inlet static pressure taps very near to the orifice vena contracta.

The measured head rise was large because of high distortion downstream of the orifice. Reference [22] presents data showing that the vena contracta of an eccentric orifice of diameter ratio 0.5 is located 0.9 diameters downstream of the orifice, so the flow at the inlet tap axial position, 1.4 diameters downstream, was highly distorted, which resulted in lowered inlet static pressure due to high dynamic pressures in the core flow. It was necessary to correct for this error, and the method used is described in Appendix A. The resulting corrected pump characteristic for the Orifice Distorted Case is shown in Figure 2.18. The agreement is not complete, but was considered adequate to argue that the pump performs similarly for all inlet flows, and that a comparison of noise for two different inlet profiles at the same flow rate is valid because the pump pressure rise is similar.

2.4.2. The Typical Acoustic Spectrum

Before undertaking a general discussion of the validity of the acoustic measurements, it is instructive to discuss the shape and features of the typical spectral distribution of measured noise. Figure 2.19 shows such a spectrum. The shaft speed of the pump was 1730 RPM or 28.83 Hz, and the primary spectral peaks, marked with circles, generally correspond to the shaft frequency, f_{sh}, and its harmonics, at approximately 30, 60, 90, 120, 180, 210, 240, 360, and 480 Hz, as labeled in the figure. The impeller was a seven-blade

design, and as a result, the highest amplitude peak is at the seventh harmonic of the shaft frequency, or the blade passage frequency, f_{bp}. The large peak at blade passage frequency is the focus of this investigation.

The noise floor of this spectrum varies significantly with frequency, and is dominated by turbulent pressure fluctuations. The turbulent spectrum level is highest at very low frequencies, where Strouhal number based on duct diameter is near 0.23, which for the present case is about 5 Hz. Measured turbulence levels could be higher for cases where the measurement point is directly downstream of a turbulence generator, a 90° elbow for example, but the difference tended to be only about 5 dB.

At higher frequencies, turbulence noise tends to drop off, and the noise floor in Figure 2.19 cannot be explained by turbulence. The broad-band maxima at approximately 460 and 850 Hz are more likely due to the presence of a damped standing wave in the steel pipe portion of the system. The standing wave is produced by reflection of noise at the steel pipe – rubber hose boundaries upstream and downstream of the pump. Although the rubber hose was intended to eliminate the standing wave, the net result was to exchange one due to the ring-around effect for one due to reflection.

There are also many sharp peaks in the spectrum which cannot be described as shaft harmonics. These occur mostly at higher frequencies, above 500 Hz, and are all more than 30 dB below the blade passage level. These peaks are most likely due to imperfect reflection of plane waves at boundaries such as elbows, flange joints, and the steel-rubber joints, where reflection produces higher-order modes which attenuate to low levels quickly.

Aside from the broad-band variation in the noise floor levels due to reflection, the spectrum is quite clean, with sharp, distinct peaks at the first seven harmonics of the shaft frequency. Relevant topics of contamination by turbulence, vibration and reflection will be discussed in the following sections.

2.4.3. Vibration

As mentioned in Section 1.2, an inherent difficulty in making acoustic measurements in a water filled duct is the potential for vibro-acoustic interaction between the fluid and its surrounding structure. Experiments were performed to estimate the significance of this interaction relative to the acoustic measurements.

Figure 2.20 is a typical vibration spectrum as measured by accelerometers mounted with axis normal to the pipe center line, near the hydrophones. Vibration levels at frequencies corresponding to shaft harmonic peaks are marked by circles. Although a detailed description of the vibration spectrum of the pump system is outside the scope of the present study, it is relevant to note that the vibration spectrum does display peaks at some shaft harmonics, including the blade passage frequency at ~205 Hz.

Because water was chosen as the working fluid for this study, and because of the strong vibrational peaks at shaft harmonic frequencies, it is therefore necessary to show that vibrations do not contaminate the acoustic measurements. There are two mechanisms by which contamination could occur: The hydrophones are slightly sensitive to acceleration and could be measuring the pipe vibration directly, or the vibration of the pipe could be radiated to the fluid acoustically. These two effects are dealt with in the following paragraphs.

The acceleration sensitivity of the three hydrophones used in this study, specified by factory calibration, varies between 0.0002 and 0.0009 psi/gee. This low sensitivity is primarily due to the design of the hydrophone, which includes a mass-driven second piezoelectric crystal which compensates for axial vibration inputs.

The actual measured ratio of fluid pressure to structural vibration was up to seven orders of magnitude higher than the specified sensitivity. Figure 2.21 shows the magnitude of a typical hydrophone – accelerometer transfer function, as defined by Equation 2.2, again with values corresponding to shaft frequency harmonics marked with circles. It can be seen that the ratio varies widely but never falls below 0.1 psi/gee, with the harmonic level falling between 1 and 100 psi/gee. With vibration levels so low compared to the acoustic levels measured, it was safe to assume that the the effect of the hydrophones measuring their own vibration did not contribute significantly to the acoustic measurements.

Although no experimental work was done to investigate the coupling of structural vibration to acoustic wave propagation in the pump loop, it is sufficient to apply an analysis based on shell theory, presented by Fuller and Fahey[11], to the present case. The two primary vibrational modes of the fluid-pipe system below the pipe ring frequency, approximately 15 kHz for the present case, are shown in Figure 2.22. The $n = 0$ symmetric mode describes

plane acoustic waves propagating down the duct, and the $n = 1$ asymmetric mode is most seen in the pipe, excited by rotational imbalance in the pump drive and impeller.

Fuller presents a definition of the general variation in reactive wall impedance,

$$Z = -i\,\rho_f\,\omega \frac{J_n(k^r r)}{k^r J_n'(k^r r)} \qquad [2.8]$$

where ρ_f is the fluid density, ω is the angular frequency, J_n is the Bessel function of the n^{th} kind, J_n' is the first derivative of the Bessel function, and k^r is the radial wave number of the shell-fluid combination, which is very small for the present case. It can be seen that for small radial wave number, the impedance of the wall will either be very large or very small depending on the modal value. For $n = 0$, J_n' goes to zero, and the wall impedance becomes very large, implying that the pipe will appear to the fluid to be extremely rigid and transmission from fluid to wall will be low. For $n = 1$, J_n goes to zero and the wall impedance is very small, which also decouples the shell and fluid behavior.

Thus, because both the fluid and the pipe wall respond primarily in single and differing spatial modes, $n = 0$ and 1 respectively, very little coupling exists between fluid and pipe. To prove this, a hydrophone and an accelerometer were mounted at 180° circumferential angle from a similar pair, at the upstream measurement station of the Straight Inlet configuration, shown in Figure 2.4. The phase angle between the each instrument, and its respective opposite, presented in Figure 2.23 gives a measure of the relative magnitudes of the $n = 0$ and $n = 1$ modes. Figure 2.23a shows the phase angle for the acoustic case to be very close to zero throughout the spectrum, implying a spatial mode $n = 0$. Similarly, Figure 2.23b shows the vibrational phase angle to be near π (or 180°), corresponding to the $n = 1$ mode.

The agreement of the acoustic case with the above arguments is very good, whereas the vibration case has some scatter, possibly due to the low vibration levels and the moderate sensitivity of the accelerometers. As expected, the single-mode structure of the vibrations breaks down at higher frequencies, above 900 Hz in Figure 2.23, where higher order modes begin to appear and the phase angle scatters significantly. But for the frequency range of interest to this investigation, the data show that the fluid and structural

behavior are of singular and differing modes, and by the above arguments, decoupled.

2.4.4. Turbulence Noise

Another difficulty with making acoustic measurements in water systems is the extraneous pressure oscillations produced by turbulence at the typically high Reynolds numbers, near 400,000 based on pipe diameter for this case. The energy produced by turbulence is not acoustic– it has been shown to have a wave speed of about 4/5 times the mean flow speed– but it is detected by the hydrophones. Because turbulence existed in the fluid flow, it was important to show that that the pressure spectrum measured was not corrupted by turbulence noise.

To prove this, the coherence of the signal over the 100 in. test section was measured at the inlet of the pump using the the Straight and Elbow Validation configurations of Figure 2.6-2.7. Both configurations were studied, in order to determine the influence of increased turbulence, due to the upstream elbow of the Straight Inlet configuration, on the coherence of the pressure field. The coherence function γ, is defined by Equation 2.3.

Because turbulence produces non-harmonic pressure disturbances, its signal tends to have little coherence, and if the pressure field at the pump inlet can be shown to be very coherent over a long distance provided by the 100 in. test section, then it can be deduced that turbulence does not significantly corrupt the data. The flow behind the 90° elbow, which is a significant turbulence generator, loses coherence over such a long distance.

Coherence spectra between hydrophones at the upstream and inlet measurement stations for both Validation configurations are shown in Figure 2.24. The two figures show that most of the labeled harmonics are very coherent, the notable exceptions being the shaft frequency, which shows extremely low coherence for the Straight Validation configuration of Figure 2.24a, and slightly low coherence for the Elbow Validation configuration of Figure 2.24b. Comparison with the autospectra of the signals, given in Figures 2.25 - 2.26 for both configurations, shows that nearly all harmonics are prominent in the signals for all configurations and measurement positions, the exceptions being the shaft frequency and the sixth harmonic (180 Hz) for the Straight Validation configuration of Figure 2.25. The shaft peak does not

even appear here, a phenomenon which corresponds to the low coherence mentioned above.

For the most part, the entire spectrum shows strong coherence, most likely because the energy levels of the standing wave overcome turbulence levels. Ranges of low coherence values are apparent near 500 and 800 Hz. for both plots, and at 300 Hz. for the Elbow Validation plot. These minima correspond to frequencies at which standing wave nodes occur at one of the two measurement stations, so that turbulence levels dominate the signal at those locations and frequencies. It is not clear why the exact location of coherence minima do not agree between the two configurations.

The important conclusion to be reached here is that coherence of shaft harmonic frequencies, especially the blade passage frequency, are very close to unity. The signal at blade passage frequency is strongly coherent, which proves, at the minimum, that the blade passage signal is not significantly corrupted by turbulence. It must be concluded, however, that turbulence can have an influence on the shaft frequency level, an argument which be employed in analysis of the final results, in Chapters 4 and 5.

2.4.5. Reflection and Standing Waves

Reflection at the steel-rubber boundary posed the most difficult problem to be dealt with in this project. The reflection caused the formation of standing waves in the steel piping at inlet and outlet, where most acoustic measurements were made. In such a case, a standing wave tends to become resonant at characteristic frequencies determined by the length of the steel pipe, the sound speed in the pipe, and the reflection coefficient at the steel rubber interface. Damping of the resonant standing wave is due to the attenuating properties of the steel pipe, which are small, and the magnitude of the reflection coefficient.

It was attempted to measure the reflection coefficient of the steel rubber boundary using the 100 in. measurement section, and applying the two microphone method as depicted below, with reference to Figure 2.27.

If two microphones, p_1 and p_2, are placed a distance s apart in a rigid duct with a broad band noise source (such as the pump) at one end and an impedance boundary (the steel-rubber interface) at the other, the one-dimensional wave field can be described by the combination of a wave

travelling in the positive direction added to its reflection travelling in the negative direction, or

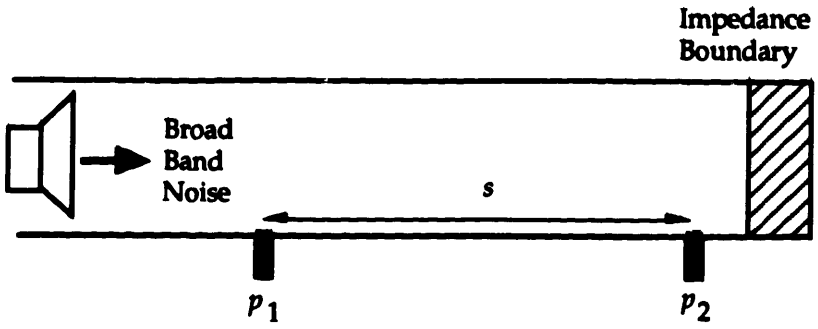

Figure 2.27 Reflection Coefficient Formulation

$$p(x,w) = A(e^{ikx} + R\,e^{-ikx}) \qquad [2.9]$$

where A is the complex amplitude of the forward travelling wave, k is the real wave number, and R is the reflection coefficient, defined as the transfer function between the the reflected, backward travelling wave and the incident, forward travelling wave. If $x_2 = 0$ is the position of microphone p_2 and $x_1 = -s$ is the position of p_1, then the transfer function H_{21} is defined as

$$H_{21} = \frac{p_2}{p_1} = \frac{1 + R}{e^{-iks} + R\,e^{iks}} \qquad [2.10]$$

and so the reflection coefficient, which is defined as the transfer function between the incident and reflected wave, can be obtained by

$$R = \frac{H_{21}e^{-iks} - 1}{1 - H_{21}e^{iks}} \qquad [2.11]$$

The data used in the reflection coefficient investigation were the same as that presented in the analysis of signal coherence given in Section 2.4.4. The initial tests were made with the Elbow Validation configuration shown in Figure 2.7. Figure 2.28a gives the results of these measurements, and shows that for the frequency range of interest, the magnitude of the reflection coefficient is near 0.5, large enough to produce a significant standing wave. The large discontinuities at 290, 560, and 850 Hz are locations of pole-zero pairs, where both the numerator and denominator of the reflection coefficient function theoretically should approach zero simultaneously. This

does not occur, because turbulence scatters the curve, and the result is a large positive-negative spike at the node-zero frequency. The most reliable values in these reflection coefficient plots are at the shaft harmonic peaks, labeled with circles. Autospectra of the two signals were presented earlier in Figure 2.25.

It was attempted to eliminate the impedance boundary by using hose clamps to compress the hose between longitudinal steel bars, starting with six meter-length bars at the boundary and three abutting meter-length bars so as to gradually transition the acoustic impedance from that of the steel pipe to that of the rubber. A diagram of this set-up is shown in Figure 2.29.

The Straight Validation configuration, shown in Figure 2.6, was used to make reflection measurements with the treated impedance boundary. In this configuration, the 90° elbow was connected directly to the hose, and although a strict interpretation of reflection at the boundary upstream of the pump for this configuration would have to include impedance of the elbow, in practice the transmission loss of such a bend is very small for sound in water, and therefore the reflection should be low. However, the presence of the elbow at the boundary should be kept in mind when comparing reflection results for this configuration with those presented above. Further discussion of the transmission loss of a 90° elbow is given in Section 2.4.7.

Unfortunately, the attempt to reduce reflection by treatment of the boundary proved unsuccessful. Figure 2.28b shows the reflection magnitude for Straight Validation configuration with the treated impedance boundary, and Figure 2.30 compares reflection magnitude at harmonic peaks for both configurations tested. As was the case in the coherence analysis of Section 2.4.4, the shaft frequency reflection result is at odds with the rest of the data. The value of 1.33 is physically impossible, and the data at that point are most likely corrupted by turbulence, due to the low signal levels shown in Figure 2.25. For the other data, the effect of the treatment seems to be an increase in reflection at blade passage frequency of more than 0.2, possibly due to the difference in configuration.

Because of time restrictions, no additional effort was expended to eliminate reflection at the steel-rubber boundary. It was therefore necessary to conduct the experiments in the presence of the standing wave, and an understanding of how the standing wave effects the measured acoustic spectrum was crucial to the evaluation of the final results.

Louie[12] presents an analysis of the standing wave structure in the steel portion of the pump loop, and her calculations were adapted to the present geometry and are compared to measured inlet spectra in Figures 2.31 - 2.32. These figures compare a normalized amplitude of the standing wave, as calculated by Louie, to the measured spectra for both the Straight Inlet and Close-Coupled Elbow configurations. The purpose here is to compare the shape of the noise floor in order to discern the resonant frequencies for a given configuration and measurement position.

The first comparison, made in Figure 2.31, is for the Straight Inlet configuration. The overall similarity of the two plots is marginal, but the model does predict resonant peaks at 400, 600 and 850 Hz. Discrepancies at frequencies below 400 Hz. may be due to high turbulence levels dominating the noise floor. This interpretation is consistent with the low coherence measurements for low frequencies mentioned in Section 2.4.4. The Close-Coupled Elbow comparison of Figures 2.32 is similar to the Straight Inlet case, with the best correlation occurring near 600 Hz.

If it is true that turbulence is the primary cause of the discrepancies between noise floor levels described in Figures 2.31 and 2.32, and if Louie's model is accurate, then it should be some cause for concern, because the calculated spectra of Figures 2.31 and 2.32 show a resonance peak near 200 Hz, near the blade passage frequency at approximately 205 Hz. The noise floor of the measured spectra may not be effected by the standing wave because the source levels are not high enough to overcome turbulence, so the similarity in noise floor shape is not seen. At the blade passage peak, however, the high source level is already above the noise floor, and the resonant standing wave amplifies it.

Therefore, the standing wave was possibly resonant near the blade passage frequency, and if so, confidence in quantitative interpretation of the acoustic spectra is low. Fortunately, the calculated standing wave for both configurations show peaks near 200 Hz, owing mainly to the identical overall length of stainless steel piping. However, the calculated amplitude of the stranding wave at f_{bp} differ between the two configurations by 2.76 dB, a value smaller than the measurement uncertainty defined in Appendix C, but significant. Therefore, it was considered valid to compare measurements for the two configurations, but confidence in the results was diminished.

2.4.6. Attenuation Performance of the Rubber Hose

In order to evaluate the performance of the rubber hose in terms of attenuation of source noise, the 28 inch test section with a single hydrophone was installed at the far-upstream measurement station, separated from the pump by one 100 ft. length of the four inch hose, as shown in Figure 2.1. The pump was installed in the Elbow Validation configuration of Figure 2.7. The data were non-dimensionalized and compared to levels measured at the upstream measurement station, and to published levels of turbulent boundary layer noise in water pipes of Clinch[13] and Rogers[14]. The results are shown in Figure 2.33, plotted as non-dimensional pressure spectral density S_p, versus Strouhal number. Non-dimensional pressure spectral density is defined as

$$S_p = \frac{\phi U}{q d}, \qquad [2.12]$$

where ϕ is the autospectral density, U is center line flow velocity, q is the center line dynamic pressure, and d the duct diameter. For reference, the Strouhal number at the shaft frequency is 1.45, and the blade passage Strouhal number is 10.17, as labeled in the Figure. The results show that the noise levels at the far upstream measurement station are attenuated by about 30 dB at f_{sh} and 40 dB at f_{bp}, compared to levels measured at the inlet test section. The far-upstream levels approach turbulence levels reported by Clinch as Strouhal number increases. The levels due to Rogers tend to be about 6 dB lower, and this discrepancy is most likely explained by differences in experimental technique, including duct diameter, hydrophone diameter, and flow velocity.

As part of the pump loop design process, an analytical prediction of acoustic transmission loss in a compliant duct was derived by Ingard[15], a summary of which is presented in Appendix B. It was desired to validate the analytical prediction by comparison to the transmission loss for the measured data presented above.

In order to make the comparison, it was necessary to calculate the coherence of the measured signals at the pump and the far-upstream stations, to prove that the signals were coherent and that a calculation of attenuation was valid. Figure 2.34 shows the coherence of the two signals, and it is clear that it is small for the majority of the frequency range shown. This is

expected, because if the hose effectively attenuates the pump signal, turbulence noise will dominate the spectrum at the far-upstream station, making its coherence with the pump inlet signal small.

An exception to this argument must be made for very strong levels in the pump signal, at shaft harmonics and particularly at blade passage frequency. Figure 2.34 shows that only three shaft harmonics- f_{sh}, $4xf_{sh}$, and f_{bp}, have coherence greater than 0.5, and only the blade passage coherence exceeds 0.9. These three frequencies are the only ones for which a calculation of transmission loss would be appropriate, and confidence in making a comparison the the model is high only for the blade passage result.

A crucial independent parameter in the attenuation model is the loss factor, ε, which is highly dependent on the material properties of the duct and very difficult to measure. For these reasons, ε was chosen so that the model fitted the experimental data at blade passage frequency, and the model would be validated to the extent that the chosen value of ε fell within a realistic range.

Figure 2.35 Compares the transmission loss, *TL*, as calculated by Equation 2.4 for the three frequencies considered, to the relation predicted by Ingard and presented in Appendix B. It can be seen that the model prediction fits the calculated transmission loss at the fourth harmonic closely, but does not match well at f_{sh}. The shaft frequency, however gave the lowest value of coherence for the three frequencies considered, so the agreement was considered good.

The best-fit value for ε was found to be 0.1215, which falls just above the range considered in the analysis, but is still realistic. It was therefore concluded that, to the extent possible using the approach presented here, experimental results adequately validated the model.

2.4.7. Component Transmission Losses

To accurately measure the pump noise output, it was important to assess the attenuating influence of flow conditioning devices such as screens, the orifice, and the 90° elbow which were placed between the pump and measurement stations. No experimental work was done in this regard, but literature review and simple analytical approaches show that acoustic losses associated with such components are small for the present conditions.

Transmission Loss Across 90° Bends

An experimental investigation of transmission loss through 90° bends was performed by Cummings[16], who shows that even for sharp bends transmission is near 100%. For curved elbows used in common practice, Cummings argues that transmission may be considered to be unity. This result is explained by the fact that the dependence of acoustic impedance on the geometry of the medium scales with the acoustic wavelength. As mentioned previously, the total length of the elbow is only 0.038 wavelengths of water-borne sound at 200 Hz. Because of this small characteristic length, the impedance of the duct does not effectively change, and transmission through the elbow is nearly unity.

At higher frequencies, however, where the acoustic wavelength is of the same order as elbow length, impedance increases and transmission losses will be significant. Furthermore, high-frequency acoustic and vibrational energy reflected at the elbow can be spectrally redistributed, and therefore some lower frequency reflection may be detected. The magnitudes of this phenomenon, however, tend to be low.

Transmission Loss Through Screens

The resistance coefficient, K of a porous screen is defined as

$$\Delta p = K \frac{\rho V^2}{2} \qquad [2.13]$$

where Δp is the pressure drop across the screen, ρ is the fluid density, and V the volume mean velocity. Differentiation yields the change in pressure drop due to a perturbation in local velocity, u, to be

$$\partial(\Delta p) = K \rho V \partial u \qquad [2.14]$$

The acoustic impedance of the screen can then be found to be

$$\zeta = \frac{Z}{\rho c} = \frac{1}{\rho c} \frac{\partial(\Delta p)}{\partial u} = \frac{K V}{c} = KM \qquad [2.15]$$

where c is the acoustic wave speed and M is the Mach number. It is therefore shown that for low Mach numbers– for the present case it is less than 0.002– the impedance of the screen is very low, and transmission loss, TL, defined as

$$TL = 20 \log_{10} \left| \frac{2 + \zeta}{2} \right| \qquad [2.16]$$

is also small. The screen used in the flow conditioner had an estimated resistance coefficient of 0.966, resulting in a calculated transmission loss of less than one thousandth of a deciBel.

Transmission Loss Through a Thin-Plate Orifice

Analysis for an orifice plate yields similar results. An empirical relation for the relative impedance of the plate, given by Ingard[17] is

$$\zeta = \frac{1 - \beta^2}{\beta^2} \left(M - i\,(0.6) k\, \beta d \right) \qquad [2.17]$$

where k is the free wave number, d the duct diameter, and β is the orifice to duct diameter ratio. This relation is similar to the one given for the porous screen in that it shows impedance to scale with Mach number for fixed geometry and working fluid. The difference is the inertial term which makes impedance a complex function of frequency. Using the blade passage frequency and the definition of transmission loss given in the previous section, the loss across the orifice can be found to be a very small 0.324 dB. Because for constant Mach number and geometry, the transmission loss varies linearly with frequency, a signal would have to be at a frequency of over 2600 Hz to experience an attenuation of 1 dB.

2.4.8. Conclusions

It is clear from the discussions above that vibration, turbulence noise, and the ring-around effect were not problematic points in this investigation. However, the reflection that was measured at the steel-rubber boundary, and its resulting standing wave, most likely have significant impact on the shape of the measured acoustic spectra and the sound pressure levels at each frequency.

The most significant drawback to dealing with the standing wave is that it becomes difficult to quantitatively compare measurements made at different locations, because the influence of the standing wave varies from station to station. The estimates of standing wave frequency distribution of Section 2.4.5, which showed the blade passage amplitude for the Straight Inlet

configuration to be 2.76 dB greater than that for the Close-Coupled Elbow, illustrates such variations. However, if comparisons are limited to data taken at a single station, the results may be at least qualitatively valid. They are not quantitatively so, because the resonant nature of the standing wave tends to amplify or ameliorate the source signal depending on the amount of damping that exists at frequencies of interest, and the relative position of the measurement station to standing wave maxima and minima at those frequencies.

2.5. Experimental Procedure

Five combinations of inlet profile and nominal flow rate were investigated in this study. They are listed in Table 2.1 below:

Table 2.1 Inlet Velocity Profile Cases

Inlet Profile	Pump Inlet Configuration	Flow Conditioner Configuration	Nominal Flow Rate (Q[gpm])
Fully Developed, High	Straight [Fig 2.4]	Open [Fig 2.8c]	340
Fully Developed, Low	Straight	Open	310
Uniform	Straight	Screen [Fig 2.8a]	340
Orifice Distorted	Straight	Ecc. Orifice [Fig 2.8b]	310
Elbow Distorted	Elbow [Fig 2.5]	Open	340

The Orifice Distorted case was considered at a lower flow rate, 310 gpm, than the other three profiles due to the large pressure losses associated with the orifice. A second fully developed profile was considered in order to provide a point of comparison with the Orifice case.

For each of these cases, a complete inlet flow field measurement was made, along with acoustic and vibration measurements, a procedure that typically required eight to ten hours. As previously mentioned, each acoustic and vibration signal was sampled for a total period of 131 seconds, and the actual acquisition of this data consisted of five data sets of period 26.2 seconds each, which were sequentially acquired every 64 to 65 samples of the total of 258 flow field measurements made.

Because the constriction throttle dissipated the power input to the system by the pump largely by friction, the system temperature tended to rise about 4° F per hour. It was desired to maintain a relatively constant water temperature, in order to avoid any extraneous variation in the data due to change in viscosity, or thermal dependence of the instrumentation. It was therefore necessary to shut down the pump every 3 hours and cool the system by flushing the warm water and replacing it with fresh city water. This procedure allowed the water temperature to remain between 77-92°F. Two exceptions are the fully developed cases, for which this procedure was not performed as often, and the water temperature was allowed to reach 102°F.

Pump performance parameters, including pressure rise, flow rate, system static pressure, and throttle pressure loss were monitored at intervals of ten flow field samples for the duration of every case. These data were used to estimate the time average system flow rate and to check for any extreme variation in experimental conditions.

At the conclusion of each flow field measurement, a skeleton set of 13 measurements were repeated to check for repeatability of the data. The measurements were repeated at radial positions 0 to 1.965 inch at .655 inch radial increment, and at 0° to 270° at an angular increment of 90°.

3. Experimental Results

3.1. Test Conditions

The average values of system operation parameters including flow rate, pump pressure rise, temperature and system static pressure are listed in Table 3.1 below. Note the high average temperatures for the first two cases, as mentioned in Section 2.5.

Table 3.1 Experimental Conditions

Inlet Profile	Average Flow Rate (Q, [gpm])	Average Pump Pressure Rise (Δp, [psid])	Average Tank Temperature [°F]	Average Tank Static Pressure [psig]
Fully Developed, High	338.6	40.83	93	67.98
Fully Developed, Low	314.6	42.06	90.2	67.34
Uniform	335.9	41.13	84.4	68.3
Orifice Distorted	308.2	46.38	84.7	68.3
Elbow Distorted	340.3	41.01	86.2	67.46

3.2. Inlet Flow Profiles

The inlet flow field data for all cases considered are presented as two sets of contour plots. The first set, Figures 3.1 - 3.5 describes the time-average,

steady state flow velocity, obtained by calculating the mean value of the sample at every measurement position. The second set, Figures 3.11 - 3.15 presents the standard deviation of flow field, which gives an indication of the unsteadiness, or turbulence levels in the flow. Numerical data for steady state and unsteady profiles for all five cases considered are tabulated in Appendix D.

All contour plots are presented in terms of velocity normalized to the area-weighted mean velocity calculated from the flow field measurements themselves, not that measured by the flow meter. Spatial coordinates are normalized to the pipe radius. The mean, maximum, and minimum velocities are listed in the caption of each figure. Not all contours are labeled with values, but the contour increment is constant and also given in the caption, and value of unlabeled contours can be determined by interpolation or extrapolation.

3.2.1. Steady-State Profiles

The contour plots of Figures 3.1 - 3.5 present the time average velocity profile of each inlet flow field case.

Fully Developed, High Flow Rate

Figure 3.1 shows the velocity contour of the Fully Developed, High Flow Rate case, which was expected to approximate a symmetric, fully developed turbulent profile. It is plain that some distortion does exist in the flow, however, as reflected in the region of maximum velocity flow at the top of the plot. The distortion most likely exists because the 23 diameters of pipe between the measurement station and the outlet of the upstream 90° elbow was insufficient to develop the flow fully.

It could not be completely explained why the higher energy flow exists in the upper portion of the pipe rather than the lower, but it is not inconceivable that the secondary flow vortices shed by the elbow simply convect to one side, the bottom portion in this case, and the flow maintains its energy by increasing the velocity of the top region. This distortion results in an asymmetry parameter for this case, as defined in Section 2.3.2, of 1.06 at an angle of 159° from horizontal.

The Pitot-averaged volume flow rate calculated from this measurement deviated from that given by the flow meter by only 1.08%,

which is low compared to the measured area error previously stated to be 4.7%. Such low deviation is not to be expected, because the lower effective cross sectional area should lead to comparably lower Pitot-averaged flow rate. However, if the wall boundary layer velocity deficit is taken into account, along with the measurement uncertainties of the flow meter and Pitot-Static probe, the expected discrepancy between Pitot-averaged and flow meter measured flow rate is decreased to about 3.5%, which is nonetheless in disagreement with experimental results.

In Figure 3.6, a comparison is made between radial velocity profiles taken from the Fully Developed High case and the classic empirical formula for turbulent flow given by Schlichting[18], which is

$$\frac{u}{U} = \left(1 - \frac{r}{a}\right)^{\frac{1}{n}} \qquad [3.1]$$

where u is the local axial velocity, U is the center line velocity, r is the radial position and a the total duct radius. The exponent variable n depends on Reynolds number. The figure shows that the center line velocity ($r/R = 0$) is much lower in the measured data than predicted by the formula, and that this momentum deficit is compensated by higher velocities, compared to the formula prediction, from mid-radius to the pipe wall. The discrepancies shown here are most likely due to insufficient development length allowed for the Fully Developed cases.

Fully Developed, Low Flow Rate

The Fully Developed, Low Flow Rate contour of Figure 3.2 is qualitatively similar to that of its 340 gpm counterpart, with the exception of the peninsulas of higher velocity which jut into lower levels at about $\theta = 45°$ and $\theta = 125°$. This pattern is comparable to that of the Elbow Distorted contour of Figure 3.5, where counter-rotating vortices entrain higher energy flow and draw it outward. Such a direct comparison supports the conjecture made above with regard to convection of the vortices. The asymmetry parameter for this case was 1.06 at and angle of 171°, and the discrepancy in Pitot-averaged flow rate was 1.06%, again smaller than the expected value based on area ratio arguments.

Uniform

The velocity gradients of Figure 3.3, the Uniform case, are very high at the pipe wall, and fairly mild otherwise. The steady-state velocity in the "flat" region varied by only ±2.5% for the most part, with the most significant exceptions being the encroachment of the 1.00 contour at $\theta = 40°$ and $\theta = 170°$.

While comparison with Figure 3.1 shows that the reduction in variation from mean velocity due to the screens was much less than the 99% predicted in the design process, the very low asymmetry parameter of 1.013 emphasizes the relative symmetry of the flow. Non-uniformities, evidenced by undulations in the profile contour, are most likely caused by variation in the spacing, diameter, and cleanliness of the screen used in the flow conditioner. Other possibilities include fusion of jets from neighboring screen openings, which tends to occur when the openings are small.

The calculated flow rate error for the Uniform case was again about 1%, very low in light of the arguments made for the fully developed cases.

Orifice Distorted

The eccentric orifice contour of Figure 3.4 depicts what was intended to be a strongly distorted inlet profile. A very high asymmetry parameter of 6.25 at $\theta = 62°$ indicates that fully 86% of the total volume flow passes through that half of the inlet duct to the right of a diametral line drawn at that angle. A large difference of 67.9% in the Pitot-averaged flow rate was obtained relative to that given by the flow meter, however, implying that caution should be used in making any type of quantitative interpretation of these data. A flow field containing such strong axial velocity gradients is a hostile environment in which to make measurements regardless of the instrument used. In the case of the Pitot-Static probe used here, secondary flow, strong axial gradients and flow separation effects can wreak havoc on any attempt to measure purely axial velocities. It is not surprising that such errors were incurred.

Elbow Distorted

The Elbow Distorted profile returns attention to more typical flow conditions. As shown in Figure 3.5, the inner radius of the elbow lies along the negative x axis. Qualitatively, the results in this case matched expectations. The high energy flow gets carried by its own momentum to the outer radius as it turns through the elbow, and the lower energy boundary

layer flow is drawn in to take its place. The net effect is the formation of two mirror-image, counter-rotating vortices, the bottom vortex rotating in the clockwise direction and the top one counter-clockwise.

The asymmetry parameter of 1.184 was 10% higher for this case than for the Fully Developed cases, and 16% higher than for the Uniform case. The error in calculated flow rate was also higher, at 3.96%, possibly because a different calibration method was used for the measurement system in this case, which resulted in improved accuracy. The discrepancy in flow rates can then be explained by loss of boundary layer flow, which in the present case was approximately 3.7%.

The mean flow profile for the Elbow Distorted case was compared to a three-dimensional, inviscid calculation by Felici[19], for flow 1.4 diameters downstream of a 90° bend of identical geometry and flow conditions as those presented here. Figure 3.7 shows the contours of both the measured and calculated profiles. The two profiles compare well in both maximum and minimum velocities, but the velocity gradients for the calculated profile are much higher than those measured, evidenced by much closer spacing of the contour lines near the outer edges of the vortices. The vortex core positions also do not match exactly, with the core for the calculated case lying approximately 0.1 diameter farther out from the inner radius wall than shown for the measured profile.

Similarly smooth measured velocity gradients were observed in the Orifice Distorted case described previously, and the same sources of error could be involved here as were suspected in that case. However, it is also possible that Felici's calculation overestimated the velocity gradients, because of a deficiency in the calculation scheme chosen. This possibility would also explain the difference in core propagation from the inner radius, because a tighter vortex induces in its mirror image a higher velocity, away from the wall.

A comparison of the Elbow Distorted contour was also made to experimental data due to Enayet[20]. These data are for much lower Reynolds number, (43,000 compared to 393,000 for the present data) and for a larger bend radius (2.8*D* compared to 1.62*D* reported here). The flow profile at the elbow inlet for the published data, assessed at 0.64 diameters upstream of the elbow, was highly symmetric, fully developed turbulent. Outlet profile

measurements were made using laser Doppler velocimetry, at a cross section one diameter downstream of the elbow outlet.

Figure 3.8 compares the two profiles, and it can be seen that the maxima and minima compare well, being [1.15, .7] for the present case, and [1.2, .8] for the quoted case. A noticeable difference is that the distance from the inner radius to the area of maximum velocity is much greater for the present results than for the published data. However, the shape of the vortex cores are more similar than was the case for the previous comparison, and Enayet's results do show relatively smooth gradients in the vortex core, and little propagation away from the inner radius, lending credence to the trends seen in the present measurements.

A more accessible qualitative comparison of the Fully Developed, Uniform, Orifice Distorted, and Elbow Distorted profiles are given in Figures 3.9 - 3.10. The first figure shows these profiles normalized to their maximum velocity, so that they are all of uniform height. Illuminated are the primary features of the different profiles- the slight distortion in the Fully Developed case, the undulation of the Uniform profile, and the vortex core in the Elbow Distorted profile. Figure 3.10 shows the same profiles, all normalized to the maximum velocity of the Orifice case. The relative magnitudes of the four profiles can thus be discerned.

3.2.2. Unsteadiness Profiles

In the interest of completeness, contour plots of the time wise standard fluctuation of the velocity as measured by the Pitot-static probe are presented in Figures 3.11 - 3.15. The time wise standard deviation is used as a simple measure of the unsteadiness of the flow, primarily due to turbulence. The primary frequencies of the turbulent fluctuations were very low compared the acoustic range of interest, typically less than 10 Hz.

As for the steady-state profiles, the contour values given are normalized to the Pitot-averaged volume mean velocity, the contour increments are constant, and the maxima, minima, and contour increment values are given in the captions.

Fully Developed, High Flow Rate

Figure 3.11 gives the unsteady contour plot for the Fully Developed, High Flow Rate case, which shows maxima in the region corresponding to minimum velocity, excluding regions near the pipe wall boundary layer. This inverse relationship was the trend throughout the data presented here, with some notable exceptions. The maximum standard deviation of 5% mean velocity seemed reasonable.

Fully Developed, Low Flow Rate

As was the case for the steady-state velocity, the Fully Developed, Low Flow Rate contour of Figure 3.12 compares well to its 340 gpm counterpart. Again, the inverse relationship between mean and deviation is manifested, with a maximum deviation of 5%.

Uniform

The unsteady velocities of the Uniform case, shown in Figure 3.3, are significantly lower than the fully developed cases. Except for a single point at approximately $\theta = 260°$, the unsteadiness is fairly uniform and less than one quarter of the value for the Fully Developed cases, reflecting the benefits of using wire mesh screen for turbulence reduction.

The discrepancy at 100° was caused by an unexplained spike in the sample for that point, which was balanced enough to have small impact on the calculation of the mean value, but caused a sharp increase in standard deviation. No other such spikes were observed before or after, and because the problem was not discovered until well after the measurement was completed, it could not be corrected. It was decided to include that large standard deviation for completeness.

Orifice Distorted

The Orifice Distorted case presented a departure from the norm in terms of unsteadiness level. As shown in Figure 3.14, the maximum deviations are found in regions of high measured velocity gradient, and reached levels of up to 62% of the volume mean velocity, meaning that the fluctuation amplitude in these regions is of the same order as the mean velocity. It should be well noted that these mean velocities are up to five times larger than those measured for the other three profile cases. Clearly,

very strong unsteadiness exists in this flow field, and it is again unsurprising that measurement errors may have been incurred.

Elbow Distorted

Figure 3.15 presents the unsteadiness contour for the last, Elbow Distorted case. As with the first three cases, velocity fluctuations vary inversely with the mean, the minima being in the high-energy region and maxima in the low energy vortex region. Maximum deviation levels of 6% mean velocity are higher but comparable to the first three cases.

3.2.3. Summary

The inlet axial velocity profiles depicted above represent a range of asymmetry sufficient for the purposes of this study. The Uniform and Orifice Distorted cases present extremes of symmetry and asymmetry respectively, and the Fully Developed and Elbow Distorted cases are flow fields found in common practice.

The Orifice Distorted case presented a hostile environment for flow measurement using a Pitot-static probe. It was not unexpected that some unusual artifacts such as the overestimate of flow rate and large turbulent fluctuation amplitudes would develop. However, if interpreted on a qualitative, order of magnitude basis, the Orifice Distorted profile still shows strong asymmetry and is therefore of significant value for the present purposes.

Table 3.2 Comparison of Flow Meter Measured and Pitot-Averaged Flow Rates

Inlet Profile	Pitot - Avg. Flow Rate [gpm]	Measured Flow Rate [gpm]	Pitot - Avg. Flow Rate Deviation	Deviation From Nominal Flow Rate
Fully Developed, High	334.9	338.6	-1.08%	-0.41%
Fully Developed, Low	311.3	314.6	-1.06%	1.49%
Uniform	332.0	335.9	-1.18%	-1.20%
Orifice Distorted	517.3	308.2	67.86%	-0.60%
Elbow Distorted	326.9	340.4	-3.96%	0.10%

The Fully Developed and Uniform profile results did not match the design intent. The Fully Developed profiles showed some distortion, and

were not as symmetric as was desired. The Uniform profiles were sufficiently symmetric, but radial variations in axial velocity were greater than predicted. Furthermore, Pitot-averaged flow rates calculated from these profiles, listed in Table 3.2, compared better with flow meter measurements than expected, the discrepancy being approximately 2.5% lower than that predicted by a consideration of area loss and boundary layer deficit. In light of these deficiencies, it is still possible to apply these data for comparison purposes because they represent valid and relevant values of the distortion parameter, as shown in Table 3.3.

The Elbow Distorted case was judged to be the most reliable profile considered, in light of the expected magnitude of its flow rate discrepancy, as shown in Figure 3.2, and its acceptable comparison to other computational and published experimental results.

In all, the four inlet profiles considered provide a range of the asymmetry parameter, listed in Table 3.3, between 1.013 and 6.257, with most of the values being near unity. This range was considered adequate for the purposes of comparison to the acoustic data.

Table 3.3 Velocity Profile Statistics

Inlet Profile	Mean Velocity ($\bar{u}$,[m/s])	Max Velocity [$/\bar{u}$]	Min Velocity [$/\bar{u}$]	Asymmetry Parameter /angle[Eq.27]	Max St. D. [$/\bar{u}$]	Min St. D. [$/\bar{u}$]
Fully Dev., High	2.707	1.105	0.729	1.060/159°	0.050	0.010
Fully Dev., Low	2.515	1.106	0.739	1.061/171°	0.051	0.012
Uniform	2.682	1.079	0.708	1.013/86°	0.020	0.006
Orifice Distorted	4.180	3.554	-0.031	6.257/62°	0.630	0.069
Elbow Distorted	2.641	1.161	0.683	1.184/102°	0.061	0.015

3.3. Pump Noise Levels

Acoustic spectra measured at the pump inlet and outlet as described in Chapter 3 are presented in Figures 3.16 - 3.33 as sound pressure level per unit bandwidth versus frequency. The complete narrow-band spectra is given as a line plot, with the levels at harmonic peaks labeled with a circle. The only peak levels considered here were those at shaft frequency and harmonics 2

through 8, 12 and 16. These harmonic peaks appeared in most but not all spectra, but were the most consistent.

Discussion of the results will focus on comparison of the spectra at the blade passage frequency, invariably the location of highest *SPL*. However, relevant variations in noise floor and other shaft harmonics were considered.

3.3.1. Inlet Spectra

Acoustic spectra from individual measurements taken at the pump inlet are given in Figures 3.16 - 3.20. Comparison Plots, discussed below, are presented in Figures 3.21 - 3.24.

Fully Developed and Uniform Cases

The first three spectra, taken in the Fully Developed High, Fully Developed Low, and Uniform cases, respectively, compare very closely, as shown in Figure 3.21. All ten harmonic peaks considered are present and show deviations in *SPL* typically less than three dB and not more than six dB. Similarly, noise floor levels vary less than three dB. At the blade passage frequency, sound pressure levels fell between 182.75 dB for the Uniform case and 179.75 for Fully Developed Low, giving a deviation of three dB which is within error for a spectral analysis of this type.

Analytical errors occur when real signal frequencies fall between lines in a digital spectrum. As outlined in the error analysis of Appendix C, the maximum possible error in peak level in this case is 3.92 dB, and the lost peak energy is redistributed to nearby bands, broadening the peak and sharply reducing losses in total spectral level. It is possible that the pump speed or the A/D clock speed may have shifted slightly– half a bandwidth or 0.076 Hz would suffice– and therefore redistributed the acoustic energy and lowered the peak level.

To check this effect, the energy density over a twenty Hz band centered at 205 Hz was calculated for all five cases and compared, these values give a second measure of the variation in SPL at the blade passage frequency. These values are summarized in Table 3.4. It can be seen that a more broad-band approach to level estimation leads to closer agreement among the first three cases, which show a level deviation at f_{bp} of just over 0.7 dB. Errors in the wide-band estimate primarily result from randomness of the noise floor due to turbulence.

Orifice Distorted

The inlet acoustic spectra for the Orifice case, compared to the Fully Developed Low case in Figure 3.22, is characterized by an almost uniform increase of about 3.5 deciBels in noise floor level compared to the fully developed spectrum. The increase is largest at low frequencies, and reaches a maximum of about 10 dB near 25 Hz. The second harmonic of the shaft frequency was diminished to the noise floor in this case, and the f_{sh} itself increased by about 9 dB. The increase in noise floor is most likely due to increased turbulence generated by the orifice.

At f_{bp}, the sound pressure level is 2.47 dB higher than the Fully Developed Low case but is comparable to the Fully Developed High and Uniform cases. A wide-band level of 163.0 dB also compares well with first three cases.

Elbow Distorted

Another sharp, 9.2 dB rise in shaft frequency level is apparent in the inlet spectrum of the Elbow Distorted case, compared to the Fully Developed High case in Figure 3.23. Because these last two cases presented the most distorted flow fields, and because the data for both contain such increases at f_{sh} it is possible that inlet distortion may have some effect on shaft tone rather than blade passage tone.

The shape of the noise floor level for the Elbow Distorted case changes subtly, increasing in some ranges and decreasing in others. At f_{bp}, the level is 1.94 dB lower than for Fully Developed, High Flow Rate, and the broad band level is also 2.07 db lower. The discrepancy in peak level can be passed off as analytical error, but that in the broad band level suggests the influence of the standing wave. The calculation using Louie's method, as presented in Section 2.4.5, found the difference in standing wave amplitude to be 2.76 dB, a fairly close match to the experimental result.

Figure 3.24 presents plots of the difference in inlet sound pressure level spectra between the two distorted cases and their fully developed counterparts, matched by flow rate. Figure 3.24a, which shows the Orifice Distorted case compared to the Fully Developed, Low Flow case, indicates that the difference in harmonic peak levels between the two cases, marked by circles, closely follows the trend in broad band noise. Some exceptions will be noted at the second, third and fifth harmonics, but the majority of harmonic

peak level differences are difficult to see in the plot because they are hidden in the noise difference distribution. Similar results are found for the comparison of the Elbow Distortion case to the Fully Developed, High Flow case shown in Figure 3.24b. The only frequencies in this plot which deviate from the broad band trend are at f_{sh} and 12 x f_{sh}.

Figure 3.24 allows a comparison to be made between the relative effects of changing inlet conditions on tonal and broad band *SPL*. It can be seen that, for the most part, both components of the sound pressure spectrum are effected similarly. The comparison is especially close near the blade passage frequency, where the tonal level differences do not.fall outside the range of neighboring broad band noise differences for either comparison made.

3.3.2. Outlet Spectra

In general, the outlet spectra shown in Figures 3.25 - 3.32 describe a "smoothing" of the noise floor compared to the inlet spectra previously considered. This effect might be produced by the change in measurement position with respect to the standing wave, which would effect the amplitude at frequencies corresponding to resonant poles and zeroes. In fact, if the acoustic impedance of the pump is significant, the standing wave formed at the inlet may not reach the outlet, and the measurements made there may be completely free of interference, because the length of steel pipe at the outlet is short enough not to generate its own resonant standing wave. If this were true, the outlet acoustic measurements would most accurately describe the acoustic output of the pump. High outlet turbulence, relative to the inlet, caused by the pump may also account for the weaker apparent variations in noise floor levels.

In addition to the change in noise floor shape, sharp reduced levels are seen in shaft frequency and its harmonics up to and including f_{bp}, compared to inlet measurements. Exceptions to this trend are the 310 gpm cases, where the f_{sh} levels actually increase. Again these discrepancies most likely reflect the significance of measurement position in light of the presence of standing waves. Still, it is surprising that the *SPL* at blade passage frequency is higher at inlet than outlet, which is physically closer to what is generally considered to be the primary source of blade passage noise- the volute cutwater.

Fully Developed and Uniform Cases

As was the case for the inlet measurements, acoustic spectra for the three most symmetric flow fields show only small variation, as shown in Figures 3.30. Noise floor levels for these spectra match within maximum deviation of 5 dB. Harmonic peak levels match within 4 dB except at the 16th harmonic, where maximum deviation is almost 5 dB.

At the blade passage frequency, peak levels compare within 2.85 dB and wide band levels compare to 0.47 dB.

Orifice Distorted

Outlet acoustic data for the eccentric orifice case, shown with the Fully Developed Low case in Figure 3.31, compare closely. Noise floor levels are similar except near f_{bp}, where Orifice case levels rise above Fully Developed Low by about 5 dB. Harmonic peak levels match within 3 dB except at f_{sh} where deviation is 3.2 dB.

A 1.3 dB deviation in blade passage peak level, and a wide band deviation of 0.8 dB indicate that the outlet blade passage levels are not significantly effected by strong inlet distortion.

Elbow Distorted

Once again, the Elbow Distorted case compares well to the uniform velocity case, as shown in Figure 3.32, with one notable exception. Noise floor levels compare extremely well with Fully Developed, High Flow Rate throughout the spectrum. Harmonic peak levels match within 3 dB except at f_{sh} and the first harmonic, the latter of which barely rises above the turbulent noise floor. The Elbow Distorted shaft frequency is 5.46 dB above the Fully Developed level, and the harmonic is 4 dB lower.

Blade passage peak levels compare extremely well, within 0.5 dB, and wide band levels compare to 0.57 dB, a notable case in which wide band levels showed greater deviation than peak levels.

As was depicted for the inlet measurements, Figure 3.33 presents plots of the difference in outlet sound pressure level spectra between the distorted and corresponding fully developed cases. Figure 3.33a, shows the Orifice Distorted case compared to the Fully Developed, Low Flow case, and it is again seen that, except for discrepancies at some low harmonics, the harmonic peak level differences fall within range of that of the broad band

noise. Results for the Elbow Distorted and Fully Developed, High Flow case shown in Figure 3.33b compare equally well. Comparisons are particularly close at blade passage frequency.

3.3.3. Summary

Figure 3.34 show plots of inlet and outlet peak sound pressure level as functions of the asymmetry parameter, α, for both shaft and blade passage frequencies. These data, along with wide-band levels, are also listed in Table 3.4. From the Figure 3.34a, for the blade passage frequency, it can be seen that the peak levels vary by only 3 dB over the range of α, and do not form any recognizable monotonic pattern versus that parameter. Figure 3.34b shows data for the shaft frequency, which did show some variation with α, being larger for the Elbow and Orifice Distorted cases than for the the more symmetric flows.

Table 3.4 Comparison of Shaft and Blade Passage Frequency Levels

Profile	Hydro-phone Position	Shaft Peak Frequency	Shaft Peak Level	Blade Passage Peak Frequency	Blade Passage Peak Level	[195-205] Hz Wide Band Level
		[Hz]	[dB]	[Hz]	[dB]	[dB]
Fully Dev., High	Inlet (A)	29.25	166.74	204.92	182.44	163.21
Fully Dev., Low		29.25	164.16	205.08	179.75	162.89
Uniform		29.25	165.52	204.92	182.75	162.91
Orifice Distorted		29.25	173.02	205.08	182.22	163.04
Elbow Distorted		29.25	175.94	204.92	180.50	161.14
Fully Dev., High	Outlet (C)	29.25	164.66	204.92	174.12	155.00
Fully Dev., Low		29.25	165.47	205.08	172.27	155.47
Uniform		29.25	167.52	204.92	175.12	155.36
Orifice Distorted		29.25	168.68	205.08	173.55	154.70
Elbow Distorted		29.25	170.12	204.92	173.62	154.43

The conclusion to be made from these data is that the asymmetric inlet profiles had no measurable or consistent effect on the blade passage tone, but did show some inconsistent influence on shaft tone. For all cases and at inlet

and outlet, deviations in *SPL* at the f_{bp} peak were less than 3 dB, less than measurement uncertainty of 4.1 dB, and broad band deviation was much smaller. Comparison of *SPL* differences between the two distorted profile cases and their fully developed counterparts showed that at both inlet and outlet, the changes in most harmonic peaks due to changes in inlet profile compared very closely to that for the broad band noise floor. This evidence suggests that whatever influence the change in inlet geometry had on blade passage noise had more to do with changes in turbulence levels and the shape of the standing wave spectrum than with inlet distortion.

A noticeable relationship, however, was observed at the shaft frequency, where sound pressure levels increased for the distorted inlet flow cases. However, the increases in SPL at f_{sh} bore no monotonic relationship to asymmetry parameter, and it would be beyond the scope of this study to pursue this phenomenon further.

4. Conclusion

An experimental study was conducted to determine the influence of asymmetry in the inlet flow profile on the noise emitted by a centrifugal pump at the blade passage frequency. A simple qualitative mechanism was presented whereby such a relationship could exist. Simultaneous measurements of inlet axial velocity and the acoustic pressure spectrum produced by the pump were then made for four different inlet velocity profiles, the aggregate of which represented a wide range of characteristic distortion levels. The results of these measurements were compared, in order to determine whether the described mechanism relating inlet distortion and blade passage noise is measurably significant.

4.1. Impact of Distortion on Pump Noise

Based on the results of Chapter 3, there is no clear evidence that inlet distortion has an effect on the level of the blade passage tone. Sound pressure levels at the blade passage peak do not vary by more than the prescribed measurement uncertainty for all inlet profiles considered, which consist of a wide range of inlet distortion.

No sign of a relationship between inlet distortion and blade passage noise was seen for the present experimental conditions. It is possible, however, that some relationship does exist, but was not detected due to saturation by other recognized sources of blade passage noise, most notably impeller wake interaction with the volute cutoff. Small changes in blade passage *SPL* were shown to be less than measurement uncertainty of 4.1 dB

and may have been related to changes in the turbulence spectrum and other extraneous effects due to changes in inlet geometry.

Moreover, resonant response of the present experimental facility, due to acoustic reflection at impedance boundaries at the pump inlet and outlet. confuses interpretation of the data. The resonant standing wave generated by these reflections is highly dependent on system geometry and material properties, and its presence in the acoustic measurement sections diminishes confidence in quantitative comparison of measured spectra for different configurations.

The information that can be gained from the present work is therefore preliminary, and further work is required to better isolate and understand the phenomenon of interest. Some suggestions for future courses of action follow.

4.2. Recommendations for Future Work

As a matter of first course, it would be desirable to eliminate all extraneous sources of blade passage noise in order to isolate the inlet distortion phenomenon. The most significant source to be eliminated in such an effort would be impeller wake interaction with the cutoff. This could be accomplished by employing a pump design with no cutoff, perhaps with an axial collector. Such a geometry would reduce that component of the blade passage tone due to wake-cutoff interaction, and improve observability of the phenomenon of interest.

With regard to the standing wave, several approaches may be taken. The most obvious would be to make further attempts to decrease reflection at the impedance boundary by treatment of the rubber hose. Reflection at such an impedance boundary is a complex phenomenon, and is highly dependent on duct geometry, material properties, and treatment method. The approach described herein was necessarily *ad hoc* due to time constraints, and it can be gathered from that experience that a more careful analysis of the problem would help considerably.

One way to simplify the problem would be to discard the wire helix, composite hose design employed in the present case, in favor of a more homogeneous shell design, at least for that length of hose that is to be acoustically treated. The wire helix may make compression of the inner hose wall very difficult to accomplish by exterior clamping, because it is designed to

bear a large portion of any applied radial loads. Uniform rubber hose would make compression easier, but it is not known whether such a design is commercially available, or practical in light of system static pressure requirements.

Reducing reflection at the impedance boundaries would be a challenging task, and it may be more practical to focus on eliminating resonance in the standing wave by shortening the overall length of steel piping at the pump inlet and outlet. Such a change would have the effect of reducing the resonant modal density of the standing wave, and it may be possible to push the fundamental resonant mode above the frequency range of interest.

The analytical model of the standing wave presented by Louie[12] would be a useful tool for assessing the effect of such geometry changes. The model could be made more accurate, however, if instrumentation were added and some labor was expended in obtaining better measurements of acoustic wave speed in the various ducts, vibration of the duct walls, and reflection at the impedance boundaries. Additionally, it would be useful to measure and account for the acoustic impedance of the pump itself, which has heretofore been neglected.

Another approach to the standing wave problem is given by Neise[21], who describes a semi-empirical method by which the measured sound field of ducted fans was successfully separated into components due to the source fan noise and to the response of the system ducting. This method was applied to a centrifugal pump system with some success by Mongeau[6], who conducted his experiments in air. In order to apply the method to the present case, it would be necessary to vary the pump shaft speed in order to change the blade passage frequency. If some mechanism were installed to allow for this, the method described by Neise may overcome the difficulties of the resonant standing wave.

Regarding the inlet flow field, some improvements to the generation schemes for the fully developed and uniform profiles are called for. Changes in flow conditioner screen geometry would most likely accomplish this goal.

Although the accuracy of inlet flow field measurement system is less crucial than that for acoustic measurements, it would be worthwhile to investigate other flow field measurement techniques which would account for the three dimensionality of the distorted profiles due to the 90° elbow and

the orifice. Improved accuracy and a more complete knowledge of the transverse flow field would be helpful in assessing the overall effect on pump noise.

5. References

1. Simpson, H.C., R. Macaskill, and T.A. Clark, "Generation of Hydraulic Noise in Centrifugal Pumps,"*Proceedings of the Institution of Mechanical Engineers*, Vol 181, Pt 3A, 1966-67, pp 84-108.

2. Simpson, H.C., T.A. Clark, and G.A. Weir, "A Theoretical Investigation of Hydraulic Noise in Pumps,"*Journal of Sound and Vibration*, Vol 5, No. 3, 1967, pp 456-488.

3. Simpson, H.C., and T.A. Clark, "Noise Generation in a Centrifugal Pump," ASME Society Paper 70-FE-37, 1970, pp 1-8.

4. Yuasa, Tatsuji, and Tatsuo Hinata, "Fluctuating Flow Behind the Impeller," *Transactions of the Japanese Society of Mechanical Engineers*, Vol. 22, No. 174, 1979, pp 1746-1753.

5. Sudo, S. et al., *The Hitachi Hyoron*, Vol. 59, No. 3, 1977, p 75.

6. Mongeau, Luc, "Experimental Study of the Mechanism of Sound Generation by Rotating Stall in Centrifugal Turbomachines," Ph.D. Thesis, The Pennsylvania State University, University Park, 1991.

7. Neise, W., "Review of Noise Reduction Methods for Centrifugal Fans," ASME Society Paper 81-WA/NCA-2, 1981, pp 1-11.

8. Deeproose W.M., and A. N. Bolton, "Current Industrial Pump and Fan Fluid-Borne Noise Level Prediction," National Engineering Laboratory, East Kilbride, C251/77, 1977, pp 43-47.

9. Taylor, G. I. , and G.K. Batchelor, "The Effect of Wire Gauze on Small Disturbances in a Uniform Stream," *Quarterly Journal of Mechanical and Applied Math*, Vol II, Pt 1, 1949, pp 1-29.

10. Bendat, Julius and Allan Piersol, *Engineering Applications of Correlation and Spectral Analysis*, John Wiley & Sons, New York, 1980.

11. Fuller, C.R, and F.J. Fahey, "Characteristics of Wave Propagation and Energy Distributions in Cylindrical Elastic Shells Filled with Fluid," *Journal of Sound and Vibration*, Vol. 81, No. 4, 1982, pp 501-518.

12. Louie, Lisa Lai Yee, "Active Control of Pipe-Borne Pump Noise," S.M. Thesis, Massachusetts Institute of Technology, Cambridge, MA, 1991.

13. Clinch, J. M, "Measurement of the Wall Pressure Field at the Surface of a Smooth-Walled Pipe Containing Turbulent Water Flow," *Journal of Sound Vibration*, Vol. 9 No. 3 1969 pp 398-419.

14. Rogers, W. L, *Transactions of the American Society of Heating and Ventilation Engineers*, Vol. 60, 1965, p 411.

15. Ingard, K. Uno, "Effect of Wall Compliance on Sound Propagation in a Pipe," Internal Report, Massachusetts Institute of Technology, Cambridge, MA, 1989.

16. Cummings, A. "Sound Transmission in Curved Duct Bends," *Journal of Sound Vibration*, Vol. 35, No. 4, 1974, pp 451-477.

17. Ingard, K. Uno, Lecture Notes for Massachusetts Institute of Technology Course 16.56, "Noise Control Engineering," Spring, 1991.

18. Schlichting, Hermann, Boundary Layer Theory, McGraw-Hill, New York, 1979, p 599-600.

19. Felici, Helene, Ph.D. Thesis, (in preparation), Department of Aeronautics and Astronautics, Massachusetts Institute of Technology, Cambridge, MA, 1991.

20. Enayet, M.M., M.M. Gibson, A.M.K.P. Taylor, and M. Yianneskis, "Laser Doppler Measurements of Laminar and Turbulent Flow in a Pipe," NASA Contractor Report 3551, 1982, pp 1-59.

21. Neise, W. and B. Barsikow, "Acoustic Similarity Laws for Fans", Journal of Engineering for Industry, Vol 104, May, 1982, pp162-168.

22. *Fluid Meters - Their Theory and Application*, Bean Howard S, Editor, The American Society of Mechanical Engineers, Sixth Edition, New York, 1971.

23. Kline, S.J. and McClintock, F.A., "Describing Uncertainties in Single Sample Experiments", *Mechanical Engineering*, Vol. 75, No. 1, 1953, pp 3-9.

24. Burgess, John C., "On Digital Spectrum Analysis of Periodic Signals", Journal of the Acoustical Society of America, Vol. 58, No. 3, 1975.

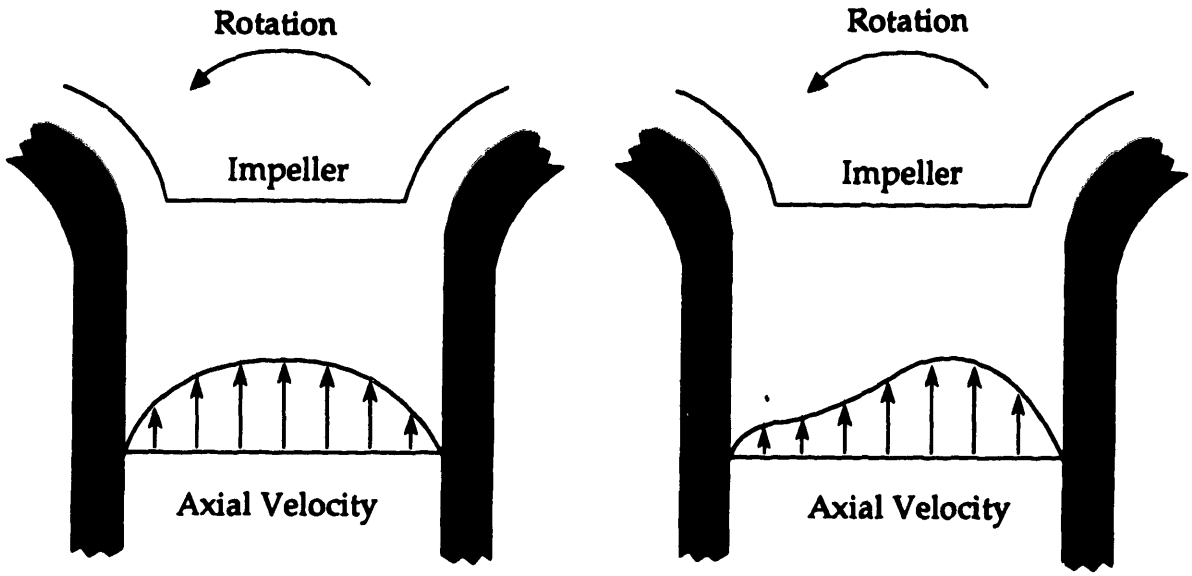

a. Symmetric Inlet Profile

b. Assymetric (Distorted) Inlet Profile

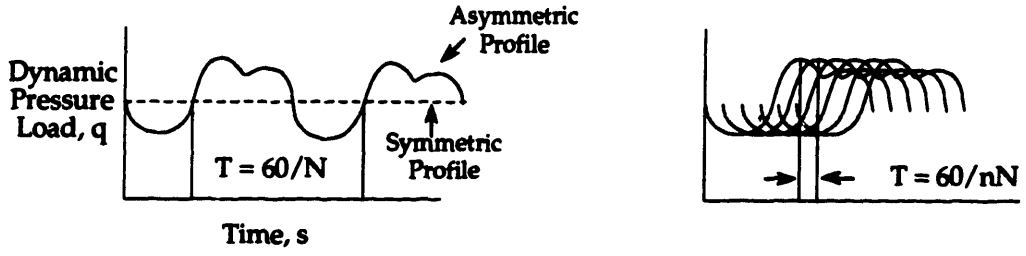

c. Single Blade Load History

d. Composite Blade Load History for all n Blades in Asymmetric Flow

Figure 1.1 Conceptual Relationship Between Inlet Distortion and Blade Passage Noise

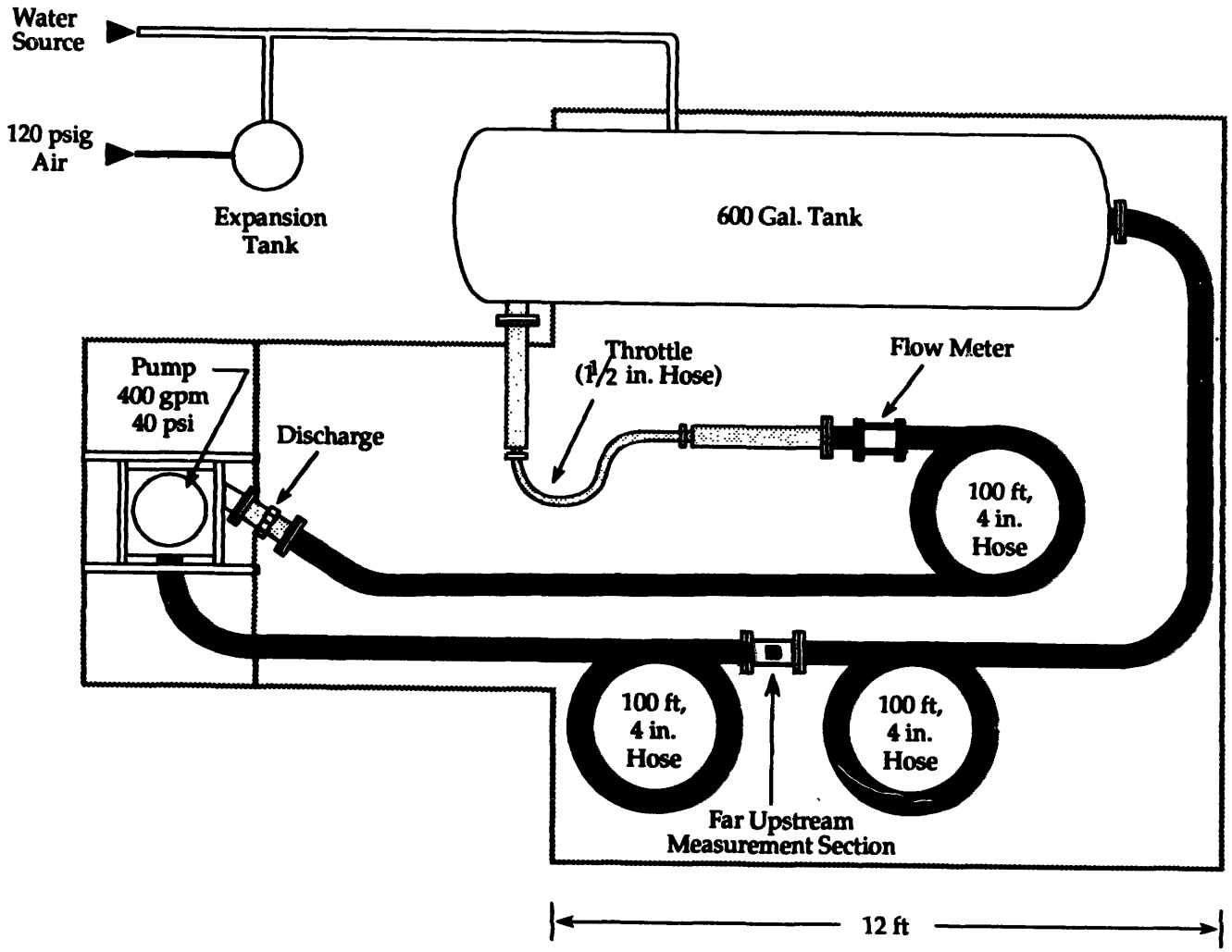

Figure 2.1 Acoustic Pump Loop

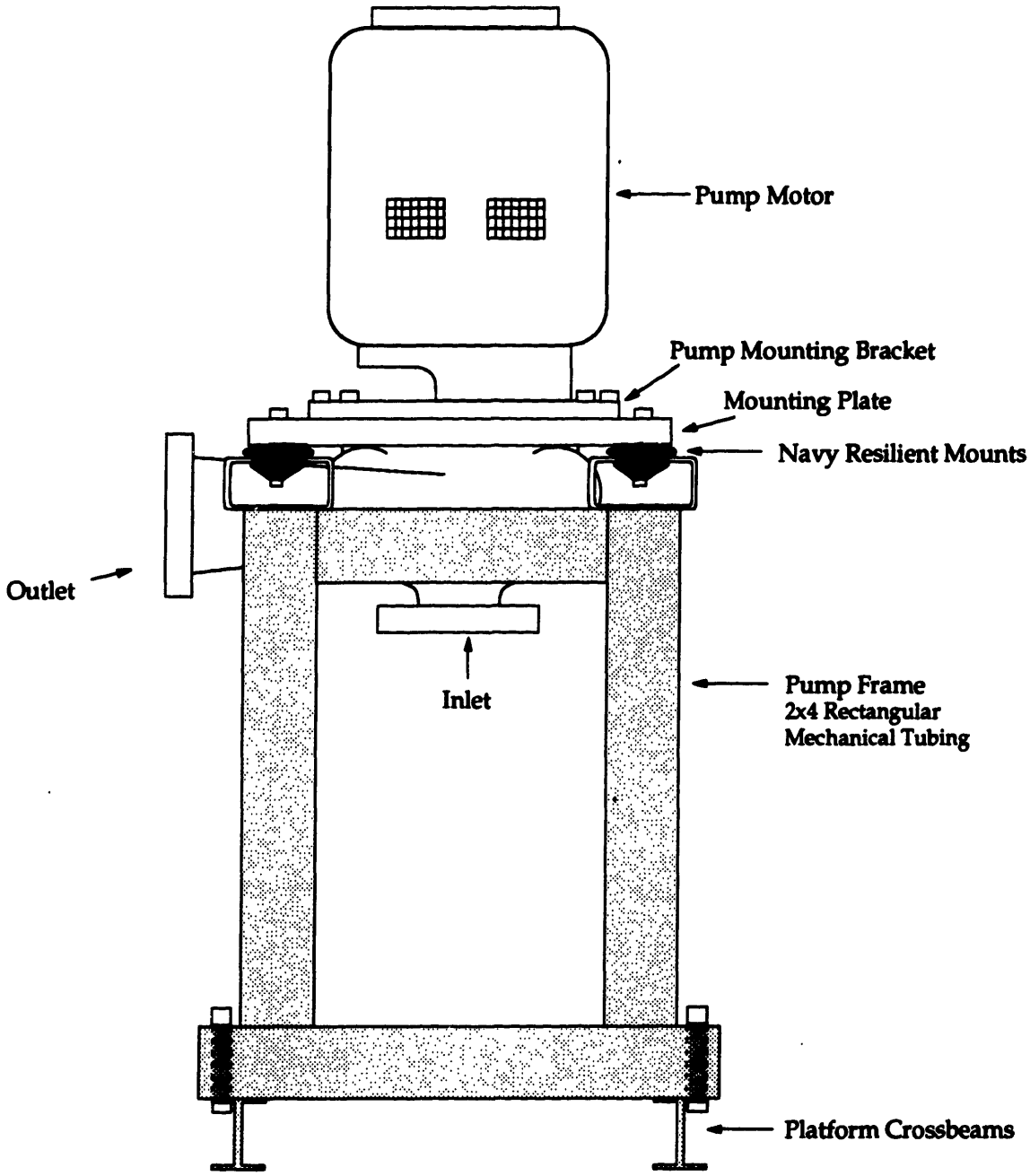

Figure 2.2 Pump Mounting Assembly

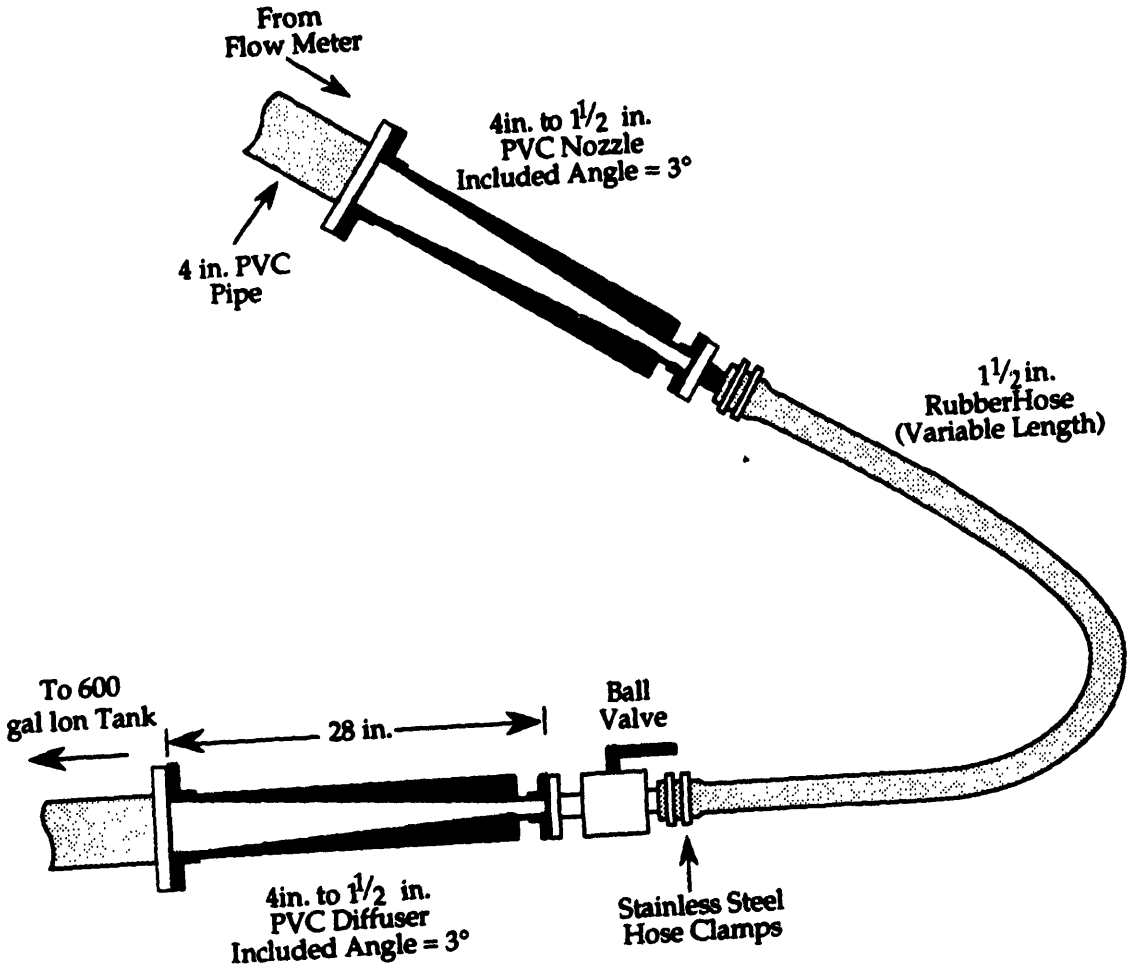

Figure 2.3 Variable Length Contraction Throttle

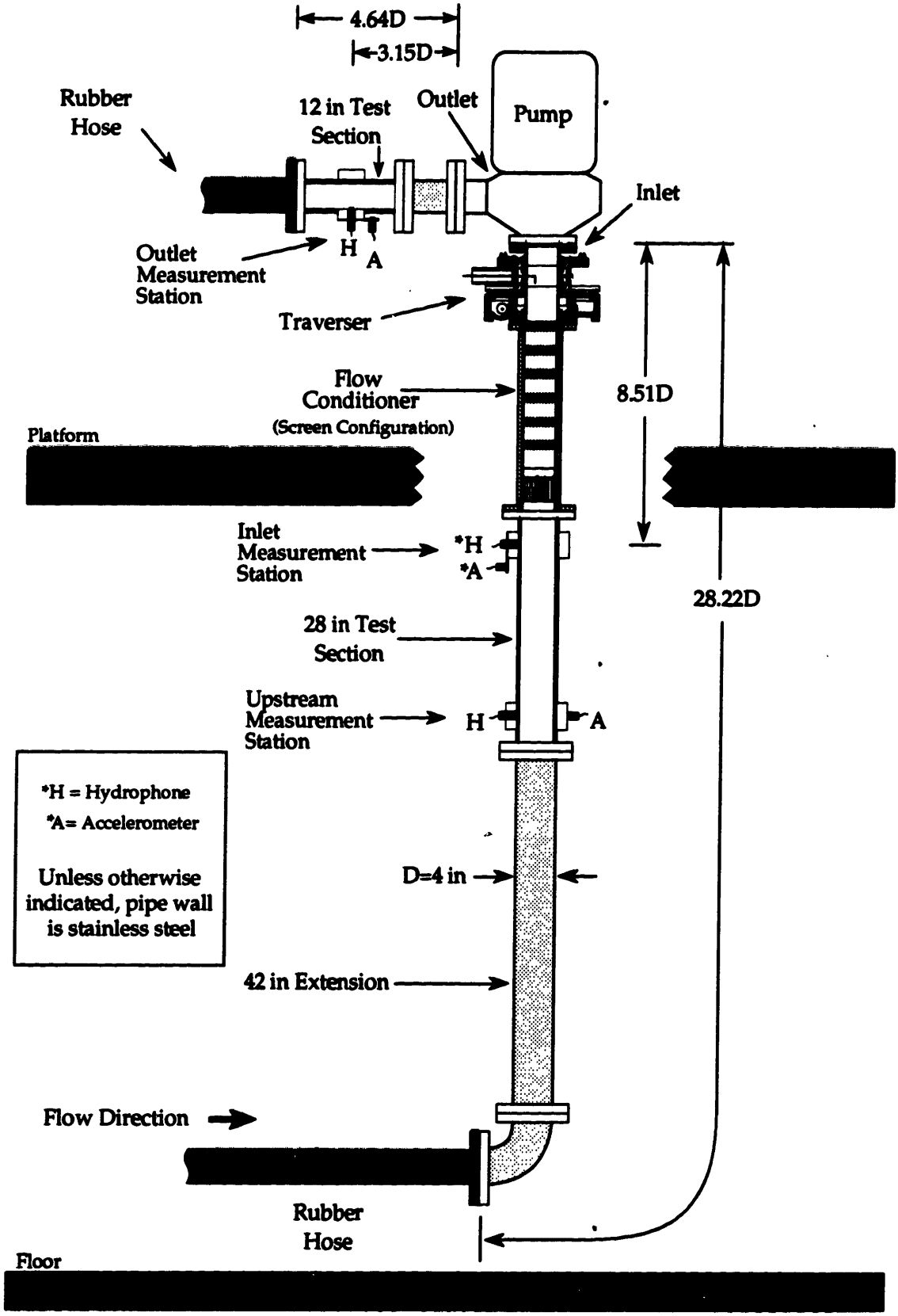

Figure 2.4 Straight Inlet Configuration

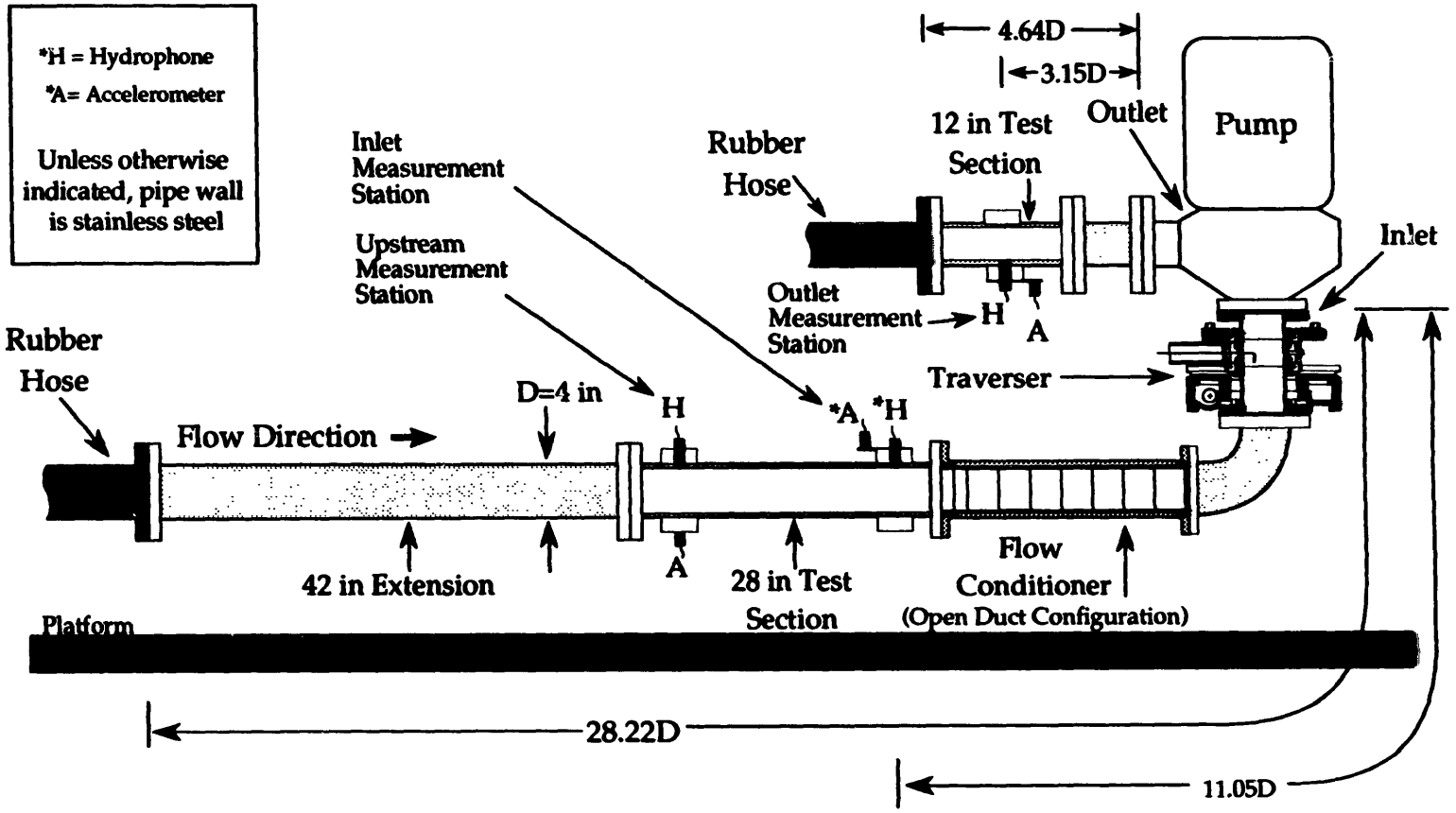

Figure 2.5 Close-Coupled Elbow Configuration

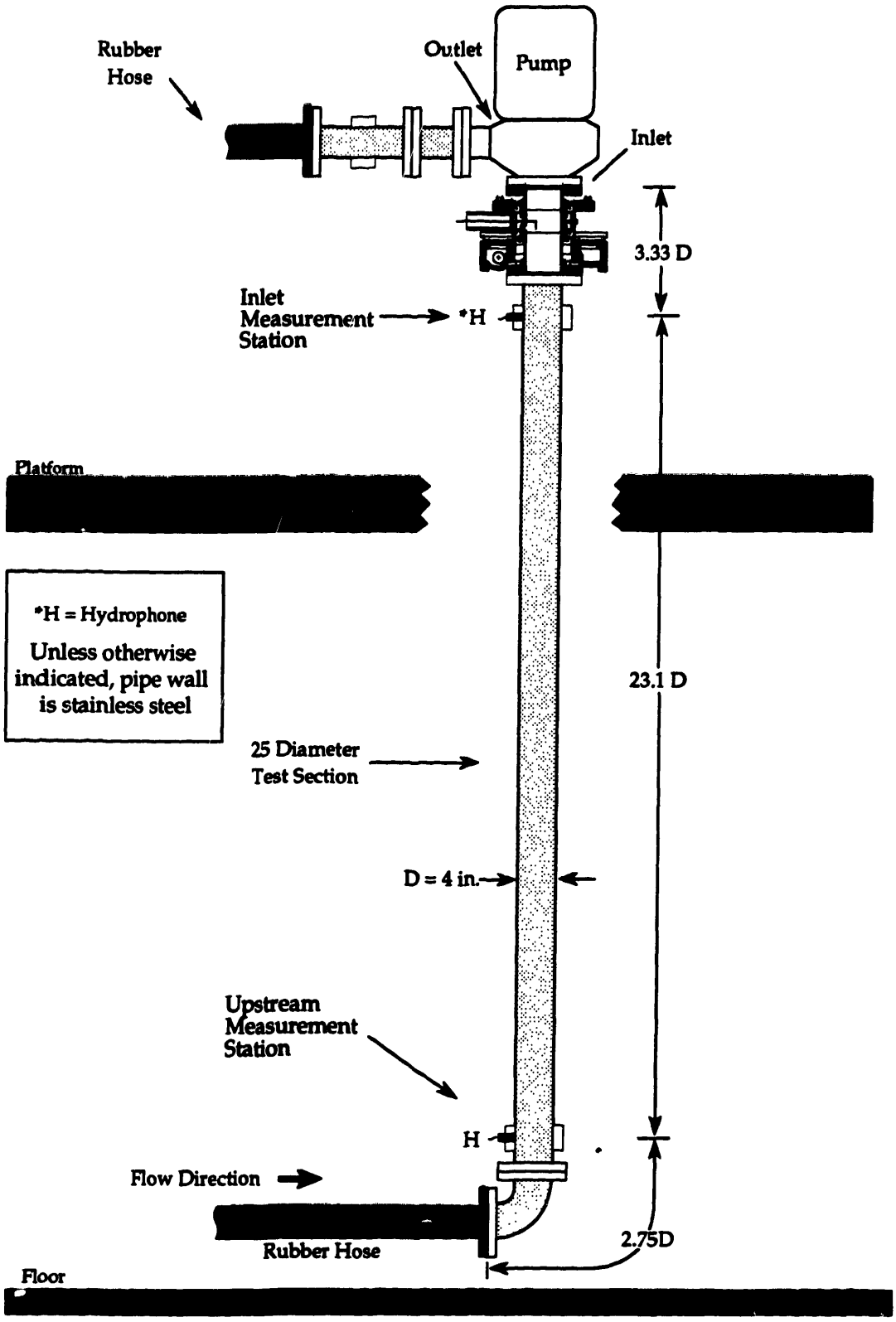

Figure 2.6 Straight Validation Configuration

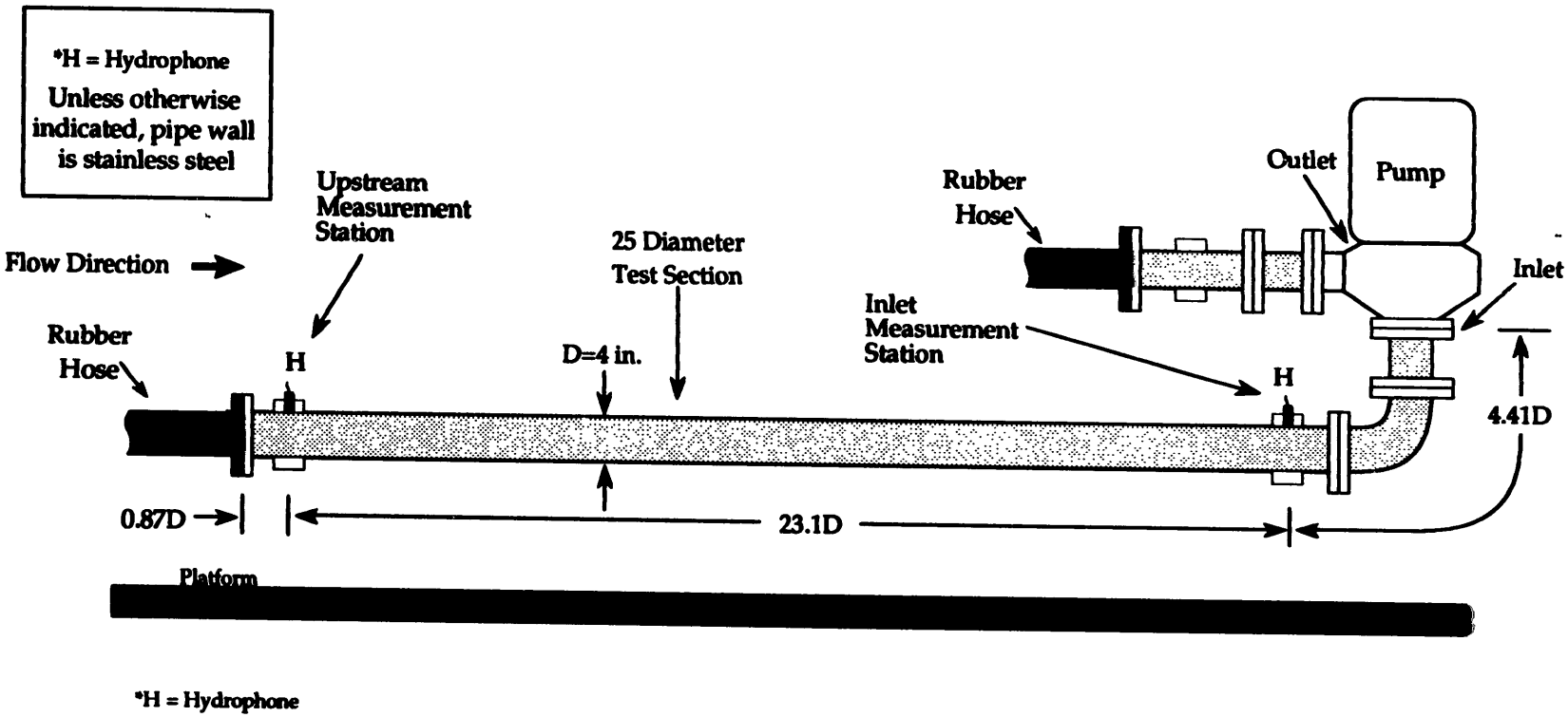

Figure 2.7 Elbow Validation Configuration

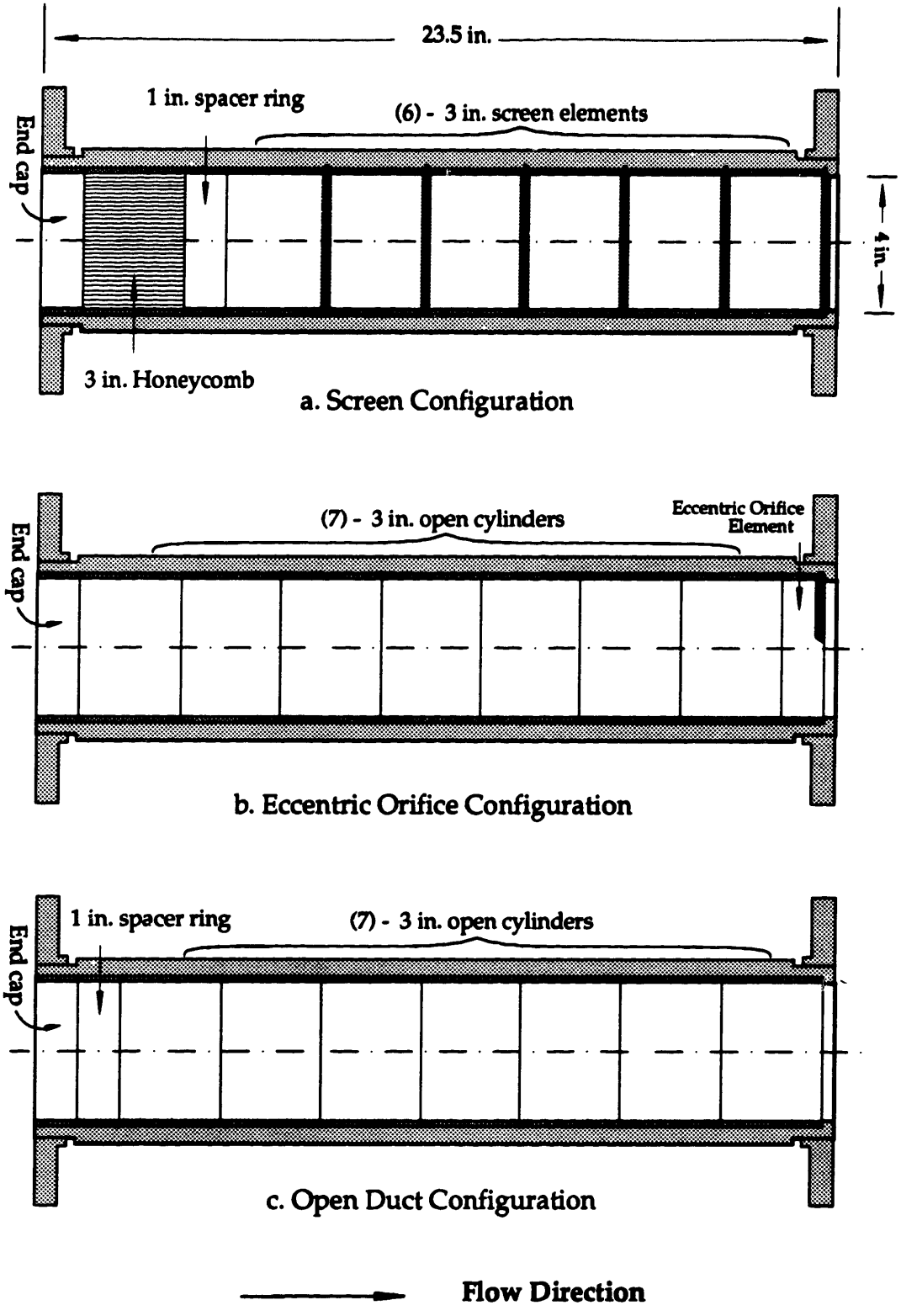

Figure 2.8 Flow Conditioner Configuration

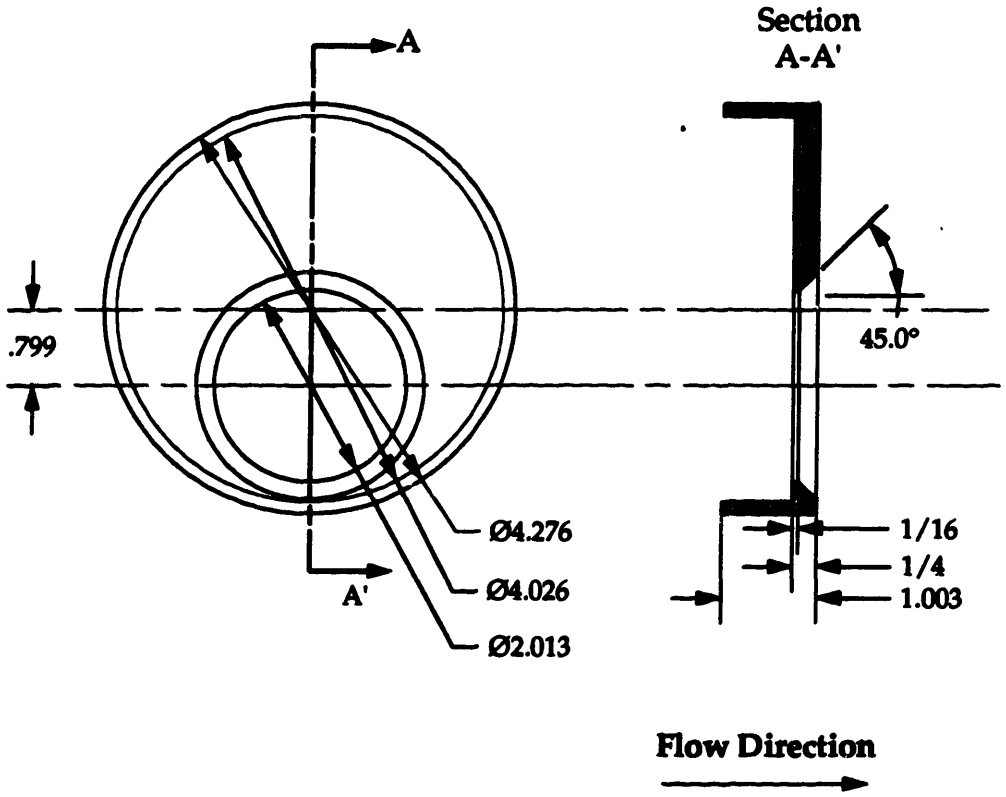

Figure 2.9 ASME Standard Eccentric Orifice, used for Distortion Generation. All Dimensions are in Inches.

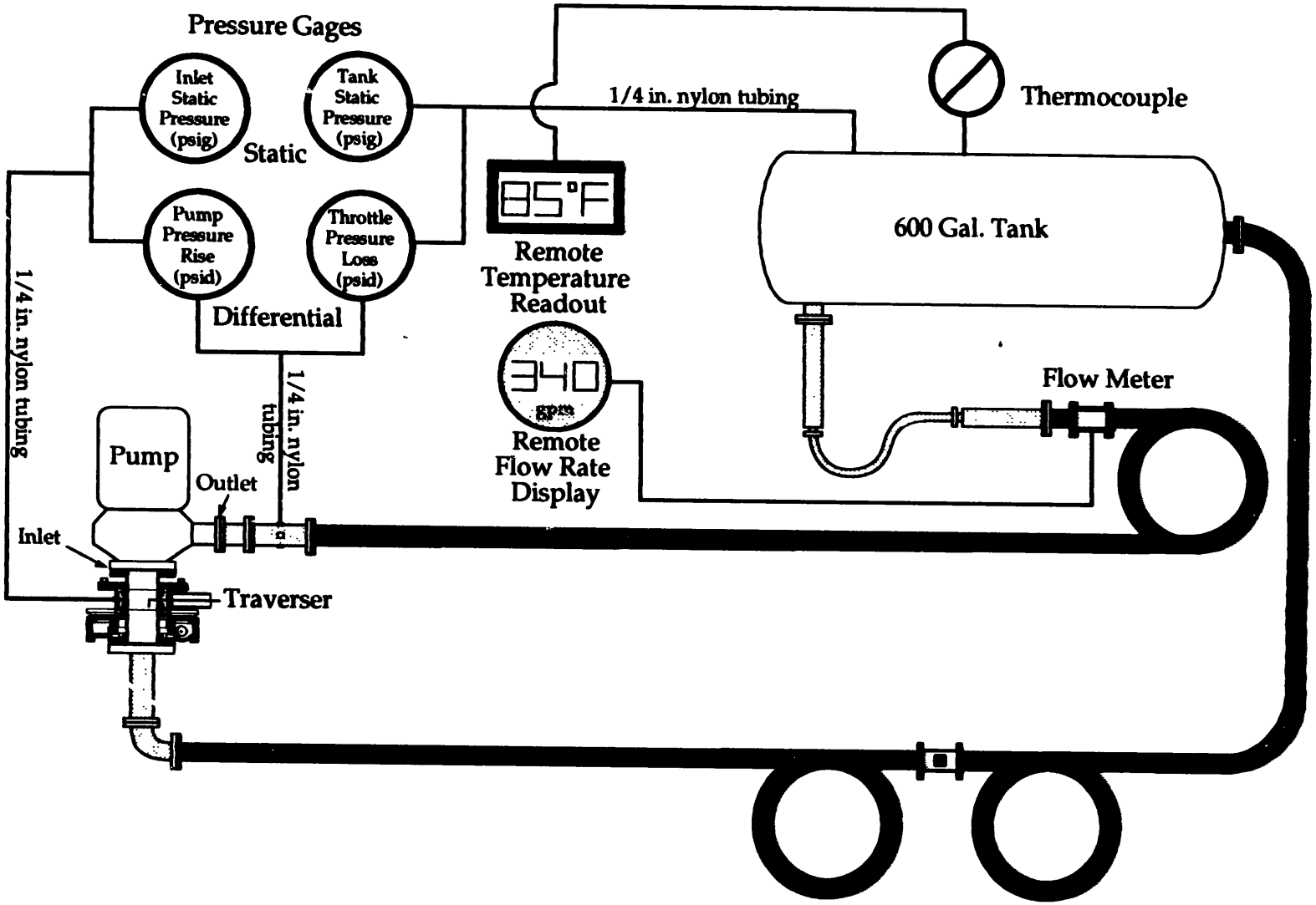

Figure 2.10 Pump Performance Measurement Schematic

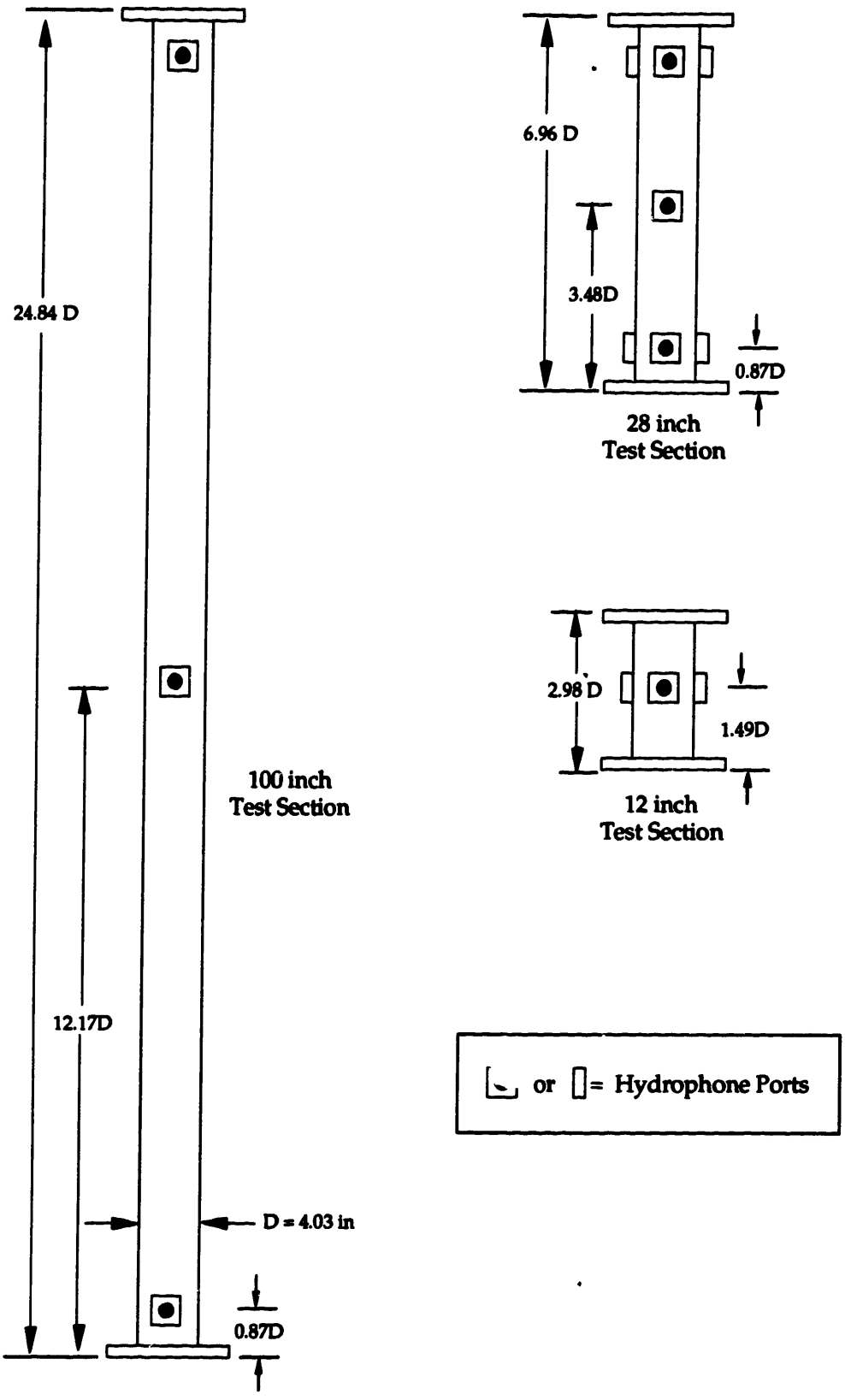

Figure 2.11 Acoustic and Vibration Measurement Sections

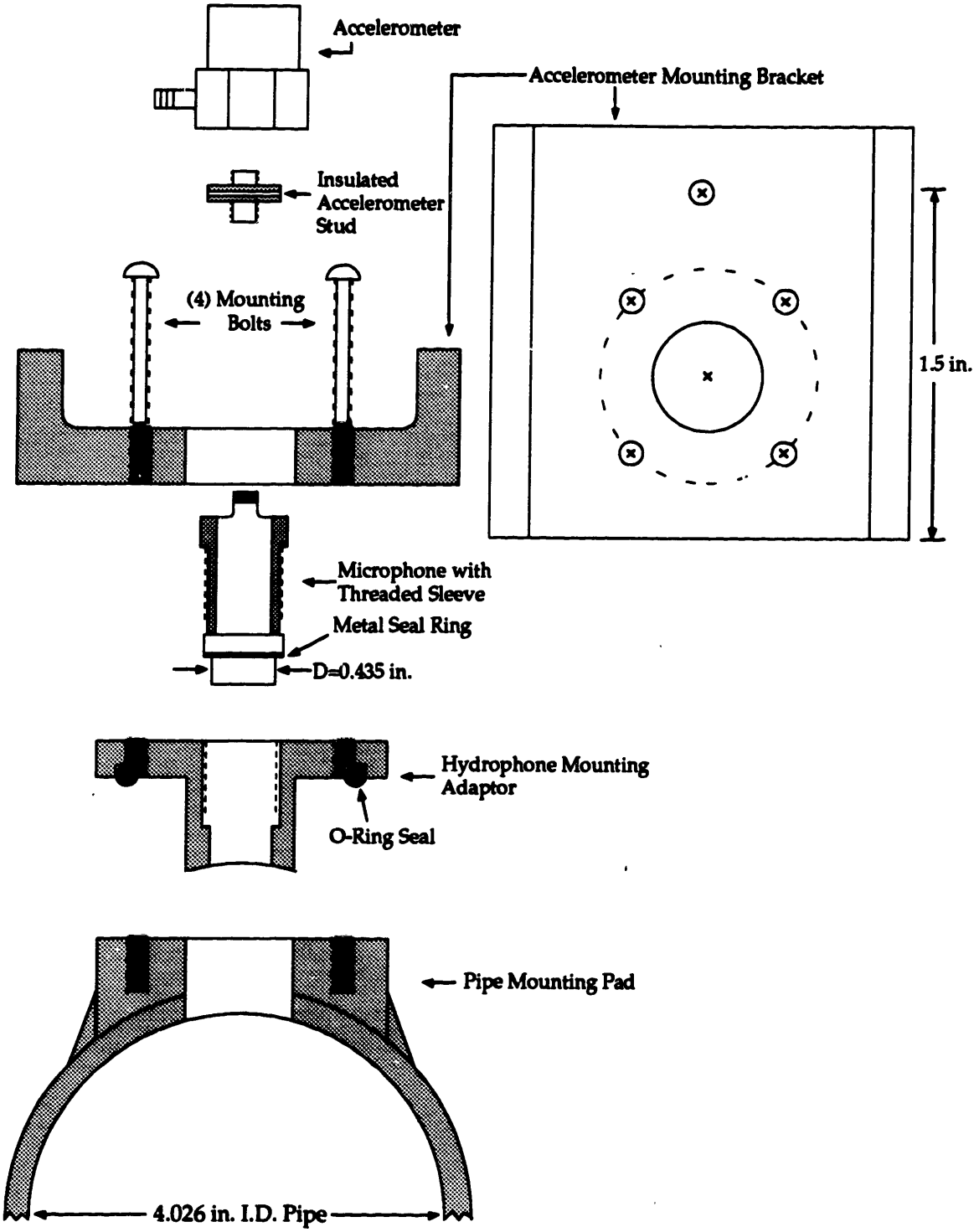

Figure 2.12 Hydrophone - Accelerometer Assembly

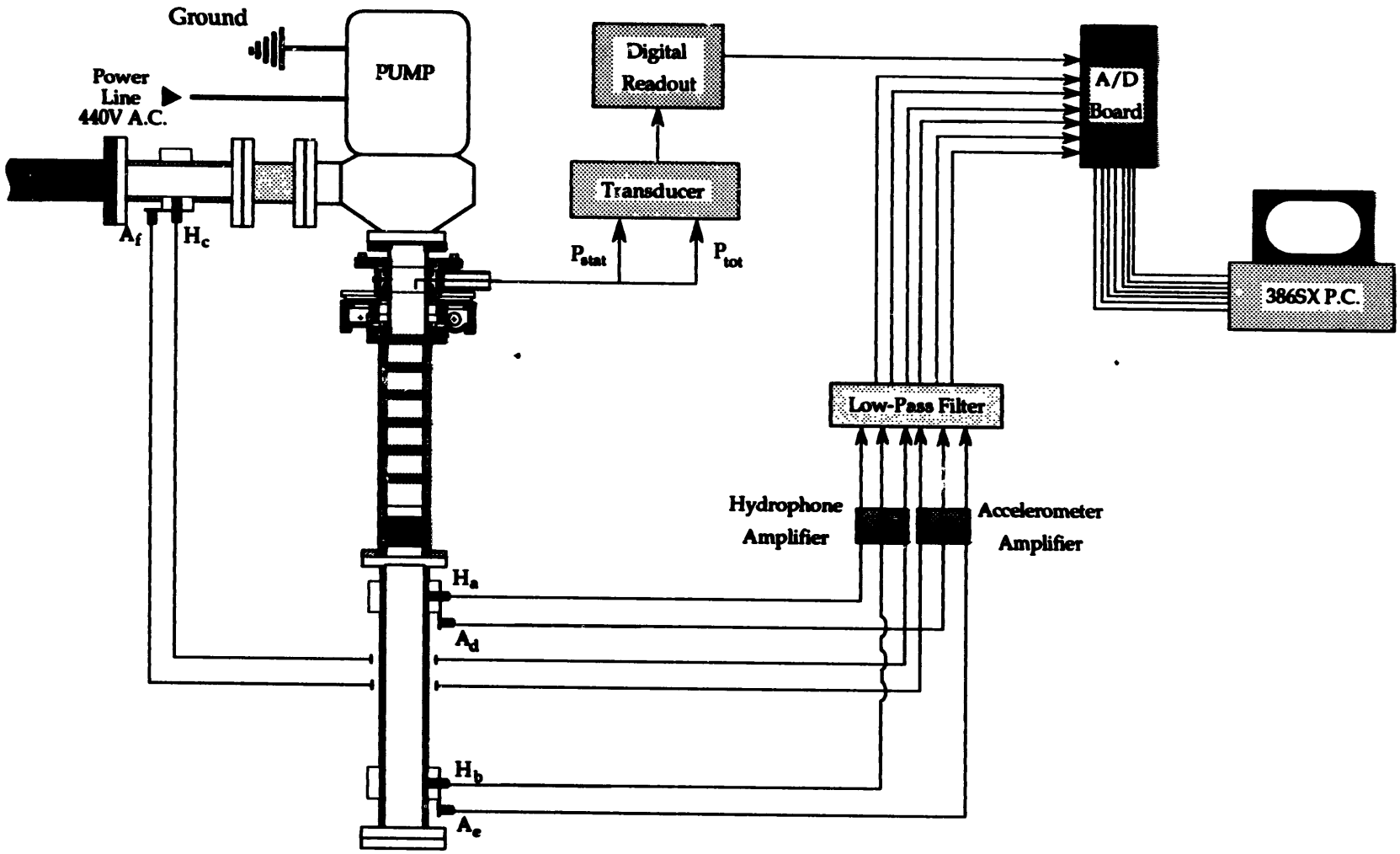

Figure 2.13 Fluid Velocity, Acoustic, and Vibration Measurement Electronics Schematic

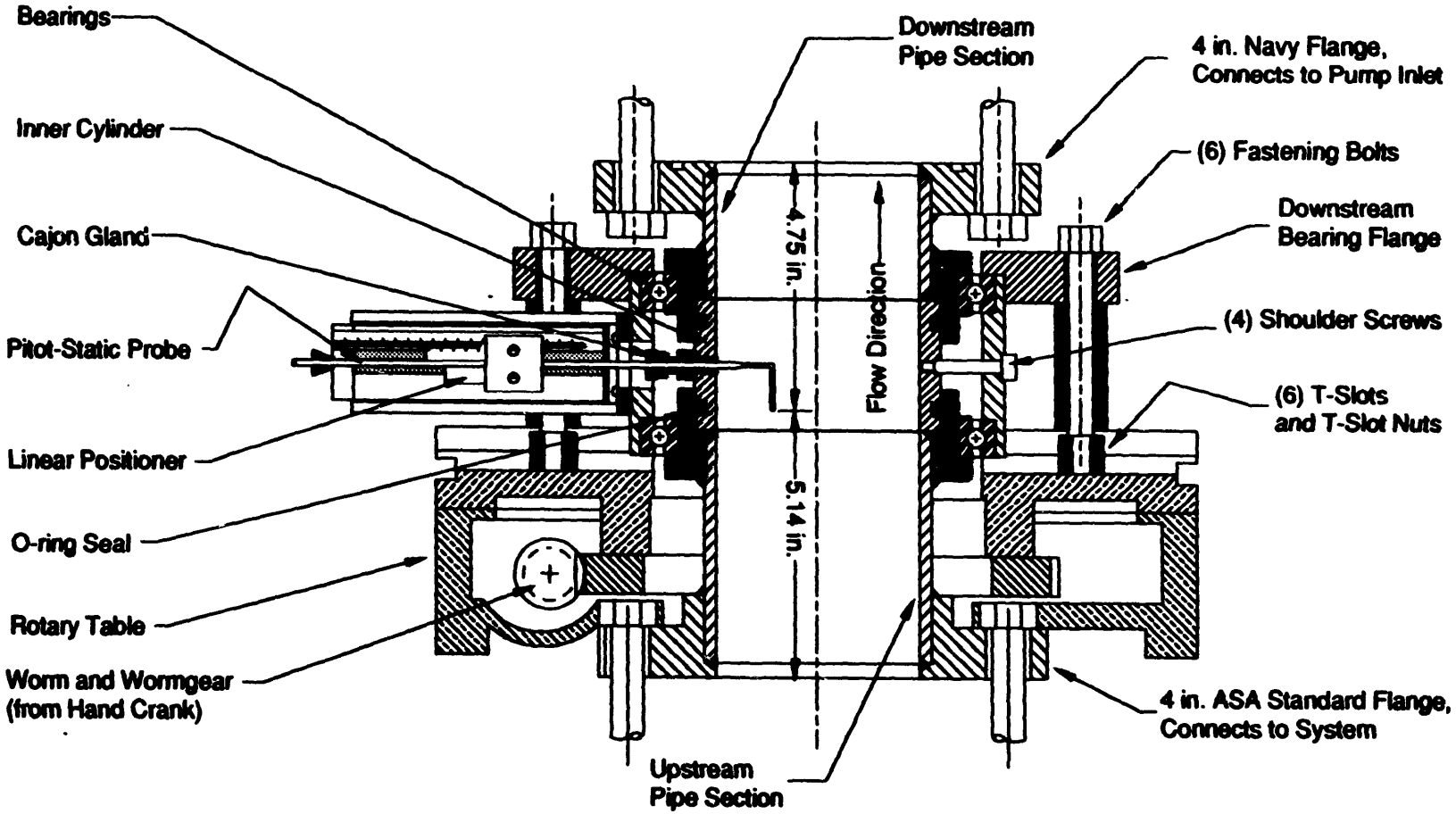

Figure 2.14 Pitot-Static Probe Traverser Assembly

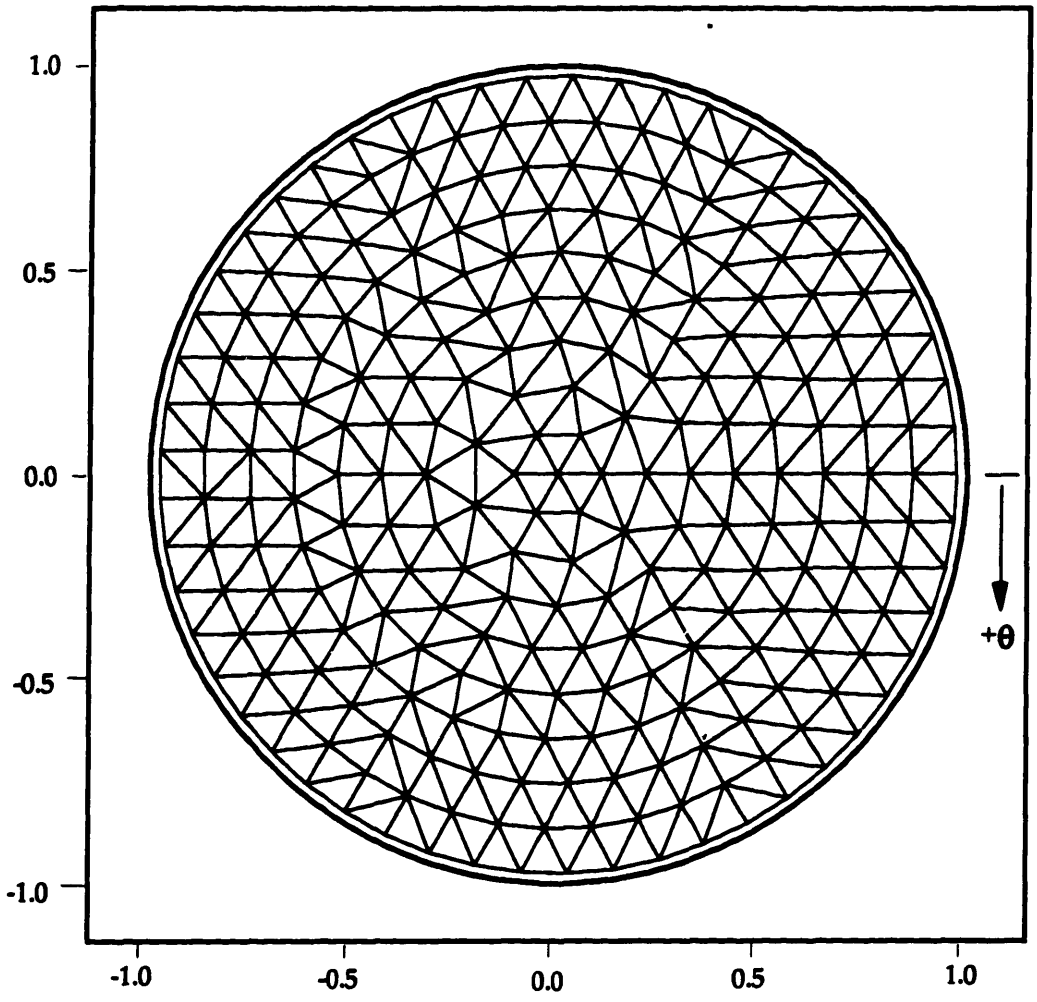

Figure 2.15 Axial Velocity Profile Measurement Grid

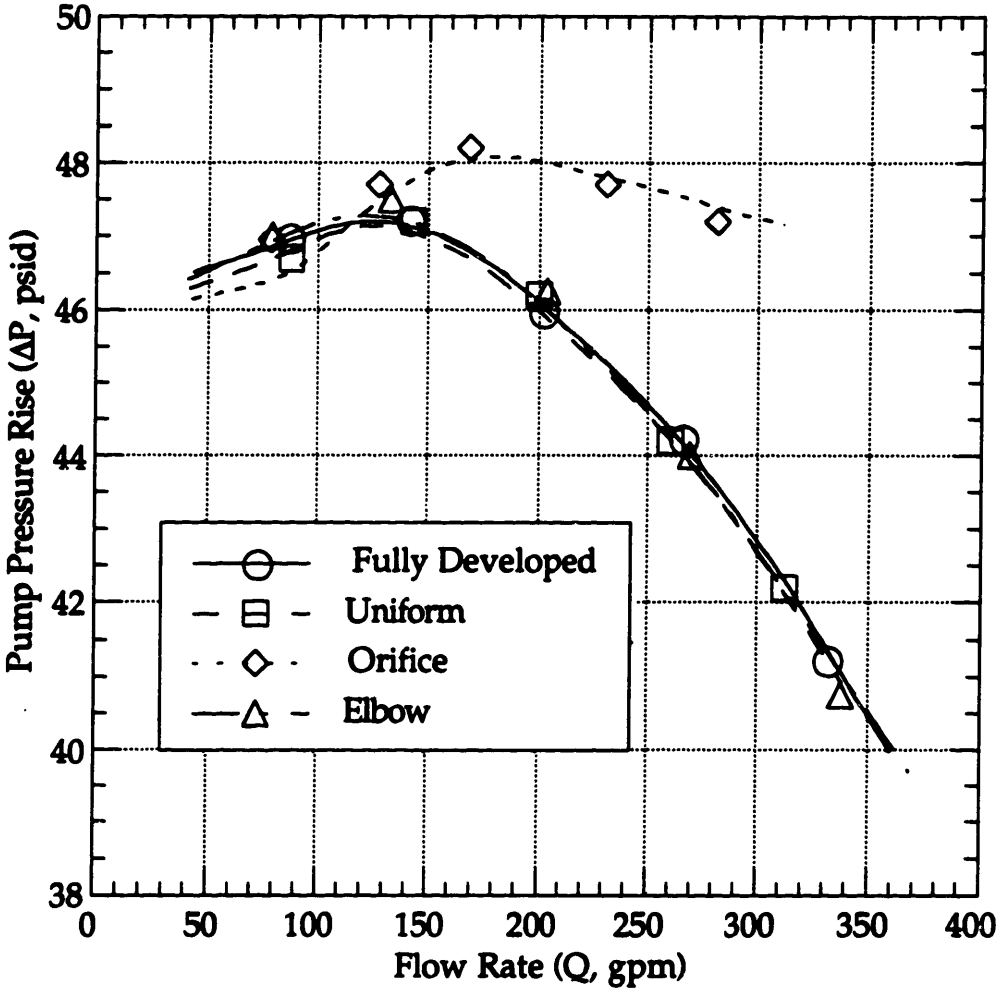

Figure 2.17 Comparison of Measured Pump Pressure Rise vs. Flow Rate for Each Inlet Profile Case

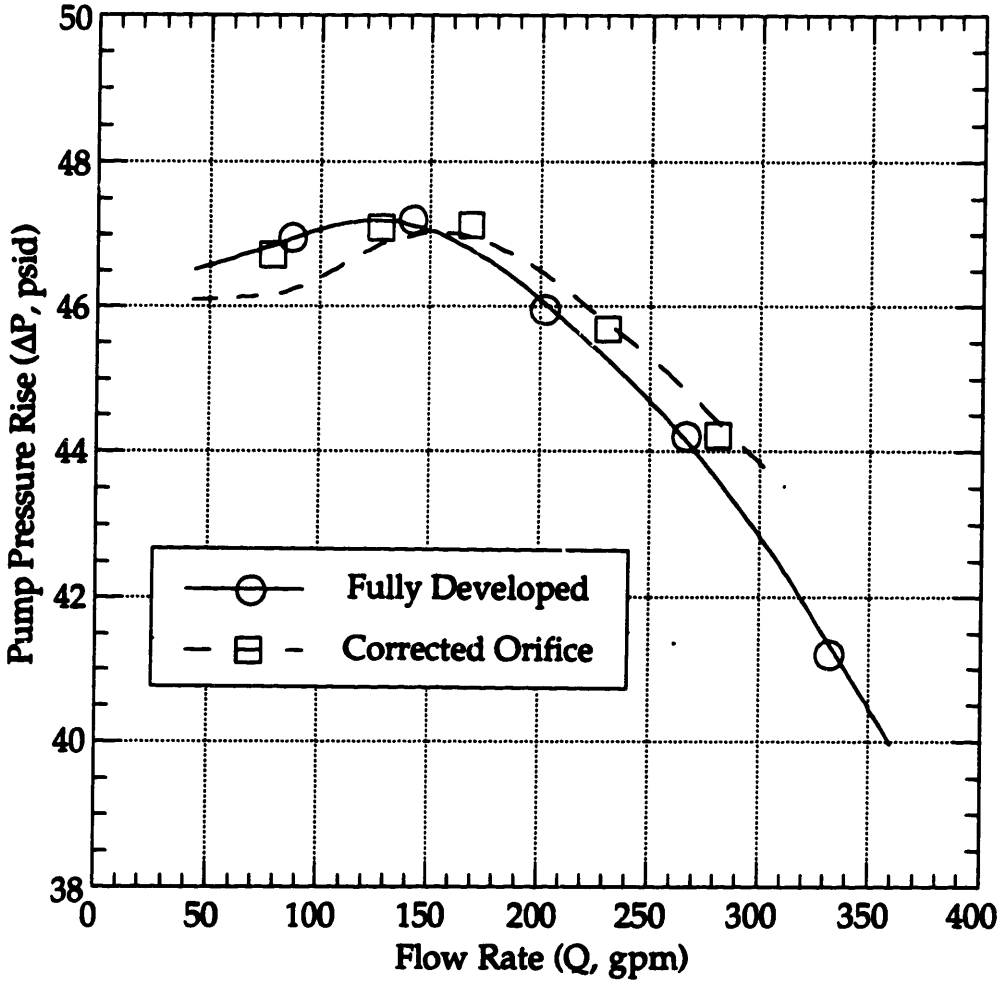

Figure 2.18 Comparison of Corrected Orifice Pump Pressure Rise vs. Flow Rate to the Fully Developed Case

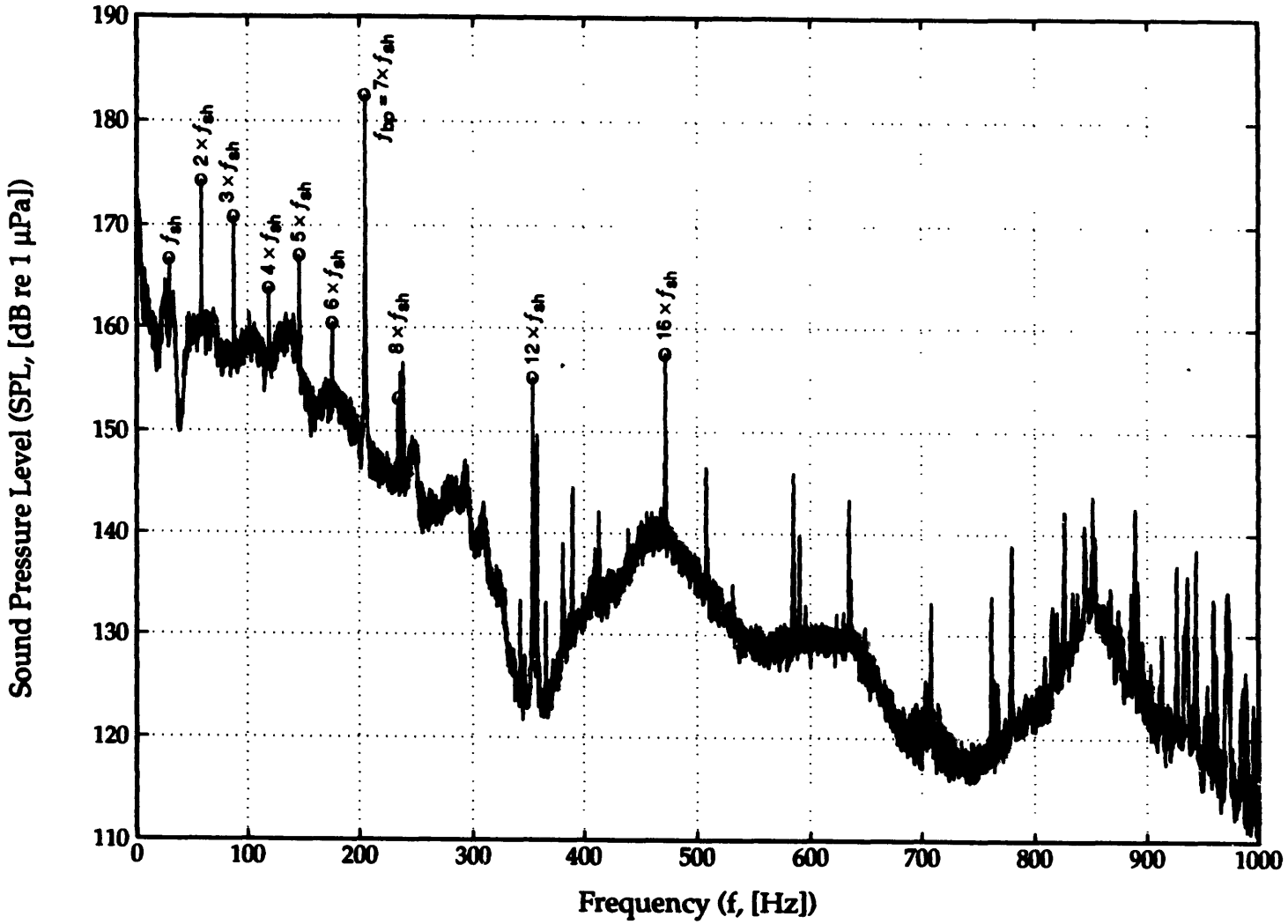

Figure 2.19 Typical Pump Inlet Sound Pressure Level Spectrum.
f_{sh} = Shaft Frequency, f_{bp} = Blade Passage Frequency.

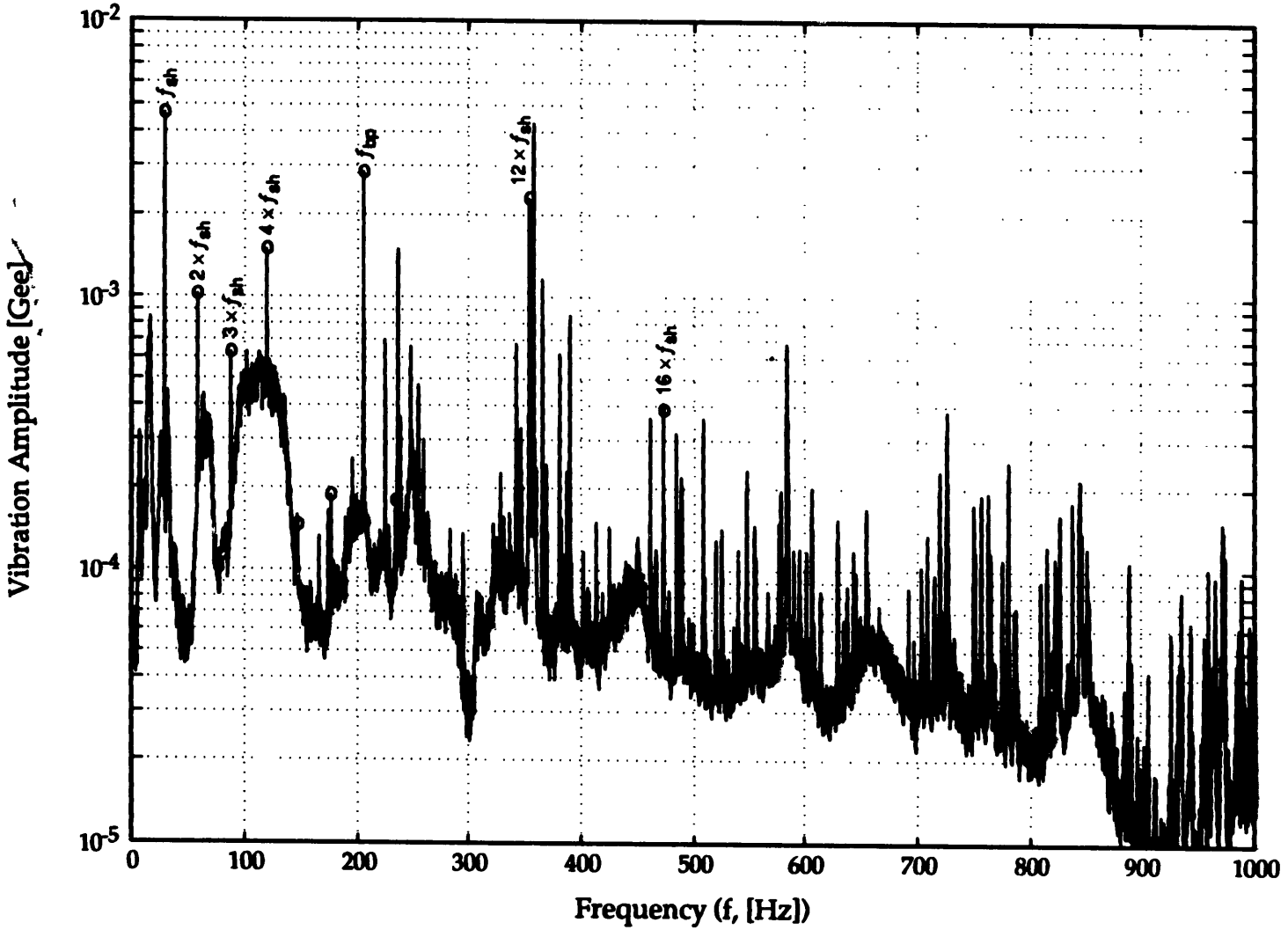

Figure 2.20 Typical Pump Inlet Vibration Spectrum.
f_{sh} = Shaft Frequency, f_{bp} = Blade Passage Frequency.

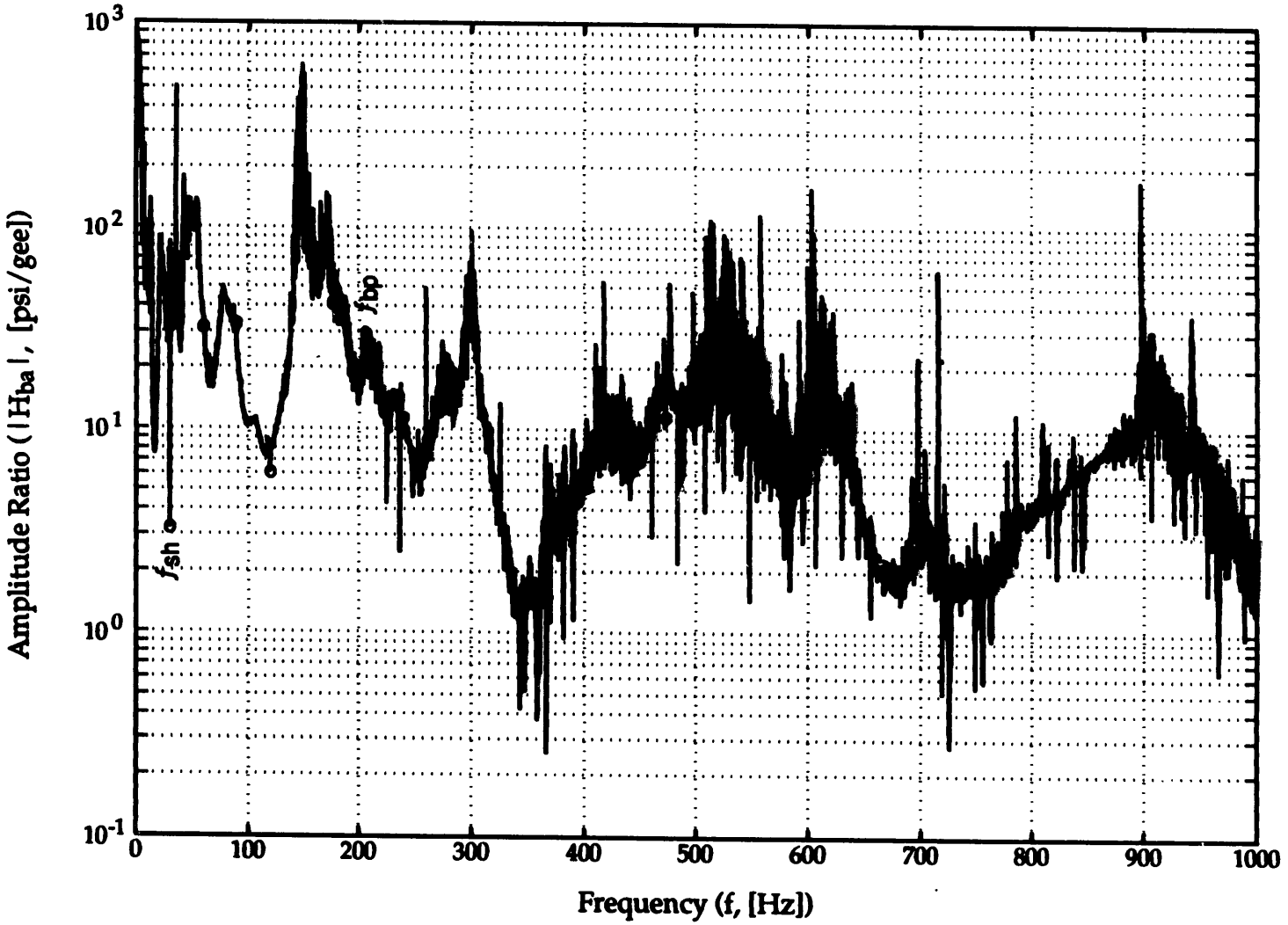

Figure 2.21 Typical Hydrophone - Accelerometer Amplitude Ratio. f_{sh} = Shaft Frequency, f_{bp} = Blade Passage Frequency.

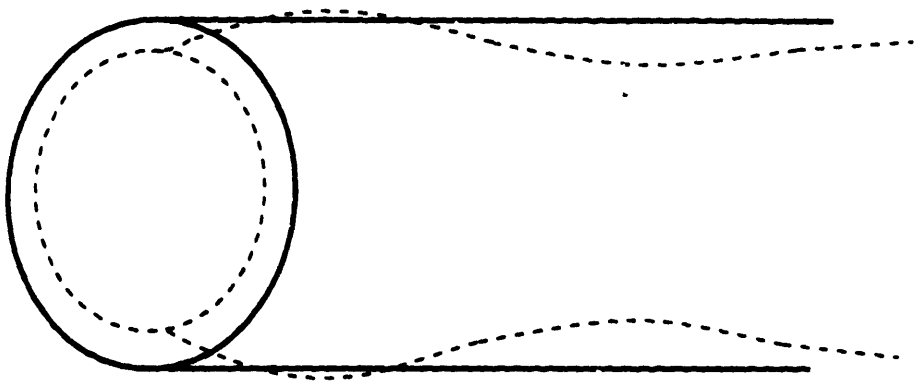

n=0 Symmetric

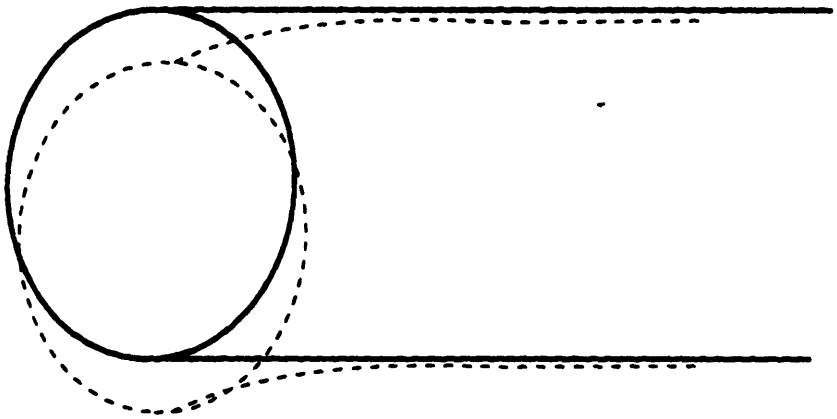

n=1 Asymmetric

Figure 2.22 Primary Circumferential Modes of a Fluid-Filled Shell

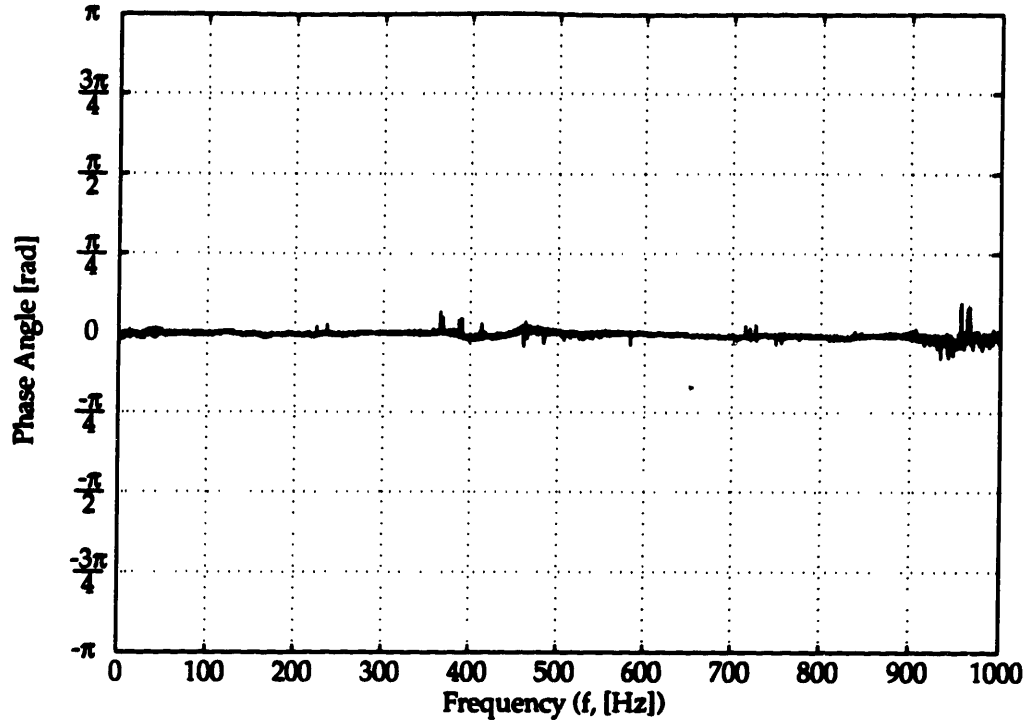

a. Acoustic Phase Across Pipe Cross Section.

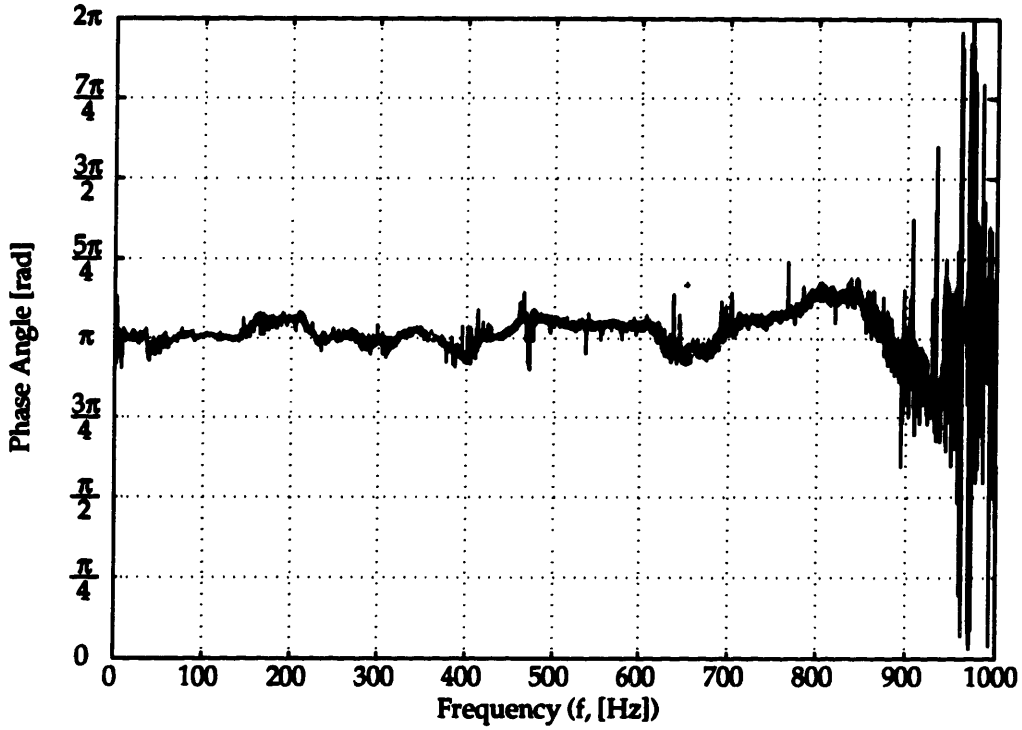

b. Vibration Phase Across Pipe Cross Section.

Figure 2.23 Comparison of Acoustic and Vibration Phase Angles Across Pipe Cross Section.

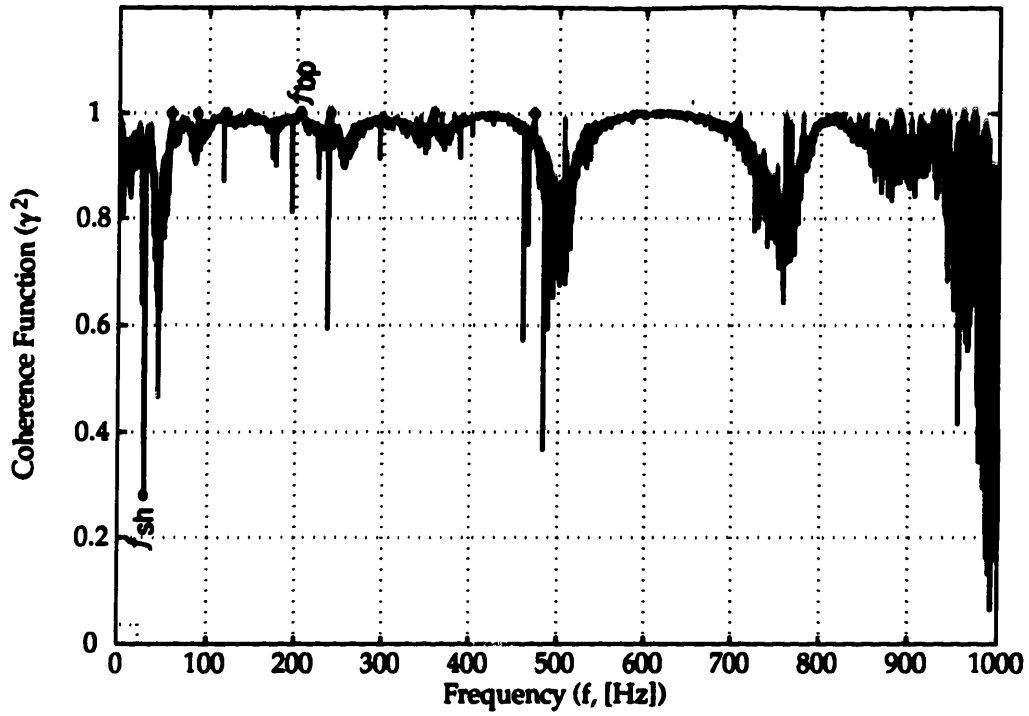

a. Pressure Field Coherence Spectrum for Straight Validation Configuration of Figure 2.6.

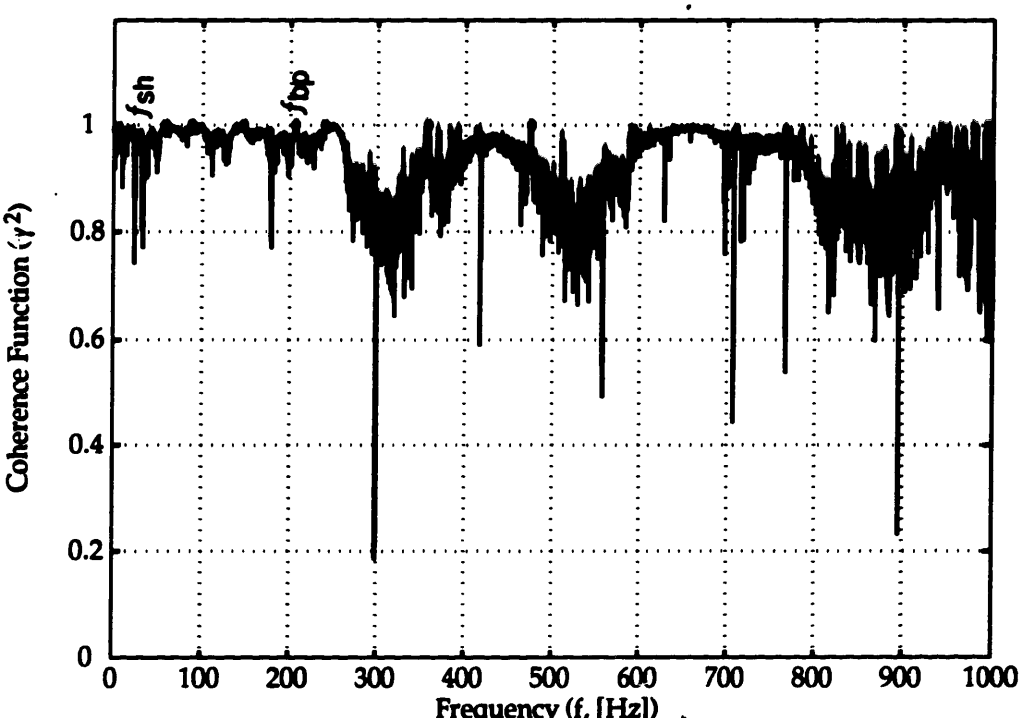

b. Pressure Field Coherence Spectrum for Elbow Validation Configuration of Figure 2.7.

Figure 2.24 Coherence of Pressure Field over 23 diameters Upstream of Pump.
f_{sh} = Shaft Frequency, f_{bp} = Blade Passage Frequency.

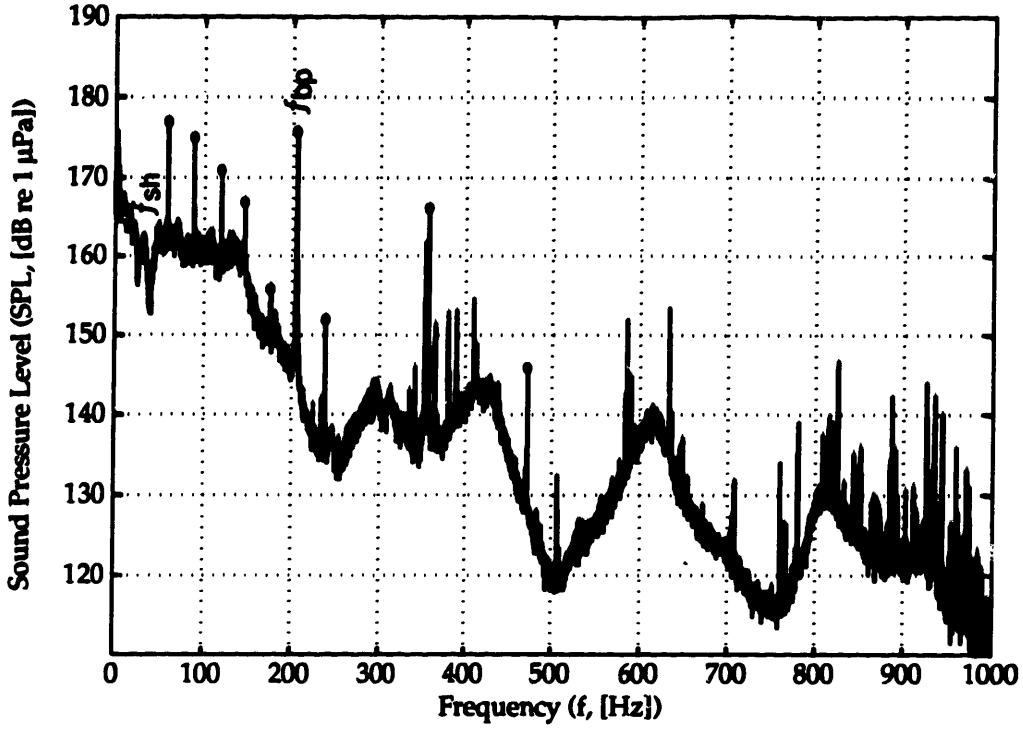

a. Pump Inlet Sound Pressure Level

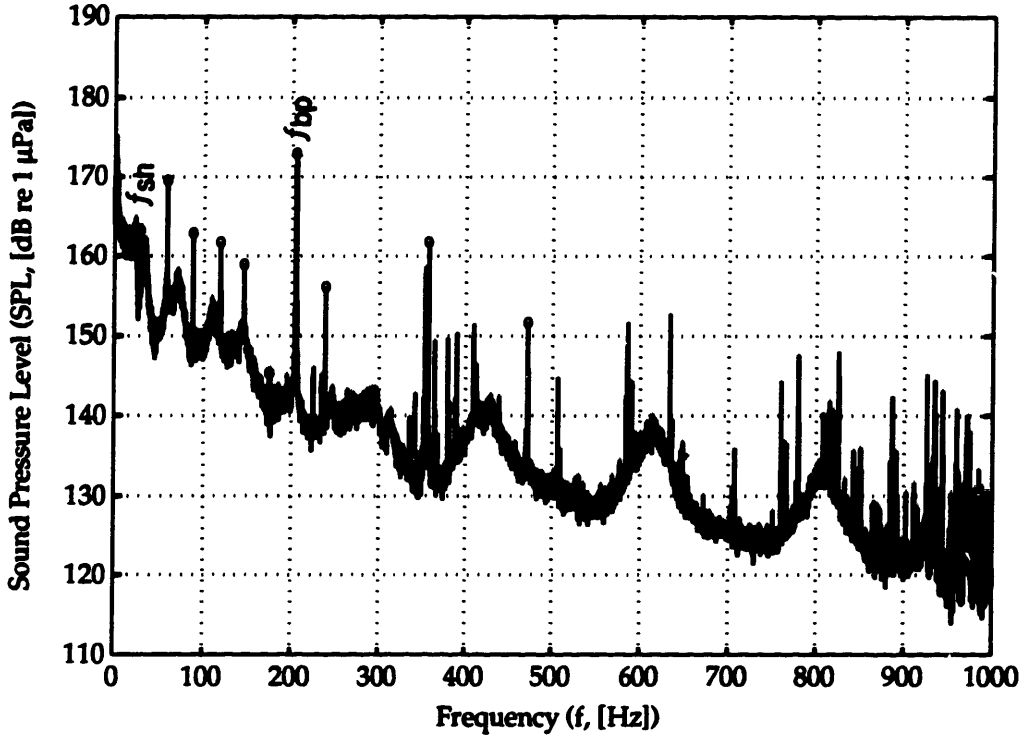

b. Pump Upstream Sound Pressure Level

Figure 2.25 SPL Spectra for Straight Validation Configuration, (Fig 2.6). f_{sh} = Shaft Frequency, f_{bp} = Blade Passage Frequency.

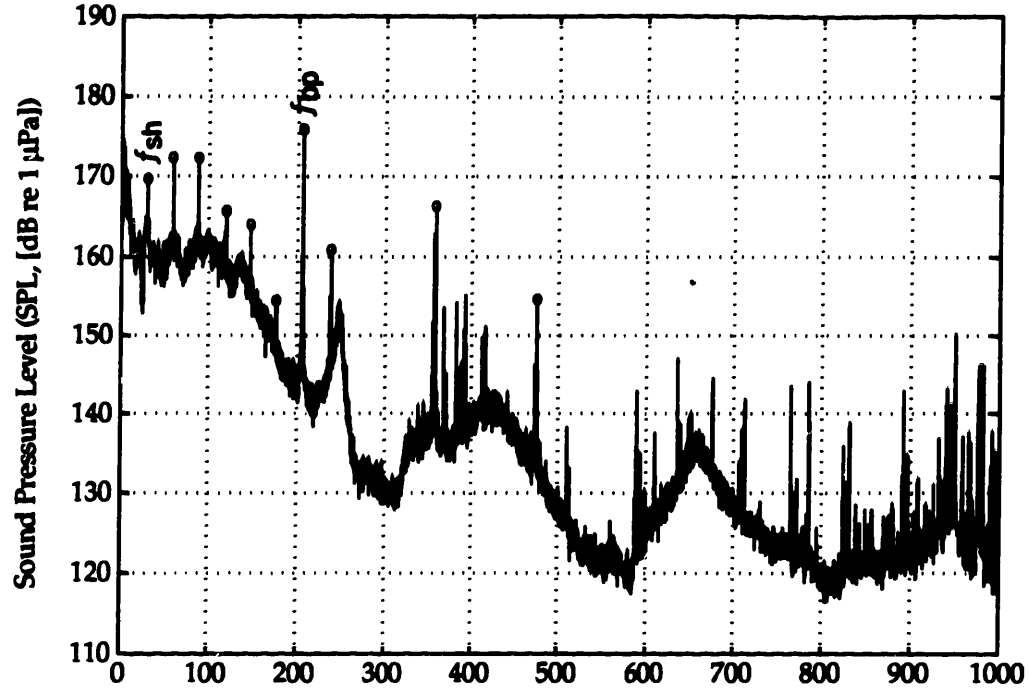

a. Pump Inlet Sound Pressure Level

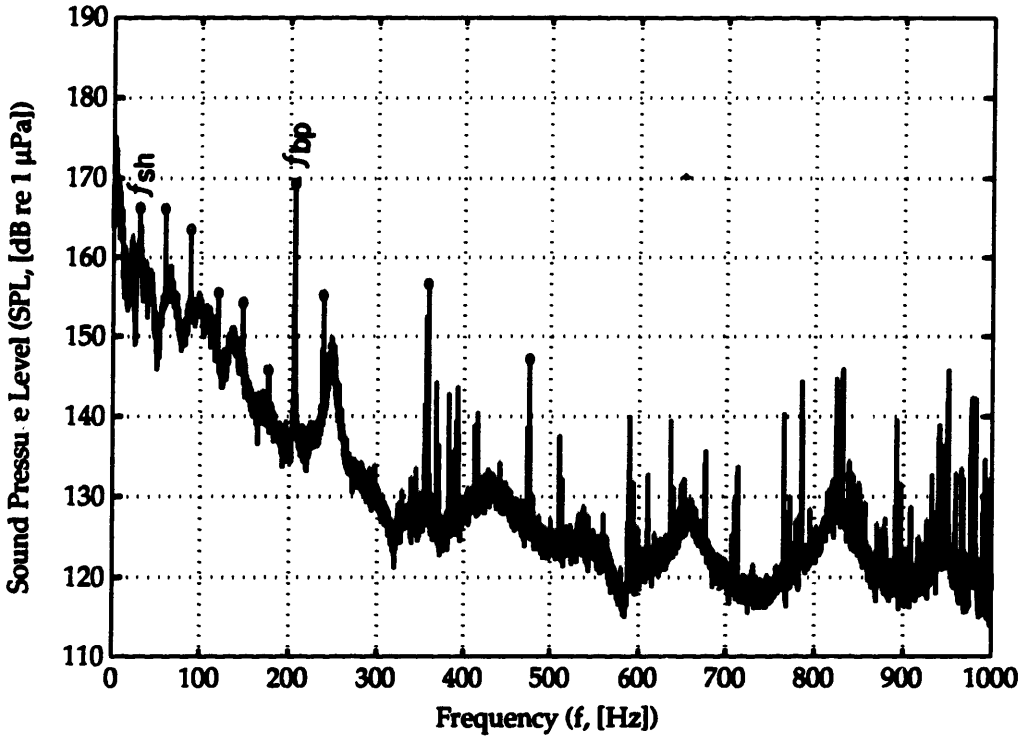

b. Pump Upstream Sound Pressure Level

Figure 2.26 SPL Spectra for Elbow Validation Configuration, (Fig 2.7). f_{sh} = Shaft Frequency, f_{bp} = Blade Passage Frequency.

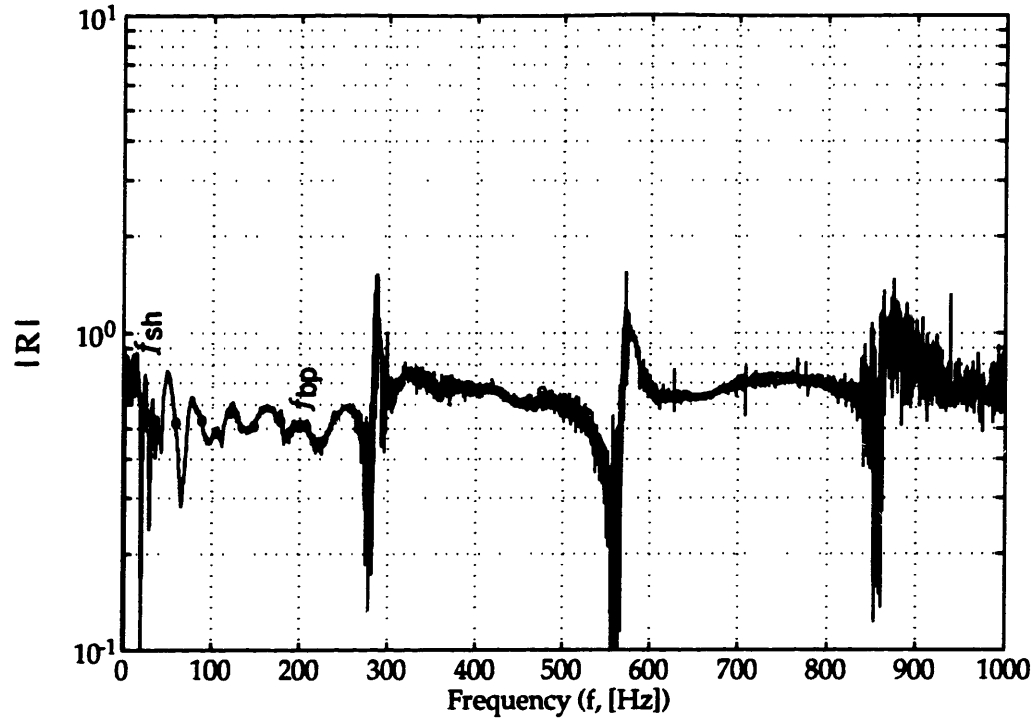

a. Reflection Magnitude for Untreated Steel - Rubber Boundary, Elbow Validation Configuration (Fig. 2.7).

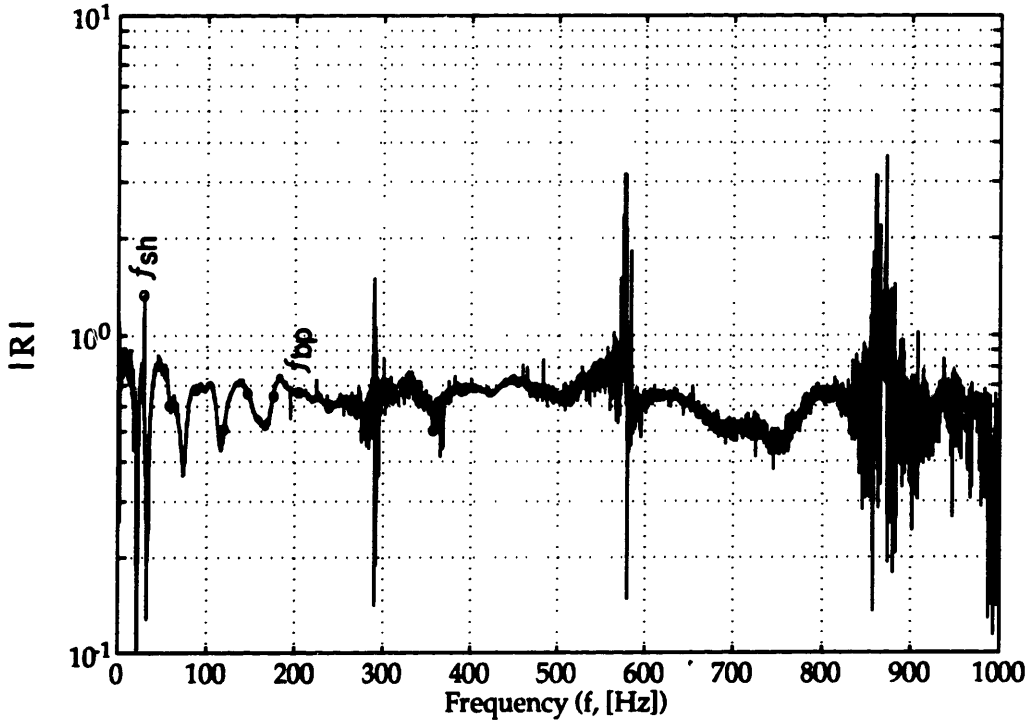

b. Reflection Magnitude for Steel - Rubber Boundary with Acoustic Treatment, Straight Validation (Fig. 2.6).

Figure 2.28 Comparison of Reflection Magnitude at the Steel-Rubber Boundary, With and Without Acoustic Treatment. f_{sh} = Shaft Frequency, f_{bp} = Blade Passage Frequency.

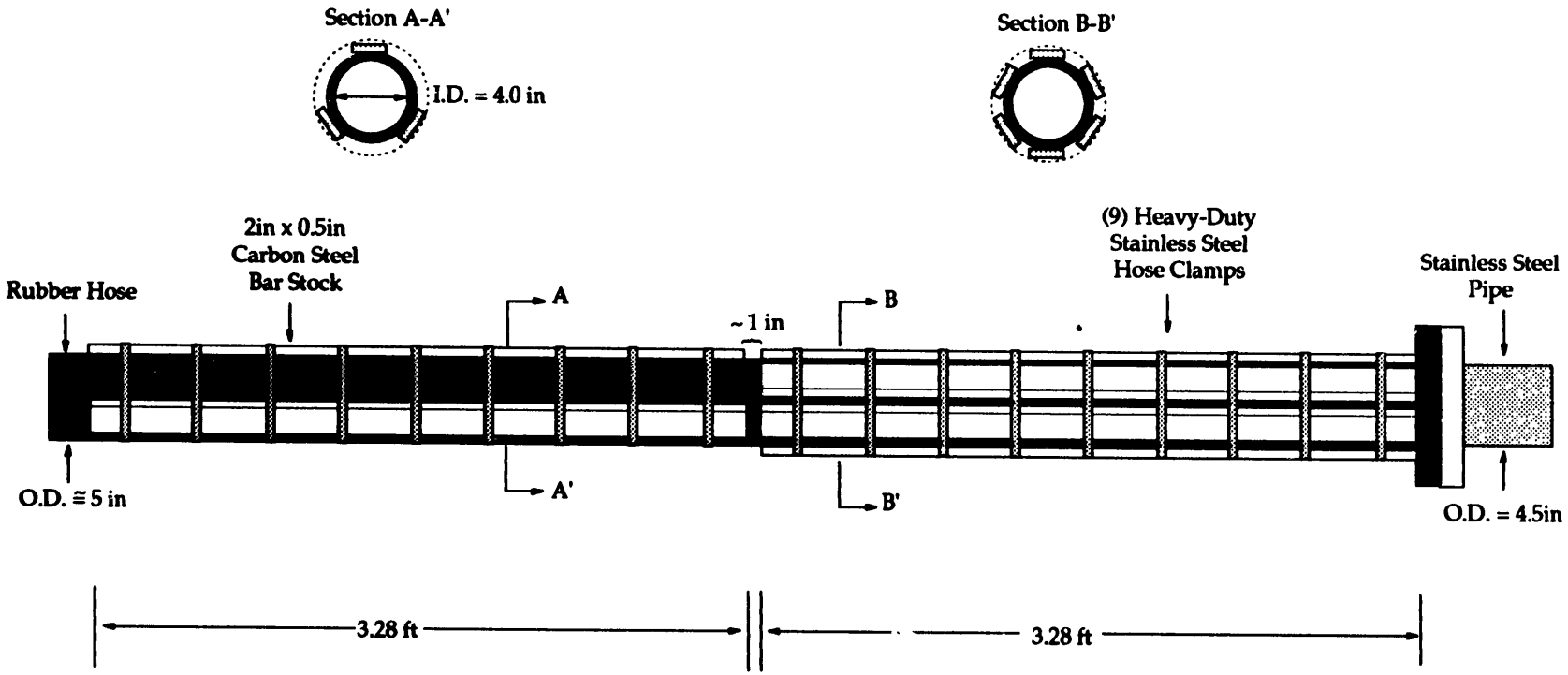

Figure 2.29 Steel-Rubber Boundary Impedance Treatment

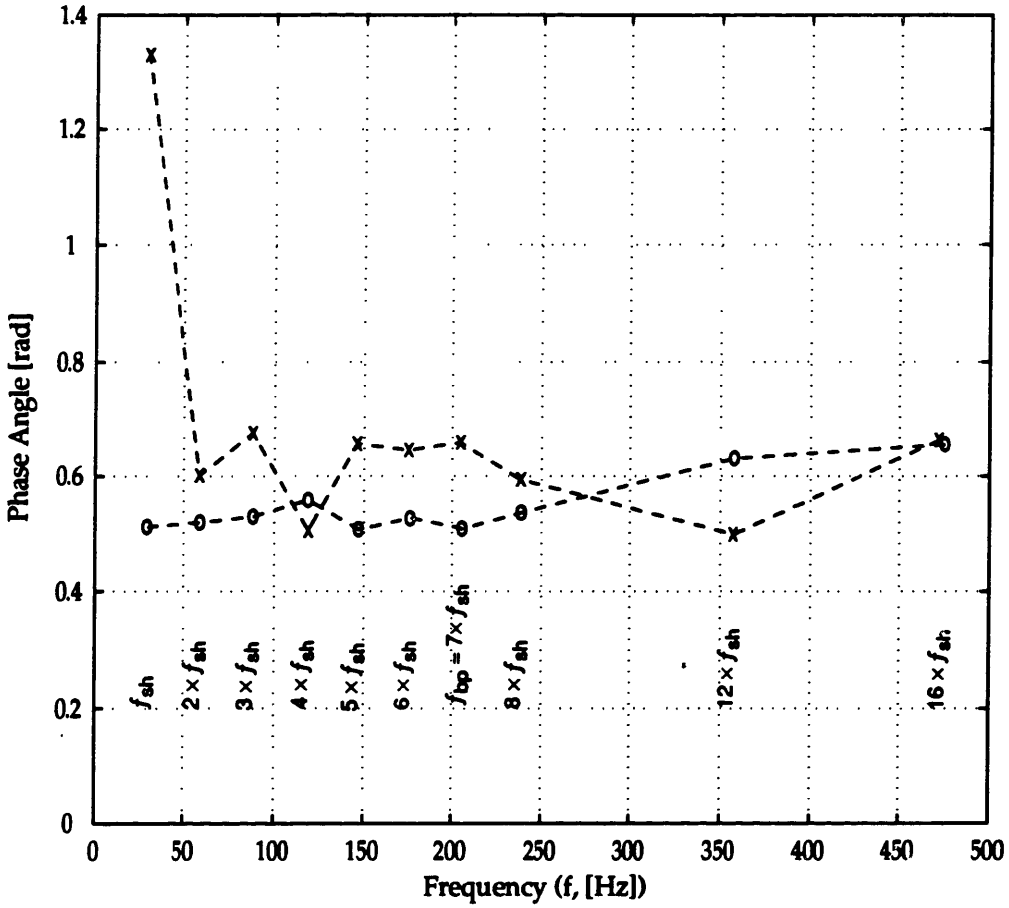

Figure 2.30 Comparison of Reflection Magnitudes at Harmonic Peaks, With and Without Acoustic Treatment.
—o—: Untreated Steel - Rubber Boundary.
- * -: Steel - Rubber Boundary Treated as Shown in Figure 3.26. f_{sh} = Shaft Frequency, f_{bp} = Blade Passage Frequency.

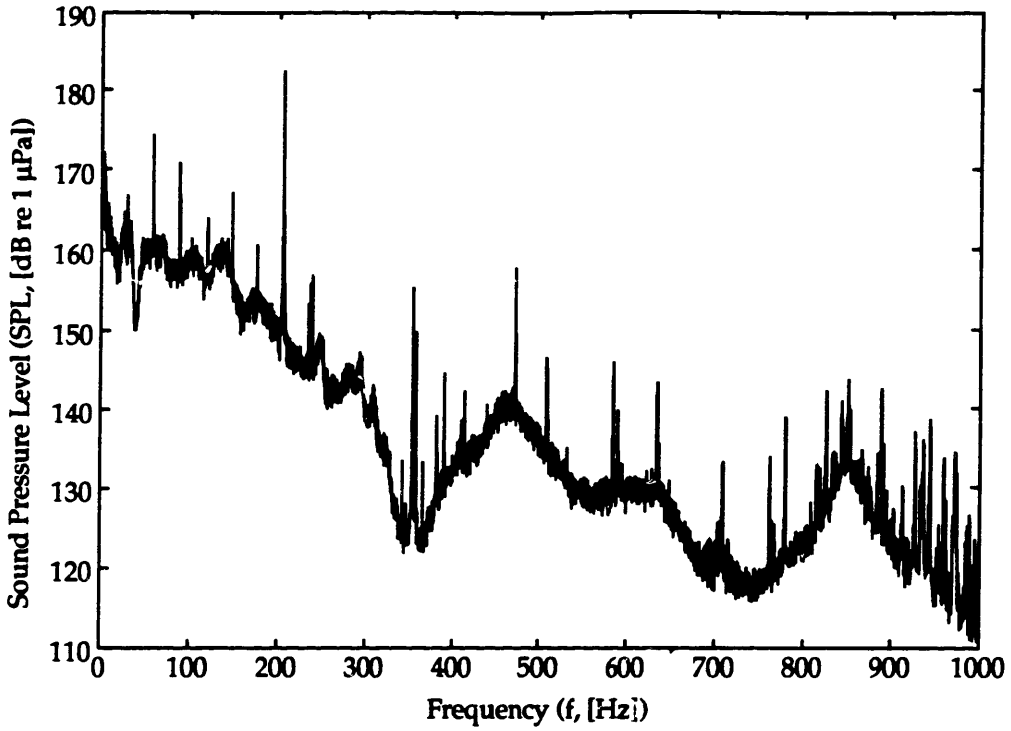

a. Measured Inlet Sound Pressure Level Spectrum.

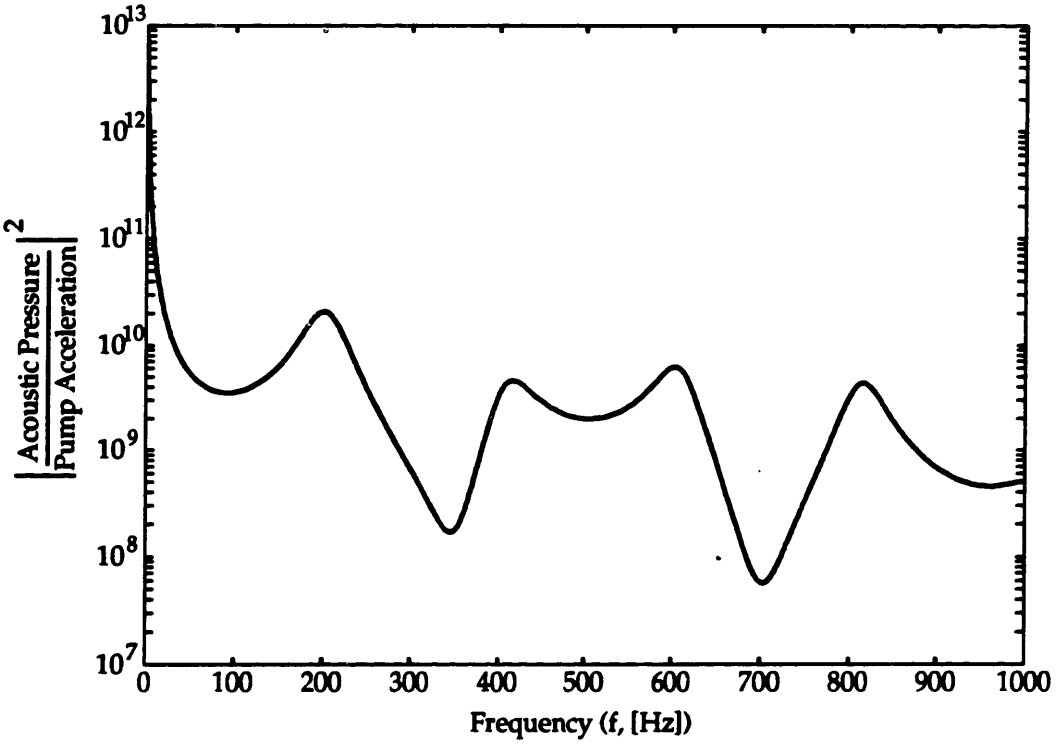

b. Calculated Inlet Standing Wave Spectrum due to Louie.

Figure 2.31 Comparison of Measured Inlet Noise Floor Contour to Standing Wave Spectrum Calculated Using the Method Described by Louie.[12] Straight Inlet Configuration.

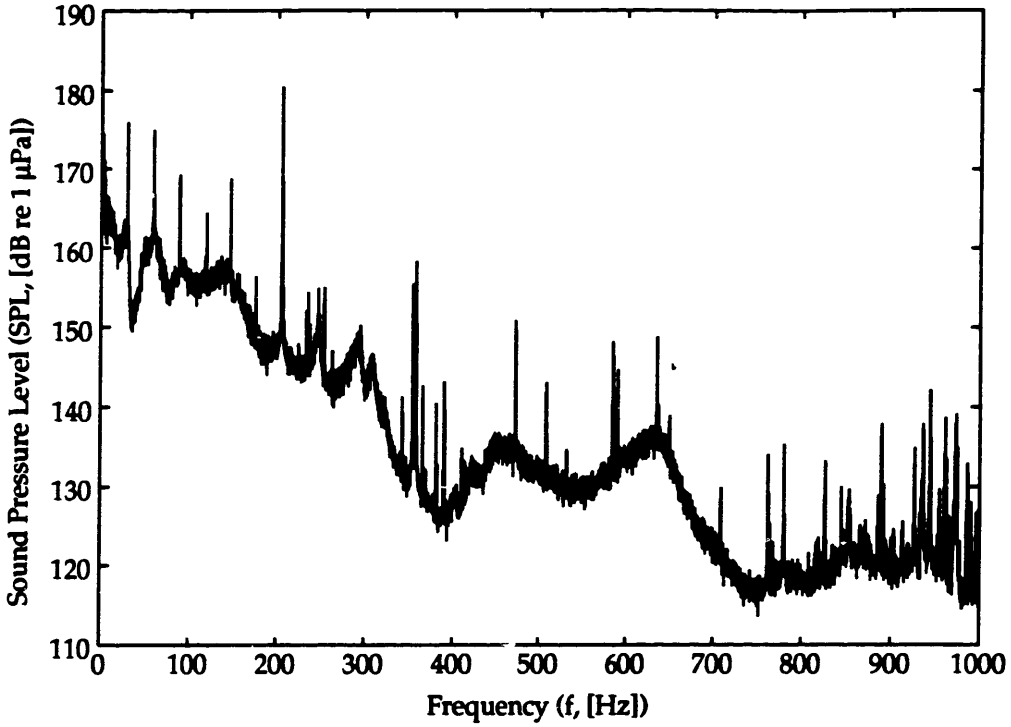

a. Measured Inlet Sound Pressure Level Spectrum.

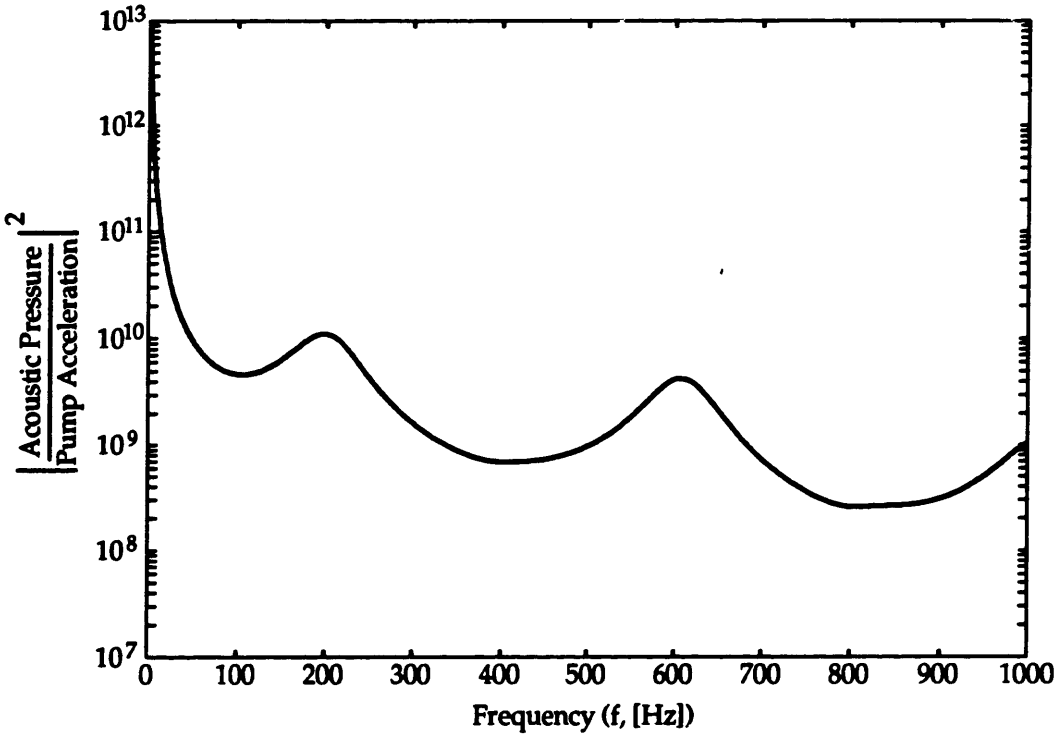

b. Calculated Inlet Standing Wave Spectrum due to Louie.

Figure 2.32 Comparison of Measured Inlet Noise Floor Contour to Standing Wave Spectrum Calculated Using the Method Described by Louie[12] Close-Coupled Elbow Configuration.

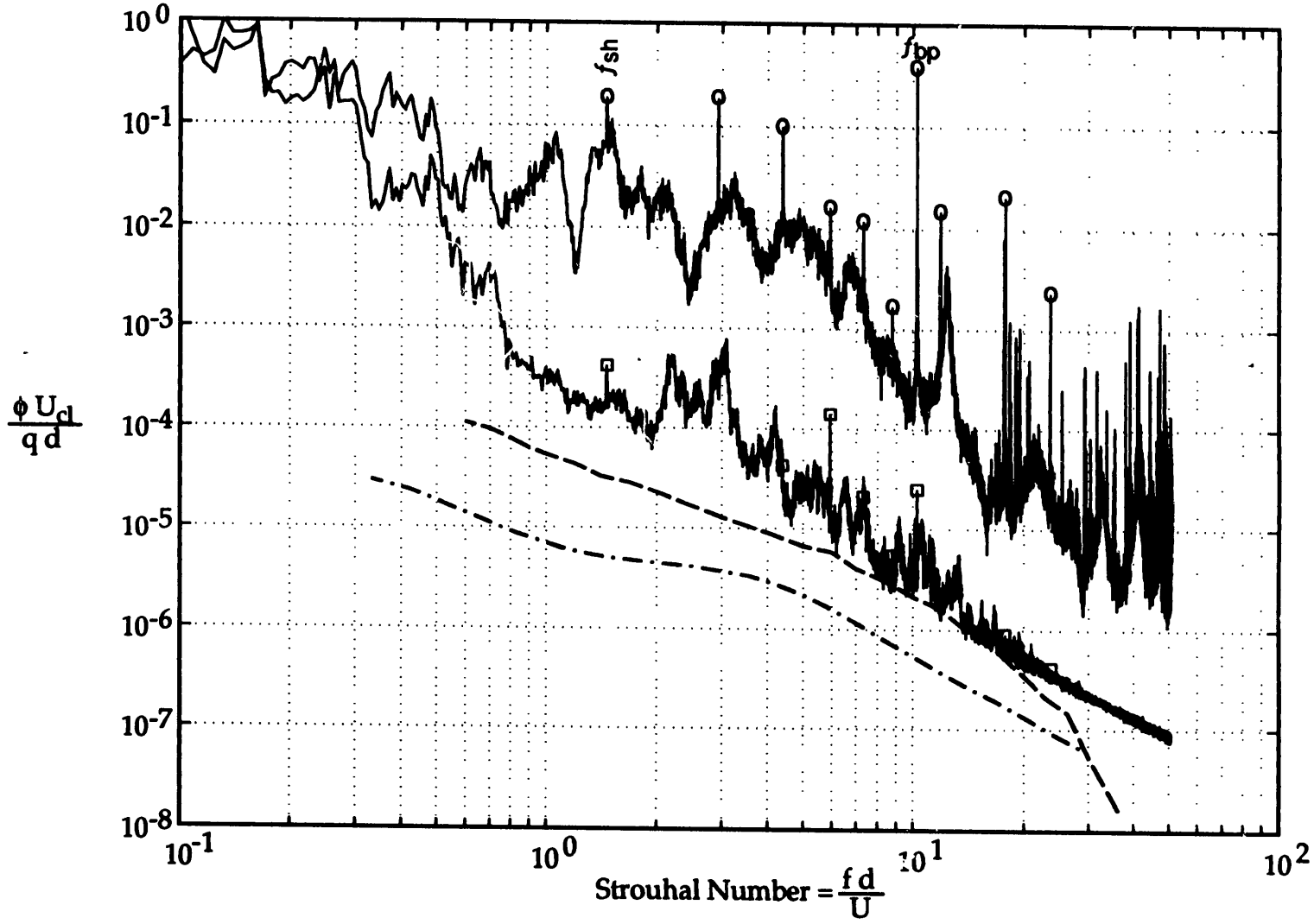

Figure 2.33 Comparison of non-dimensional pressure spectral density at far-upstream measurement section to that at the pump inlet and to published spectra due to turbulence. —o—: at pump inlet; —□—: at upstream measurement section; — — —: turbulence spectrum due to Clinch; · — · — ·: turbulence spectrum due to Rogers. f_{sh}: shaft frequency; f_{bp}: blade passage frequency.

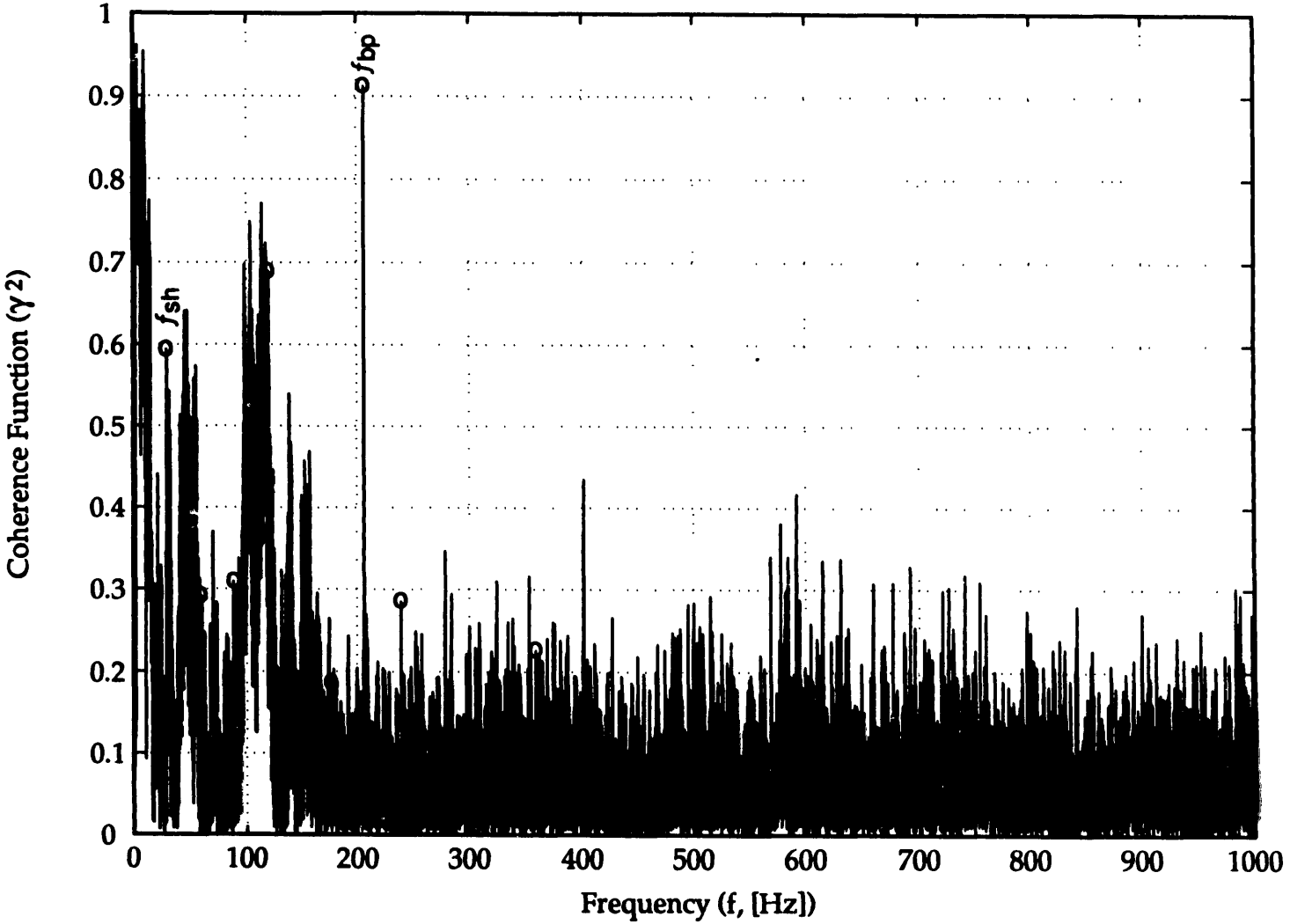

Figure 2.34 Coherence of the Unsteady Pressure Field over a 100 foot Hose between the Pump Inlet and The Far-Upstream Measurement Section. f_{sh} = Shaft Frequency, f_{bp} = Blade Passage Frequency.

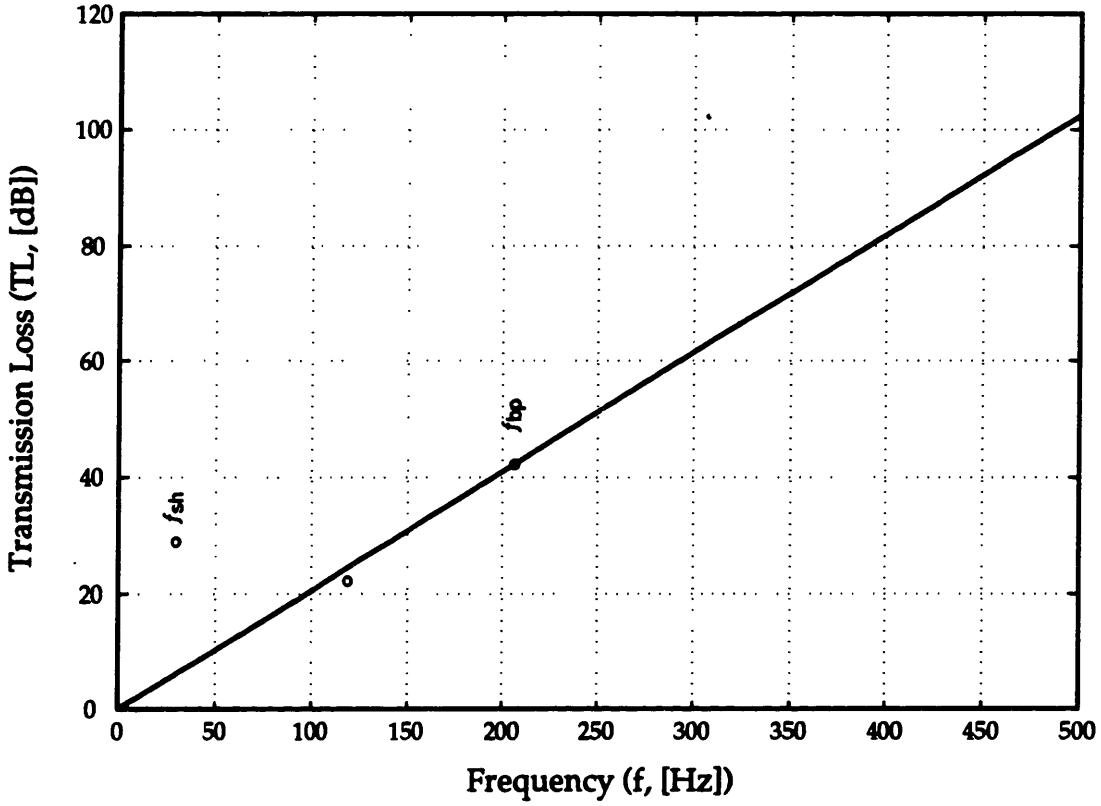

Figure 2.35 Comparison of Transmission Loss Measured over the 100 foot Hose to that predicted by Ingard[20] for $\chi = 10.326$, $\varepsilon = .1215$.
o: Measured Values; ———: Relation Predicted by Ingard[20] [Appendix B]; f_{sh} = Shaft Frequency, f_{bp} = Blade Passage Frequency.

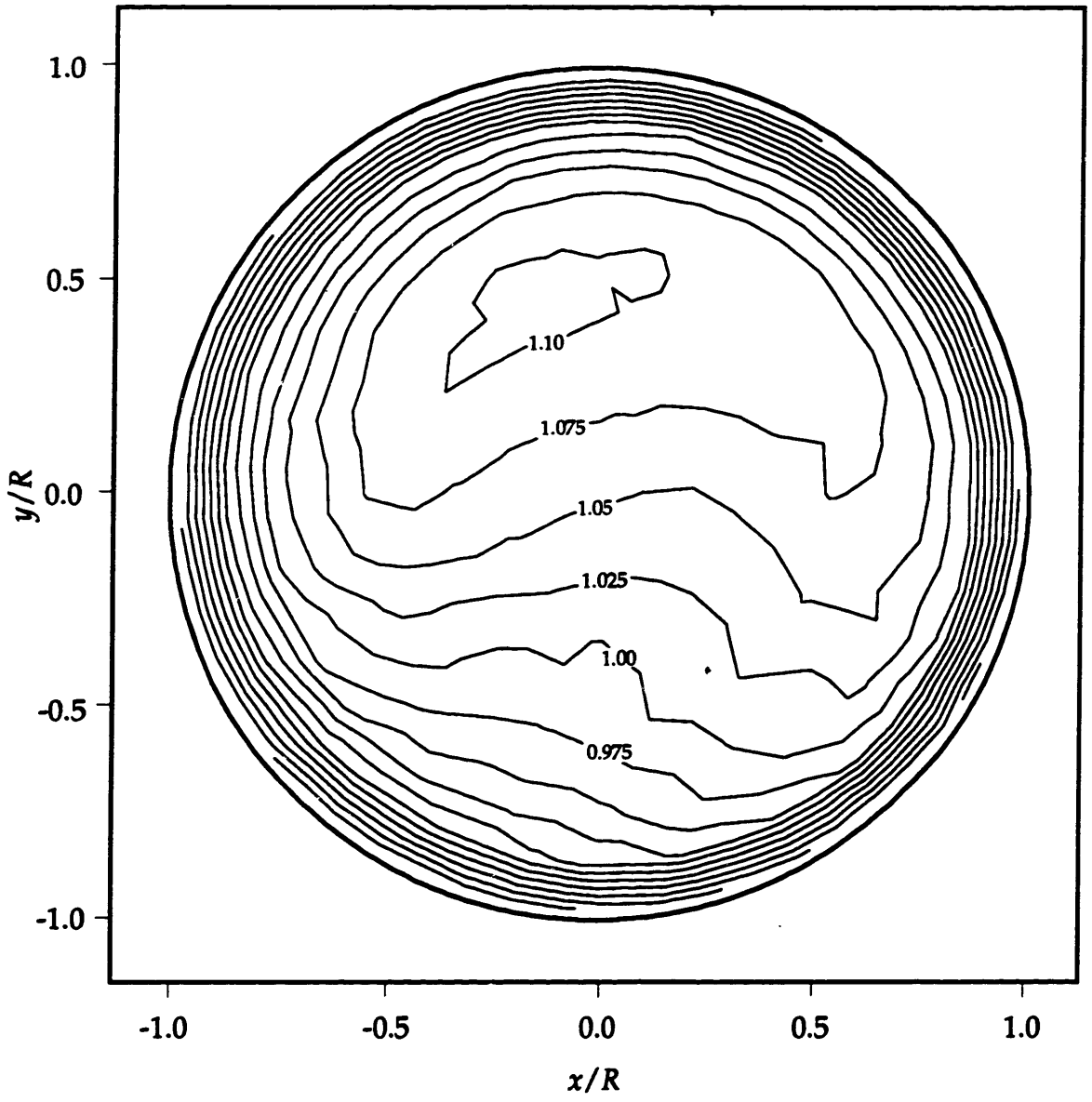

Figure 3.1 Steady Velocity Contour at Pump Inlet. Fully Developed, High Flow Case.

Normalized to Volume Mean Velocity

Mean Velocity ($\bar{u}$) = 2.7065 m/s
Maximum Velocity = 1.10 $\bar{u}$
Minimum Velocity = 0.729 $\bar{u}$
Contour Increment = 0.025 $\bar{u}$

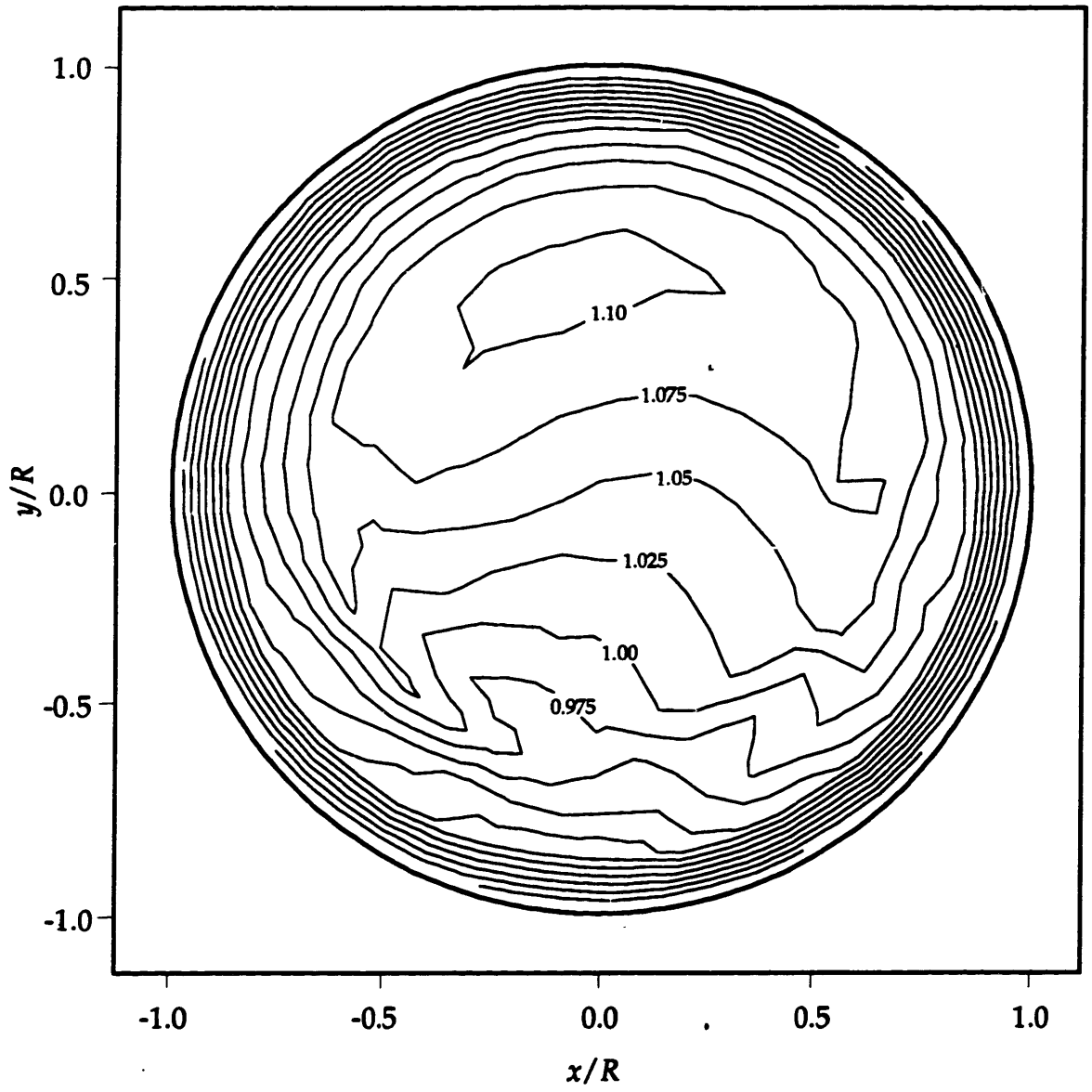

Figure 3.2 Steady Velocity Contour at Pump Inlet. Fully Developed, Low Flow Case.

Normalized to Volume Mean Velocity

Mean Velocity ($\bar{u}$) = 2.5153 m/s
Maximum Velocity = 1.10 $\bar{u}$
Minimum Velocity = 0.73 $\bar{u}$
Contour Increment = 0.025 $\bar{u}$

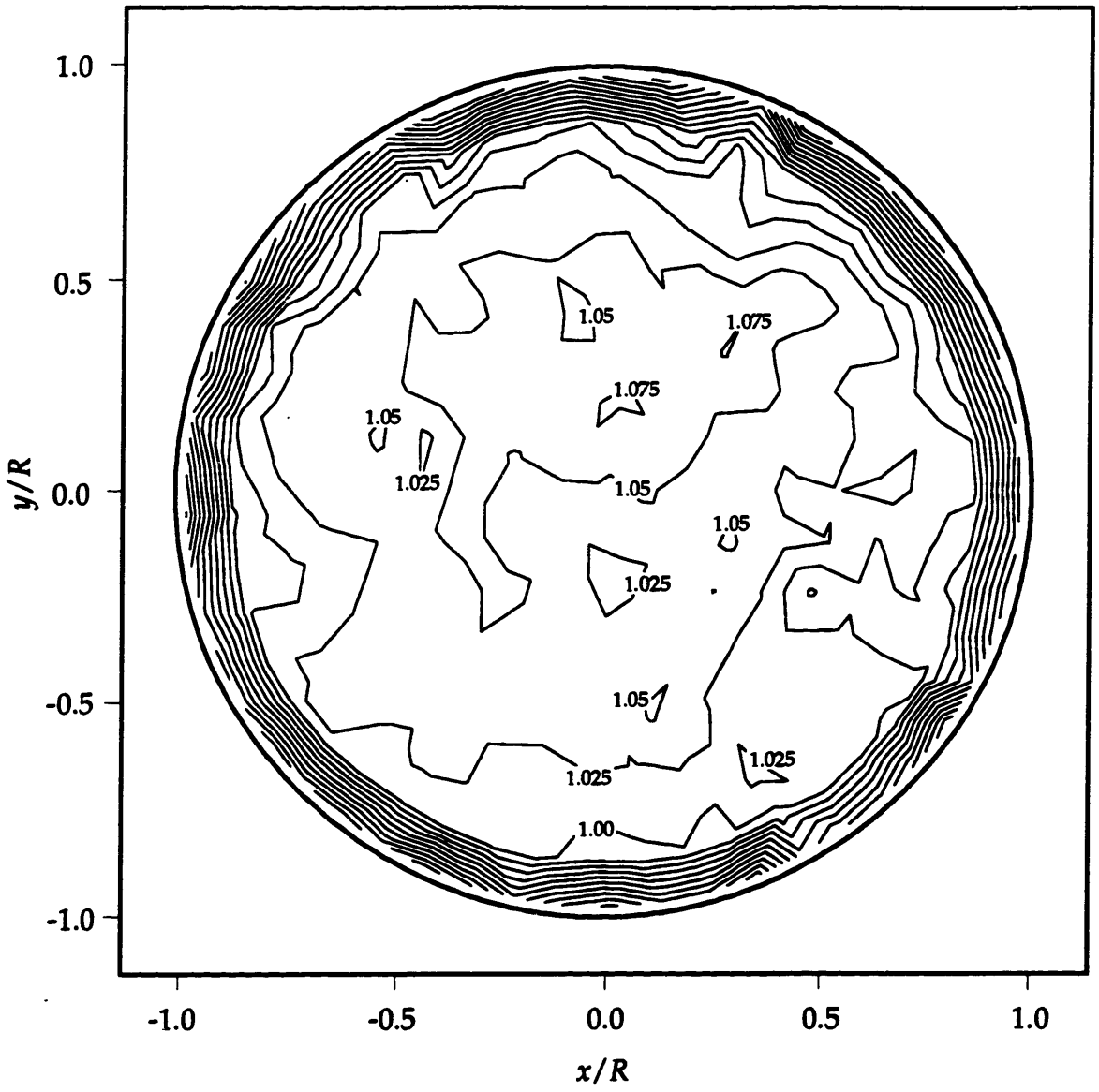

Figure 3.3 Steady Velocity Contour at Pump Inlet. Uniform Case.

Normalized to Volume Mean Velocity

Mean Velocity ($\bar{u}$) = 2.6824 m/s
Maximum Velocity = 1.07 $\bar{u}$
Minimum Velocity = 0.70 $\bar{u}$
Contour Increment = 0.025 $\bar{u}$

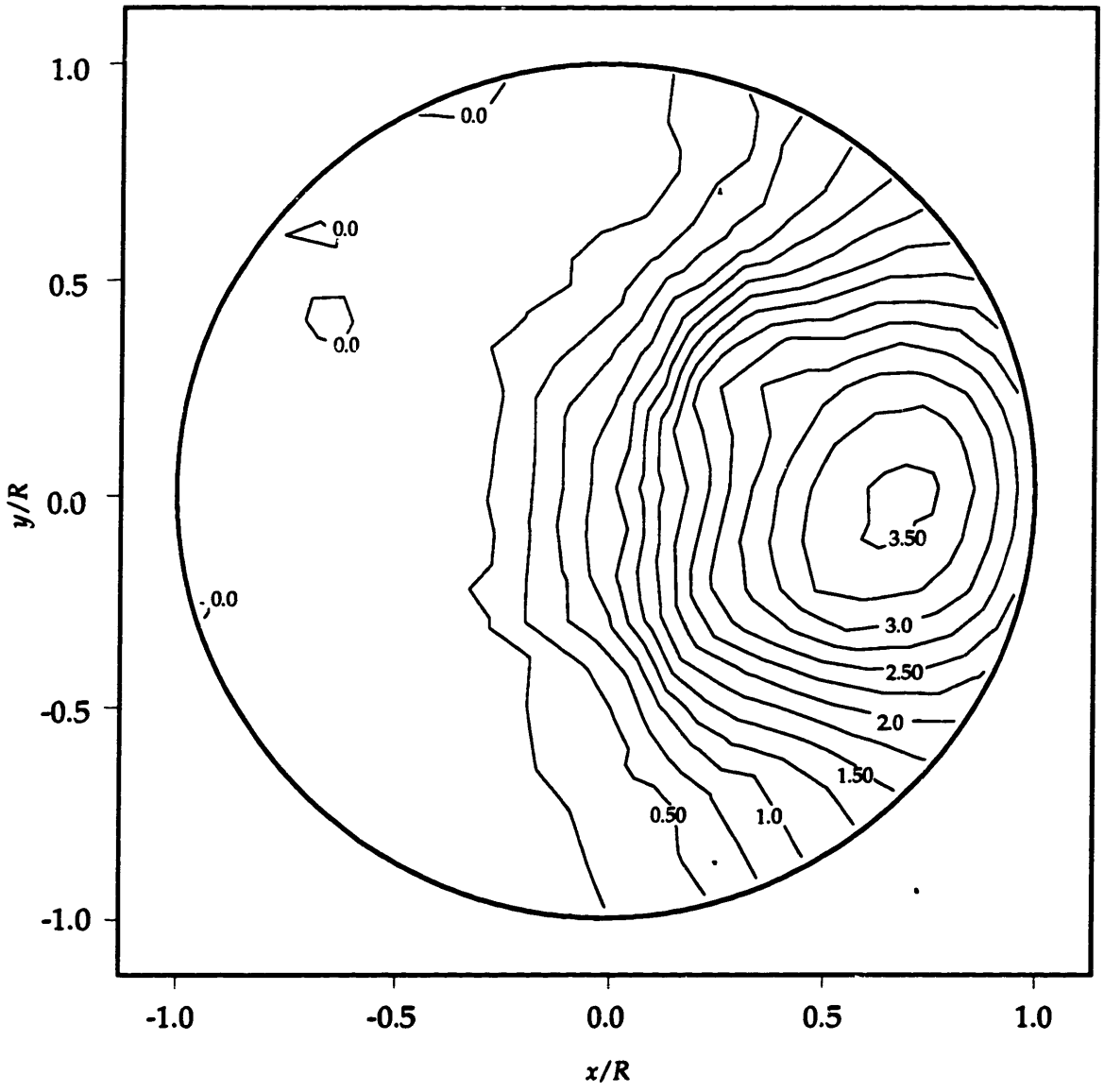

Figure 3.4 Steady Velocity Contour at Pump Inlet. Orifice Distorted Case.

Normalized to Volume Mean Velocity

Mean Velocity ($\bar{u}$) = 4.1797 m/s
Maximum Velocity = 3.55 $\bar{u}$
Minimum Velocity = 0.00 $\bar{u}$
Contour Increment = 0.25 $\bar{u}$

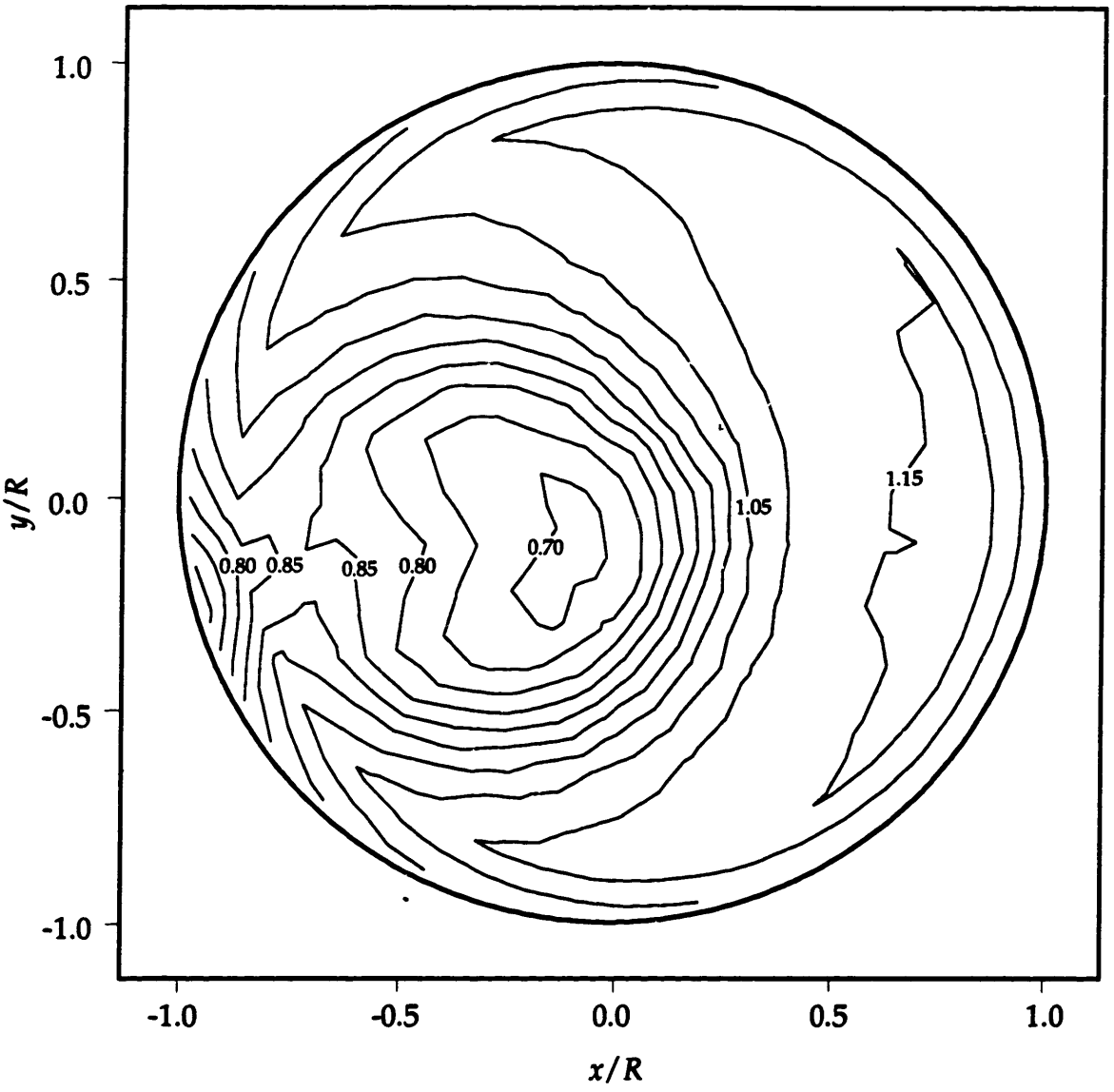

Figure 3.5 Steady Velocity Contour at Pump Inlet. Elbow Distorted Case.

Normalized to Volume Mean Velocity

Mean Velocity ($\bar{u}$) = 2.6414 m/s
Maximum Velocity = 1.16 $\bar{u}$
Minimum Velocity = 0.68 $\bar{u}$
Contour Increment = 0.05 $\bar{u}$

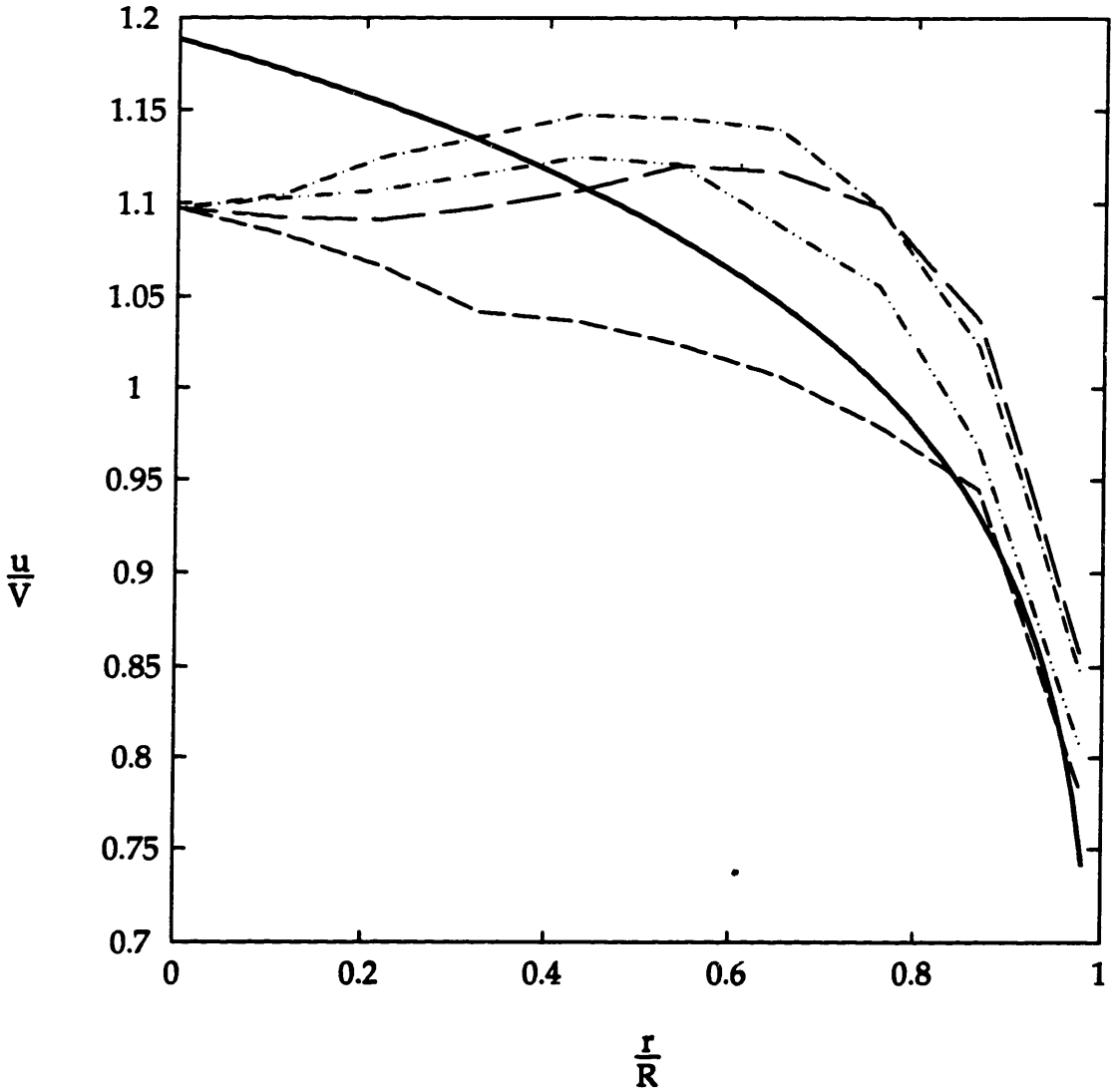

Figure 3.6 Comparison of the MeasuredRadial Velocity Profile for the Fully Developed, High Flow Case to the Empirical Formula [Eq. 3.1].
——— :Emperical Formula; — — θ = 0°;
– – – – : θ = 90°; –·–·– : θ = 180°; –··–··– θ = 270°.

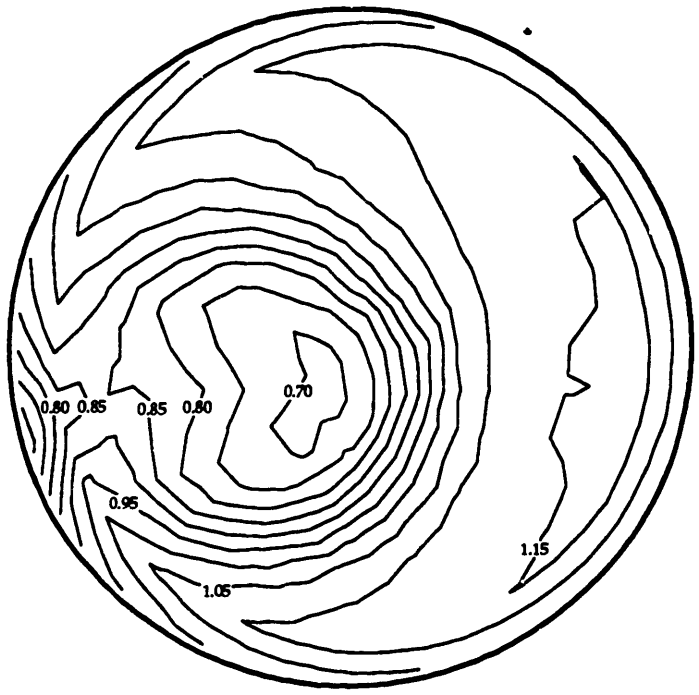

a. Axial Velocity Contour for the Elbow Distorted Case

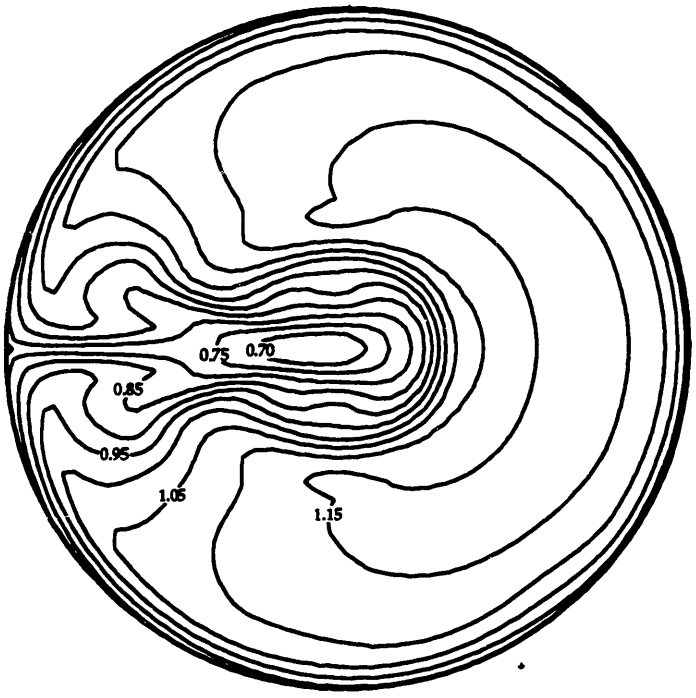

b. Numerical Result due to Felici

Figure 3.7 Comparison of the Elbow Distorted Profile to the Numerical Results of Felici.[17]

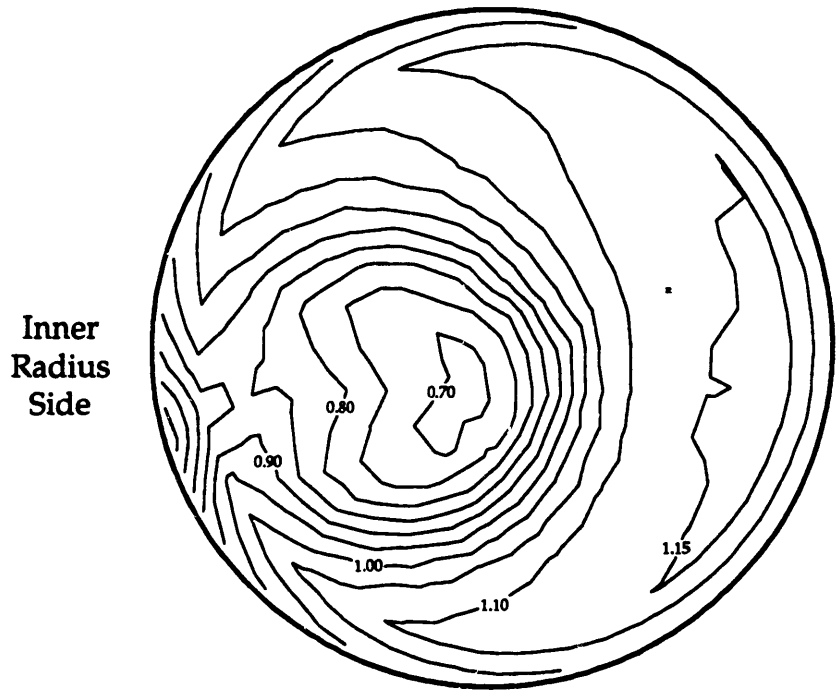

a. Axial Velocity Contour for the Elbow Distorted Case

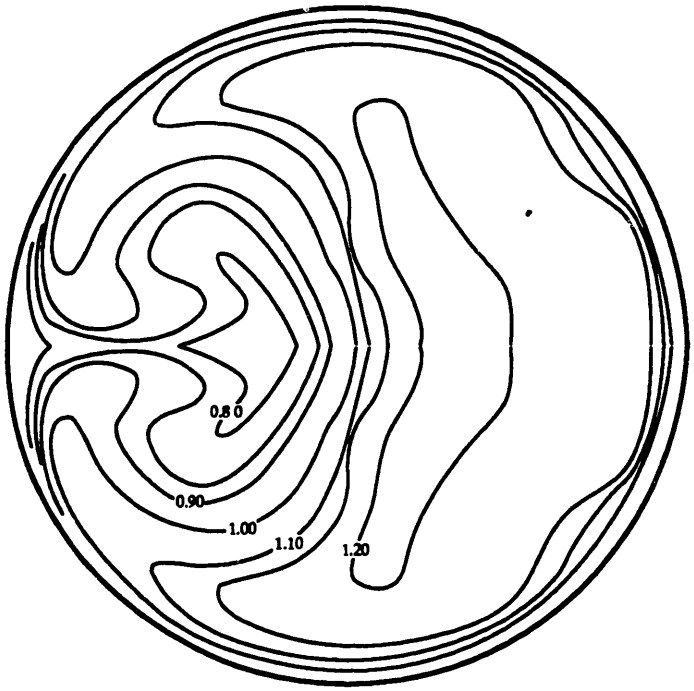

b. Experimental Result due to Enayet

Figure 3.8 Comparison of the Elbow Distorted Profile to the Experimental Results of Enayet.[18]

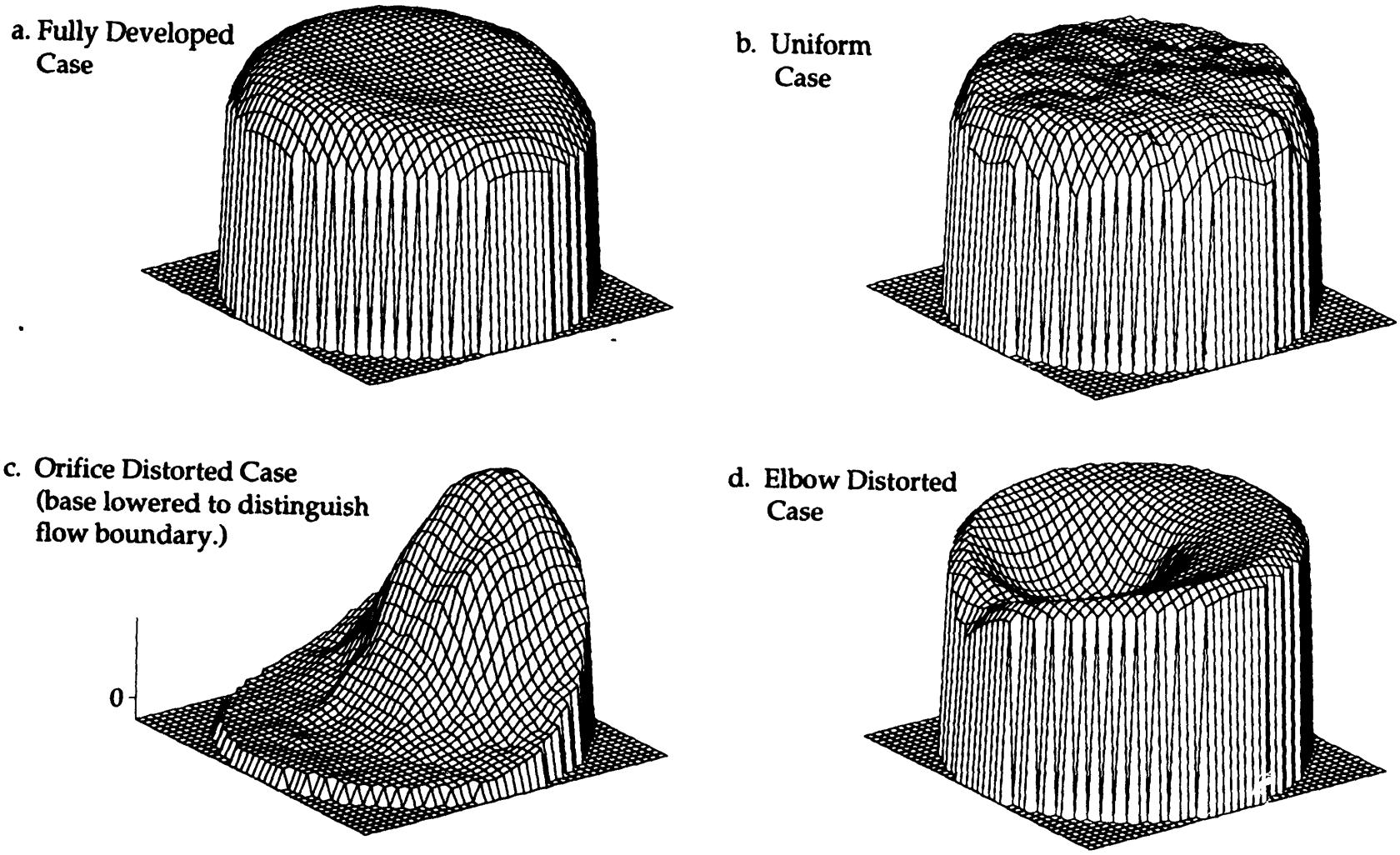

Figure 3.9 Comparison of Velocity Profiles via Surface Plots. All plots are normalized by their maximum for consistent plot height.

a. Fully Developed Case

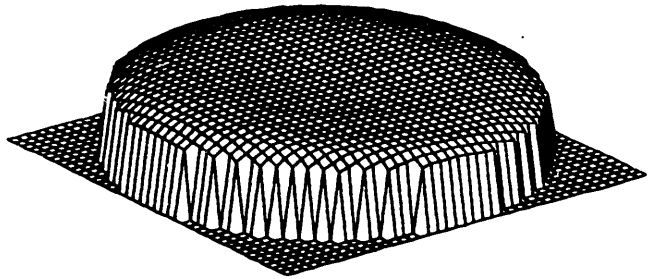

b. Uniform Case

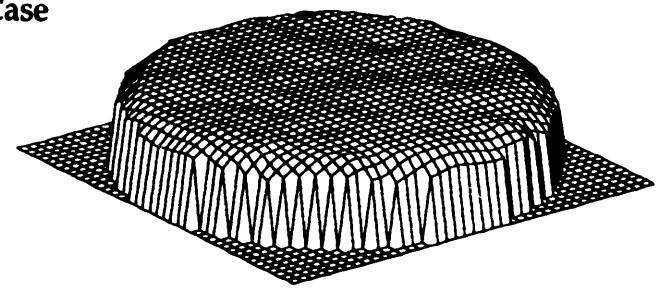

c. Orifice Distorted Case

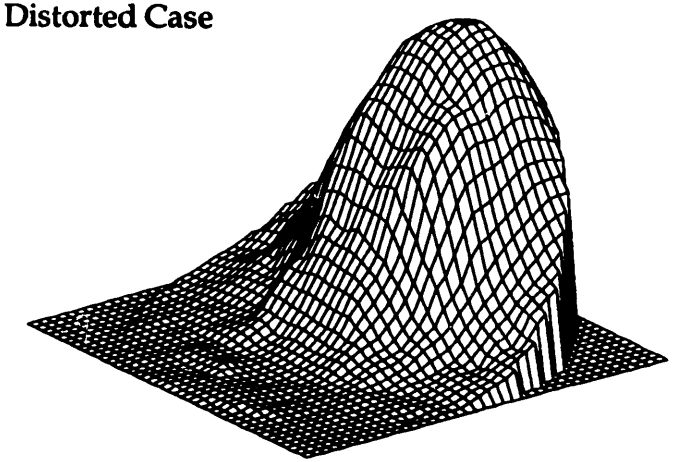

d. Elbow Distorted Case

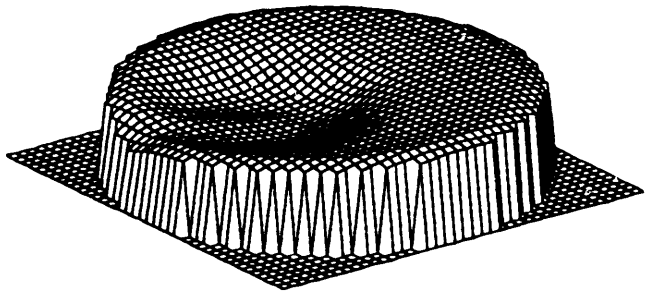

Figure 3.10 Comparison of Velocity Magnitudes via Surface Plots. All plots are normalized by the maximum for the orifice case.

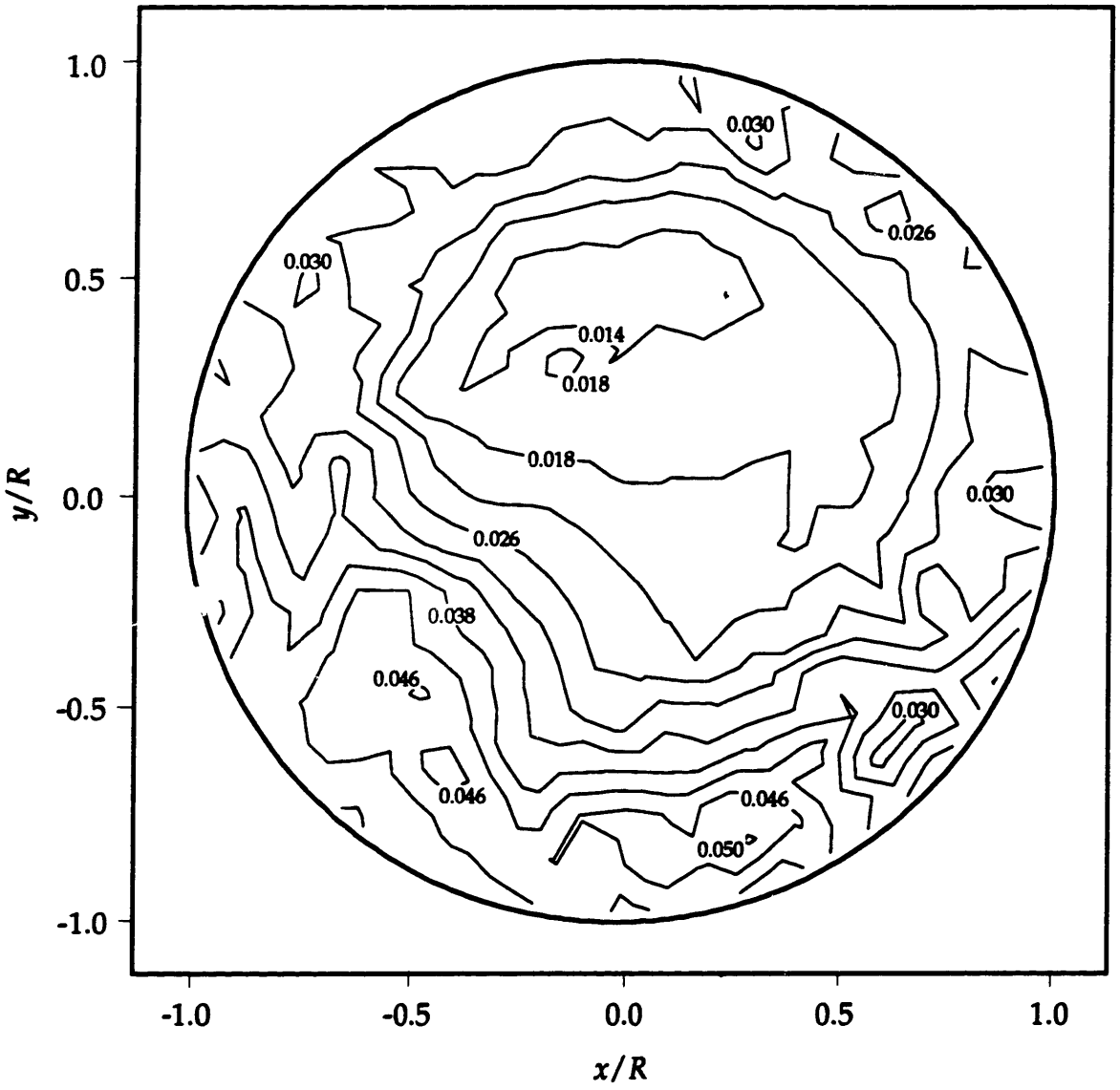

Figure 3.11 Unsteady Velocity Contour at Pump Inlet. Fully Developed, High Flow Case.

Standard Deviation Normalized to Volume Mean Velocity

Mean Velocity ($\bar{u}$) = 2.7065 m/s
Maximum Deviation = 0.05 $\bar{u}$
Minimum Deviation = 0.01 $\bar{u}$
Contour Increment = 0.004 $\bar{u}$

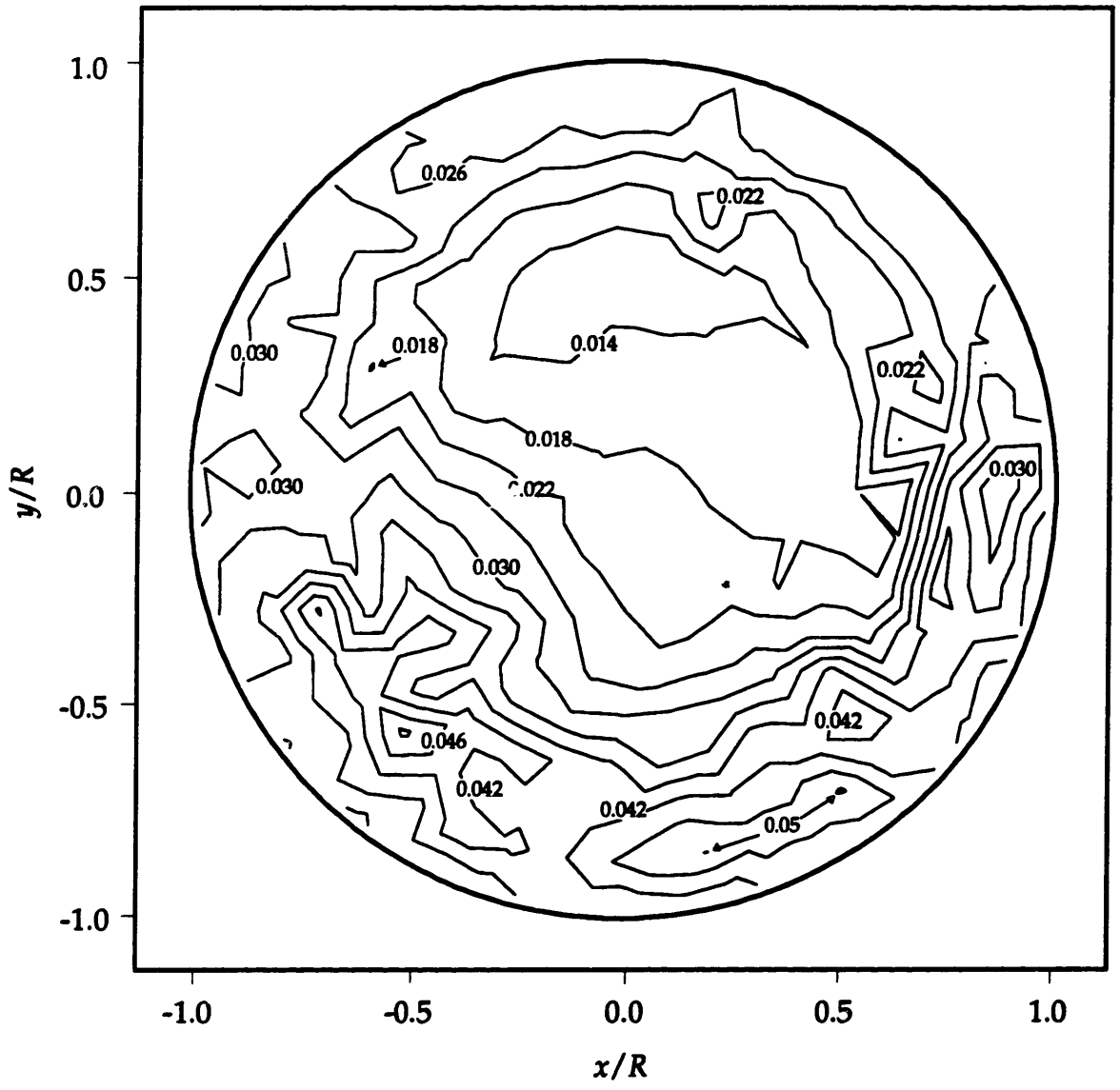

Figure 3.12 Unsteady Velocity Contour at Pump Inlet. Fully Developed, Low Flow Case.

Standard Deviation Normalized to Volume Mean Velocity

Mean Velocity ($\bar{u}$) = 2.5153 m/s
Maximum Deviation = 0.05 $\bar{u}$
Minimum Deviation = 0.01 $\bar{u}$
Contour Increment = 0.004 $\bar{u}$

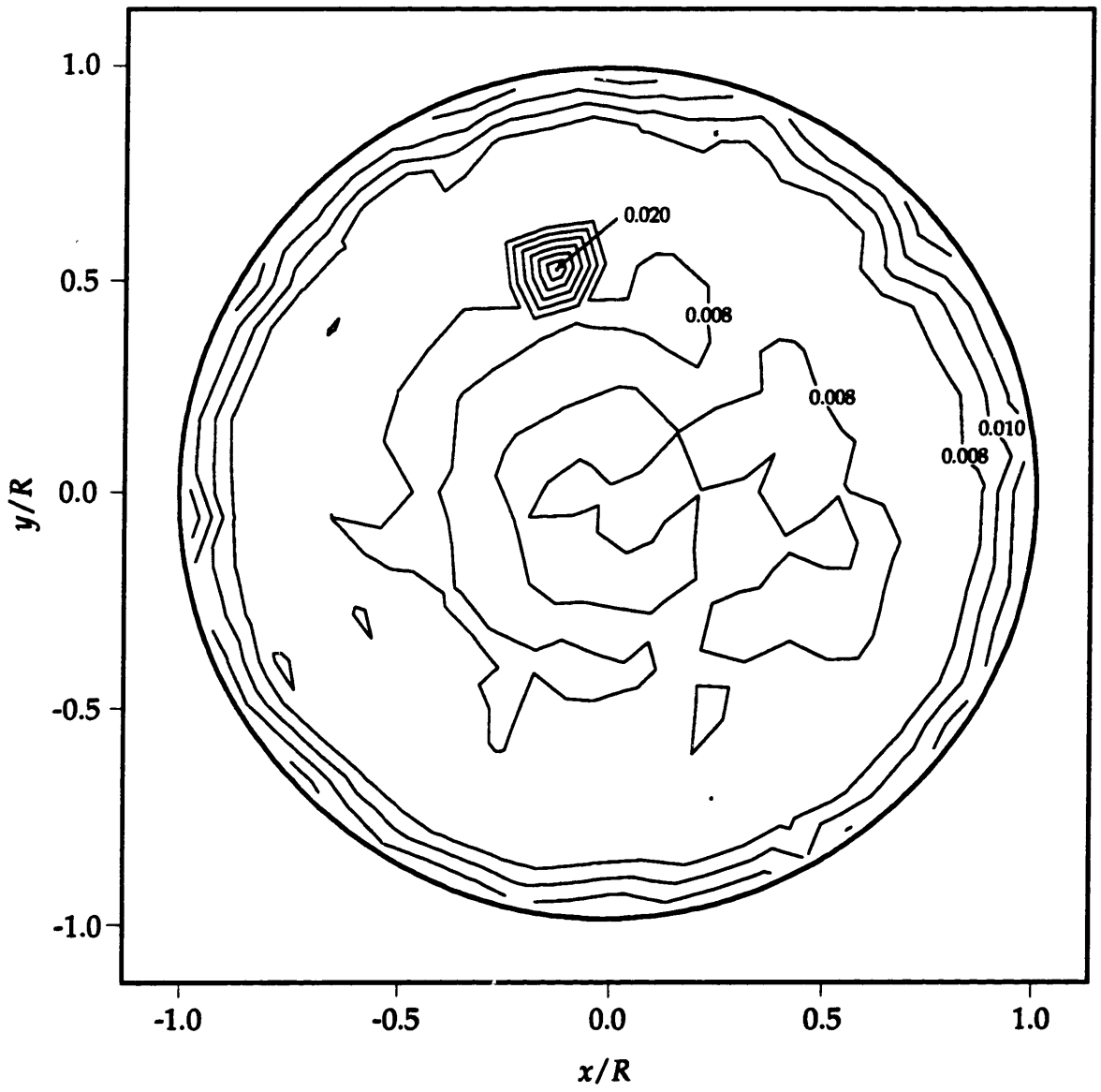

Figure 3.13 Unsteady Velocity Contour at Pump Inlet. Uniform Case.

Standard Deviation Normalized to Volume Mean Velocity
Mean Velocity ($\bar{u}$) = 2.6824 m/s
Maximum Deviation = 0.02 $\bar{u}$
Minimum Deviation = 0.006 $\bar{u}$
Contour Increment = 0.002 $\bar{u}$

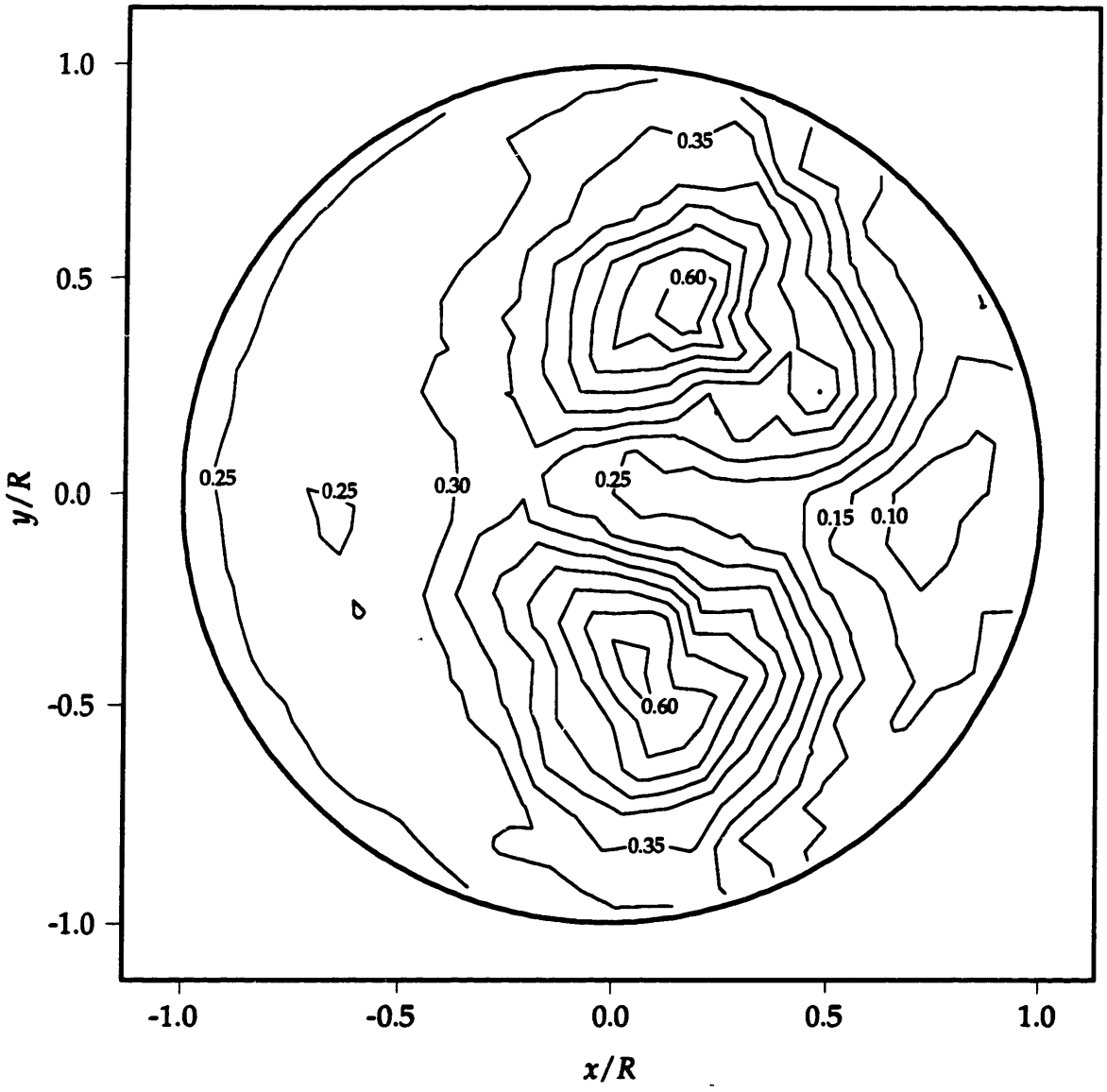

Figure 3.14 Unsteady Velocity Contour at Pump Inlet. Orifice Distorted Case.

Standard Deviation Normalized to Volume Mean Velocity
Mean Velocity ($\bar{u}$) = 4.1797 m/s
Maximum Deviation = 0.62 $\bar{u}$
Minimum Deviation = 0.07 $\bar{u}$
Contour Increment = 0.05 $\bar{u}$

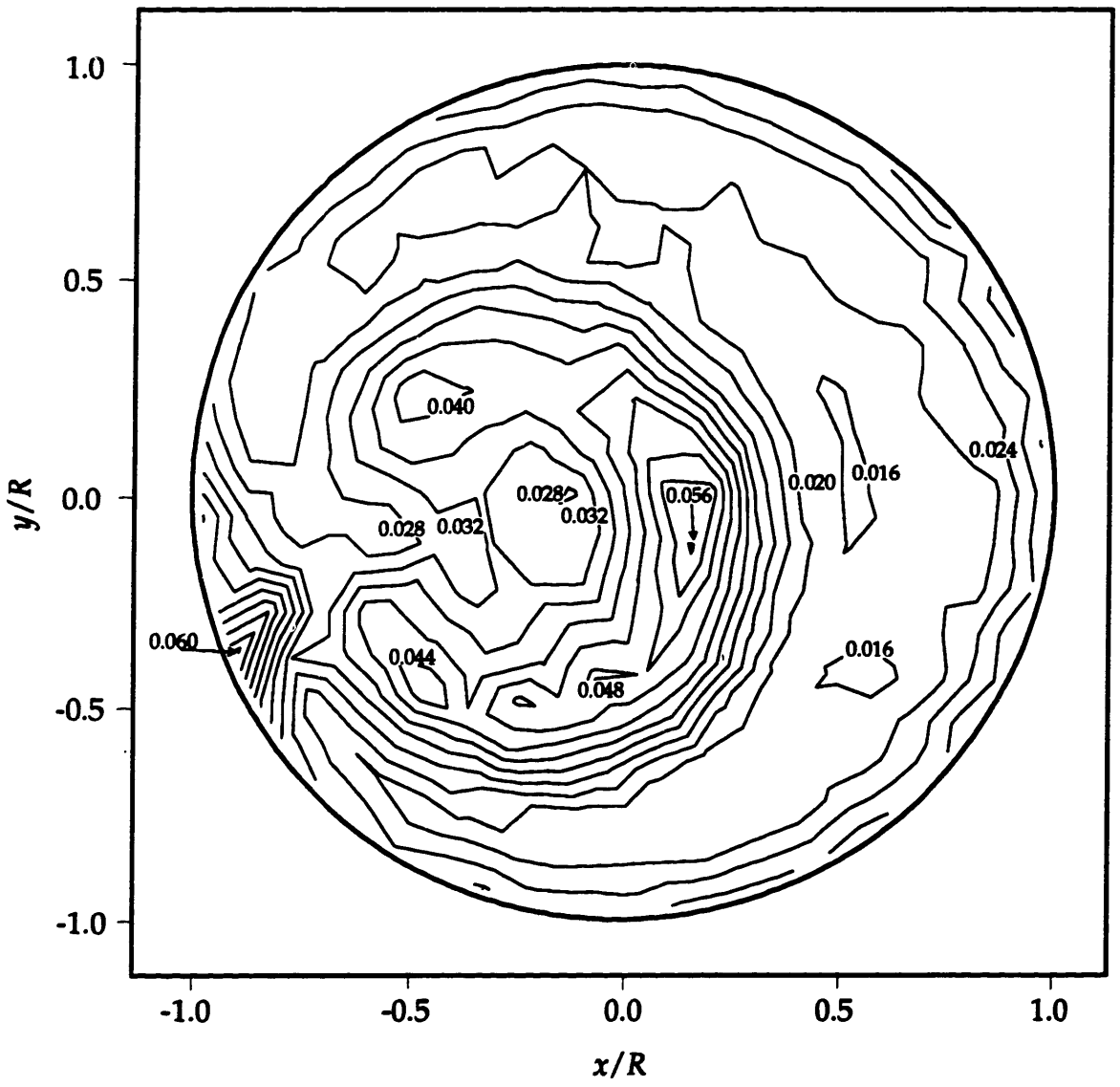

Figure 3.15 Unsteady Velocity Contour at Pump Inlet. Elbow Distorted Case.

Standard Deviation Normalized to Volume Mean Velocity

Mean Velocity ($\bar{u}$) = 2.6414 m/s
Maximum Deviation = 0.061 $\bar{u}$
Minimum Deviation = 0.015 $\bar{u}$
Contour Increment = 0.004 $\bar{u}$

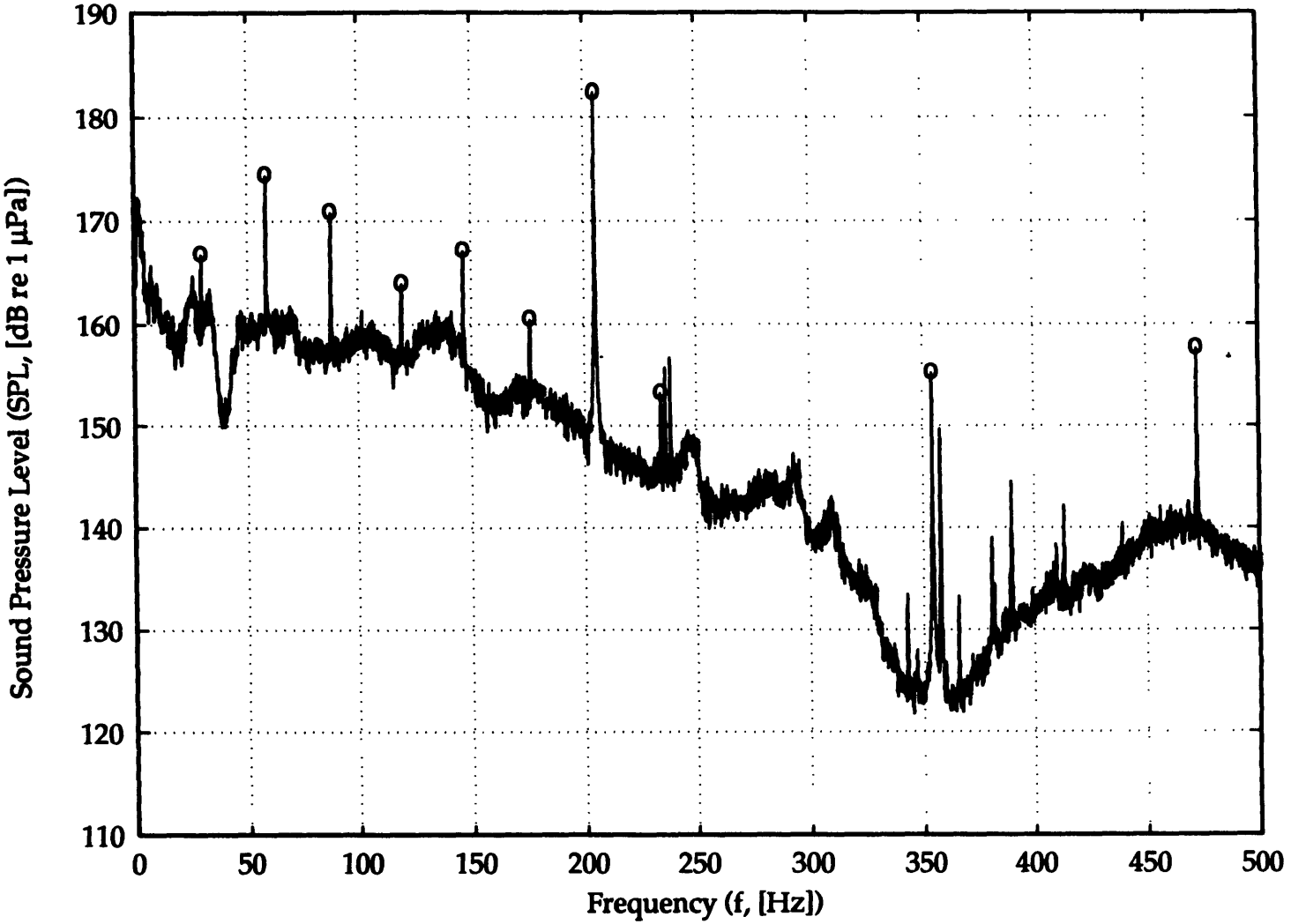

Figure 3.16 Pump Inlet Sound Pressure Level. Fully Developed, High Flow Case. f_{sh} = Shaft Frequency, f_{bp} = Blade Passage Frequency.

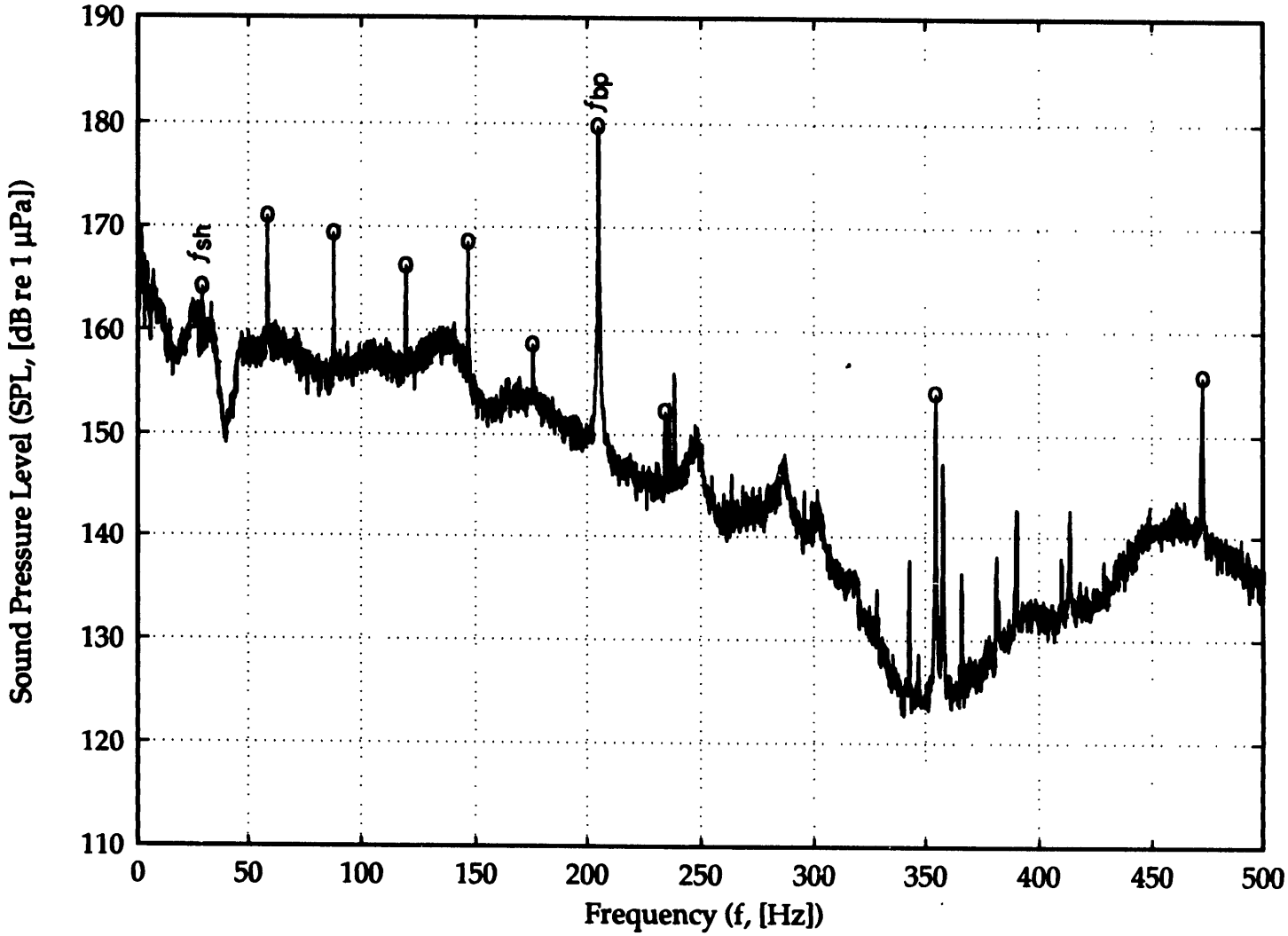

Figure 3.17 Pump Inlet Sound Pressure Level. Fully Developed, Low Flow Case. f_{sh} = Shaft Frequency, f_{bp} = Blade Passage Frequency.

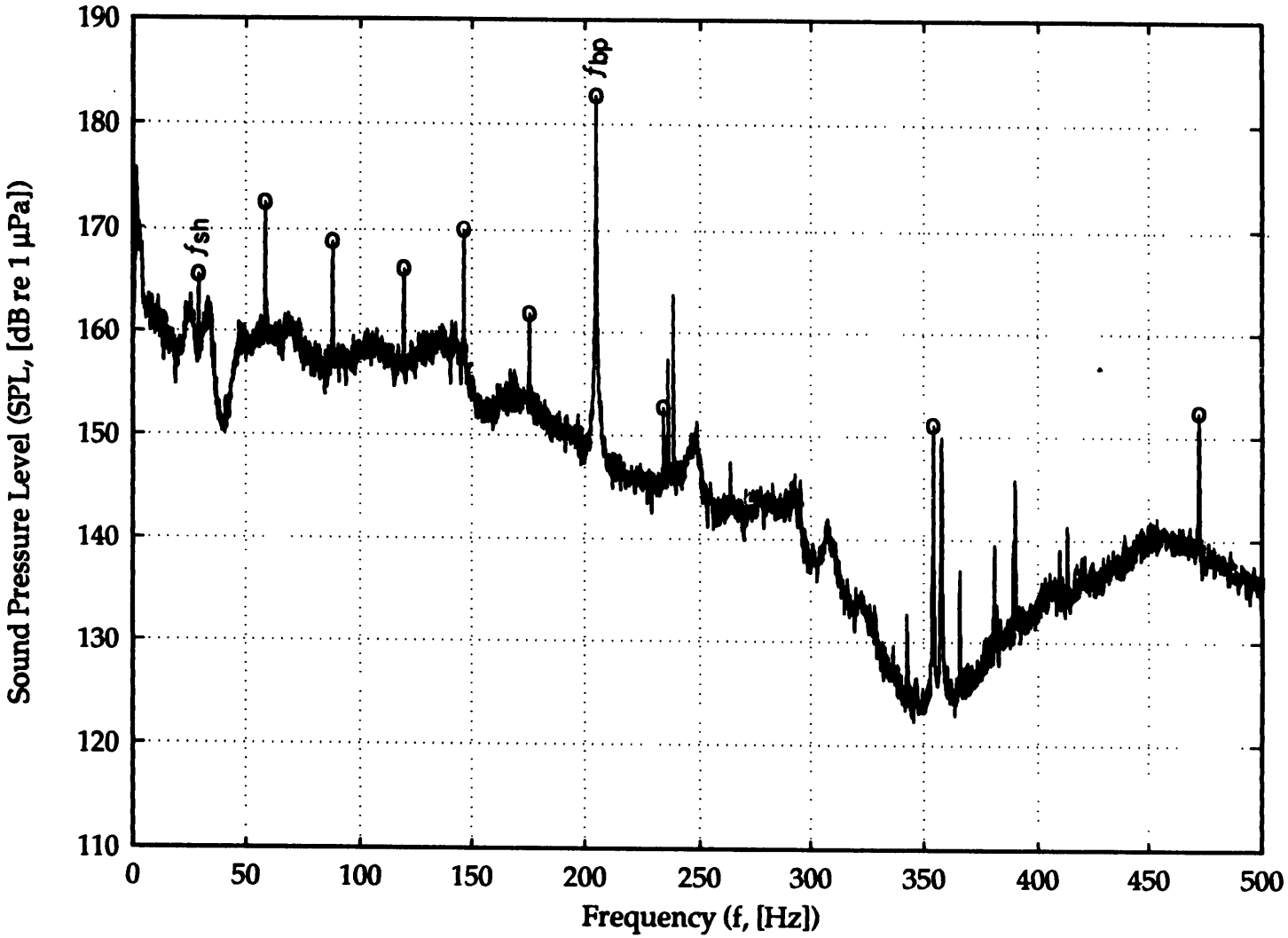

Figure 3.18 Pump Inlet Sound Pressure Level. Uniform Case.
f_{sh} = Shaft Frequency, f_{bp} = Blade Passage Frequency.

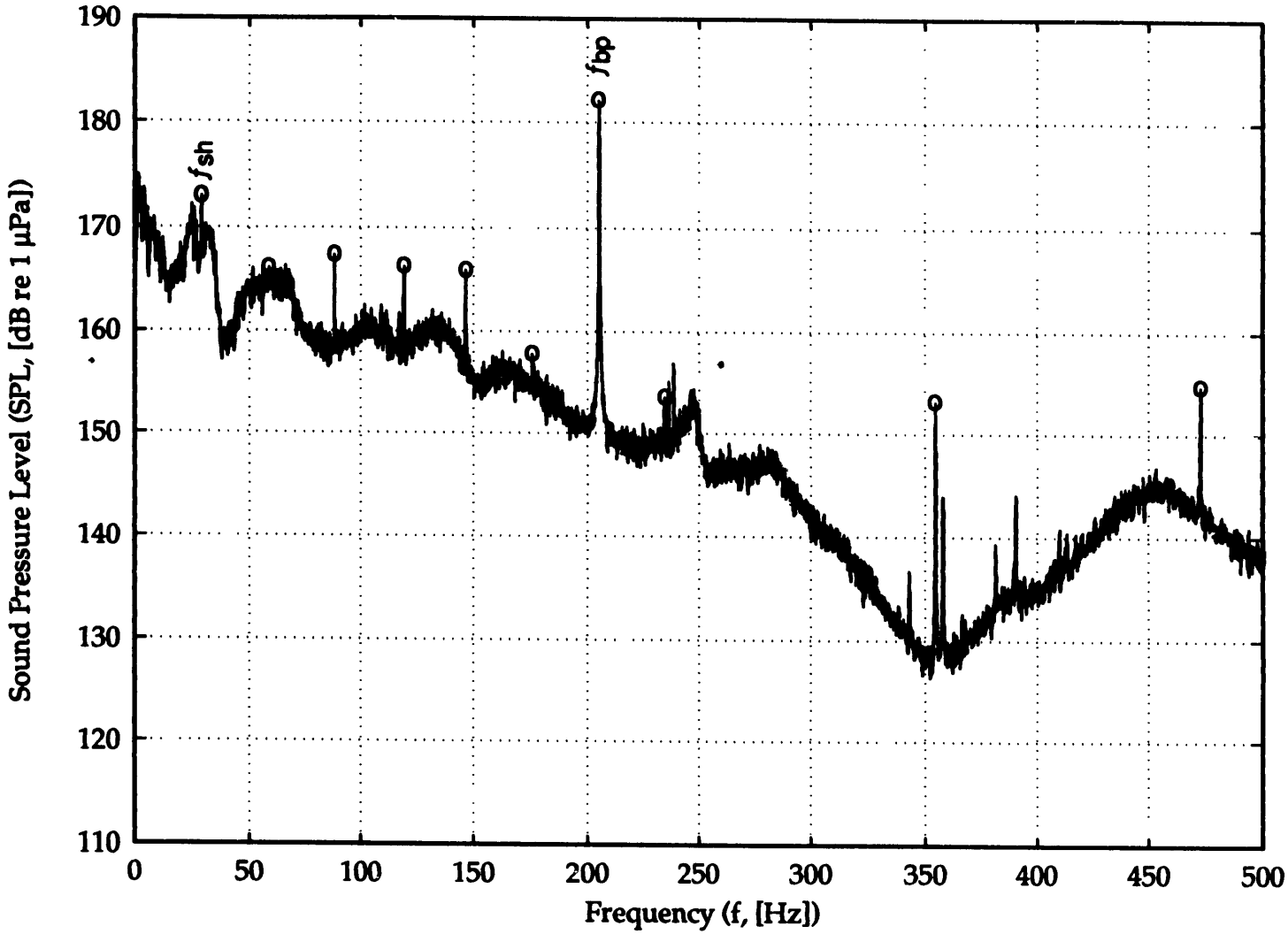

Figure 3.19 Pump Inlet Sound Pressure Level. Orifice Distorted Case. f_{sh} = Shaft Frequency, f_{bp} = Blade Passage Frequency.

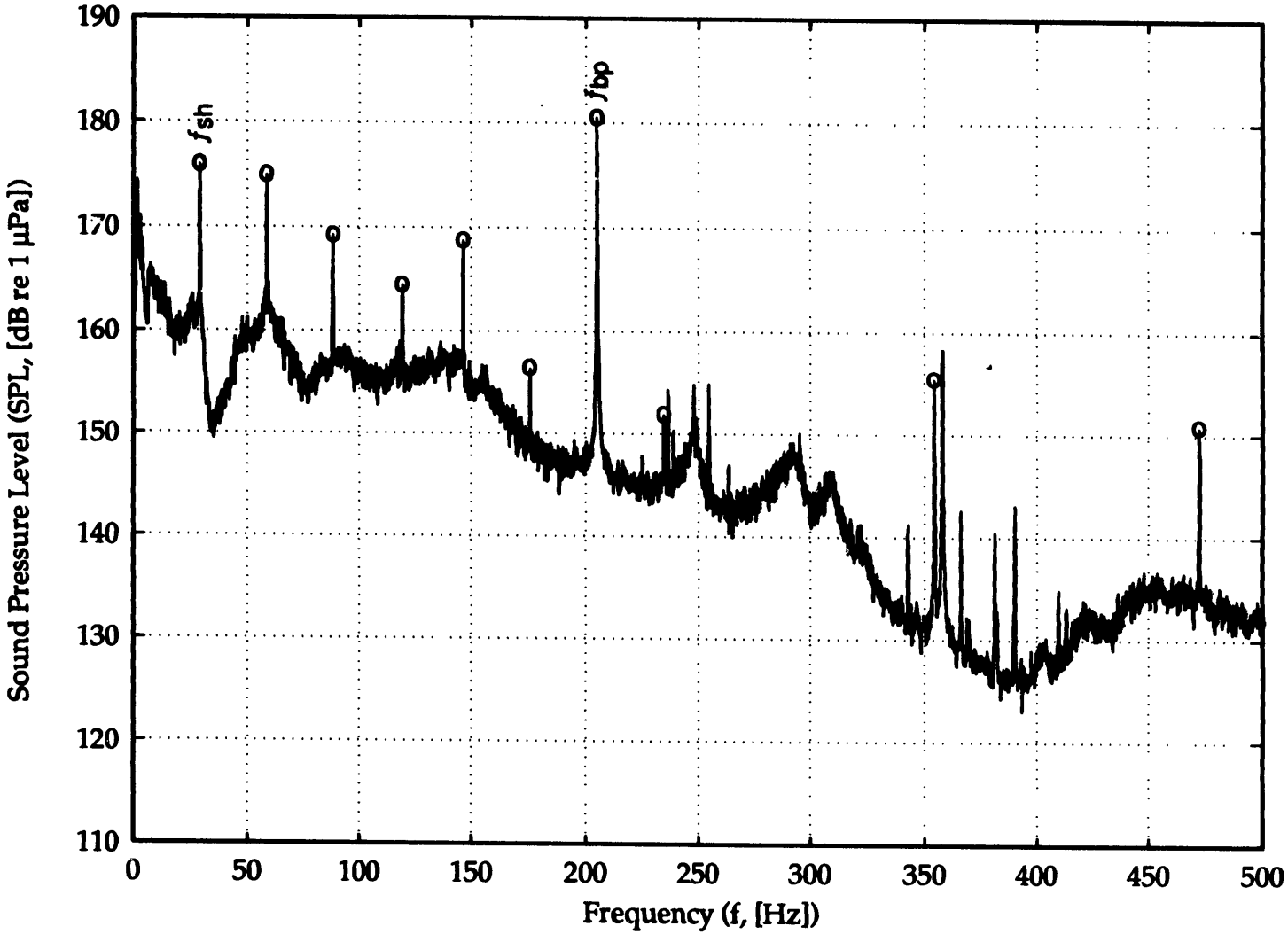

Figure 3.20 Pump Inlet Sound Pressure Level. Elbow Distorted Case. f_{sh} = Shaft Frequency, f_{bp} = Blade Passage Frequency.

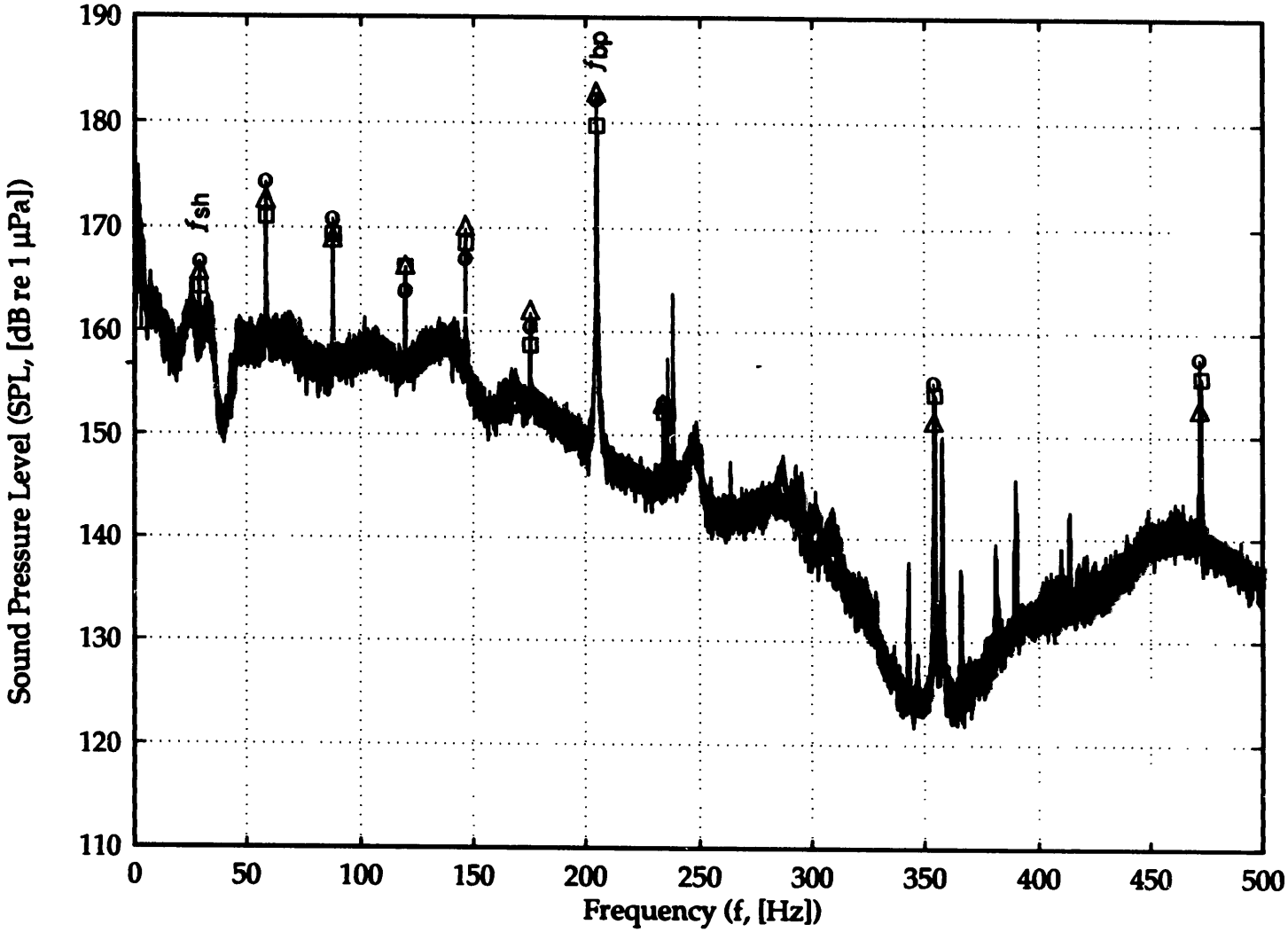

Figure 3.21 Comparison of Inlet SPL Spectra for Fully Developed High Flow, Fully Developed Low Flow, and Uniform Profile Cases. —o— = Fully Developed High; —□— = Fully Developed Low; —△— = Uniform. f_{sh} = Shaft Frequency, f_{bp} = Blade Passage Frequency.

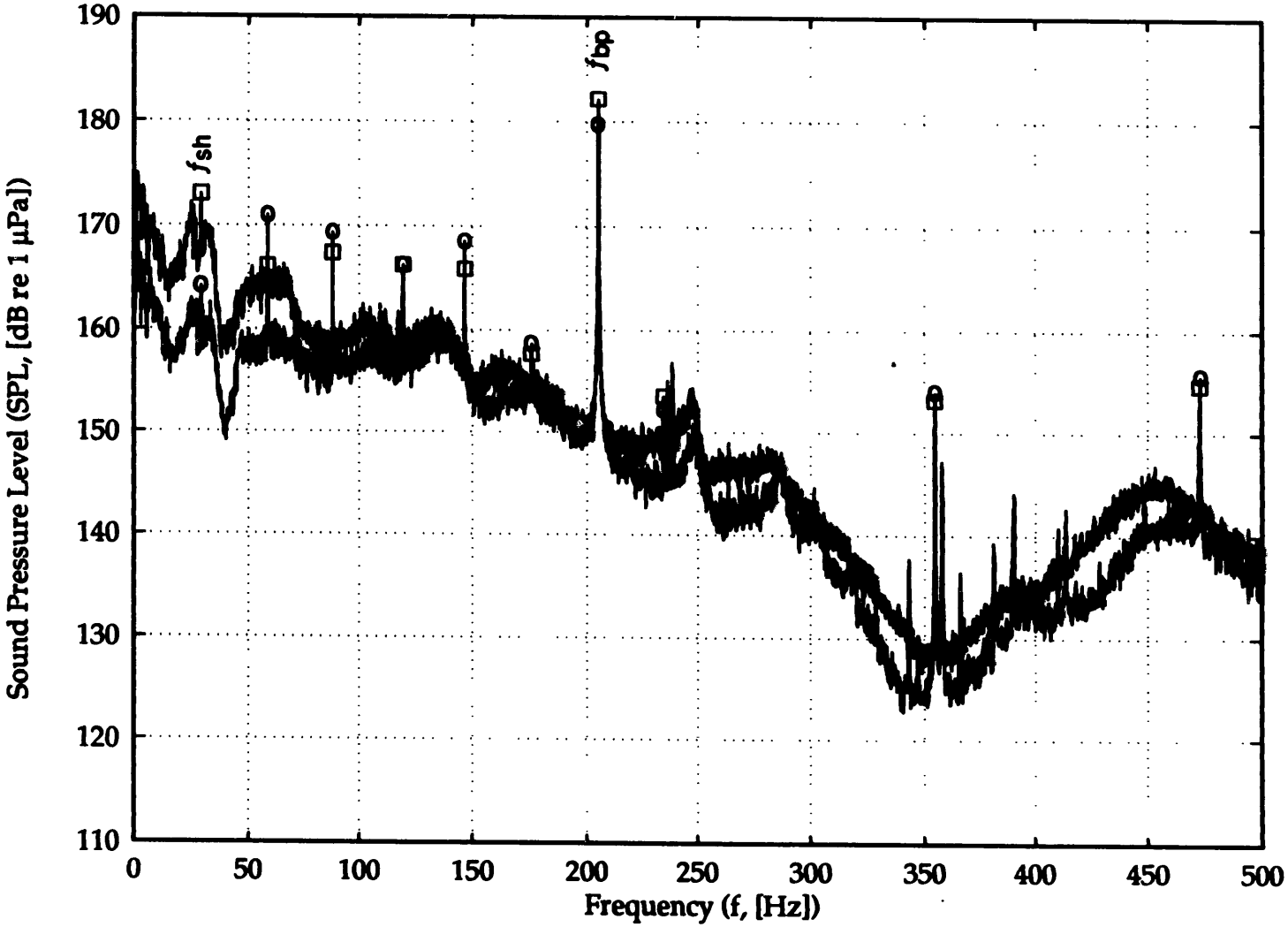

Figure 3.22 Comparison of Inlet SPL Spectra for Fully Developed Low Flow and Orifice Distorted Profile Cases. —o— = Fully Developed Low; —□— = Orifice Distorted. f_{sh} = Shaft Frequency, f_{bp} = Blade Passage Frequency.

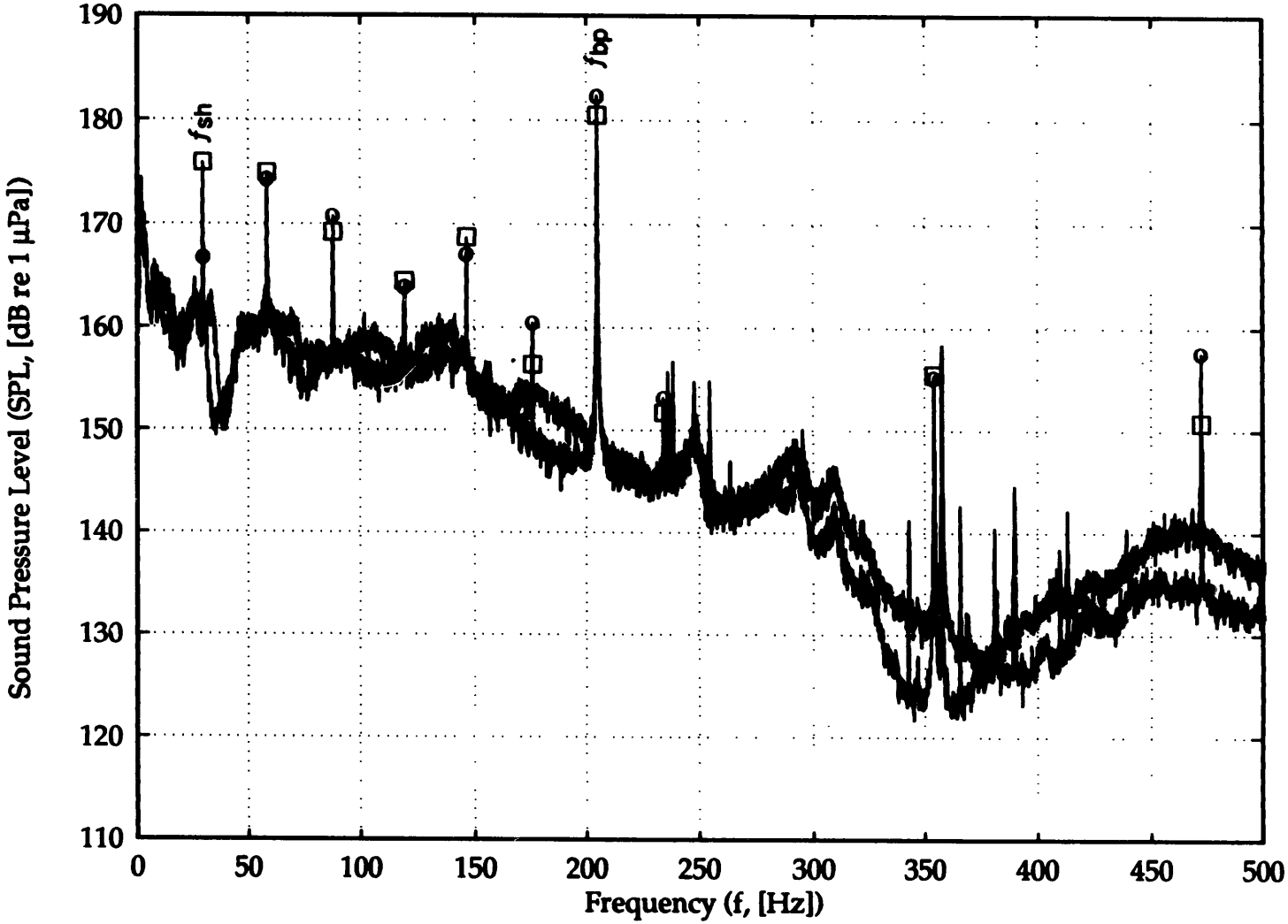

Figure 3.23 Comparison of Inlet SPL Spectra for Fully Developed High Flow and Elbow Distorted Cases. —o— = Fully Developed High; —□— = Elbow Distorted. f_{sh} = Shaft Frequency, f_{bp} = Blade Passage Frequency.

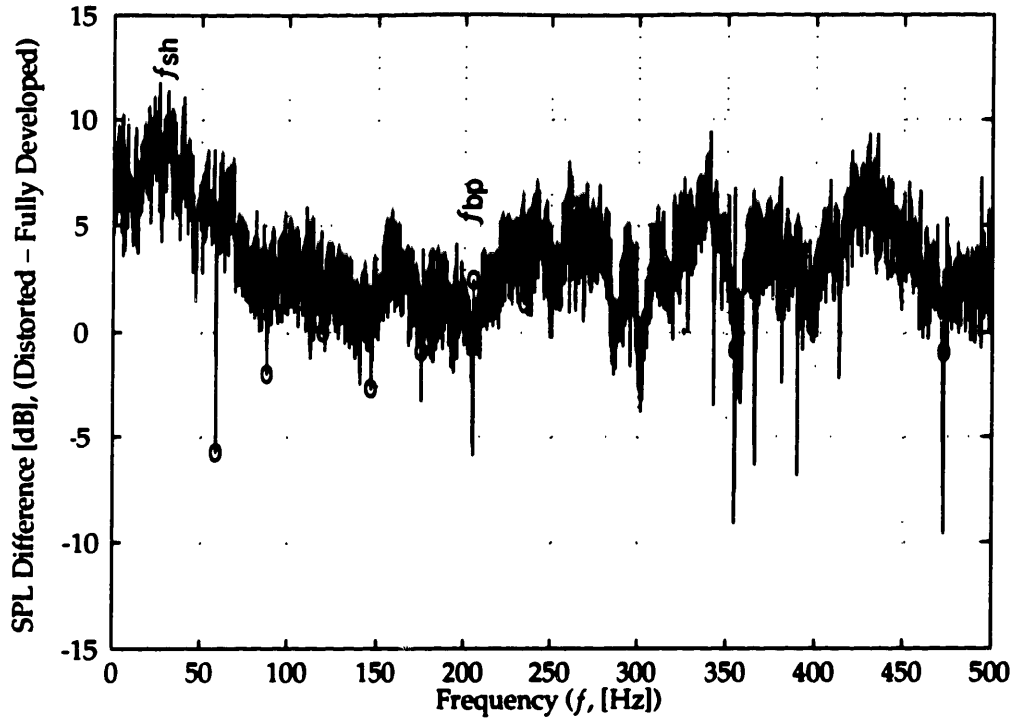

a. Orifice Distorted Case Compared to Fully Developed, Low Case.

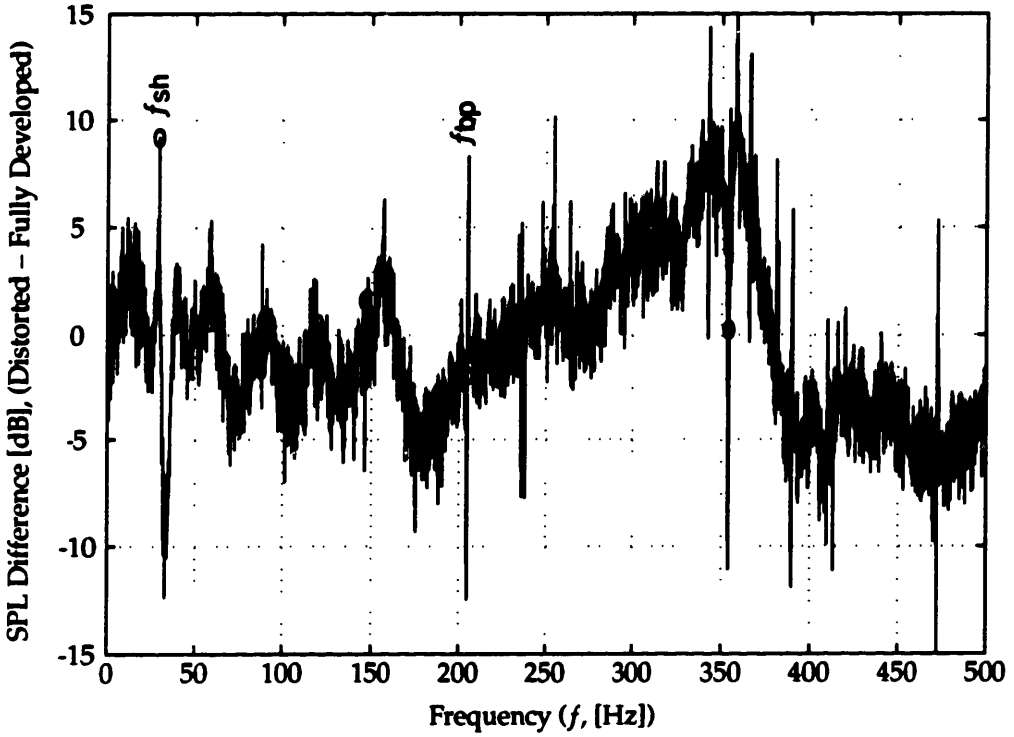

b. Elbow Distorted Case Compared to Fully Developed, High Case.

Figure 3.24 Pump Inlet Sound Pressure Level Difference Between Distorted and Corresponding Fully Developed Cases. f_{sh} = Shaft frequency, f_{bp} = Blade Passage Frequency.

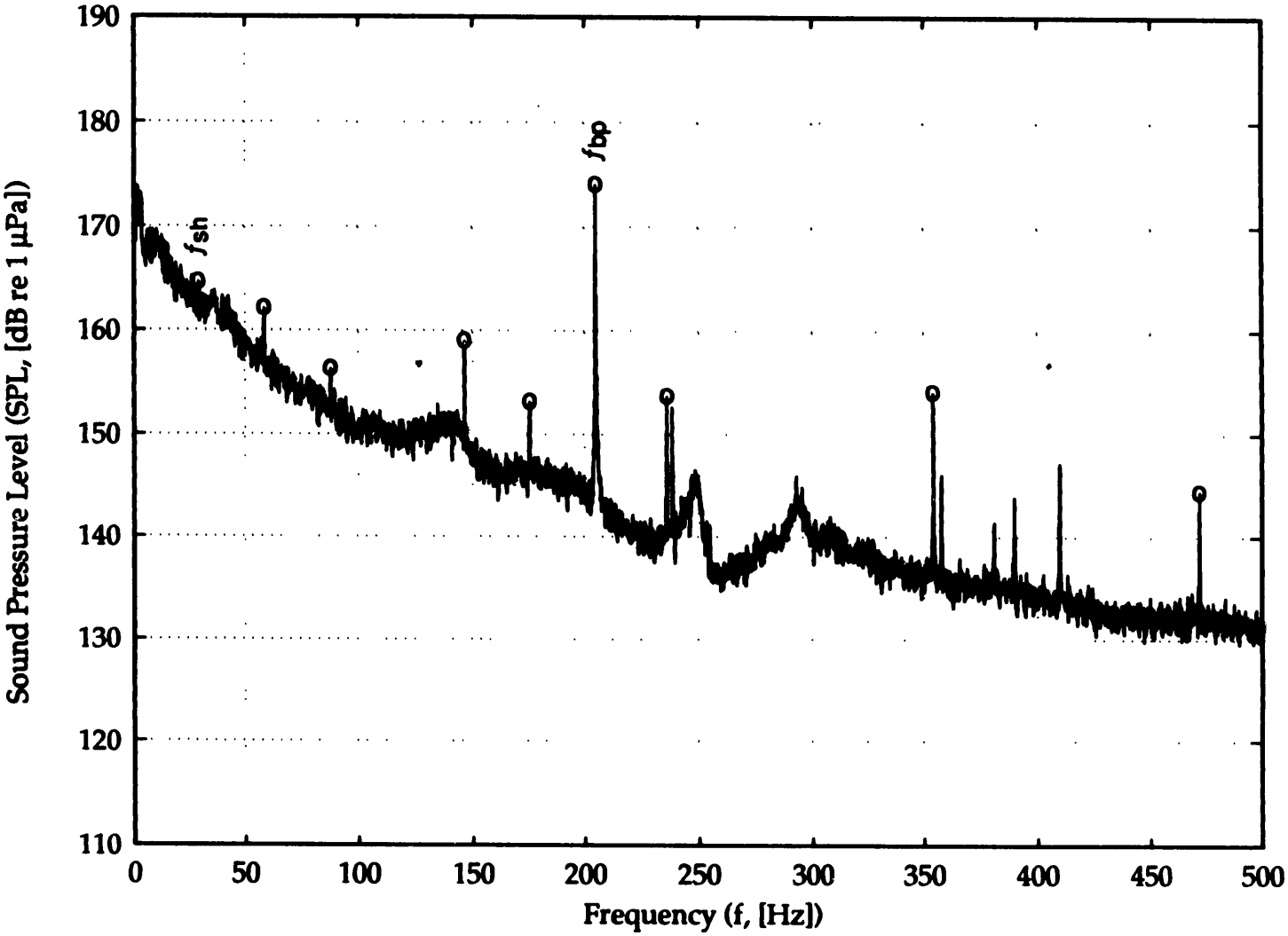

Figure 3.25 Pump Outlet Sound Pressure Level. Fully Developed, High Flow Case. f_{sh} = Shaft Frequency, f_{bp} = Blade Passage Frequency.

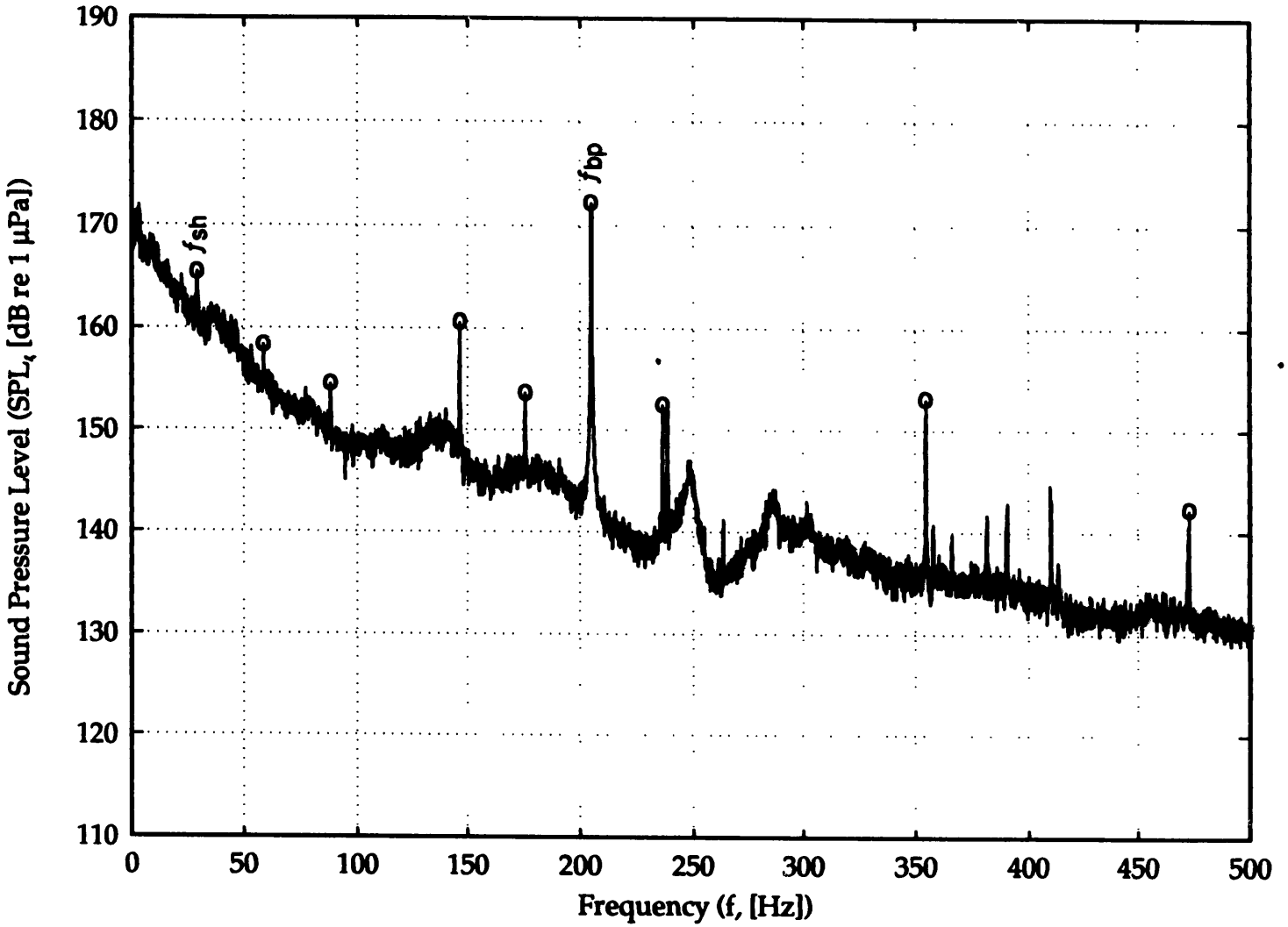

Figure 3.26 Pump Outlet Sound Pressure Level. Fully Developed, Low Flow Case. f_{sh} = Shaft Frequency, f_{bp} = Blade Passage Frequency.

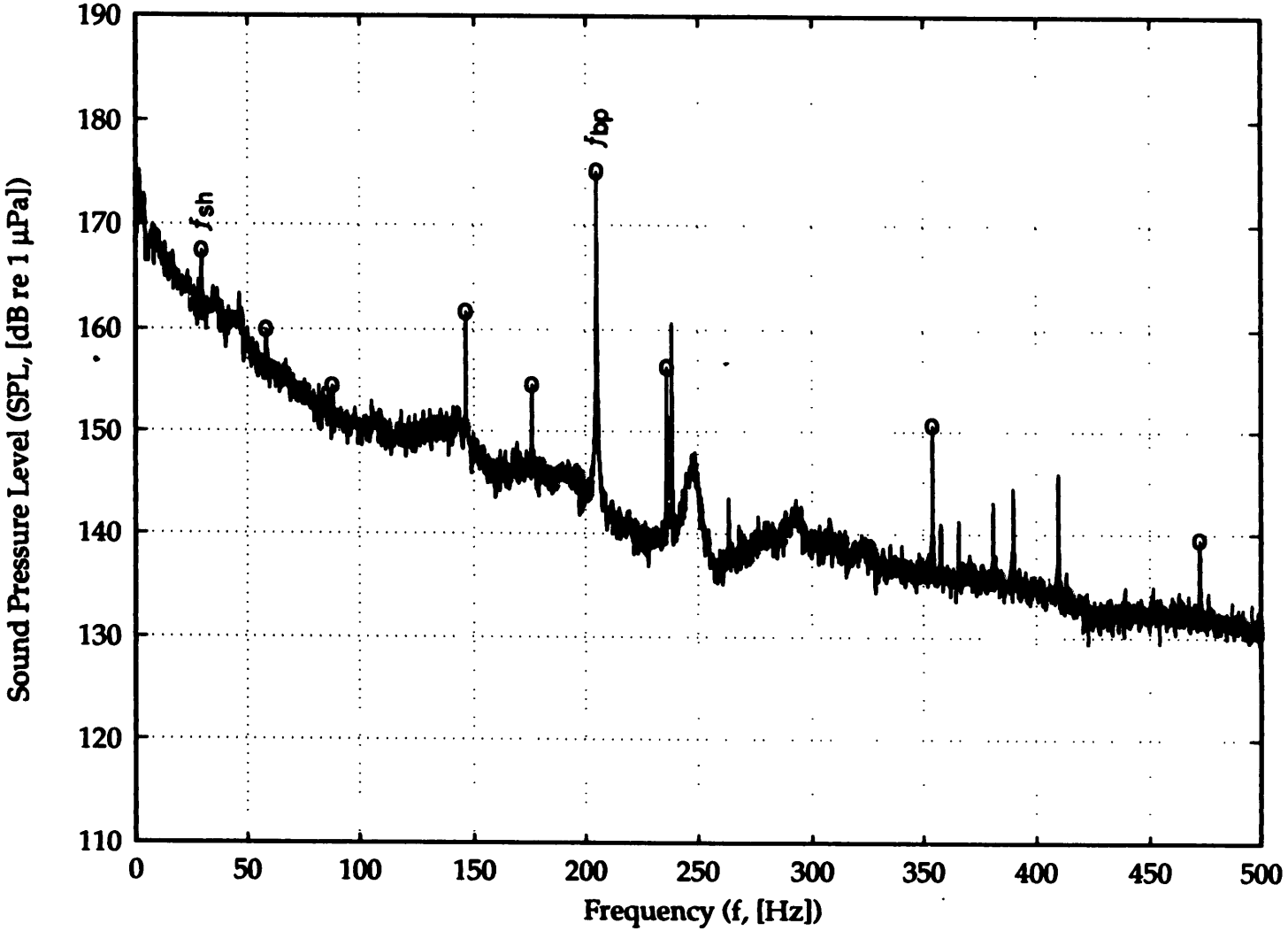

Figure 3.27 Pump Outlet Sound Pressure Level. Uniform Case.
f_{sh} = Shaft Frequency, f_{bp} = Blade Passage Frequency.

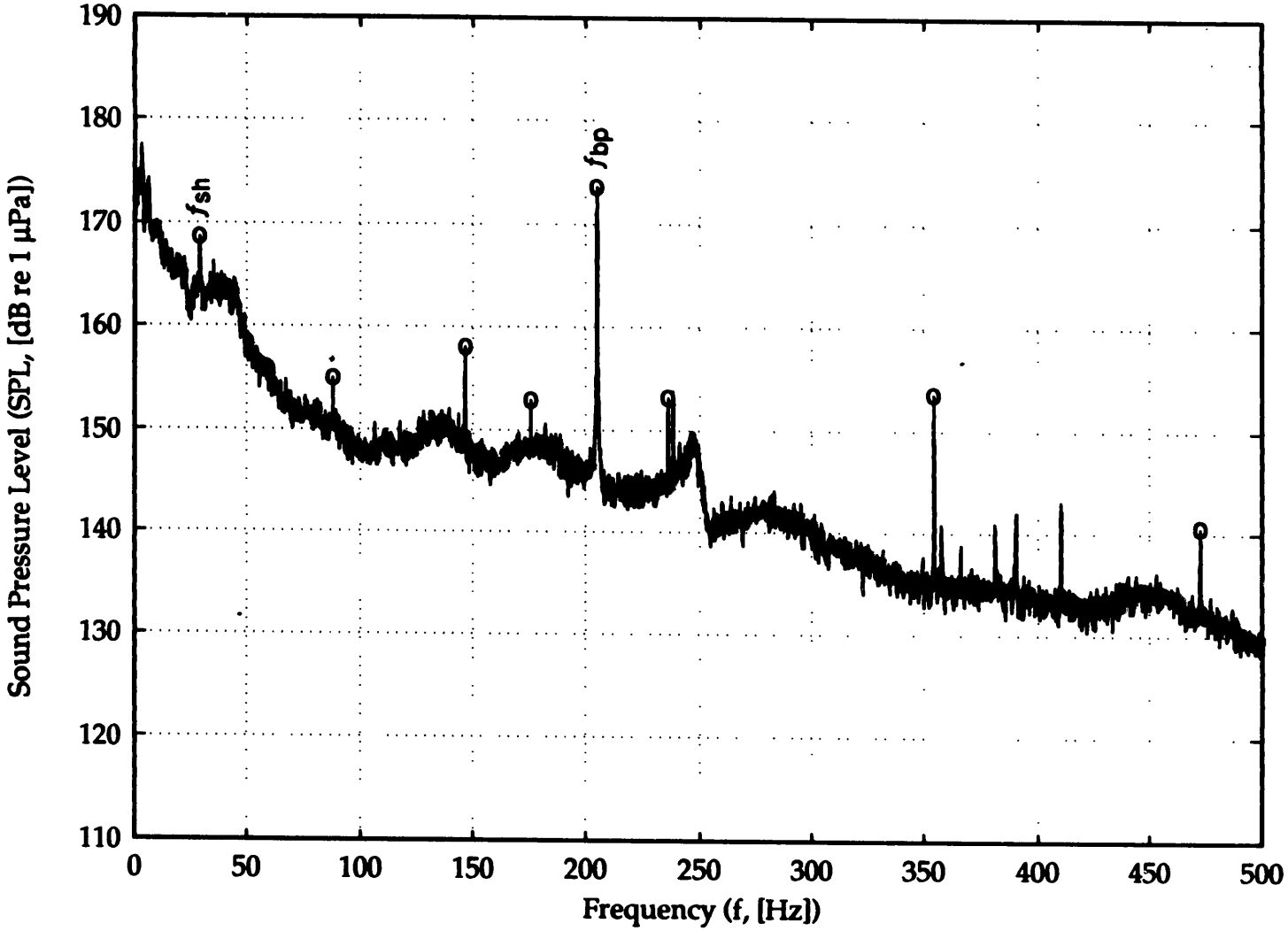

Figure 3.28 Pump Outlet Sound Pressure Level. Orifice Distorted Case. f_{sh} = Shaft Frequency, f_{bp} = Blade Passage Frequency.

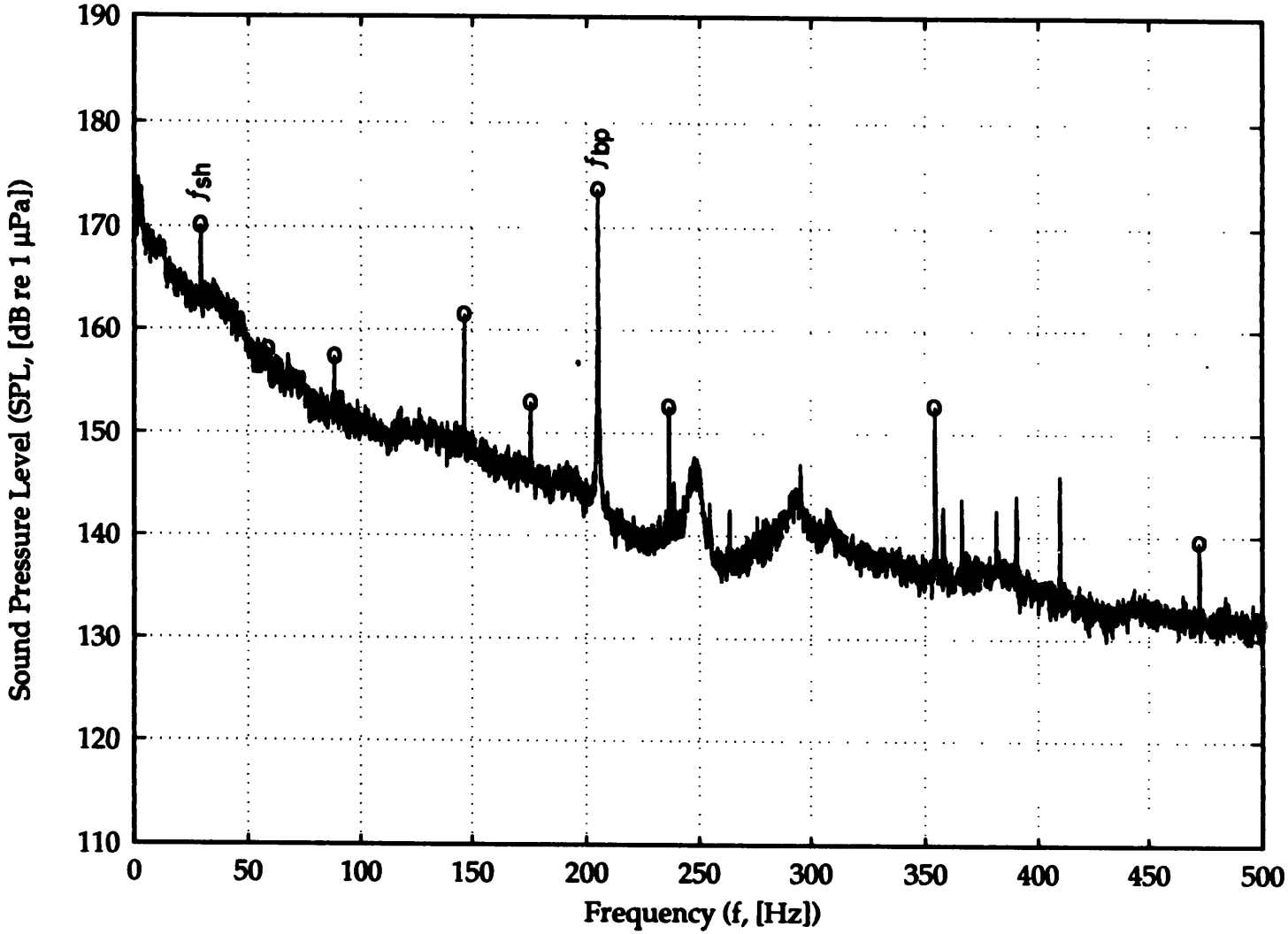

Figure 3.29 Pump Outlet Sound Pressure Level. Elbow Distorted Case. f_{sh} = Shaft Frequency, f_{bp} = Blade Passage Frequency.

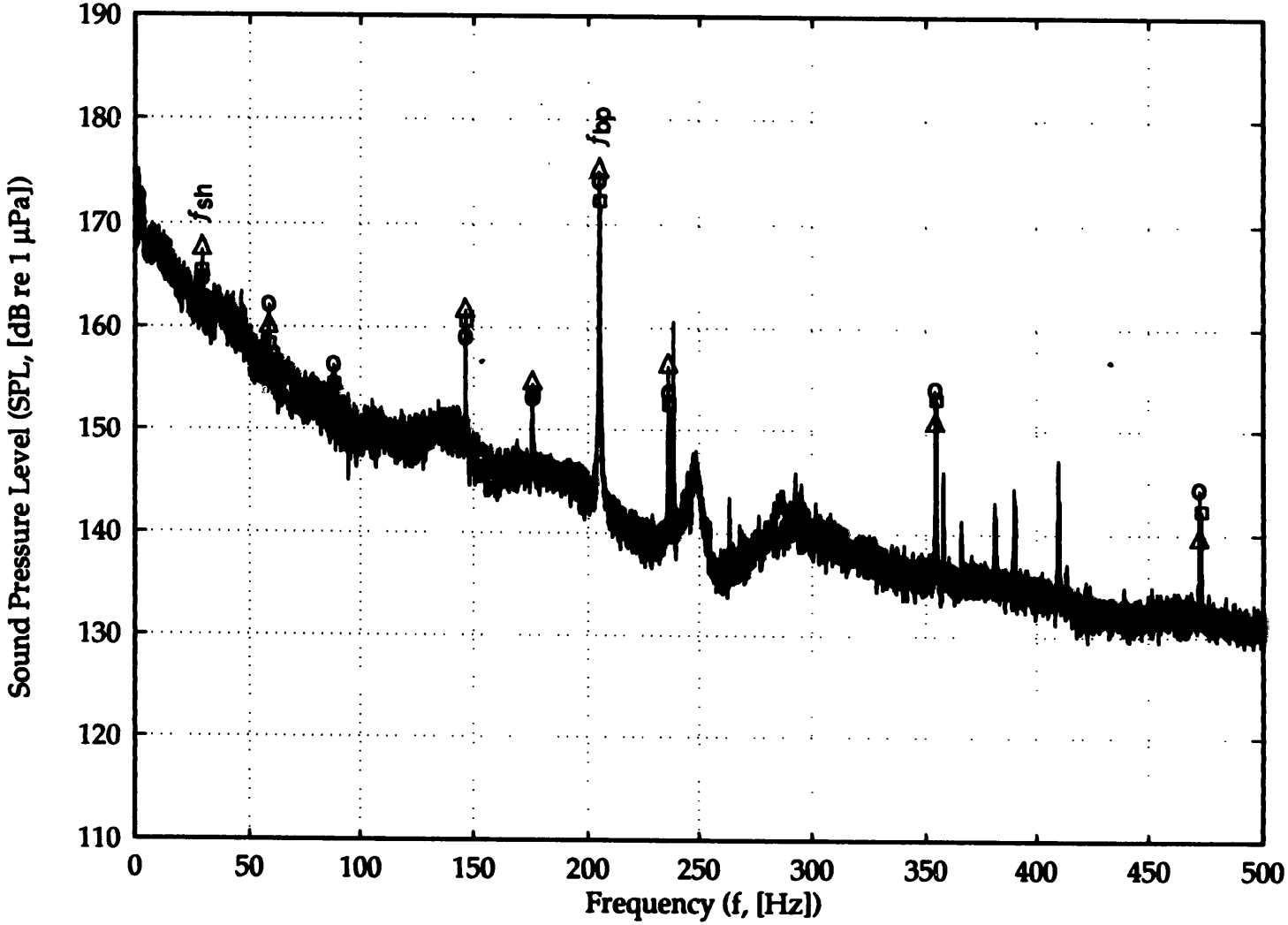

Figure 3.30 Comparison of Outlet SPL Spectra for Fully Developed High Flow, Fully Developed Low Flow, and Uniform Profile Cases. -o- = Fully Developed High; -□- = Fully Developed Low; -△- = Uniform. f_{sh} = Shaft Frequency, f_{bp} = Blade Passage Frequency.

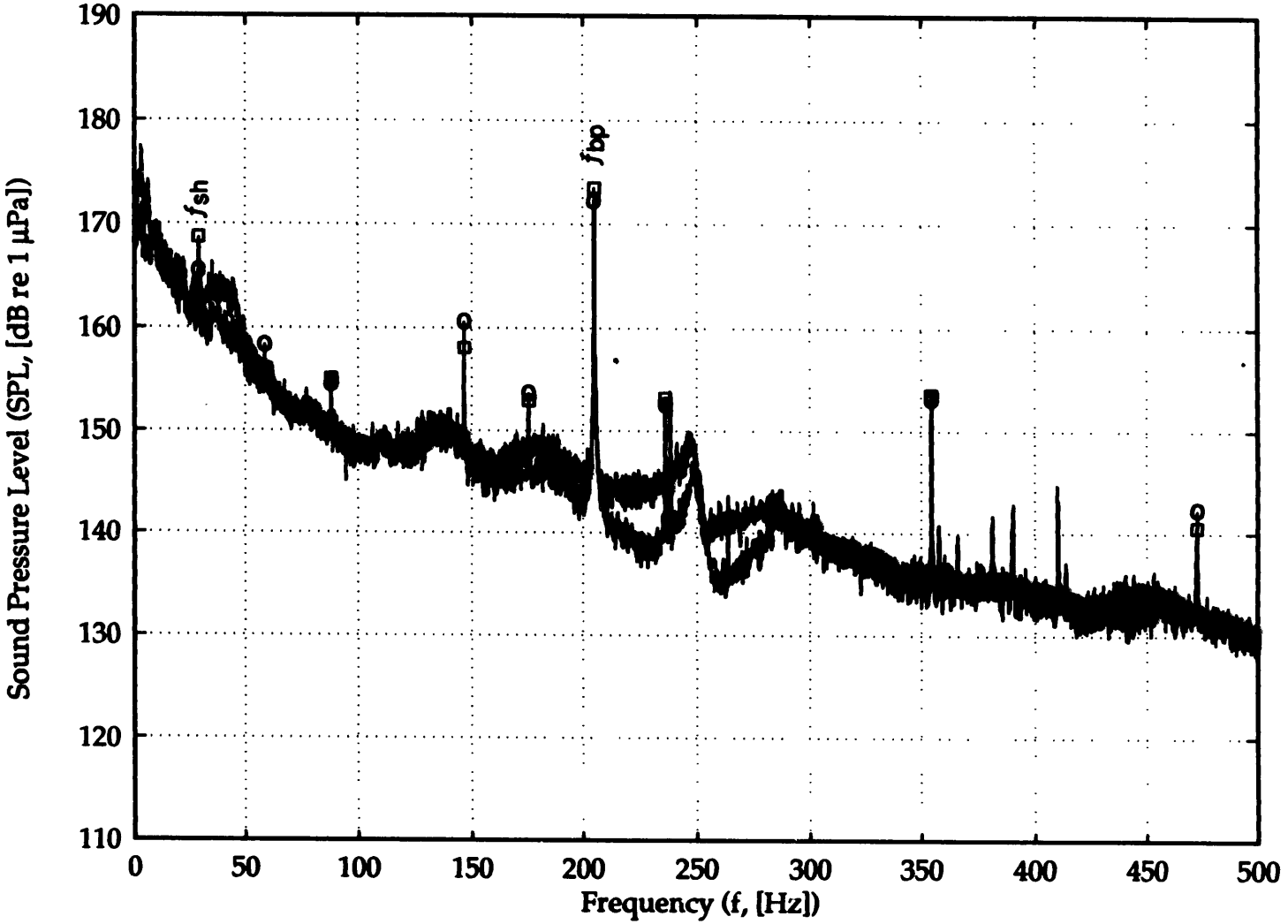

Figure 3.31 Comparison of Outlet SPL Spectra for Fully Developed Low Flow and Orifice Distorted Cases. -o- = Fully Developed Low; -□- = Orifice Distorted. f_{sh} = Shaft Frequency, f_{bp} = Blade Passage Frequency.

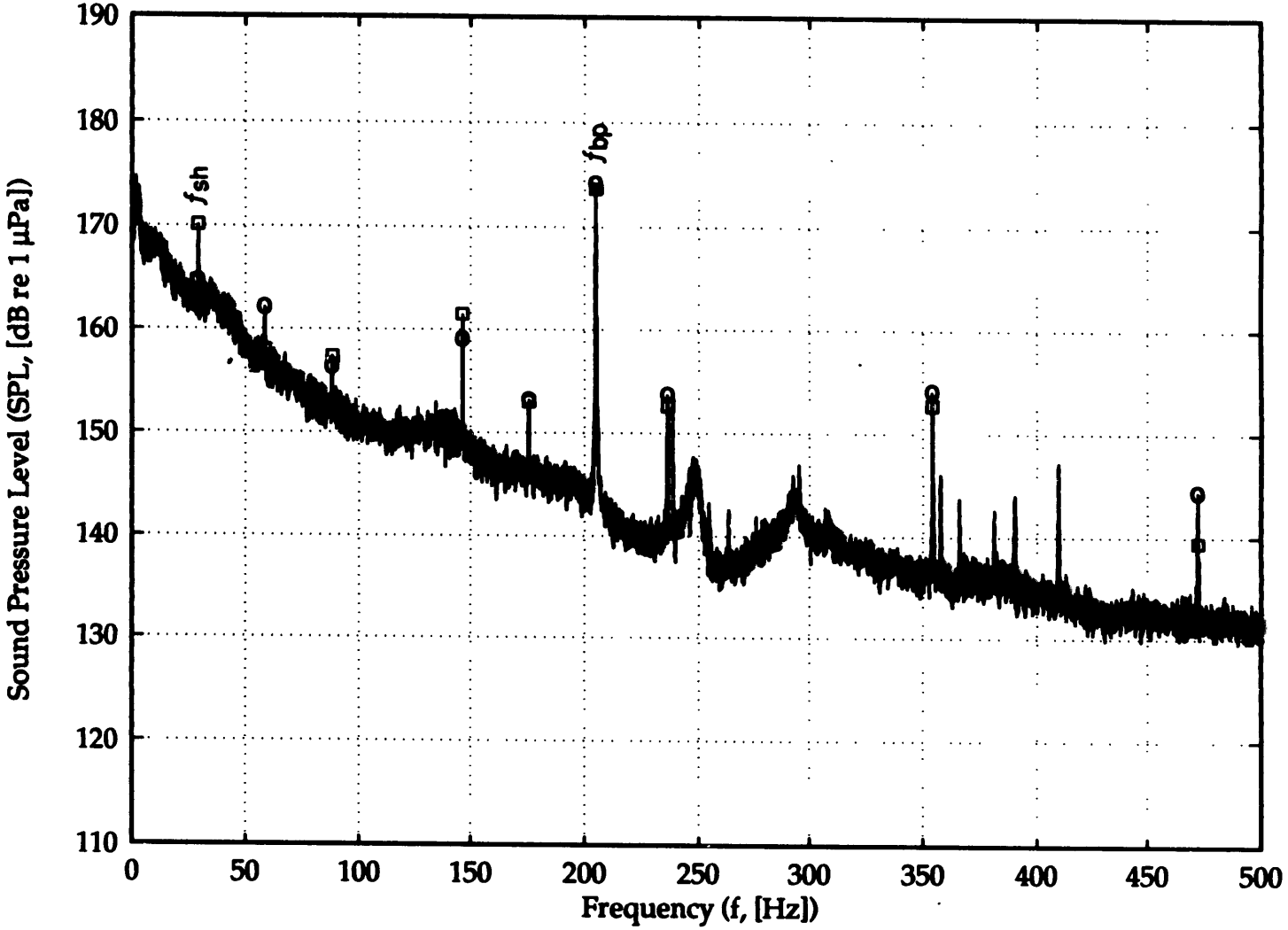

Figure 3.32 Comparison of Outlet SPL Spectra for Fully Developed High Flow and Elbow Distorted Cases. o = Fully Developed High; —⊟— = Elbow Distorted. f_{sh} = Shaft Frequency, f_{bp} = Blade Passage Frequency.

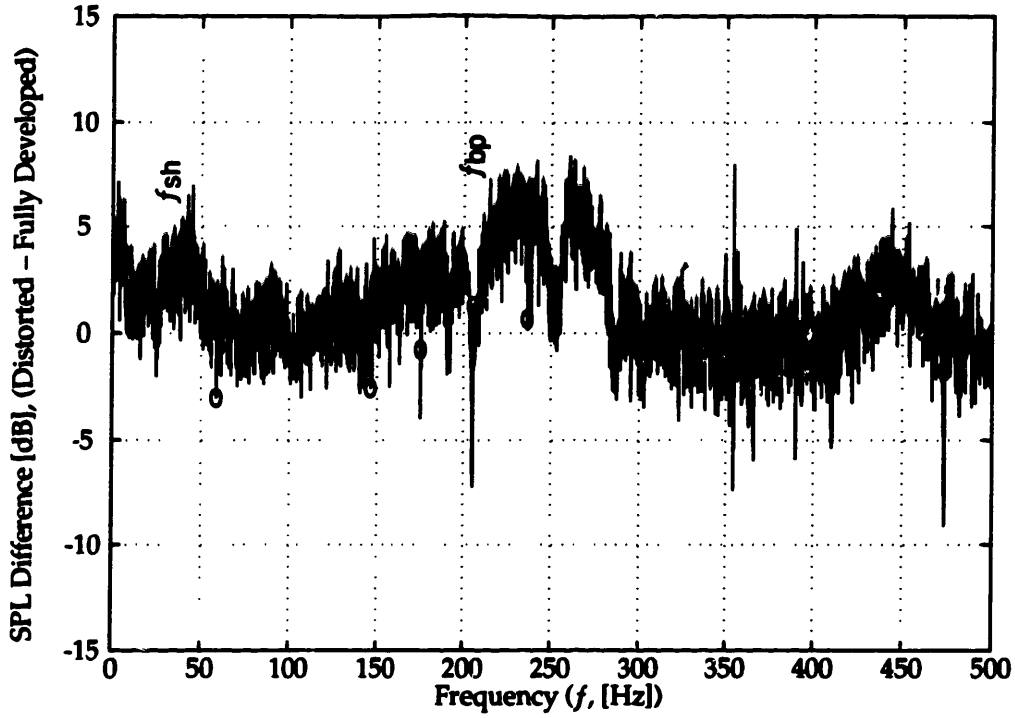

a. Orifice Distorted Case Compared to Fully Developed, Low Case.

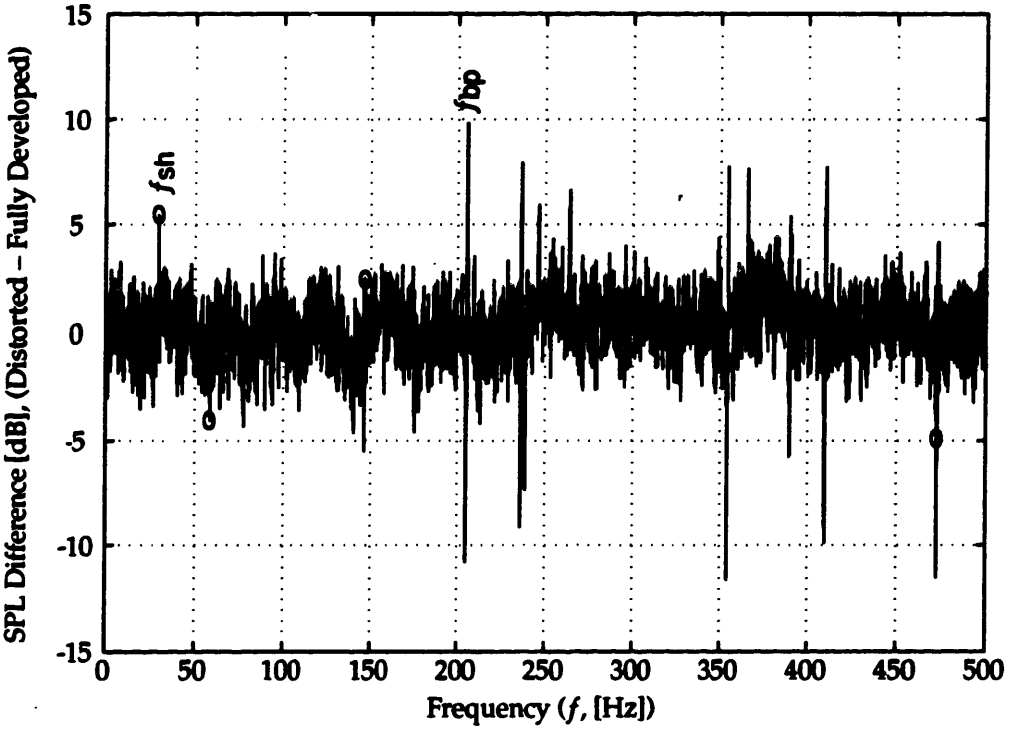

b. Elbow Distorted Case Compared to Fully Developed, High Case.

Figure 3.33 Pump Outlet Sound Pressure Level Difference Between Distorted and Corresponding Fully Developed Cases. f_{sh} = Shaft frequency, f_{bp} = Blade Passage Frequency.

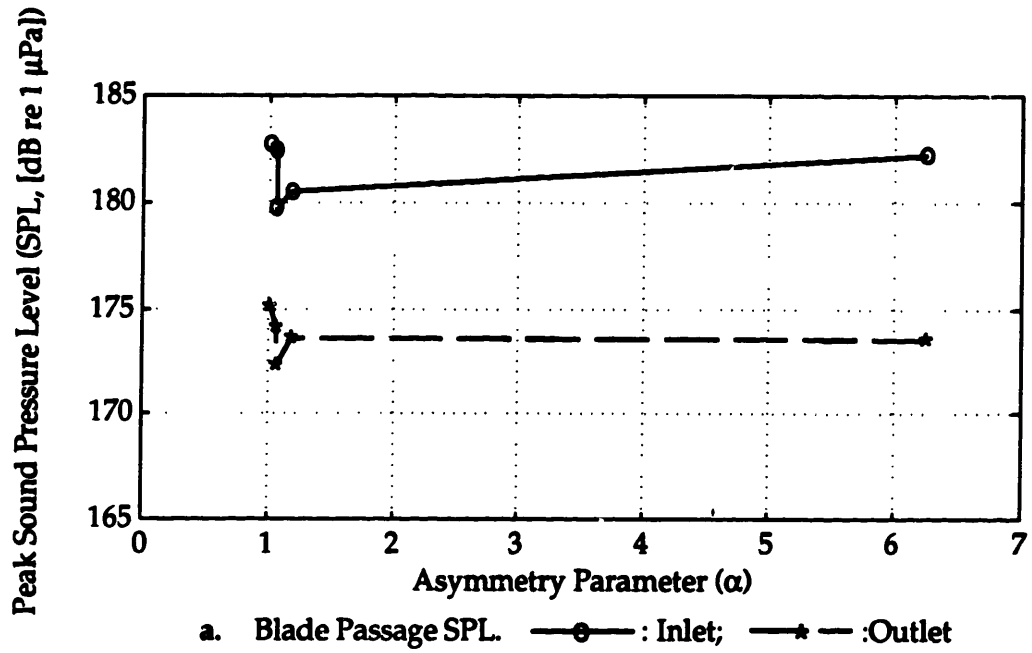

a. Blade Passage SPL. —o— : Inlet; —*— :Outlet

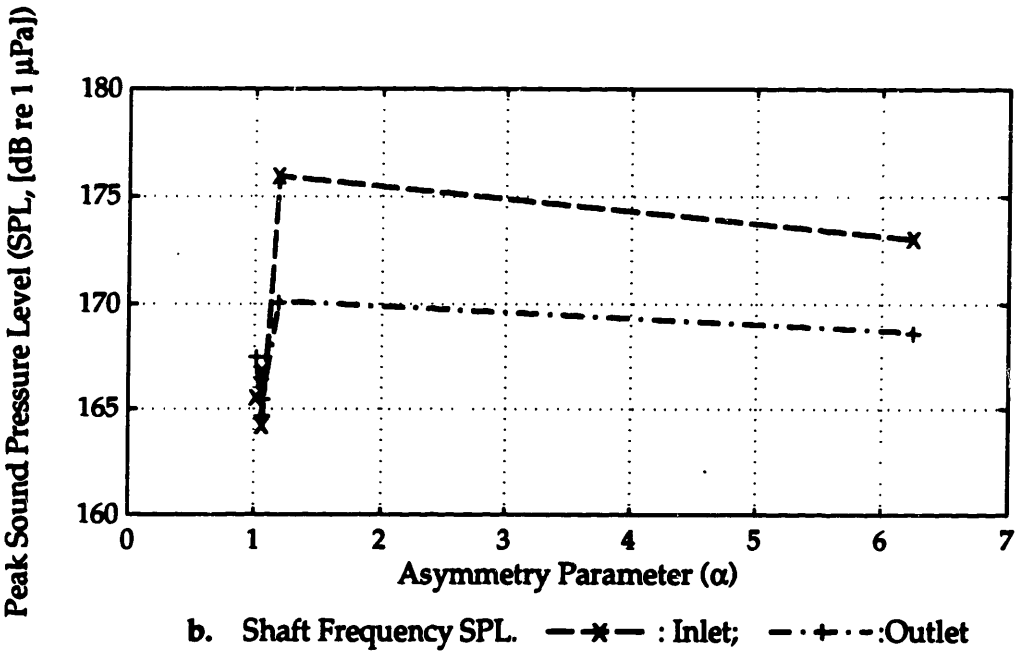

b. Shaft Frequency SPL. —x— : Inlet; —·+·—:Outlet

Figure 3.34 Variation of Inlet and Outlet Sound Pressure Levels at Shaft and Blade Passage Frequencies (f_{sh} & f_{bp}) with the Asymmetry Parameter, α, Defined in Section [2.3.2].

Appendices

A. Derivation of Correction Term for Orifice Distorted Pump Pressure Rise

It was desired to improve the accuracy of pump static pressure rise measurements made when the inlet static pressure tap is near the vena contracta of an upstream thin plate orifice. This arrangement is problematic in that the static pressure over the duct cross section at the plane of the vena contracta is lowered by the high dynamic pressure of the core flow. The outlet pressure tap, in contrast, is placed at a location where the flow is relatively uniform, and the difference between measurements at these two locations will significantly overestimate the pressure rise across the pump.

In order to make a proper correction, it is necessary then to obtain the difference between the inlet and outlet static pressure where the velocity profile at both locations are similar. The approach taken here was to calculate the pressure drop across the orifice, as would be measured in two cases- with the downstream tap at first the vena contracta location and then a far-downstream location, where the irrecoverable pressure drop due to the orifice could be measured. The difference between these two pressure drops, which depends on flow rate, is the desired correction term. For purposes of approximation, viscous losses in the ducts are neglected.

Figure A.1 shows the approach schematically. The desired pump pressure rise, Δp_d, shown in Figure A.1b, can be obtained by subtracting from the experimentally determined pump pressure rise, Δp_e, shown in Figure A.1a, the correction term Δp_c of Figure A.1c. But $\Delta p_c = \Delta p_v - \Delta p_f$, the difference in pressure drop across the orifice as measured at the two locations, where $\Delta p_v > \Delta p_f$, due to the high dynamic pressure at the vena contracta. Therefore, the desired value of pump pressure rise can be found by

$$\Delta p_d = \Delta p_e - (\Delta p_v - \Delta p_f) \qquad [A.1]$$

and it was necessary only to estimate Δp_v and Δp_f over the relevant range of flow rate and to subtract their difference from the experimental measurements. Reference 22 was used to estimate these values, with a simplifying assumption that for the eccentric orifice is equivalent to that of a symmetric orifice of identical geometry. The reader is referred to that source for the method of calculation. Results are presented in Figure 2.18.

B. Attenuation of Noise in a Cylindrical Duct with Compliant Walls

The following is a discussion of the influence of wall compliance on the propagation of sound within a cylindrical duct. The original analysis was performed by Ingard[15], whose work is summarized here.

For present purposes, it is assumed that the frequencies of interest are low compared to the fundamental circumferential mode of the duct, defined below, and are below the cutoff frequency of the first higher order acoustic mode, defined by $\lambda \approx 1.7D$, where λ is the acoustic wavelength and D is the duct diameter. The first condition allows the duct wall to be treated as locally reacting, meaning that its response to the acoustic field in the contained fluid is a radial displacement of the wall which depends only on the local sound pressure. The second condition allows only planar acoustic waves to propagate in the duct, so that the sound pressure amplitude is approximately constant across the duct cross section, and is dependent only on axial position.

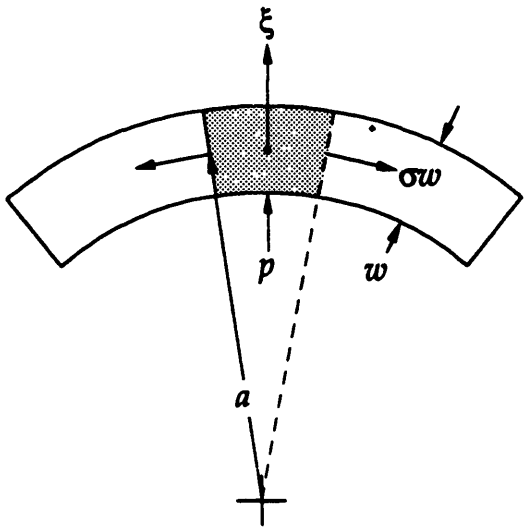

Figure B.1 Duct Wall Model for Calculation of Wall Impedance

The stress in the duct wall, σ, can be defined as

$$\sigma = E(\xi/a) \qquad [B.1]$$

where E is the elastic modulus, a the radius of the duct, and ξ the induced radial displacement. This relation is true for $w << a$, where w is the duct wall thickness, as shown in Figure B.1 above.

If the mass density of the duct material is denoted by ρ_1, then the mass per unit area of the wall is $m = \rho_1 w$, and the equation of motion of an element of the duct wall, as modeled in Figure B.1, can be written

$$m \frac{\partial^2 \xi}{\partial t^2} = -Ew\xi/a + pa \qquad [B.2]$$

where the external radiation load on the duct has been neglected.

Considering harmonic time dependence and substituting the complex amplitudes $\xi(\omega)$, $p(\omega)$ and the velocity amplitude of the wall $u_1 = -i\omega\xi$, the wall admittance can be found from Equation B.2 to be

$$Y \equiv \frac{u(\omega)}{p(\omega)} = \frac{i}{\omega m} \frac{\omega^2}{\omega^2 - \omega_0^2} \qquad [B.3]$$

where ω_0 is the resonance, or *ring frequency* of the pipe

$$f_0 = \frac{\omega_0}{2\pi} = \frac{1}{2\pi a}\sqrt{\frac{E}{\rho_1}} = \frac{c_1}{2\pi a} \qquad [B.4]$$

and c_1 is the longitudinal wave speed of the wall material. For 4 in. stainless steel pipe, f_0 = 7.24 kHz; for 4 in. rubber hose f_0 = 1.43 kHz. The admittance can be normalized by $1/\rho_0 c_0$, where c_0 is the free sound speed in the fluid, and by substituting $\omega_0^2 = c_1^2/a^2$, $m = \rho_1 w$, and $k_0 = \omega/c_0$, the normalized admittance $\eta = Y\rho_0 c_0$ can be written

$$\eta = -i\frac{a}{w} k_0 a \frac{\rho_0 c_0^2}{\rho_1 c_1^2} \frac{1}{1 - \omega^2/\omega_0^2} \qquad [B.5]$$

To obtain an expression for the propagation of sound in the compliant duct, the linearized form of the continuity equation may be used

$$\frac{\partial \rho}{dt} + \rho_o \, \mathrm{div} u + U \, \mathrm{div} \rho = 0 \qquad \text{[B.6]}$$

where ρ is the fluid density, ρ_o the unperturbed density, u the acoustic velocity perturbation, and U the mean flow velocity. For low flow Mach number, the third term is small and may be neglected. Substituting the equation of state

$$\frac{1}{\rho}\frac{\partial \rho}{dt} = \kappa \frac{\partial p}{dt} \qquad \text{[B.7]}$$

where κ is the compressibility of the fluid, and introducing harmonic time dependence, continuity becomes

$$-i\omega\kappa p + \mathrm{div} u = 0 \qquad \text{[B.8]}$$

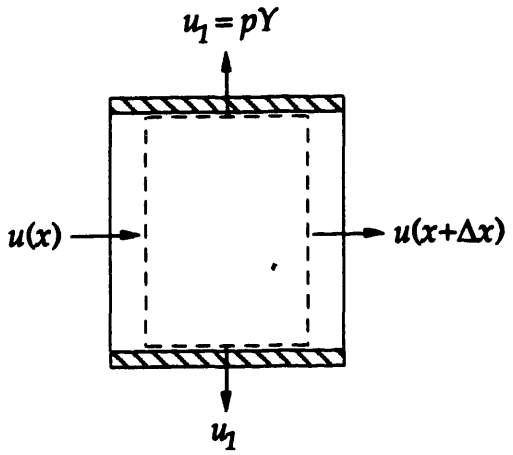

Figure B.2 Control Volume for Derivation of the Propagation Constant

Integration over the control volume of Figure B.2, using $A=\pi a^2$, and substitution of Equation. B.5 yields

$$-i\omega\kappa A p + 2\pi a p Y + A\frac{\partial u}{\partial x} = 0 \qquad \text{[B.9]}$$

which can be simplified to

$$-i\omega\kappa_e p = -\frac{\partial u}{\partial x} \qquad \text{[B.10]}$$

where κ_e, the equivalent compressibility in the presence of the duct wall, is

$$\kappa_e = \kappa(1+i2Y/aw\kappa) = k\left(1+\frac{i2\eta}{k_o a}\right) \qquad [B.11]$$

where $k_o = \omega/c_o$ and the normalized admittance $\eta = Y \rho_o c_o$.

Along with the momentum equation, which in harmonic terms is written

$$-i\omega\rho_o u = -\frac{\partial p}{\partial x} \qquad [B.12]$$

the wave equation is obtained

$$\frac{\partial^2 p}{\partial x^2} + k^2 p = 0 \qquad [B.13]$$

where the propagation constant, k, is

$$k = k_o\sqrt{1+\frac{i2\eta}{k_o a}} = k_o\sqrt{1+\frac{d}{w}\frac{\rho_o c_o}{\rho_1^2 c_1^2}\frac{1}{\left(1-\omega^2/\omega_0^2\right)}}$$

$$\approx k_o\sqrt{1+\frac{d}{w}\frac{\rho_o c_o}{\rho_1^2 c_1^2}} \quad (\omega << \omega_o) \qquad [B.14]$$

where $d = 2a$.. If the internal energy dissipation of the wall material is included in the preceding analysis, it can be accounted for by considering E, the elastic modulus, to be complex, which can be expressed as

$$\tilde{E} = E(1 - i\varepsilon) \qquad [B.15]$$

where ε is the *loss factor* of the wall material. To account for energy dissipation in the expression for the propagation constant, k, it is necessary to replace c_1^2 in equation B.5 by $c_1^2(1\text{-}i\varepsilon)$ which yields

$$k = k_r + ik_i \approx k_o\sqrt{1+\frac{\chi}{1-i\varepsilon}} \qquad [B.16]$$

where χ, the compliance ratio of the fluid and the duct wall is

$$\chi = \frac{d}{w}\frac{\rho_o c_o^2}{\rho_1 c_1^2} \qquad [B.17]$$

The decay in sound pressure amplitude as acoustic waves travel a distance x through the duct is found by $p \propto \exp(-ikx)$ and the transmission loss in dB per unit wavelength is

$$TL\,(\mathrm{dB}/\lambda) = 20\,(2\pi)\log_{10}(e)\frac{k_i}{k_o} \approx 54.7\frac{k_i}{k_o} \qquad [B.18]$$

and the speed of sound in the contained fluid is given by

$$\frac{c}{c_o} = \frac{k_o}{k_r} \qquad [B.19]$$

Sound speed and transmission loss per wavelength are plotted in Figures B.3 and B.4. For four inch i.d. stainless steel pipe of wall thickness w = 0.5 inches, c_1 = 4912 m/s, $\rho_1 \approx 8000$ kg/m^3. These values yield $\chi \approx 0.210$, and ε is small, probably less that 0.01. It can be found from the relations above that $c \approx .911c_o$, and transmission loss, TL = .052 dB/λ.

For the four inch i.d. rubber hose, it was necessary to estimate the elastic modulus of the hose using the reflection coefficient measured at the steel-rubber boundary, which at blade passage frequency was $|R| \approx 0.5$. A general relation for reflection of a wave at normal incidence to an impedance boundary is

$$|R| = \left|\frac{\rho_a c_a - \rho_b c_b}{\rho_a c_a + \rho_b c_b}\right| = \left|\frac{c_a - c_b}{c_a + c_b}\right| \quad (\rho_a = \rho_b) \qquad [B.20]$$

where the subscripts a and b refer to the initial and secondary medium, respectively. In the present case, the initial medium was the stainless steel pipe, and the secondary medium was the rubber hose. For $|R| \approx 0.5$ and $c_a \approx .911c_o$ in the steel pipe, Equation B.19 gives $c_b \approx .297c_o$ for the rubber hose, and if w = .688, then χ = 10.326. Comparison of Equation B.18 to the measured transmission loss of 42.17 dB presented in Section 3.4.6 gives a value for the loss factor of ε = .1215, which is high but realistic. The transmission loss relation for the values of χ and ε given above is compared to experimental results in Figure 2.35.

C. Uncertainty and Repeatability Analyses

It was desired to estimate the measurement uncertainty for two quantities of interest- the sound pressure level, *SPL*, measured by the hydrophones, and the local steady-state axial velocity, u, as determined by Pitot-static probe measurements. The approach taken in estimating these uncertainties, and the results obtained, are presented in the following paragraphs.

For both uncertainty estimates, the Kline-McClintock[23] method was applied, in which the uncertainty of a derived quantity of interest, which is a function of N measured quantities, is related to the uncertainty of the raw measurements by

$$\omega_q = \sqrt{\sum_{n=1}^{N} \left[\frac{\partial q}{\partial x_n} \omega_n \right]^2} \qquad [C.1]$$

where q is the derived quantity, ω_q is its uncertainty, x_n is the n^{th} measured quantity, and ω_n is its uncertainty. The differential $\partial q / \partial x_n$ is evaluated at a representative value of x_n.

C.1 Acoustic Pressure Uncertainty

Sources of uncertainty in measurement of the sound pressure level, *SPL*, are listed in table C.1 below, along with typical values and estimated uncertainties. The resulting SPL uncertainty was obtained by applying Equation C.1 to the definition of sound pressure level given in Equation 2.1.

The first five source quantities signify direct acoustic measurement uncertainty, and the sound pressure varies linearly with these terms. The statistics for these quantities were therefore converted into equivalent pressure units in order to evaluate their influence on that of the sound pressure level. The derivative in Equation C.1 was considered to be $\partial(\text{SPL})/\partial p$, where the equivalent pressure, p^2, was substituted for $\overline{p_{xx}}$ in Equation 2.1.

Table C.1 Estimate of Sound Pressure Level Uncertainty

Source of Uncertainty	Units	Typical Value	Estimated Uncertainty (ω,units)	Resulting *SPL* Uncertainty (ω_s, [dB])
Hydrophone Output	[mV]	44.1465	.03089	6.079E-3
Amplifier Output	[mV]	1324.4	1.324E+1	8.687E-2
Analog Filter Output	[mV]	1324.4	3.052E+0	2.002E-2
A/D Output	[mV]	1324.4	3.000E+0	1.968E-2
A/D Discretization	[bits]	271.236	5000E+1	1.601E-2
DFT Bias	[dB]	180	3.922E+0	3.922E+0
DFT Random Error	[dB]	180	0.8042	8.042E-1
Electrical Noise	[dB]	180	.2791	2.791E-1
Sampling Frequency	[Hz]	5000	20	1.737E-2
Total Uncertainty				4.015

DFT bias is the inherent error incurred by discretization of a continuous spectrum. If a pure tone, for example, occurs at a frequency between the two nearest spectral lines in the DFT discrete spectrum, the transform approximates that tone by redistributing its energy to the two nearest spectral lines, and error is incurred. It can by shown by applying the definition of the digital Fourier transform to a pure tone that the bias, ω_b, due to discretization of the frequency spectrum is independent of frequency and is given by:

$$\omega_b\,[\mathrm{dB}] = 20\log_{10}\left|\frac{1}{2\pi\varepsilon_f}\left[\sin(2\pi\varepsilon_f) + i\left(\cos(2\pi\varepsilon_f) - 1\right)\right]\right| \qquad [C.2]$$

where ε_f is the frequency error normalized by the bandwidth Δf. The maximum possible frequency error ε is 0.5, and the corresponding maximum bias in *SPL* is given by Equation C.2 to be 3.922 dB.

DFT random error, due to finite averaging of a signal with random components, can be found from Bendat and Piersol[10] to be

$$\omega_r\,[\mathrm{dB}] = -10\log_{10}\left(1 - \frac{1}{n_d}\right) \qquad [C.3]$$

where n_d is the number of data sets averaged, and the randomness is assumed to be white noise. In the present case $n_d = 35$, so that $\omega_r = .8042$ dB. Figure C.1 shows the effect of averaging on a SPL estimation. Figure C.1a

shows a spectrum resulting from the Fourier transform of a single data set. Figure C.1b shows the averaged spectrum of 35 data sets. Notable differences are the increased resolution of harmonic peaks, and the reduced variation of noise floor levels in the averaged spectrum.

Another source of measurement error in the SPL was electrical background noise due to ground loops. The pump casing was grounded for safety, and all hydrophones, the electronics of which were not isolated from their casing, were grounded to the pump by electrical conduction through the water. It was found that this grounding had a direct effect on background electrical noise levels. Figure C.2 compares a plot of the typical background noise spectrum, shown as Equivalent sound pressure level, to the typical pump inlet spectrum. The most prominent peak is at 8 Hz, and the level at that frequency is 29 dB lower than corresponding levels in the main spectrum. All other background levels are similarly low.

Sound Pressure Level is dependent on sampling frequency due to normalization by the bandwidth, $\Delta f = f_s / N$, where f_s is the sampling frequency and N is the sample length. The derivative in Equation C.1 is then given by $\partial(\text{SPL})/\partial(f_s) = \partial(\text{SPL})/\partial(\Delta f)/N$. The 0.4% error in sampling frequency is due primarily to rounding error in the data acquisition software.

The resulting total uncertainty of 4.015 is dominated by bias. Because of the small bandwidth $\Delta f = .1526$ Hz used, small changes in signal or sampling frequency can have large effects on the resulting peak level. The best way to avoid such error is to strive for extremely stable signal and sampling frequencies, and conduct extensive calibration procedures, such as those suggested by Burgess[24].

C.2 Local Steady-State Axial Velocity Uncertainty

The analysis of axial velocity uncertainty was approached in the same manner as for sound pressure level. Table C.2 gives the significant sources of error in dynamic pressure as measured by the Pitot-static probe and differential pressure transducer. Local steady-state axial velocity was calculated by Equation 2.5., and this equation was used to obtain the differentials necessary to apply Equation C.1 to estimate uncertainty. As was the case with sound pressure level, the quantities listed in Table C.2 signify direct pressure measurement uncertainty, and so the statistics for these

quantities were therefore converted into equivalent pressure units in order to evaluate their influence on velocity uncertainty.

Table C.2 Sources of Local Axial Velocity Uncertainty

Source of Uncertainty	Estimated Dynamic Pressure Uncertainty (ω_q, [% Full Scale])
Transducer Output	Range Dependent (see Table C.3, col. 2)
Amplifier Output	0.01
A/D Output	0.03
A/D Discretization	0.09766

The transducer output scale and uncertainty, which depended on the diaphragm used for a given profile case, is listed in Table C.2. As stated in Section 2.2.3, the 0.8 psid diaphragm was calibrated with a 1% full scale error compared to the other diaphragms. Because confidence in the calibration method used for the 20 psid and 1 psid diaphragms was higher than for the 0.8 psid calibration, it was decided to assign the full 1% error to the uncertainty of that diaphragm.

Table C.2 shows the total estimated uncertainty in axial velocity for the five profile cases considered, normalized by the Pitot-averaged mean velocity. It can be seen that the uncertainty for all profiles measured with the 0.8 psid diaphragm approached 1%, while that Elbow Distorted case was found to be less than 0.3%. This comparison shows that the effect of the 1% calibration error was to increase uncertainty in the velocity measurements by about 0.5%.

The Orifice Distorted case resulted in higher uncertainty, mostly due to the high ratio of maximum measured pressure to the Pitot-averaged mean. A higher range diaphragm was necessary to measure the maxima, which resulted in higher uncertainty for all measurements.

Table C.3 Local Axial Velocity Uncertainty for Each Inlet Profile Case

Inlet Profile	Full Scale Dynamic Pressure [psid]	Transducer Uncertainty [% F.S.]	Pitot Avg. Mean Velocity ($\bar{u}$, [m/s])	Axial Velocity Uncertainty [$\%\bar{u}$]
Fully Developed, High	0.8	1.031	2.707	0.7797
Fully Developed, Low	0.8	1.031	2.515	0.9033
Uniform	0.8	1.031	2.682	0.7943
Orifice Distorted	20	0.25	4.18	2.1329
Elbow Distorted	1	0.25	2.641	0.2671

Uncertainties estimated here for steady-state, local, axial velocity remain below 1% for the more conventional inlet profiles, and are kept small even for the extreme case of Orifice Distortion. It should be noted here that the estimates presented here account for uncertainty in the measurement system only, and do not account for the effect of extraneous flow phenomena or unsteadiness. In cases where distortion existed, these effects may have been significant.

C.3 Local Axial Velocity Repeatability

As mentioned is Section 2.5, a set of 13 local velocity measurements were repeated for every profile considered in order to assess repeatability of the data. Figure C.4, next page, gives the root mean square deviation of the 13 measurements from the previously measured values, normalized by the standard deviation in the measurements made at that grid point. It can be seen that the measurements for all profiles were, on average, repeatable to within one standard deviation. The normalized r.m.s. deviation for the uniform case was highest, primarily because standard deviations for that case were relatively low. The opposite is true for the orifice case, for which standard deviations were high.

Figure C.4 Axial Velocity Repeatability

Inlet Profile	R.M.S. Repeatability Deviation (Normalized by Std. Dev.)
Fully Developed, High	0.3709
Fully Developed, Low	0.9810
Uniform	0.9965
Orifice Distorted	0.1818
Elbow Distorted	0.1555

D. Velocity Profile Data

Table D.1 Traverser Grid Coordinates

Node Number	Radial Position [in]	Angular Position (θ, [deg])	Angular Position (θ, [rad])	X coordinate (+ ‖ θ = 0°) [in]	Y coordinate (- ‖ θ = 90°) [in]
1	0	0	0	0	0
2	0.218	0	0	0.218	0
3	0.218	-60	1.047	0.109	-0.189
4	0.218	-120	2.094	-0.109	-0.189
5	0.218	-180	3.142	-0.218	0
6	0.218	-240	4.189	-0.109	0.189
7	0.218	-300	5.236	0.109	0.189
8	0.437	0	0	0.437	0
9	0.437	-40	0.698	0.335	-0.281
10	0.437	-80	1.396	0.076	-0.43
11	0.437	-120	2.094	-0.219	-0.378
12	0.437	-160	2.793	-0.411	-0.149
13	0.437	-200	3.491	-0.411	0.149
14	0.437	-240	4.189	-0.218	0.378
15	0.437	-280	4.887	0.076	0.43
16	0.437	-320	5.585	0.335	0.281
17	0.655	0	0	0.655	0
18	0.655	-23	0.393	0.605	-0.251
19	0.655	-45	0.785	0.463	-0.463
20	0.655	-68	1.178	0.251	-0.605
21	0.655	-90	1.571	0	-0.655
22	0.655	-113	1.964	-0.251	-0.605
23	0.655	-135	2.356	-0.463	-0.463
24	0.655	-158	2.749	-0.605	-0.251
25	0.655	-180	3.142	-0.655	0
26	0.655	-203	3.534	-0.605	0.251
27	0.655	-225	3.927	-0.463	0.463
28	0.655	-248	4.32	-0.251	0.605
29	0.655	-270	4.712	0	0.655
30	0.655	-293	5.105	0.251	0.605
31	0.655	-315	5.498	0.463	0.463
32	0.655	-338	5.891	0.605	0.251
33	0.873	0	0	0.873	0
34	0.873	-16	0.286	0.838	-0.246
35	0.873	-33	0.571	0.734	-0.472
36	0.873	-49	0.857	0.572	-0.66
37	0.873	-65	1.142	0.363	-0.794

Table D.1 Traverser Grid Coordinates (cont.)

Node Number	Radial Position [in]	Angular Position (θ, [deg])	Angular Position (θ, [rad])	X coordinate (+ ‖ θ = 0°) [in]	Y coordinate (– ‖ θ = 90°) [in]
38	0.873	-82	1.428	0.124	-0.864
39	0.873	-98	1.714	-0.124	-0.864
40	0.873	-115	1.999	-0.363	-0.794
41	0.873	-131	2.285	-0.572	-0.66
42	0.873	-147	2.57	-0.734	-0.472
43	0.873	-164	2.856	-0.838	-0.246
44	0.873	-180	3.142	-0.873	0
45	0.873	-196	3.427	-0.838	0.246
46	0.873	-213	3.713	-0.734	0.472
47	0.873	-229	3.998	-0.572	0.66
48	0.873	-245	4.284	-0.363	0.794
49	0.873	-262	4.57	-0.124	0.864
50	0.873	-278	4.855	0.124	0.864
51	0.873	-295	5.141	0.363	0.794
52	0.873	-311	5.426	0.572	0.66
53	0.873	-327	5.712	0.734	0.472
54	0.873	-344	5.998	0.838	0.246
55	1.092	0	0	1.092	0
56	1.092	-13	0.224	1.065	-0.243
57	1.092	-26	0.449	0.984	-0.474
58	1.092	-39	0.673	0.854	-0.681
59	1.092	-51	0.898	0.681	-0.854
60	1.092	-64	1.122	0.474	-0.984
61	1.092	-77	1.346	0.243	-1.065
62	1.092	-90	1.571	0	-1.092
63	1.092	-103	1.795	-0.243	-1.065
64	1.092	-116	2.02	-0.474	-0.984
65	1.092	-129	2.244	-0.681	-0.854
66	1.092	-141	2.468	-0.854	-0.681
67	1.092	-154	2.693	-0.984	-0.474
68	1.092	-167	2.917	-1.065	-0.243
69	1.092	-180	3.142	-1.092	0
70	1.092	-193	3.366	-1.065	0.243
71	1.092	-206	3.59	-0.984	0.474
72	1.092	-219	3.815	-0.854	0.681
73	1.092	-231	4.039	-0.681	0.854
74	1.092	-244	4.264	-0.474	0.984
75	1.092	-257	4.488	-0.243	1.065
76	1.092	-270	4.712	0	1.092
77	1.092	-283	4.937	0.243	1.065
78	1.092	-296	5.161	0.474	0.984
79	1.092	-309	5.386	0.681	0.854

Table D.1 Traverser Grid Coordinates (cont.)

Node Number	Radial Position [in]	Angular Position (θ, [deg])	Angular Position (θ, [rad])	X coordinate (+ ‖ θ = 0°) [in]	Y coordinate (- ‖ θ = 90°) [in]
80	1.092	-321	5.61	0.854	0.681
81	1.092	-334	5.834	0.984	0.474
82	1.092	-347	6.059	1.065	0.243
83	1.31	0	0	1.31	0
84	1.31	-10	0.18	1.289	-0.234
85	1.31	-21	0.359	1.226	-0.46
86	1.31	-31	0.539	1.125	-0.672
87	1.31	-41	0.718	0.987	-0.862
88	1.31	-51	0.898	0.817	-1.024
89	1.31	-62	1.077	0.621	-1.154
90	1.31	-72	1.257	0.405	-1.246
91	1.31	-82	1.436	0.176	-1.298
92	1.31	-93	1.616	-0.059	-1.309
93	1.31	-103	1.795	-0.292	-1.277
94	1.31	-113	1.975	-0.515	-1.205
95	1.31	-123	2.154	-0.722	-1.093
96	1.31	-134	2.334	-0.905	-0.947
97	1.31	-144	2.513	-1.06	-0.77
98	1.31	-154	2.693	-1.18	-0.568
99	1.31	-165	2.872	-1.263	-0.349
100	1.31	-175	3.052	-1.305	-0.117
101	1.31	-185	3.231	-1.305	0.117
102	1.31	-195	3.411	-1.263	0.349
103	1.31	-206	3.59	-1.18	0.568
104	1.31	-216	3.77	-1.06	0.77
105	1.31	-226	3.949	-0.905	0.947
106	1.31	-237	4.129	-0.722	1.093
107	1.31	-247	4.309	-0.515	1.205
108	1.31	-257	4.488	-0.291	1.277
109	1.31	-267	4.668	-0.059	1.309
110	1.31	-278	4.847	0.176	1.298
111	1.31	-288	5.027	0.405	1.246
112	1.31	-298	5.206	0.621	1.154
113	1.31	-309	5.386	0.817	1.024
114	1.31	-319	5.565	0.987	0.862
115	1.31	-329	5.745	1.125	0.672
116	1.31	-339	5.924	1.226	0.46
117	1.31	-350	6.104	1.289	0.234
118	1.528	0	0	1.528	0
119	1.528	-9	0.153	1.51	-0.233
120	1.528	-18	0.307	1.457	-0.461
121	1.528	-26	0.46	1.369	-0.678

Table D.1 Traverser Grid Coordinates (cont.)

Node Number	Radial Position [in]	Angular Position (θ, [deg])	Angular Position (θ, [rad])	X coordinate (+ ‖ θ = 0°) [in]	Y coordinate (– ‖ θ = 90°) [in]
122	1.528	-35	0.613	1.25	-0.879
123	1.528	-44	0.766	1.101	-1.06
124	1.528	-53	0.92	0.926	-1.215
125	1.528	-61	1.073	0.73	-1.342
126	1.528	-70	1.226	0.516	-1.438
127	1.528	-79	1.379	0.291	-1.5
128	1.528	-88	1.533	0.059	-1.527
129	1.528	-97	1.686	-0.175	-1.518
130	1.528	-105	1.839	-0.405	-1.473
131	1.528	-114	1.992	-0.625	-1.394
132	1.528	-123	2.146	-0.831	-1.283
133	1.528	-132	2.299	-1.017	-1.141
134	1.528	-140	2.452	-1.179	-0.972
135	1.528	-149	2.605	-1.313	-0.781
136	1.528	-158	2.759	-1.417	-0.571
137	1.528	-167	2.912	-1.488	-0.348
138	1.528	-176	3.065	-1.524	-0.117
139	1.528	-184	3.218	-1.524	0.117
140	1.528	-193	3.372	-1.488	0.348
141	1.528	-202	3.525	-1.417	0.571
142	1.528	-211	3.678	-1.313	0.781
143	1.528	-220	3.831	-1.179	0.972
144	1.528	-228	3.985	-1.017	1.141
145	1.528	-237	4.138	-0.831	1.283
146	1.528	-246	4.291	-0.625	1.394
147	1.528	-255	4.444	-0.405	1.473
148	1.528	-263	4.598	-0.175	1.518
149	1.528	-272	4.751	0.059	1.527
150	1.528	-281	4.904	0.291	1.5
151	1.528	-290	5.057	0.516	1.438
152	1.528	-299	5.21	0.73	1.342
153	1.528	-307	5.364	0.926	1.215
154	1.528	-316	5.517	1.101	1.06
155	1.528	-325	5.67	1.25	0.879
156	1.528	-334	5.823	1.369	0.678
157	1.528	-342	5.977	1.457	0.461
158	1.528	-351	6.13	1.51	0.233
159	1.747	0	0	1.747	0
160	1.747	-8	0.134	1.731	-0.233
161	1.747	-15	0.267	1.685	-0.462
162	1.747	-23	0.401	1.608	-0.682
163	1.747	-31	0.535	1.503	-0.89

Table D.1 Traverser Grid Coordinates (cont.)

Node Number	Radial Position [in]	Angular Position (θ, [deg])	Angular Position (θ, [rad])	X coordinate (+ ∥ θ = 0°) [in]	Y coordinate (− ∥ θ = 90°) [in]
164	1.747	-38	0.668	1.371	-1.083
165	1.747	-46	0.802	1.215	-1.256
166	1.747	-54	0.936	1.036	-1.406
167	1.747	-61	1.07	0.84	-1.532
168	1.747	-69	1.203	0.628	-1.63
169	1.747	-77	1.337	0.405	-1.699
170	1.747	-84	1.471	0.175	-1.738
171	1.747	-92	1.604	-0.058	-1.746
172	1.747	-100	1.738	-0.291	-1.723
173	1.747	-107	1.872	-0.518	-1.669
174	1.747	-115	2.005	-0.735	-1.585
175	1.747	-123	2.139	-0.94	-1.472
176	1.747	-130	2.273	-1.128	-1.334
177	1.747	-138	2.406	-1.296	-1.172
178	1.747	-146	2.54	-1.44	-0.989
179	1.747	-153	2.674	-1.559	-0.788
180	1.747	-161	2.807	-1.65	-0.573
181	1.747	-169	2.941	-1.712	-0.348
182	1.747	-176	3.075	-1.743	-0.117
183	1.747	-184	3.208	-1.743	0.117
184	1.747	-191	3.342	-1.712	0.348
185	1.747	-199	3.476	-1.65	0.573
186	1.747	-207	3.61	-1.559	0.788
187	1.747	-214	3.743	-1.44	0.989
188	1.747	-222	3.877	-1.296	1.172
189	1.747	-230	4.011	-1.128	1.334
190	1.747	-237	4.144	-0.94	1.473
191	1.747	-245	4.278	-0.735	1.585
192	1.747	-253	4.412	-0.518	1.669
193	1.747	-260	4.545	-0.291	1.723
194	1.747	-268	4.679	-0.058	1.746
195	1.747	-276	4.813	0.175	1.738
196	1.747	-283	4.946	0.405	1.699
197	1.747	-291	5.08	0.628	1.63
198	1.747	-299	5.214	0.84	1.532
199	1.747	-306	5.347	1.036	1.406
200	1.747	-314	5.481	1.215	1.256
201	1.747	-322	5.615	1.371	1.083
202	1.747	-329	5.748	1.503	0.89
203	1.747	-337	5.882	1.608	0.682
204	1.747	-345	6.016	1.685	0.462
205	1.747	-352	6.15	1.731	0.233

Table D.1 Traverser Grid Coordinates (cont.)

Node Number	Radial Position [in]	Angular Position (θ, [deg])	Angular Position (θ, [rad])	X coordinate (+ ‖ θ = 0°) [in]	Y coordinate (– ‖ θ = 90°) [in]
206	1.965	0	0	1.965	0
207	1.965	-7	0.119	1.951	-0.233
208	1.965	-14	0.237	1.91	-0.462
209	1.965	-20	0.356	1.842	-0.684
210	1.965	-27	0.474	1.748	-0.897
211	1.965	-34	0.593	1.63	-1.098
212	1.965	-41	0.711	1.489	-1.283
213	1.965	-48	0.83	1.326	-1.45
214	1.965	-54	0.948	1.146	-1.597
215	1.965	-61	1.067	0.949	-1.721
216	1.965	-68	1.186	0.739	-1.821
217	1.965	-75	1.304	0.518	-1.896
218	1.965	-82	1.423	0.29	-1.943
219	1.965	-88	1.541	0.058	-1.964
220	1.965	-95	1.66	-0.174	-1.957
221	1.965	-102	1.778	-0.405	-1.923
222	1.965	-109	1.897	-0.629	-1.862
223	1.965	-115	2.015	-0.845	-1.774
224	1.965	-122	2.134	-1.049	-1.662
225	1.965	-129	2.253	-1.238	-1.526
226	1.965	-136	2.371	-1.41	-1.369
227	1.965	-143	2.49	-1.562	-1.192
228	1.965	-149	2.608	-1.692	-0.999
229	1.965	-156	2.727	-1.798	-0.792
230	1.965	-163	2.845	-1.879	-0.574
231	1.965	-170	2.964	-1.934	-0.348
232	1.965	-177	3.082	-1.962	-0.116
233	1.965	-183	3.201	-1.962	0.116
234	1.965	-190	3.319	-1.934	0.348
235	1.965	-197	3.438	-1.879	0.574
236	1.965	-204	3.557	-1.798	0.792
237	1.965	-211	3.675	-1.692	0.999
238	1.965	-217	3.794	-1.562	1.192
239	1.965	-224	3.912	-1.41	1.369
240	1.965	-231	4.031	-1.238	1.526
241	1.965	-238	4.149	-1.049	1.662
242	1.965	-245	4.268	-0.845	1.774
243	1.965	-251	4.386	-0.629	1.862
244	1.965	-258	4.505	-0.405	1.923
245	1.965	-265	4.624	-0.174	1.957
246	1.965	-272	4.742	0.058	1.964
247	1.965	-278	4.861	0.29	1.943

Table D.1 Traverser Grid Coordinates (cont.)

Node Number	Radial Position [in]	Angular Position (θ, [deg])	Angular Position (θ, [rad])	X coordinate (+ ∥ θ = 0°) [in]	Y coordinate (– ∥ θ = 90°) [in]
248	1.965	-285	4.979	0.518	1.896
249	1.965	-292	5.098	0.739	1.821
250	1.965	-299	5.216	0.949	1.721
251	1.965	-306	5.335	1.146	1.597
252	1.965	-312	5.453	1.326	1.45
253	1.965	-319	5.572	1.489	1.283
254	1.965	-326	5.69	1.63	1.098
255	1.965	-333	5.809	1.748	0.897
256	1.965	-340	5.928	1.842	0.684
257	1.965	-346	6.046	1.91	0.462
258	1.965	-353	6.165	1.951	0.232

Table D.2a Fully Developed and Uniform Profile Data

	Fully Developed, High		Fully Developed, Low		Uniform Velocity	
Node Number	Mean Velocity [m/s]	Standard Deviation [m/s x100]	Mean Velocity [m/s]	Standard Deviation [m/s x100]	Mean Velocity [m/s]	Standard Deviation [m/s x100]
1	2.854	4.991	2.635	4.707	2.804	2.119
2	2.841	4.977	2.629	4.834	2.825	2.021
3	2.815	5.056	2.610	5.169	2.797	2.032
4	2.823	5.847	2.610	4.887	2.765	2.196
5	2.867	5.445	2.656	5.321	2.797	2.078
6	2.884	4.665	2.676	4.485	2.875	2.161
7	2.859	4.455	2.666	4.536	2.838	2.269
8	2.838	4.976	2.634	4.347	2.783	2.138
9	2.797	5.117	2.595	4.962	2.785	2.268
10	2.767	5.981	2.562	5.048	2.707	2.315
11	2.796	6.564	2.564	5.840	2.799	2.316
12	2.859	6.368	2.642	6.094	2.765	2.165
13	2.899	4.907	2.693	4.829	2.811	2.300
14	2.925	4.011	2.711	4.148	2.861	2.154
15	2.923	4.288	2.706	4.083	2.893	2.191
16	2.888	4.504	2.676	4.029	2.873	2.148
17	2.855	5.232	2.650	4.117	2.800	2.075
18	2.817	5.069	2.621	4.561	2.824	1.838
19	2.777	5.061	2.590	5.087	2.772	2.089
20	2.743	5.902	2.547	5.062	2.809	2.098
21	2.709	6.264	2.522	5.747	2.768	1.971
22	2.741	7.356	2.531	6.650	2.792	2.047
23	2.780	7.746	2.559	7.277	2.836	2.032
24	2.860	7.236	2.626	7.093	2.834	1.961
25	2.902	5.694	2.686	6.375	2.852	1.979
26	2.945	4.684	2.727	4.879	2.839	1.921
27	2.960	4.211	2.746	3.965	2.857	1.908
28	2.964	5.409	2.752	3.482	2.834	1.932
29	2.952	3.726	2.742	3.917	2.826	2.046
30	2.939	4.221	2.732	3.871	2.865	2.063
31	2.918	4.429	2.709	4.178	2.850	2.046
32	2.887	4.555	2.686	4.009	2.779	2.359
33	2.878	4.644	2.683	4.328	2.730	2.342
34	2.844	4.737	2.647	4.510	2.770	2.106
35	2.805	5.646	2.614	4.521	2.759	2.183
36	2.765	6.265	2.588	6.031	2.771	2.279
37	2.729	5.943	2.545	5.948	2.811	2.057
38	2.695	6.949	2.509	5.904	2.799	2.224

Table D.2a Fully Developed and Uniform Profile Data (cont.)

	Fully Developed, High		Fully Developed, Low		Uniform Velocity	
Node Number	Mean Velocity [m/s]	Standard Deviation [m/s x100]	Mean Velocity [m/s]	Standard Deviation [m/s x100]	Mean Velocity [m/s]	Standard Deviation [m/s x100]
39	2.696	7.163	2.494	6.344	2.778	2.341
40	2.688	8.653	2.480	7.373	2.779	2.187
41	2.725	9.548	2.511	9.338	2.816	2.163
42	2.792	9.770	2.589	8.180	2.786	2.169
43	2.877	7.833	2.633	8.002	2.805	2.290
44	2.925	6.450	2.700	6.793	2.751	2.230
45	2.953	5.399	2.734	5.397	2.737	2.354
46	2.977	3.769	2.765	3.743	2.854	2.194
47	2.984	3.476	2.769	3.438	2.868	2.271
48	2.987	3.362	2.778	3.030	2.882	2.262
49	2.991	2.807	2.781	3.105	2.796	2.204
50	2.975	3.524	2.768	3.076	2.864	2.212
51	2.968	3.548	2.758	3.308	2.828	2.299
52	2.956	4.119	2.743	3.948	2.888	2.025
53	2.932	4.396	2.724	4.156	2.845	2.154
54	2.905	4.758	2.704	4.236	2.773	2.173
55	2.913	4.627	2.710	4.524	2.746	2.162
56	2.883	5.436	2.689	4.209	2.752	1.972
57	2.846	6.621	2.652	5.234	2.608	2.333
58	2.821	6.449	2.626	6.055	2.693	2.161
59	2.776	7.651	2.592	7.062	2.713	2.090
60	2.732	7.982	2.549	7.539	2.752	2.204
61	2.705	8.861	2.509	7.742	2.823	1.929
62	2.662	7.740	2.470	7.761	2.753	1.966
63	2.646	8.349	2.423	7.669	2.784	1.973
64	2.659	9.463	2.431	8.112	2.811	2.223
65	2.694	10.958	2.463	9.260	2.797	2.100
66	2.752	10.848	2.521	11.067	2.758	2.090
67	2.800	11.421	2.580	9.736	2.798	2.029
68	2.870	8.782	2.628	9.000	2.750	2.269
69	2.914	7.699	2.665	7.834	2.787	1.871
70	2.934	7.166	2.711	6.857	2.827	2.141
71	2.963	4.198	2.726	5.402	2.807	2.165
72	2.969	4.424	2.750	4.647	2.850	2.149
73	2.969	4.179	2.767	3.806	2.768	2.177
74	2.989	3.340	2.774	3.413	2.860	2.015
75	2.986	3.413	2.775	3.194	2.823	5.424
76	2.979	3.619	2.780	2.990	2.863	1.960
77	2.983	3.332	2.775	3.041	2.810	2.288
78	2.967	3.564	2.771	3.398	2.856	2.142
79	2.962	3.807	2.763	3.349	2.883	1.839

Table D.2a Fully Developed and Uniform Profile Data (cont.)

	Fully Developed, High		Fully Developed, Low		Uniform Velocity	
Node Number	Mean Velocity [m/s]	Standard Deviation [m/s x100]	Mean Velocity [m/s]	Standard Deviation [m/s x100]	Mean Velocity [m/s]	Standard Deviation [m/s x100]
80	2.944	4.147	2.753	3.508	2.800	2.262
81	2.944	3.838	2.739	3.650	2.773	2.160
82	2.910	4.755	2.722	3.830	2.808	2.229
83	2.904	5.698	2.712	3.994	2.767	2.091
84	2.884	6.250	2.697	4.552	2.681	2.302
85	2.861	5.961	2.679	4.609	2.672	2.302
86	2.819	7.813	2.651	5.895	2.690	2.393
87	2.765	10.248	2.522	9.878	2.708	1.978
88	2.736	9.165	2.469	9.055	2.697	2.094
89	2.713	9.642	2.431	9.928	2.743	2.091
90	2.655	9.587	2.424	8.627	2.756	2.144
91	2.638	10.078	2.381	8.533	2.748	2.038
92	2.609	10.254	2.409	9.925	2.755	1.903
93	2.605	9.796	2.441	10.509	2.730	1.953
94	2.595	9.770	2.476	10.928	2.747	2.184
95	2.620	11.700	2.549	11.041	2.772	1.974
96	2.656	12.583	2.591	9.032	2.807	2.078
97	2.701	11.958	2.586	10.760	2.781	2.125
98	2.732	12.345	2.650	8.119	2.749	2.173
99	2.804	10.290	2.669	7.325	2.700	1.982
100	2.828	9.324	2.666	7.274	2.769	2.148
101	2.830	9.581	2.684	6.641	2.759	2.118
102	2.878	7.474	2.708	5.166	2.781	1.769
103	2.881	6.856	2.725	4.482	2.790	1.911
104	2.911	6.909	2.723	4.907	2.754	1.784
105	2.927	5.788	2.740	4.205	2.813	1.783
106	2.941	5.412	2.745	4.606	2.809	1.835
107	2.956	4.394	2.749	4.048	2.798	1.794
108	2.949	4.680	2.751	4.184	2.778	1.879
109	2.961	4.458	2.752	3.892	2.783	1.862
110	2.968	4.024	2.758	4.028	2.793	1.828
111	2.966	3.936	2.750	5.824	2.746	1.910
112	2.968	3.958	2.747	3.810	2.721	2.008
113	2.962	4.261	2.737	4.423	2.835	1.893
114	2.953	4.289	2.720	4.732	2.842	1.717
115	2.945	4.198	2.718	5.483	2.768	1.822
116	2.939	4.435	2.695	6.009	2.720	1.884
117	2.917	5.164	2.667	7.572	2.697	2.047
118	2.855	7.507	2.605	8.994	2.740	1.833
119	2.841	7.247	2.583	9.705	2.705	1.934
120	2.815	9.034	2.555	9.984	2.688	1.864

Table D.2a Fully Developed and Uniform Profile Data (cont.)

	Fully Developed, High		Fully Developed, Low		Uniform Velocity	
Node Number	Mean Velocity [m/s]	Standard Deviation [m/s x100]	Mean Velocity [m/s]	Standard Deviation [m/s x100]	Mean Velocity [m/s]	Standard Deviation [m/s x100]
121	2.830	7.404	2.585	8.413	2.660	1.945
122	2.789	9.937	2.576	8.215	2.711	1.909
123	2.756	10.324	2.531	11.471	2.715	1.894
124	2.712	11.829	2.492	10.246	2.690	1.934
125	2.682	11.754	2.461	10.855	2.769	1.779
126	2.641	12.766	2.395	10.630	2.685	1.974
127	2.605	12.203	2.337	11.255	2.734	1.789
128	2.554	12.895	2.330	10.547	2.705	1.712
129	2.519	12.503	2.339	10.159	2.738	1.813
130	2.521	10.535	2.331	10.371	2.711	1.674
131	2.520	12.153	2.309	9.879	2.748	1.741
132	2.544	13.027	2.343	11.048	2.762	1.719
133	2.543	11.741	2.391	12.779	2.734	1.752
134	2.602	12.040	2.426	10.977	2.796	1.711
135	2.651	11.608	2.431	10.803	2.762	1.759
136	2.664	9.870	2.474	11.684	2.686	1.850
137	2.715	8.913	2.519	7.868	2.672	1.794
138	2.737	8.525	2.552	7.302	2.709	1.912
139	2.755	7.830	2.564	7.183	2.763	1.643
140	2.758	7.279	2.569	6.483	2.817	1.777
141	2.756	7.551	2.573	6.853	2.787	1.702
142	2.778	7.439	2.588	6.386	2.790	1.594
143	2.799	6.358	2.620	5.627	2.748	1.648
144	2.803	6.602	2.626	6.740	2.789	1.809
145	2.816	6.712	2.629	5.919	2.727	1.782
146	2.822	6.674	2.633	5.634	2.757	1.659
147	2.847	6.750	2.648	5.408	2.743	1.692
148	2.850	6.351	2.653	5.585	2.796	1.771
149	2.857	6.690	2.663	5.046	2.742	1.776
150	2.861	5.720	2.673	5.256	2.697	1.738
151	2.871	5.533	2.674	5.435	2.729	1.795
152	2.883	5.733	2.682	4.756	2.650	1.824
153	2.888	5.499	2.689	5.046	2.732	1.728
154	2.894	5.545	2.685	5.122	2.790	1.738
155	2.887	5.419	2.691	5.224	2.785	1.727
156	2.893	5.293	2.675	5.617	2.761	1.779
157	2.885	5.771	2.673	5.126	2.688	1.697
158	2.879	6.348	2.658	6.813	2.746	1.793
159	2.697	8.459	2.497	6.602	2.705	2.030
160	2.709	7.576	2.505	7.252	2.624	1.994
161	2.706	7.283	2.500	7.800	2.582	2.106

Table D.2a Fully Developed and Uniform Profile Data (cont.)

	Fully Developed, High		Fully Developed, Low		Uniform Velocity	
Node Number	Mean Velocity [m/s]	Standard Deviation [m/s x100]	Mean Velocity [m/s]	Standard Deviation [m/s x100]	Mean Velocity [m/s]	Standard Deviation [m/s x100]
162	2.694	8.491	2.470	9.134	2.665	1.932
163	2.665	9.630	2.457	9.317	2.690	1.788
164	2.673	7.739	2.448	9.897	2.673	1.855
165	2.662	7.656	2.420	9.929	2.693	1.863
166	2.604	10.421	2.352	12.667	2.730	1.708
167	2.573	12.645	2.342	11.950	2.662	1.913
168	2.531	13.649	2.320	12.090	2.673	1.803
169	2.522	12.651	2.301	12.591	2.678	1.765
170	2.464	13.214	2.233	12.359	2.656	2.146
171	2.455	11.927	2.212	11.490	2.628	2.088
172	2.419	12.489	2.208	10.346	2.718	1.776
173	2.366	12.157	2.224	10.709	2.713	1.787
174	2.365	11.606	2.257	11.349	2.702	1.740
175	2.350	11.206	2.295	9.332	2.687	1.880
176	2.365	10.802	2.304	10.561	2.706	2.012
177	2.377	12.001	2.341	9.306	2.740	1.912
178	2.383	11.480	2.372	9.545	2.740	1.631
179	2.433	10.371	2.377	8.395	2.738	1.561
180	2.462	10.731	2.383	8.790	2.683	1.866
181	2.481	10.592	2.377	8.133	2.638	1.931
182	2.503	10.442	2.404	7.245	2.605	2.044
183	2.527	9.634	2.416	8.197	2.664	1.953
184	2.539	8.309	2.408	7.280	2.694	1.731
185	2.570	8.852	2.425	7.101	2.622	1.959
186	2.579	8.009	2.436	6.492	2.689	1.901
187	2.589	8.342	2.436	7.248	2.549	2.174
188	2.602	6.898	2.443	6.986	2.585	2.216
189	2.616	7.419	2.466	6.429	2.700	1.805
190	2.630	6.816	2.465	6.756	2.750	1.790
191	2.636	7.423	2.484	6.698	2.507	2.527
192	2.639	7.792	2.468	7.423	2.661	2.063
193	2.652	7.124	2.483	6.662	2.658	2.139
194	2.656	7.029	2.488	7.289	2.682	1.864
195	2.669	7.289	2.490	7.169	2.578	2.206
196	2.692	7.058	2.516	5.998	2.481	2.322
197	2.675	8.358	2.502	6.889	2.694	1.984
198	2.692	6.564	2.497	7.542	2.549	2.264
199	2.709	6.517	2.513	6.573	2.574	2.163
200	2.704	7.432	2.519	7.167	2.600	2.194
201	2.713	6.203	2.521	7.040	2.553	2.991
202	2.718	6.794	2.511	7.090	2.638	2.303

Table D.2a Fully Developed and Uniform Profile Data (cont.)

	Fully Developed, High		Fully Developed, Low		Uniform Velocity	
Node Number	Mean Velocity [m/s]	Standard Deviation [m/s x100]	Mean Velocity [m/s]	Standard Deviation [m/s x100]	Mean Velocity [m/s]	Standard Deviation [m/s x100]
203	2.722	6.965	2.517	7.506	2.590	2.337
204	2.726	7.628	2.493	9.011	2.593	2.208
205	2.723	7.568	2.498	8.872	2.681	2.289
206	2.230	8.635	2.053	8.830	2.111	3.669
207	2.231	7.953	2.019	10.312	2.166	3.611
208	2.207	9.142	2.023	9.973	2.102	3.388
209	2.187	10.475	2.009	9.473	2.174	3.411
210	2.146	11.460	2.000	11.281	2.398	3.095
211	2.206	9.571	1.976	10.733	2.014	3.389
212	2.188	10.926	1.943	10.396	2.196	3.107
213	2.178	10.160	1.924	11.335	2.324	3.007
214	2.185	10.304	1.898	11.151	2.351	3.240
215	2.157	11.729	1.886	11.198	2.461	2.639
216	2.116	10.699	1.883	11.049	2.040	3.366
217	2.087	11.630	1.867	9.957	2.205	3.360
218	2.075	11.820	1.870	10.151	2.204	3.259
219	2.046	11.037	1.868	9.761	2.060	3.679
220	2.021	11.939	1.859	9.880	2.144	3.420
221	2.017	11.332	1.865	9.854	2.327	3.125
222	2.003	10.974	1.896	9.002	2.128	3.452
223	1.973	10.962	1.913	8.645	2.048	3.489
224	1.998	10.721	1.913	8.931	2.180	3.214
225	1.998	10.108	1.925	8.372	2.105	3.484
226	1.993	10.740	1.941	9.114	2.165	3.881
227	2.046	10.841	1.952	8.484	2.113	3.639
228	2.045	10.744	1.959	9.175	2.227	3.226
229	2.058	10.341	1.979	7.854	2.203	3.334
230	2.070	8.850	1.997	7.516	2.253	3.163
231	2.073	9.500	1.996	7.321	2.143	3.123
232	2.105	8.289	2.007	7.617	1.939	4.195
233	2.098	9.391	2.013	7.567	2.027	3.393
234	2.129	8.799	2.006	6.869	2.237	3.305
235	2.140	8.014	2.010	7.911	2.040	3.564
236	2.157	8.733	2.021	7.825	2.132	3.592
237	2.151	7.277	2.029	7.860	1.942	4.009
238	2.164	7.359	2.031	7.457	2.068	3.488
239	2.170	7.960	2.046	6.645	2.217	3.659
240	2.184	7.124	2.033	6.322	2.249	3.492
241	2.195	7.778	2.054	6.448	2.299	3.546
242	2.201	7.230	2.047	7.205	1.965	3.756
243	2.190	7.956	2.043	7.140	1.971	3.953

Table D.2a Fully Developed and Uniform Profile Data (cont.)

	Fully Developed, High		Fully Developed, Low		Uniform Velocity	
Node Number	Mean Velocity [m/s]	Standard Deviation [m/s x100]	Mean Velocity [m/s]	Standard Deviation [m/s x100]	Mean Velocity [m/s]	Standard Deviation [m/s x100]
244	2.193	7.871	2.050	7.170	2.033	3.706
245	2.194	7.758	2.055	6.889	2.110	3.598
246	2.210	7.818	2.048	6.924	1.976	3.951
247	2.211	6.991	2.060	7.225	1.932	3.675
248	2.213	7.215	2.056	6.593	2.121	3.341
249	2.214	7.102	2.068	7.257	2.350	2.872
250	2.227	6.784	2.056	7.023	1.899	3.534
251	2.239	7.594	2.079	6.603	1.973	3.748
252	2.247	6.909	2.071	7.207	2.021	3.540
253	2.246	6.602	2.079	6.674	1.973	4.048
254	2.250	7.141	2.053	7.007	2.022	3.702
255	2.271	6.804	2.062	7.722	2.071	3.487
256	2.256	6.482	2.059	7.618	2.067	3.482
257	2.271	7.345	2.060	8.210	2.117	3.398
258	2.262	7.590	2.063	8.758	2.163	2.932

Table D.2b Orifice Distorted and Elbow Distorted Data

	Orifice Distorted		Elbow Distorted	
Node Number	Mean Velocity [m/s]	Standard Deviation [m/s]	Mean Velocity [m/s]	Standard Deviation [m/s x100]
1	4.713	1.056	1.890	10.273
2	6.845	0.916	2.141	14.170
3	5.251	1.129	1.934	11.490
4	4.053	1.392	1.806	8.313
5	3.000	1.102	1.814	7.322
6	3.818	1.178	1.969	10.142
7	5.198	1.020	2.126	12.352
8	8.794	0.866	2.455	14.048
9	8.426	1.292	2.245	14.875
10	5.377	2.029	1.893	11.502
11	3.002	1.955	1.803	7.700
12	1.706	1.521	1.893	7.526
13	1.522	1.379	1.874	7.811
14	2.924	1.669	2.076	10.518
15	4.253	1.789	2.428	11.706
16	8.516	1.287	2.566	11.818
17	11.228	0.915	2.803	7.909
18	11.275	1.086	2.732	9.352
19	10.188	1.491	2.569	11.560
20	7.126	2.412	2.314	13.192
21	3.737	2.487	2.015	11.169
22	2.867	2.069	1.825	10.313
23	1.535	1.771	1.848	8.655
24	0.581	1.509	1.969	8.497
25	0.616	1.305	1.913	8.522
26	0.711	1.363	1.894	9.153
27	1.118	1.468	2.078	10.169
28	1.941	1.772	2.366	9.473
29	2.787	2.283	2.578	9.860
30	4.940	2.134	2.707	7.630
31	9.988	1.461	2.776	7.382
32	10.526	1.480	2.808	7.666
33	13.089	0.900	2.934	4.742
34	13.059	0.958	2.914	5.674
35	11.963	1.544	2.880	6.258
36	10.091	1.875	2.790	8.091
37	7.411	2.150	2.622	11.311
38	3.335	2.609	2.407	12.647

Table D.2b Orifice Distorted and Elbow Distorted Profile Data (cont.)

	Orifice Distorted		Elbow Distorted	
Node Number	Mean Velocity [m/s]	Standard Deviation [m/s]	Mean Velocity [m/s]	Standard Deviation [m/s x100]
39	1.764	2.103	2.132	12.859
40	1.014	1.667	1.937	10.388
41	0.869	1.526	1.908	8.853
42	0.788	1.452	1.987	8.175
43	0.229	1.206	2.103	7.959
44	0.204	1.170	2.028	8.783
45	0.240	1.171	1.966	9.871
46	0.360	1.428	2.083	10.633
47	0.965	1.346	2.324	9.814
48	1.090	1.564	2.535	8.593
49	1.198	2.008	2.688	7.575
50	2.331	2.434	2.787	6.407
51	5.259	2.632	2.852	5.301
52	9.229	2.210	2.893	5.222
53	11.529	1.521	2.917	4.635
54	11.884	1.402	2.928	4.760
55	14.294	0.682	3.001	4.054
56	14.418	0.579	2.996	4.199
57	13.600	0.880	2.989	4.324
58	11.286	1.446	2.967	4.529
59	8.577	2.050	2.931	5.442
60	6.400	2.356	2.853	6.693
61	3.665	2.482	2.721	9.493
62	1.695	2.051	2.583	10.908
63	1.391	1.886	2.356	12.316
64	0.747	1.501	2.158	12.877
65	0.510	1.300	2.004	10.078
66	0.530	1.201	2.009	10.275
67	0.214	1.109	2.133	9.972
68	0.121	1.148	2.189	6.660
69	0.144	1.113	2.124	7.644
70	0.050	1.120	2.062	10.089
71	0.017	1.161	2.197	11.349
72	0.142	1.215	2.382	9.559
73	0.360	1.355	2.551	8.553
74	0.733	1.409	2.675	7.131
75	0.843	1.720	2.766	5.415
76	1.499	2.090	2.828	4.996
77	2.200	2.458	2.873	5.417
78	4.019	2.561	2.910	4.941
79	7.954	1.761	2.949	4.554

Table D.2b Orifice Distorted and Elbow Distorted Profile Data (cont.)

	Orifice Distorted		Elbow Distorted	
Node Number	Mean Velocity [m/s]	Standard Deviation [m/s]	Mean Velocity [m/s]	Standard Deviation [m/s x100]
80	10.672	1.688	2.970	4.536
81	11.953	1.889	2.993	4.082
82	13.427	1.303	2.995	4.144
83	14.853	0.430	3.039	4.625
84	14.777	0.422	3.037	4.387
85	14.021	0.702	3.039	4.490
86	12.491	0.847	3.034	4.323
87	9.780	1.276	3.020	4.161
88	7.376	1.570	2.997	4.330
89	5.675	1.816	2.969	4.812
90	3.817	2.230	2.920	5.114
91	2.285	2.244	2.863	5.572
92	1.668	1.896	2.782	7.491
93	1.152	1.696	2.671	9.120
94	0.536	1.255	2.526	10.788
95	0.496	1.171	2.364	10.785
96	0.271	1.141	2.204	12.553
97	0.076	1.180	2.160	11.520
98	0.226	1.035	2.250	11.221
99	0.249	1.068	2.279	7.855
100	0.441	0.986	2.215	7.103
101	0.087	1.121	2.213	7.856
102	0.002	1.068	2.246	8.569
103	0.074	1.174	2.390	8.502
104	0.084	1.141	2.526	7.359
105	0.127	1.176	2.616	6.609
106	0.291	1.236	2.698	5.461
107	0.165	1.276	2.761	5.327
108	0.431	1.420	2.799	5.364
109	0.583	1.541	2.843	5.228
110	0.954	1.729	2.883	5.243
111	2.088	2.146	2.917	5.135
112	3.543	2.110	2.946	5.241
113	5.925	1.647	2.965	5.140
114	8.485	1.602	2.984	5.195
115	10.745	1.489	3.002	4.974
116	13.065	1.284	3.010	4.633
117	14.113	0.891	3.013	4.574
118	14.742	0.290	3.040	4.661
119	14.518	0.311	3.038	5.042
120	13.709	0.423	3.039	5.034

Table D.2b Orifice Distorted and Elbow Distorted Profile Data (cont.)

	Orifice Distorted		Elbow Distorted	
Node Number	Mean Velocity [m/s]	Standard Deviation [m/s]	Mean Velocity [m/s]	Standard Deviation [m/s x100]
121	12.212	0.607	3.040	4.781
122	10.146	0.727	3.036	4.021
123	8.019	0.765	3.030	4.429
124	5.980	1.085	3.015	4.776
125	4.314	1.382	2.991	4.802
126	3.199	1.556	2.977	4.750
127	1.902	1.619	2.947	4.343
128	1.611	1.623	2.911	4.597
129	1.009	1.449	2.880	4.684
130	0.702	1.242	2.826	5.263
131	0.416	1.198	2.761	6.283
132	0.253	1.160	2.663	7.482
133	0.084	1.076	2.546	8.262
134	0.153	1.091	2.485	8.608
135	0.091	1.178	2.422	9.200
136	0.174	1.139	2.408	7.635
137	0.024	1.152	2.260	7.863
138	0.057	1.155	2.282	6.595
139	0.161	1.087	2.339	6.403
140	0.206	1.151	2.421	6.365
141	0.138	1.118	2.525	6.533
142	-0.080	1.188	2.610	5.580
143	0.054	1.142	2.678	5.196
144	0.125	1.160	2.730	5.331
145	0.196	1.171	2.774	5.186
146	0.174	1.150	2.811	5.125
147	0.117	1.250	2.849	4.938
148	0.364	1.431	2.883	5.281
149	0.776	1.499	2.911	5.448
150	0.794	1.583	2.941	5.631
151	2.057	1.671	2.971	5.258
152	3.120	1.742	2.991	5.467
153	4.827	1.482	3.002	5.521
154	6.750	1.093	3.016	5.664
155	9.274	0.975	3.029	5.509
156	11.466	0.936	3.042	5.088
157	13.158	0.772	3.041	5.556
158	14.365	0.475	3.046	5.183
159	13.360	0.411	3.060	5.131
160	13.129	0.520	3.067	5.183
161	12.673	0.572	3.061	5.138

Table D.2b Orifice Distorted and Elbow Distorted Profile Data (cont.)

	Orifice Distorted		Elbow Distorted	
Node Number	Mean Velocity [m/s]	Standard Deviation [m/s]	Mean Velocity [m/s]	Standard Deviation [m/s x100]
162	11.549	0.533	3.059	5.648
163	10.028	0.589	3.065	5.182
164	8.435	0.600	3.055	5.564
165	6.690	0.724	3.051	5.214
166	5.209	0.767	3.041	5.384
167	4.267	0.882	3.033	5.084
168	3.188	1.043	3.030	5.201
169	2.289	1.450	3.007	4.935
170	1.371	1.363	2.993	5.256
171	1.097	1.394	2.980	5.212
172	0.601	1.271	2.947	4.966
173	0.344	1.266	2.924	4.900
174	0.236	1.160	2.887	4.824
175	0.238	1.099	2.839	4.529
176	0.271	1.148	2.796	5.207
177	0.126	1.141	2.723	5.326
178	0.039	1.122	2.638	5.588
179	0.042	1.185	2.533	8.387
180	0.103	1.159	2.292	13.774
181	0.079	1.133	2.186	9.167
182	0.128	1.133	2.327	8.340
183	0.162	1.148	2.462	6.517
184	0.186	1.116	2.538	5.358
185	0.229	1.154	2.612	5.396
186	0.129	1.167	2.683	5.312
187	0.074	1.190	2.726	5.513
188	-0.014	1.224	2.768	4.946
189	0.107	1.195	2.810	5.182
190	0.029	1.202	2.844	4.865
191	0.150	1.210	2.888	5.000
192	0.151	1.251	2.911	5.691
193	0.129	1.287	2.934	5.470
194	0.494	1.370	2.950	5.527
195	0.765	1.458	2.974	5.787
196	1.362	1.443	2.986	5.993
197	1.652	1.585	3.003	6.050
198	3.423	1.058	3.016	6.165
199	4.229	1.069	3.028	5.896
200	5.858	0.774	3.036	6.171
201	7.622	0.786	3.039	6.023
202	9.230	0.770	3.038	6.820

Table D.2b Orifice Distorted and Elbow Distorted Profile Data (cont.)

	Orifice Distorted		Elbow Distorted	
Node Number	Mean Velocity [m/s]	Standard Deviation [m/s]	Mean Velocity [m/s]	Standard Deviation [m/s x100]
203	10.986	0.663	3.046	6.390
204	12.374	0.478	3.041	6.273
205	13.108	0.397	3.042	5.803
206	10.967	0.475	2.847	7.856
207	10.887	0.590	2.845	8.012
208	10.511	0.578	2.851	7.290
209	10.084	0.701	2.833	8.270
210	9.283	0.658	2.826	7.449
211	8.370	0.766	2.831	8.199
212	7.273	0.791	2.836	7.017
213	6.067	0.771	2.826	7.179
214	5.118	0.806	2.818	7.725
215	4.270	0.825	2.805	7.312
216	3.226	1.105	2.792	7.449
217	2.214	1.293	2.782	7.503
218	1.461	1.250	2.761	7.498
219	1.134	1.242	2.746	6.873
220	0.707	1.143	2.721	6.963
221	0.443	1.139	2.707	6.796
222	0.352	1.052	2.679	7.468
223	0.256	0.997	2.644	7.133
224	0.161	0.948	2.615	6.329
225	0.051	0.964	2.540	7.098
226	0.147	0.976	2.487	7.329
227	0.083	0.944	2.393	7.978
228	0.099	0.891	2.272	10.797
229	0.097	0.914	2.032	16.102
230	-0.015	0.899	1.809	11.655
231	0.070	0.929	1.850	10.892
232	0.168	0.924	2.055	11.702
233	0.018	0.970	2.198	9.267
234	0.094	0.936	2.323	7.688
235	0.130	0.946	2.391	6.673
236	0.240	0.909	2.460	6.550
237	0.155	0.954	2.503	6.238
238	0.004	0.992	2.546	6.740
239	0.019	0.995	2.570	6.821
240	0.022	1.008	2.595	7.149
241	0.072	1.015	2.629	6.960
242	-0.023	1.037	2.661	7.483
243	-0.128	1.076	2.674	7.977

Table D.2b Orifice Distorted and Elbow Distorted Profile Data (cont.)

	Orifice Distorted		Elbow Distorted	
Node Number	Mean Velocity [m/s]	Standard Deviation [m/s]	Mean Velocity [m/s]	Standard Deviation [m/s x100]
244	0.081	1.173	2.693	7.698
245	0.024	1.195	2.727	7.549
246	0.533	1.217	2.742	7.924
247	0.991	1.274	2.761	7.662
248	1.641	1.324	2.776	8.274
249	2.310	1.147	2.786	8.382
250	3.347	1.037	2.797	8.440
251	4.216	0.953	2.800	8.271
252	5.258	0.768	2.809	8.580
253	6.468	0.726	2.816	8.795
254	7.676	0.644	2.825	7.560
255	8.827	0.623	2.826	8.816
256	9.654	0.695	2.831	8.361
257	10.412	0.545	2.850	7.573
258	10.875	0.464	2.844	8.507

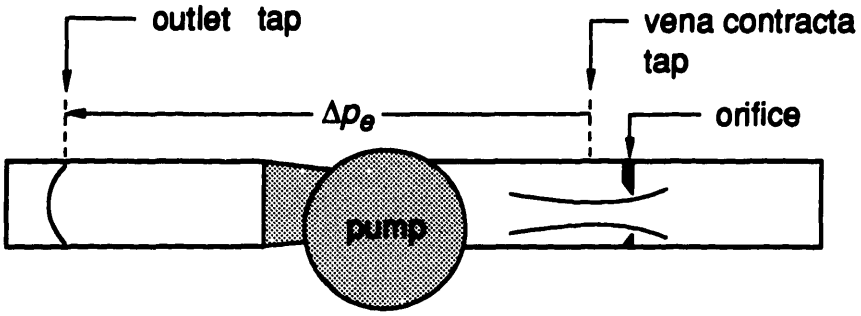

a. Actual experimental conditions: pressure rise across pump with inlet station at vena contracta of orifice.

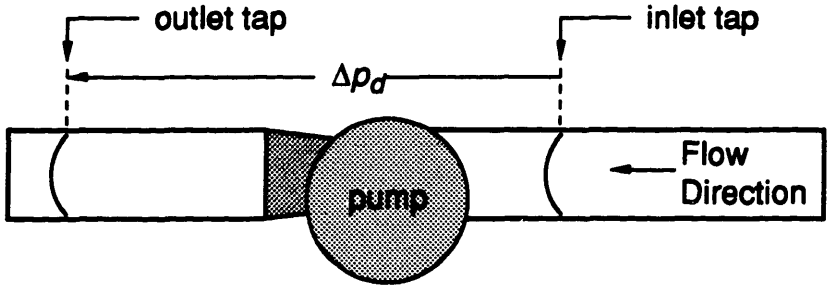

b. Desired conditions: pressure rise across pump with fully developed flow at both inlet and outlet stations.

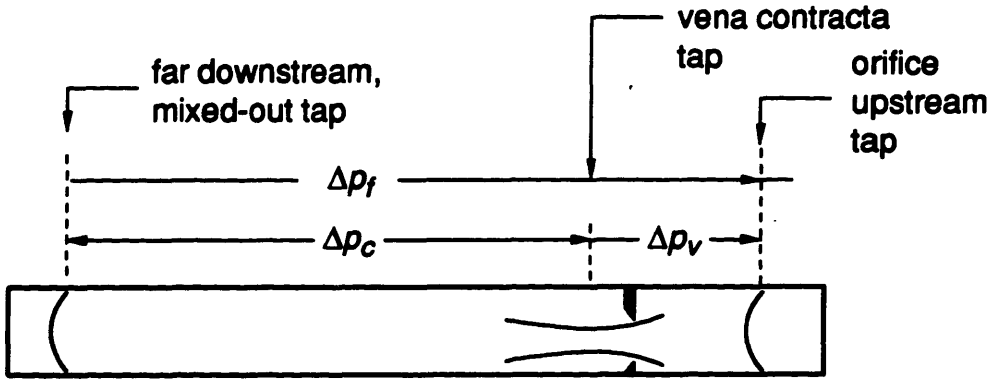

c. Correction Term: pressure rise across orifice with outlet tap at vena contracta and at fully developed conditions

Figure A.1 Model For Corrected Pump Pressure Rise with An Eccentric Orifice at the Pump Inlet

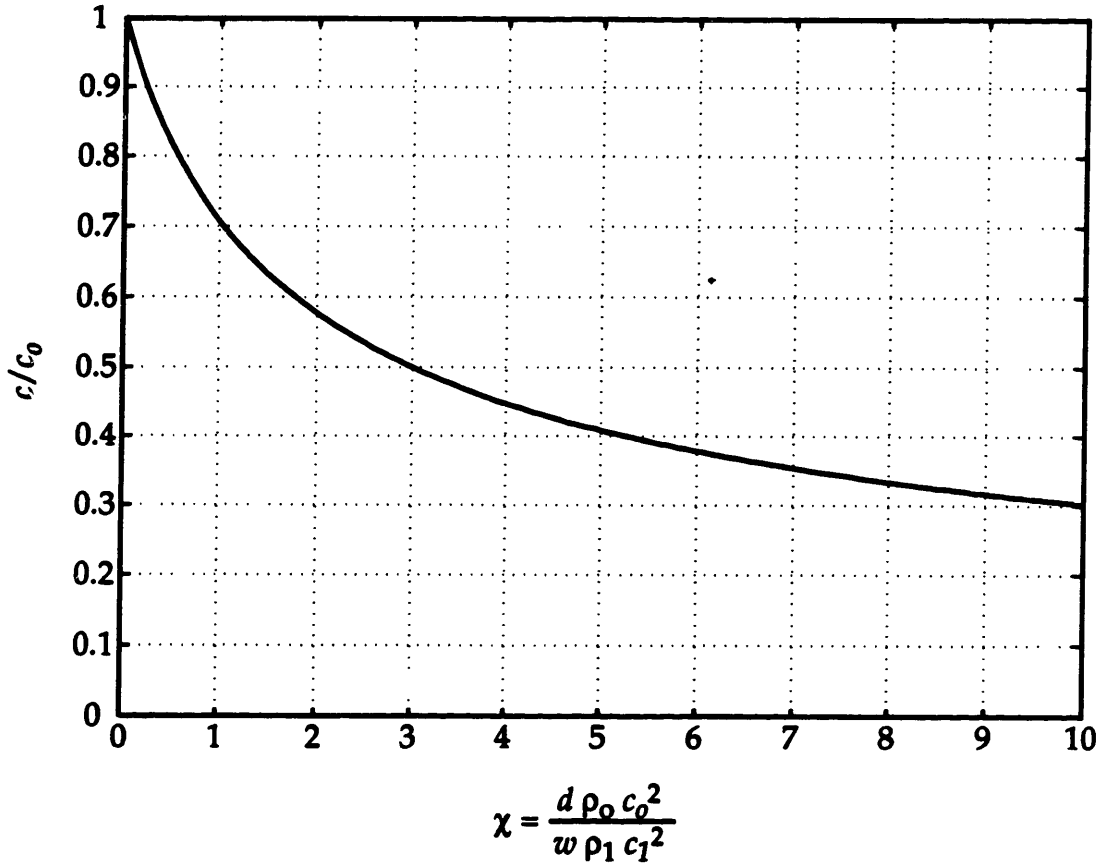

Figure B.3 Sound speed in a compliant cylindrical duct vs. the compliance parameter χ, where c is the fluid sound speed in the compliant duct, c_0 is the sound speed if the duct walls were rigid, d is the duct diameter, h is the duct thickness, and ρ is the mass density. The subscripts *0* and *1* refer to the fluid and duct material properties, respectively.

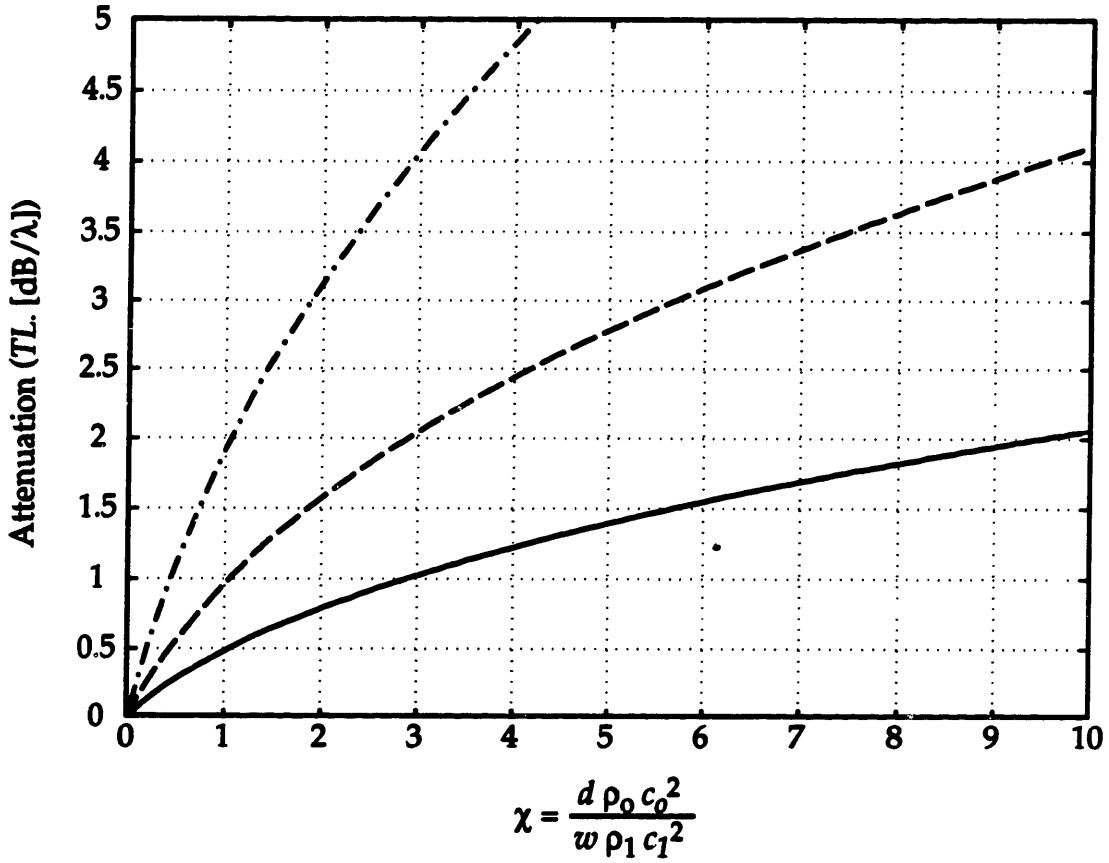

Figure B.4 Attenuation in deciBels per wavelength in a cylindrical duct with compliant walls vs. the compliance parameter χ, where c is the fluid sound speed in the compliant duct, c_0 is the sound speed if the duct walls were rigid, d is the duct diameter, w is the duct thickness, and ρ the mass density. The subscripts 0 and 1 refer to the fluid and duct material, respectively. ———: e = 0.025;
— — —: e = 0.05;
·—·—··: e = 0.10.

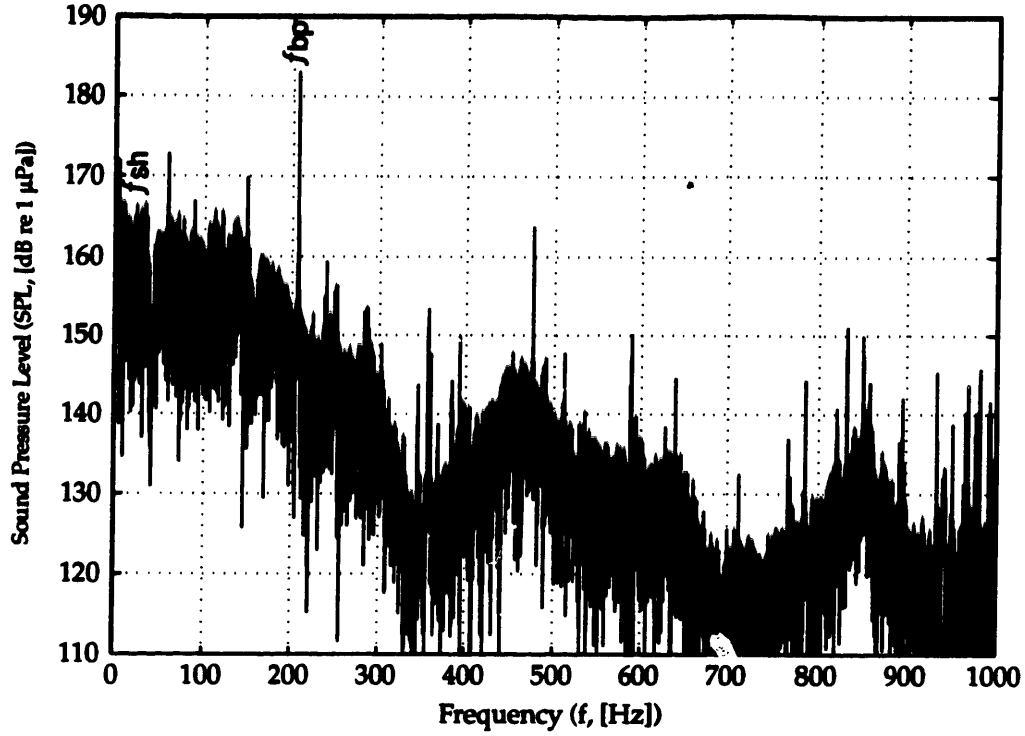

a. Typical Unaveraged Sound Pressure Level Spectrum.

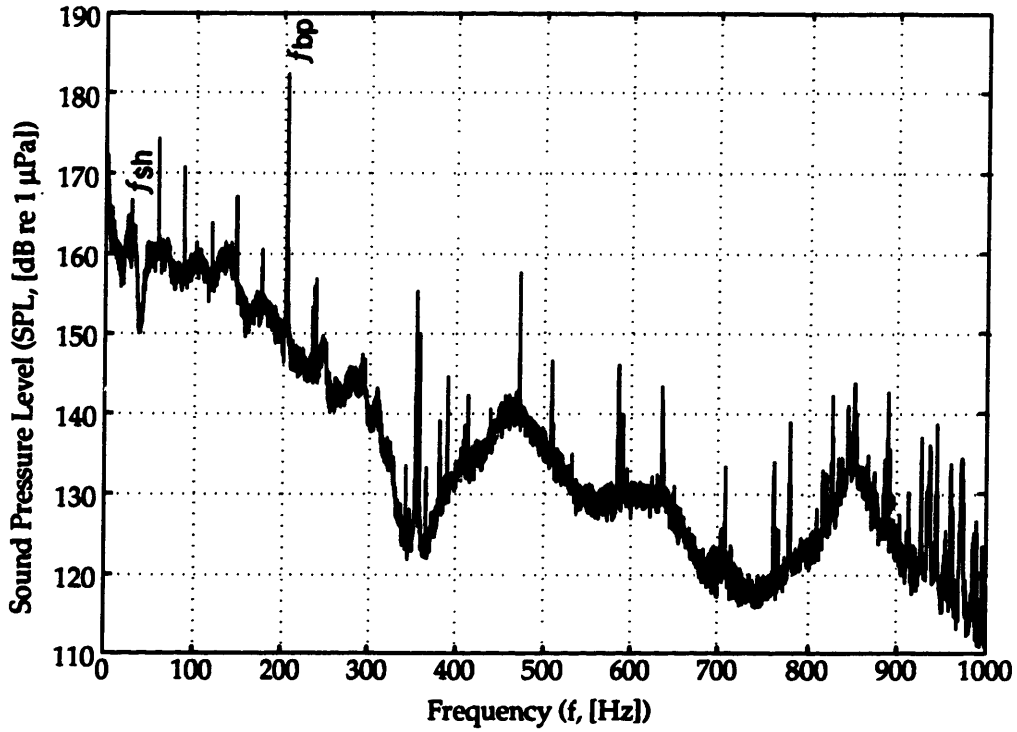

b. Average Sound Pressure Level Spectrum of 35 Data Sets

Figure C.1 Comparison of Averaged and Unaveraged Sound Pressure Level Spectra. Fully Developed, High Flow Case.
f_{sh} = Shaft frequency, f_{bp} = Blade Passage Frequency.

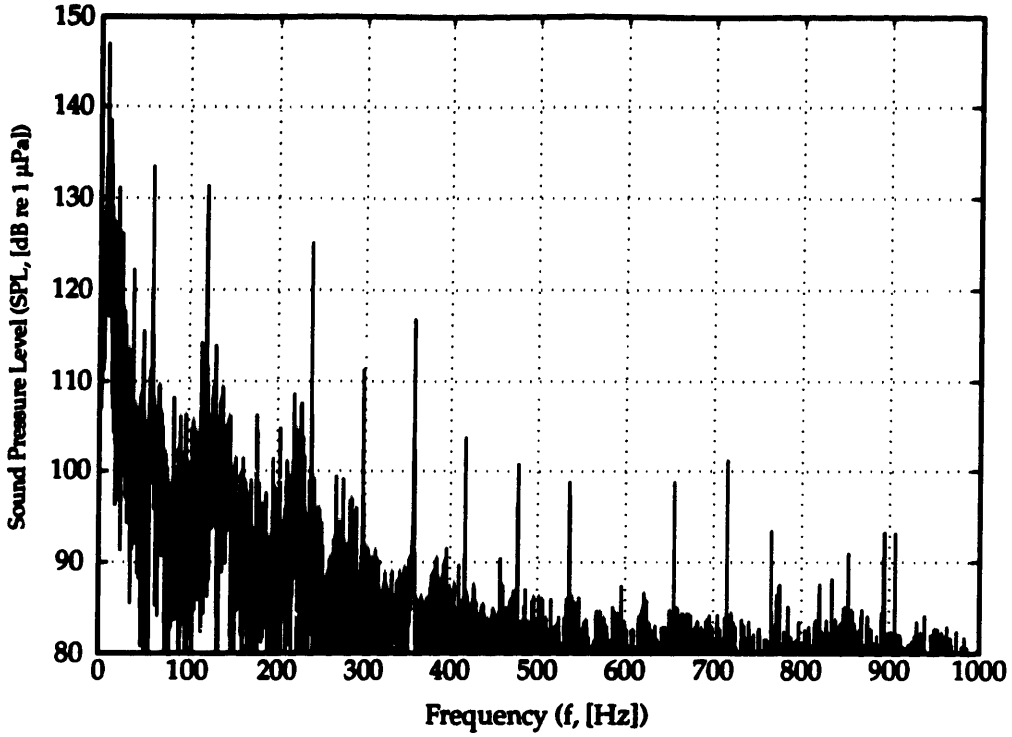

a. Typical Spectrum of Measured Background Sound Pressure Level with Pump Not Running.

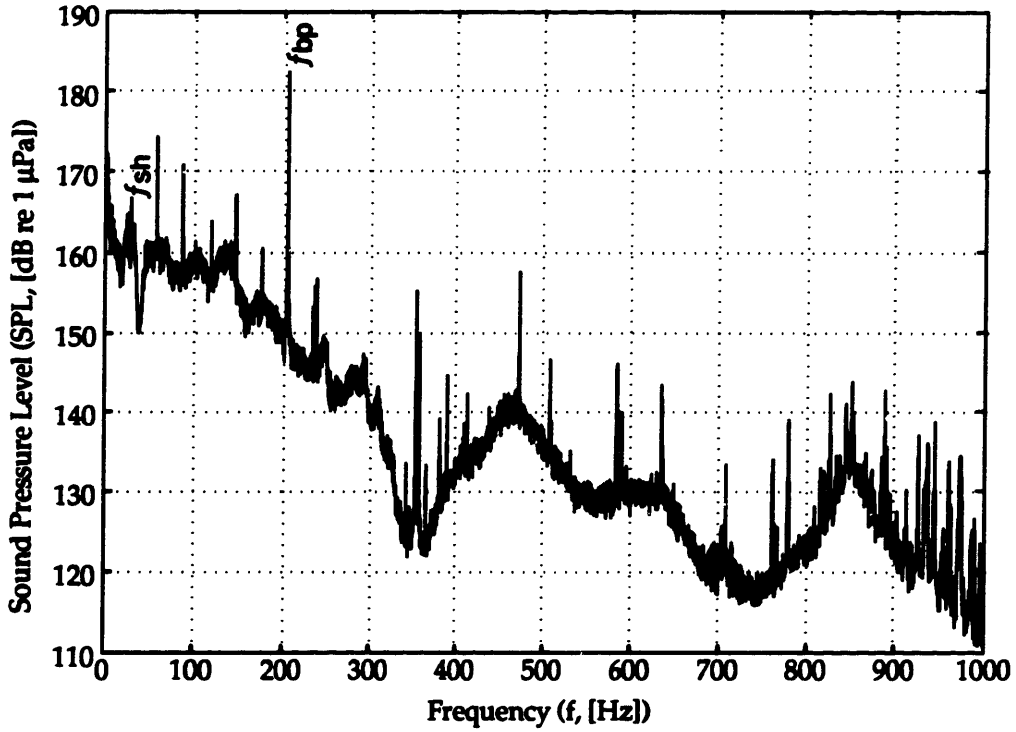

b. Pump Sound Pressure Level Spectrum with Pump Running.

Figure C.2 Comparison of Background Noise to Inlet Pump Noise Spectrum. *f*sh = Shaft Frequency; *f*bp = Blade Passage Frequency.